Improved shot noise limit of the YbF EDM experiment

by

Isabel Makeba Rabey

Thesis submitted in partial fulfilment for the requirements
for the degree of Doctor of Philosophy

Imperial College London

Department of Physics

November, 2016

Declaration of Authorship

I declare that this is my own work. Where I have used the work of others, the sources are appropriately referenced and acknowledged.

The copyright of this thesis rests with the author and is made available under a Creative Commons Attribution Non-Commercial No Derivatives licence. Researchers are free to copy, distribute or transmit the thesis on the condition that they attribute it, that they do not use it for commercial purposes and that they do not alter, transform or build upon it. For any reuse or redistribution, researchers must make clear to others the licence terms of this work

Abstract

The electron is predicted to have a small electric dipole moment (EDM). This fundamental property characterises the distortion of the electron's almost perfectly spherical charge distribution. The size of this distortion (d_e) is intimately connected to the breaking of time reversal symmetry (T) in nature. The Standard Model of particle physics, which contains a small amount of T-asymmetry, predicts a tiny, non-zero value of the electron EDM, $|d_e| \simeq 10^{-38}$ e.cm. However, many extensions to the Standard Model, which naturally include additional T-violating effects, also predict much larger values of d_e that should be detectable using current experimental techniques. Measurements of the electron's EDM constrains these theories, making these experiments a powerful tool in the search for physics beyond the Standard Model.

The most precise measurements of the electron EDM have been made using paramagnetic atoms and moleules. This thesis describes the progress made towards a new measurement of the electron EDM using the polar, paramagnetic molecule, YbF. A new state preparation technique is described that optically pumps most of the population from the first and second rotationally excited states into a single hyperfine component of the ground state. This increases the number of molecules entering the experiment by a factor of 6. A new state-selective detection scheme is also described, where multiple laser frequencies are used so that each molecule scatters many photons. This has increased detection efficiency by a factor of 20. In order to reduce magnetic noise in the experiment, new electric field plates have been introduced into the interaction region which have reduced the magnetic Johnson noise by a factor of 100. Together, these improvements increase statistical sensitivity by a factor of 11.4 over the last EDM measurement made using YbF. With an enhanced sensitivity of $\sigma_{d_e} = \left(5 \times 10^{-27}/\sqrt{N_\mathrm{b}}\right)$ e.cm, we can expect to measure the electron's EDM more precisely than ever before, constraining T-violating physics at a higher energy scale.

Acknowledgements

I have been very fortunate to work with and learn from such an amazing group of people, and I would like to acknowledge all of them. First and foremost, I would like to thank everyone who has contributed to this experiment, making it the monster it is today. To Joe, for introducing me to the world of precision measurement and to all the intricacies of the EDM experiment. To Jack, for being the most awesome teacher, collaborator and friend. I'm truly grateful to have shared the past few years with you. To Ben, for all your technical expertise (some of which you have passed on to me) and for all your motivational comments. To Mike, for your very prompt and detailed thesis corrections! Throughout the past few years, your thoughtful and clear explanations have helped me enormously. To Jony, even though you have abandoned me, I am very grateful for both your scientific and general life guidance. Finally, to Ed, for your enthusiasm and insight during our group meetings.

This experiment would also not be possible without the awesome technical support we receive from Jon, Steve and Gio, thank you. Also thanks to the one and only Sanja for all her administrative support. To the rest of CCM and CQD, and in particular, big shout out to the members of bay 3 and cohort 4 – you've made my PhD so much more than just physics and it has been an incredibly enjoyable experience.

Finally, thank you to all my friends, family, and especially to Graham, for all the love and support you have given me over the last few years. Your interest and enthusiasm in my work has been amazing and I couldn't have done it without you. This thesis is dedicated to you all.

Contents

Abstract ii
Acknowledgements iii

List of Figures **x**

List of Tables **xi**

1 Introduction **1**
1.1 Electric dipole moments 1
1.2 Measuring the size of the electron EDM 5
1.2.1 The EDM interaction in atoms and molecules 5
1.2.2 Choice of molecule? 7
1.2.3 Electron EDM measurements — past, present and future 8
1.3 Thesis overview 11

2 Overview of the experiment **12**
2.1 Principle of the experiment 12
2.2 YbF 13
2.2.1 Electronic structure 14
2.2.2 Vibrational, rotational and hyperfine structure of the X $^2\Sigma^+$ state . . 14
2.2.3 The A $^2\Pi_{1/2}$ state 16
2.2.4 Transitions 17
2.2.5 Simplified energy level structure 20
2.3 Experimental setup 21
2.3.1 Beam machine overview 21
2.3.2 Laser beam generation 23
2.3.3 Electric field generation 24
2.3.4 rf generation 25
2.3.5 Magnetic field generation 25
2.4 Experimental sequence 26
2.4.1 A shot 26
2.4.2 The simplest block 30
2.4.3 A real block 32
2.4.4 A cluster 34

2.5 Detectors and data analysis . . . 34
2.5.1 Detectors . . . 34
2.5.2 Extracting signals from detectors . . . 36
2.5.3 Analysis techniques . . . 38

3 Sensitivity and systematics **40**
3.1 Sensitivity . . . 40
3.1.1 Shot noise limit . . . 40
3.1.2 Increasing sensitivity . . . 43
3.1.3 Noise . . . 44
3.2 Systematic effects . . . 45
3.2.1 Introduction . . . 45
3.2.2 Current systematic effects . . . 46

4 The new pump scheme **49**
4.1 Introduction . . . 49
4.1.1 The new pump scheme . . . 50
4.1.2 How much population is available? . . . 51
4.1.3 How much population do we expect? . . . 52
4.2 Equipment . . . 54
4.2.1 Lasers . . . 54
4.2.2 Microwaves & rf . . . 56
4.2.3 Summary . . . 59
4.3 Results . . . 60
4.3.1 Introduction . . . 60
4.3.2 Spectroscopy: Looking at leftover population . . . 61
4.3.3 Spectroscopy: Signal gains . . . 66
4.3.4 Conclusion . . . 68

5 The new interaction region **69**
5.1 Introduction . . . 69
5.2 Magnetic Johnson noise . . . 70
5.2.1 Magnetic noise introduction . . . 70
5.2.2 Magnetic noise in the experiment . . . 72
5.3 Design . . . 74
5.3.1 Construction of gold film plates . . . 74
5.3.2 Mounting the field plates . . . 76
5.3.3 High voltage . . . 76
5.4 Performance . . . 78
5.4.1 Electric field uniformity . . . 78
5.4.2 Leakage currents . . . 79
5.5 Improvements to the rf system . . . 80

5.5.1 Conclusion . . . 82

6 The new probe region **84**
6.1 Introduction . . . 84
6.1.1 The new detection scheme . . . 85
6.1.2 How many photons can we scatter? . . . 86
6.1.3 How many photons do we expect to scatter? . . . 87
6.2 Equipment . . . 89
6.2.1 Microwaves . . . 90
6.2.2 Lasers . . . 91
6.2.3 Collection optics . . . 92
6.3 Results . . . 94
6.3.1 Introduction . . . 94
6.3.2 Spectroscopy: Single laser sideband . . . 97
6.3.3 Detecting in region A . . . 98
6.3.4 Detecting in both regions . . . 102
6.4 Conclusions . . . 104
6.5 Alternative scheme . . . 105
6.5.1 Introduction . . . 105
6.5.2 The lasers . . . 105
6.5.3 The microwaves . . . 106

7 Conclusions and Outlook **113**
7.1 Overview of improvements . . . 113
7.1.1 Experimental setup . . . 113
7.1.2 New experimental sequence: A shot . . . 115
7.1.3 New experimental sequence: A block . . . 119
7.2 Sensitivity . . . 121
7.2.1 Polarisation factor, η . . . 121
7.2.2 Contrast, $\mathcal{C}$ . . . 122
7.2.3 Number of photons, P^A, P^B . . . 123
7.2.4 Conclusion . . . 123
7.3 Outlook . . . 124

Bibliography **134**

List of Figures

1.1 P, T-violation of the electron 2
1.2 Review of electron EDM experimental upper limits 4
1.3 ηE_{eff} as a function of applied electric field for the YbF molecule 8
1.4 Schematic of the YbF fountain 10

2.1 An illustration of the spin precession technique used to measure the electron's EDM 12
2.2 Energy level diagram of the ground state of YbF, X $^2\Sigma^+$ 15
2.3 Energy level diagram of the first excited electronic state of YbF, A $^2\Pi_{1/2}$ . . 17
2.4 A diagram showing the relevant allowed transitions in YbF 18
2.5 Dark states created when pumping from a state of total angular momentum $F = 2$ to $F' = 1$ 20
2.6 Simplified energy level scheme of YbF 21
2.7 Front and side cross-section of the main vacuum chamber 22
2.8 Schematic overview of the hardware used to control the experiment 24
2.9 Optical pumping on Q(0)($F = 1$) 27
2.10 Stark and Zeeman shifts of the magnetic sublevels in X $^2\Sigma^+(v = 0, N = 0, F = 1)$ state 27
2.11 Energy level structure in the interaction region 28
2.12 An rf π-pulse 29
2.13 A second rf π-pulse 30
2.14 Detecting the population in $|0, 0\rangle$ using Q(0)($F = 0$) 31
2.15 The simplest block 32

3.1 A simple EDM experiment used to estimate the shot noise limit 41
3.2 Zeeman shifts caused by magnetic fields perpendicular and parallel to the electric field 45

4.1 Transitions driven in the improved pump scheme 50
4.2 Probability of occupying a state X $^2\Sigma^+(v = 0,\ N)$ for a given rotational temperature T 52
4.3 Predicted signal increase using the new pump scheme as a function of temperature T 53
4.4 Schematic overview of the hardware used to control the new pump scheme . . 55

4.5 Setup of the new pump region . . . 56
4.6 Back reflected power as a function of frequency for the resonant rf pump coils 58
4.7 A spectrum of the YbF molecular beam . . . 60
4.8 Pumping with Q(0)($F = 0$) . . . 62
4.9 Add in $N = 2$ sidebands . . . 63
4.10 Effects of polarisation modulation . . . 64
4.11 Add in microwaves . . . 64
4.12 Add in rf . . . 65
4.13 Population in $F = 0$ . . . 66
4.14 Rotational temperature dependence of the fractional signal increase . . . 67

5.1 Frequency sensitivity of a simplified EDM experiment . . . 72
5.2 Schematic cross-sections of the electric field plates . . . 72
5.3 Magnetic Johnson noise contributions . . . 73
5.4 Photos of the electric field plates . . . 76
5.5 Photos of the mounted electric field plates . . . 77
5.6 Photos of the high voltage connection to the electric field plates . . . 78
5.7 Fractional variation of the electric field . . . 79
5.8 Illustration of the leakage current path used to model the magnetic field generated by the leakage current . . . 80
5.9 Changes made to the rf system to reduce multipactor discharges . . . 81
5.10 Plot of the rf power required for a π-pulse in 10 μs . . . 82

6.1 The new detection scheme . . . 86
6.2 Average number of photons scattered per molecule, predicted by the rate equation model . . . 88
6.3 Schematic overview of the new hardware used to control the detection scheme 89
6.4 Microwave horn assembly . . . 90
6.5 New collection optics . . . 93
6.6 YbF spectrum from 542 806 GHz to 542 816 GHz . . . 95
6.7 P(1) spectrum . . . 96
6.8 Relevant microwave transitions and their frequencies . . . 96
6.9 Schematic of single frequency laser spectroscopy experiment . . . 97
6.10 Results of single frequency spectroscopy . . . 98
6.11 Schematic of the experiment used to test the new detection scheme . . . 99
6.12 Detecting with the full probe scheme in region A, looking for leftover population in region B . . . 101
6.13 Schematic of the experiment used to record interference fringes . . . 103
6.14 Interference fringes . . . 104
6.15 The alternative detection scheme . . . 106
6.16 Illustration of the transverse extent of the molecular beam in the detection region . . . 108

6.17 Designs of microwave π-pulse devices 109
6.18 π-pulse efficiency of the microwave waveguide 110
6.19 π-pulse efficiency of the microwave transmission line 112

7.1 Front and side cross-sections of the new beamline vacuum chamber 114
7.2 Schematic of the new pump scheme and time-of-flight profile 116
7.3 Stark shift and effective electric field in the new interaction region 117
7.4 Schematic of the microwave and laser fields used to detect the $F = 1$ population in region A 118
7.5 Schematic of the microwave and laser fields used to detect the $F = 0$ population in region B 119
7.6 Comparison of interference fringes 122

List of Tables

1.1 Effective electric field of some interesting molecules 8

2.1 Calculated J composition of each mixed hyperfine state in the $N = 1$ and $N = 2$ rotational states 16
2.2 Parameters held constant during a block 33
2.3 Switched parameters 33
2.4 List of single point detectors 35
2.5 List of time dependent detectors 35
2.6 Some interesting analysis channels and their meanings 37

3.1 Table of of current systematic errors and their contributions 47

4.1 Comparison of available experimental powers and interaction time with suggested requirements from OBE simulations 59
4.2 Fractional gain in signal from the new pump scheme 67

5.1 Summary of the Johnson noise analysis for the two electric field plate designs 74
5.2 Summary of magnetic Johnson noise contributions from other conductors . . 75

6.1 Table of microwave Clebsch-Gordon coefficients 96

7.1 Table of of current and projected systematic errors and their contributions . . 125

Chapter 1

Introduction

1.1 Electric dipole moments

The search for electric dipole moments (EDMs) dates back to the suggestion made by Purcell and Ramsey in 1950 [1]. They argued that the symmetries that forbid fundamental particles from having an EDM were based on assumptions, rather than experimental evidence. This paper challenged the well established point of view that the three discrete symmetries; space inversion (parity, P), the interchange of particles and anti-particles (charge conjugation, C), and time reversal (T), were all conserved operations.

A few years later, Lee and Yang also discussed the possibility that P-symmetry could be broken, this time by the weak interaction [2]. In 1957, less than a year after this proposal, the famous experiment by Wu *et al.* [3] did indeed confirm that parity is violated by the weak force. This lead to a flurry of experimental and theoretical activity, which confirmed P-violation of weak interactions in many different nuclear, particle and atomic physics experiments [4] [5].

In an attempt to reconcile this discovery with symmetry conservation, Landau [6] proposed that instead, it was the combined transformation of CP that was the symmetrical operation. However, this resolution did not last long and in 1964, CP-violation was observed for the first time in the neutral K meson system [7]. Since then, CP-violation has also been observed in both B meson [8] [9] [10] and D meson [11] experiments.

Despite these discoveries, the hope for an overall symmetry is not lost. It is now the total combined operation of C, P and T that is expected to always be conserved. Since any field theory that obeys the general constraints of Lorentz invariance and locality is also invariant under the CPT transformation [12], this symmetry is generally accepted to be true. In this case, to compensate for the CP-violation we have observed, T-symmetry must also be broken in just the right way in order to maintain the total conservation of CPT.

Returning to the suggestion made by Purcell and Ramsey that an elementary particle may have a non-zero EDM, Figure 1.1 shows a spin-1/2 particle, i.e. the electron, proton or neutron, which has spin $\boldsymbol{S}$, and electric dipole moment $\boldsymbol{d_e}$. By the Wigner-Eckhart theorem [13], these two properties must lie along the same axis such that $\boldsymbol{d_e} = d_e \frac{\boldsymbol{S}}{|\boldsymbol{S}|}$. For the

electric dipole moment to specify an additional, independent direction to the spin, an extra quantum number would be required to describe the state of the particle [14]. There is strong experimental evidence — from the precise measurements of the hydrogen structure [15] to the layout of the periodic table — that is consistent with these particles having spin as their only degree of freedom [16]. Therefore, the orientation of the electric dipole is fixed relative to the spin, where the sign of d_e determines if it is oriented parallel or anti-parallel to this axis. Although the EDM is constrained to the spin axis, experiments will typically compare the orientation of the electric dipole moment to the magnetic dipole moment $\boldsymbol{\mu}$, as its effects are easier to observe. As with the electric dipole moment, the magnetic dipole moment is constrained to the spin axis, where $\boldsymbol{\mu} = \mu\frac{\boldsymbol{S}}{|\boldsymbol{S}|}$, as shown in Figure 1.1. It is the relative orientation of the electric and magnetic dipole moments that is of interest when considering the three discrete symmetries acting on the particle. Applying the parity transformation

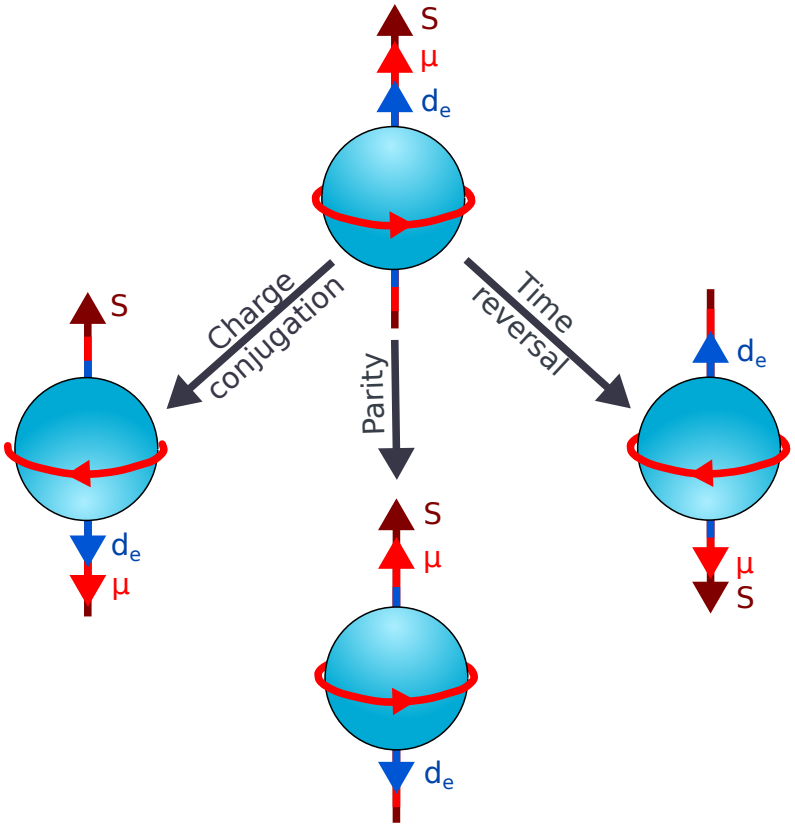


Figure 1.1: An elementary particle with spin $\boldsymbol{S}$, magnetic dipole moment $\boldsymbol{\mu}$, and permanent electric dipole moment $\boldsymbol{d_e}$. A non-zero EDM violates both P and T symmetry.

reverses the direction of the electric dipole moment but has no effect on the magnetic dipole moment, changing their orientation. This implies that either the electric dipole moment is zero, or that P-symmetry is violated. Similarly, the T-operation reverses the direction of the magnetic dipole moment, but has no effect on the electric dipole moment. The final discrete symmetry C, reverses the direction of both dipole moments, leaving this symmetry unbroken and the combined operation of CPT conserving the relative orientation of these two proper-

ties[1]. Consequently, a measurement of an electric dipole moment provides direct evidence for both P and T violation.

Purcell and Ramsey's orginal interest in EDMs was as a test of parity and, along with their student J. H. Smith, they began to measure the neutron EDM throughout the early 1950s [17]. At the time, it wasn't a surprise to them that they recorded an EDM consistent with zero and so never bothered to publish their result until after the discovery of parity violation. Since we now know that both P and CP are violated by the weak interaction, EDM measurements are far more interesting as direct probes of time reversal symmetry. To date, only studies of the B meson [18] and K meson [19] systems have shown evidence of T-asymmetry; but with some controversy surrounding the K meson result [20] [21], it is worthwhile looking for T-violation in other systems, of which EDMs are ideal.

It took several years from the discovery of CP-violation before a theoretical framework was established and included into the Standard Model (SM) of particle physics [22]. The amount of CP-violation that the SM now accounts for predicts that every fundamental particle has an electric dipole moment. However, they are incredibly tiny. For example, the SM prediction of the electric dipole moment of the electron, on which we will now focus, is [23],

$$|d_e^{\mathrm{SM}}| \simeq 10^{-38}\ e.\mathrm{cm}. \tag{1.1}$$

If we compare this to the current upper limit of of the electron EDM, set by an experiment using ThO molecules [24],

$$|d_e^{\mathrm{ThO}}| < 8.7 \times 10^{-29}\ e.\mathrm{cm} \quad (90\%\ \text{confidence}), \tag{1.2}$$

we can see that the SM prediction is likely to be unobservably small. It is difficult to imagine that the sensitivity of current electron EDM measurements will improve by an additional 10 orders of magnitude and record this result.

However, there is still value in perservering with these measurements, in particular as a test of the SM. Few physicists would describe the SM as complete, despite its success at describing the fundamental particles and their interactions. One common criticism is its inability to explain the huge amount of matter we find in the universe, compared to anti-matter. To generate this imbalance, CP-violating effects are required [25], but to account for the matter/anti-matter asymmetry we see, some additional sources of CP-asymmetry are essential [26]. There are many proposals that go beyond the Standard Model (BSM), with theories that attempt to reconcile this problem (along with many others) into the SM. Measuring the electron EDM constrains these theories, as they must contain enough T-violation to explain the observed matter/anti-matter asymmetry, but also must not produce an EDM larger than the current upper limit.

[1]The magnetic dipole moment and the spin have the same properties under the P and T transformations. However, under C, the magnetic dipole moment changes direction while the spin does not — this operation changes the particle to its anti-particle partner, which has the opposite orientation of spin and magnetic dipole moment.

The right hand-side of Figure 1.2 shows a range of theoretical predictions for the electron EDM, based on [27]. Of course, there are many more theoretical models that suppress the value of d_e even further, see [28], but these examples show how measurements of the electron's EDM can constrain BSM theories. In particular, the current experimental upper limit [24] places a huge amount of pressure on some of these models, or even rules them out entirely.

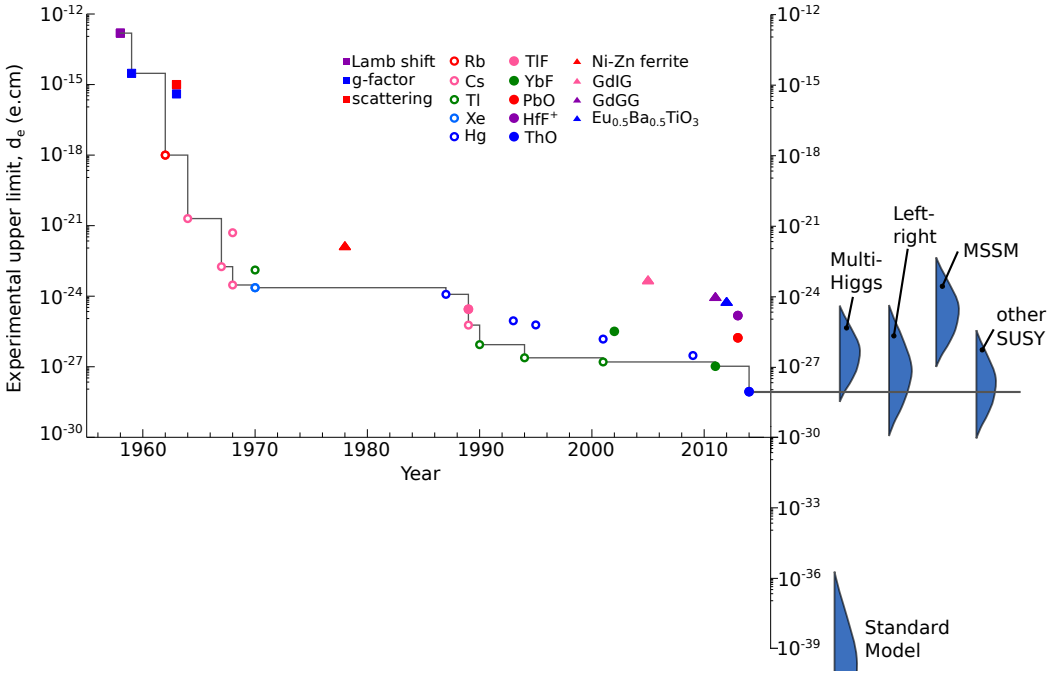


Figure 1.2: Review of experimental upper limits (68% confidence level (C.L.), unless otherwise stated) of the electron's EDM, compared to some theoretical predictions. The earliest electron EDM measurements were set using the Lamb shift [29], electron g-factor measurements [30][31], and scattering experiments [32]. Following the calculation of the enhancement of the EDM in atoms lead to measurements using the paramagnetic atoms Rb [33][34], Cs [35][36][37][38, 90% C.L.][39], and Tl [40][41][42][43, 90% C.L.]. Measurements on diamagnetic atoms are also sensitive to the EDM, including Xe [44, 90% C.L.] and ^{199}Hg [45][46, 95% C.L.][47, 95% C.L.][48, 95% C.L.][49, 95% C.L.]. Measurements using diatomic molecules now lead the field, where TlF [50], YbF [51][52, 90% C.L.], PbO [53, 90% C.L.], HfF^+ [54], and ThO [24, 90% C.L.] have all been explored. In addition, some solid state searches have been performed, which includes nickel-zinc ferrite [55], gadolinium-iron garnet (GdIG) [56], gadolinium gallium garnet (GdGG) [57] and $Eu_{0.5}Ba_{0.5}TiO_3$ [58, 90% C.L.]. Figure adapted from [27].

Another generic feature of these BSM theories is that they include additional particles, which do not necessarily have to obey CP-symmetry. Other experiments, such as the CMS and ATLAS collaborations at the LHC, are constraining BSM models by looking for the new particles at higher and higher mass scales. The search for EDMs and new particles are complimentary, with the size of the dipole moment being closely related to the interaction

between the electron and a new particle. The specifics of the interaction depends entirely on the theory. However, in an attempt to relate these very different experimental fields, we can estimate this new particle's contribution to the value of d_e with the simplest possible interaction [59],

$$d_e \sim \mathcal{C}\ \frac{m_e}{m_X^2}\ \frac{e\hbar}{c}\ \sin\left(\phi_{\mathsf{CP}}\right), \tag{1.3}$$

where m_e is the mass of the electron, m_X the mass of the new particle, ϕ_{CP} the phase that characterises how much the interaction violates CP-symmetry and $\mathcal{C}$ the coupling constant that determines how strongly the new particle interacts with the electron. The problem is that no one really knows what $\mathcal{C}$, m_X and ϕ_{CP} should be, although typically it is assumed that $\mathcal{C} \simeq \alpha/2\pi$, where α is the fine structure constant, and $\phi_{\mathsf{CP}} \sim 1$ [60]. Making these crude assumptions, the recent upper limit of $|d_e| < 8.7 \times 10^{-29}$ e.cm (90% confidence), predicts that if new particles exist, they will have energy scalings around ~ 10 TeV/c^2 or higher. In comparison, analysis of LHC data from 2015 shows that no new particles have been observed with masses below ~ 1 TeV/c^2 [61]. However, over the past year, the energy of the collider has almost doubled from 7 TeV to 13 TeV. With this increase, and with new electron EDM measurements imminent, theories beyond the Standard Model are expected to be even further constrained in the near future.

1.2 Measuring the size of the electron EDM

1.2.1 The EDM interaction in atoms and molecules

The underlying principle of measuring an electric dipole moment is simple — we place the particle of interest, in this case the electron, into an electric field $\boldsymbol{E}$, and record the change in energy proportional to the electric field, due to the interaction, $-\boldsymbol{d_e} \cdot \boldsymbol{E}$. Indeed, some of the earliest EDM measurements were performed on free electrons, as part of the experiments that measured the electron's anomalous magnetic dipole moment [30] [31]. However, the electric field causes the free electrons to accelerate, limiting sensitivity and making the experiments very complicated. Instead, modern measurement techniques bind electrons inside neutral paramagnetic atoms, molecules, or solid state samples. The response of the system is then interpreted as the EDM of the unpaired electron. To make this interpretation, we need an understanding of how the electron EDM changes the response of the atom/molecule it is held in when an electric field is applied.

Theoretical investigation into these interactions began in the early 1960s. In his famous paper [62], Schiff proved that by treating an atom as an electrostatically bound set of point charges, the permanent EDMs of the constituent parts will have no observable effect on the system as a whole. In the quantum mechanical treatment [63], the interaction energy of the system in an external electric field has no contribution to first order in $\boldsymbol{d_e}$. Effectively [23], the electrons in a neutral atom or molecule will always rearrange themselves such that each individual component feels zero force, even in an applied electric field. Any effects caused by the external electric field, such as the interaction with the electron's EDM, will be screened

out by the system's own internal polarising field. This result is often called Schiff's Theorem. However, the main point of his 1963 paper was to show that real atoms do not actually obey this result. Of course, atoms are not really electrostatically bound point charges; both the finite size of the nucleus and relativistic effects are important considerations. It is through these two effects that an electron EDM *can* create an observable response in the atom or molecule it is held in.

A few years later, Sandars discovered that for heavy atoms, the relativistic effects can be so strong that the EDM interaction is actually enhanced [64]. In fact, the response of the atomic system can be several orders of magnitude larger than that of the free electron. This result lead to many EDM experiments using heavy atoms; the most successful using Cs [35] [36] [38] [39] and then Tl [41] [42] [43], which have enhancements of $120d_e$ and $-585d_e$ [65] respectively. Since 1960, the experimental upper limit of the electron's EDM has been reduced by over 12 orders of magnitude by experiments using paramagnetic atoms, see Figure 1.2.

In atomic measurements, the enhancement of the EDM depends on the polarisation of the atom in the applied electric field. Sandars was the first to suggest, that by changing the system to a highly polar, heavy, diatomic molecule, the enhancement of T-violating effects could be increased enormously [66]. In these systems, the polarising effect of the additional electronegative atom is much larger than any achievable atomic polarisation. This discovery lead to a new generation of modern electron EDM experiments using polar molecules, which will be briefly reviewed in Section 1.2.3.

In a molecular system, the electric field that interacts with the electron EDM is the molecule's own strong internal electric field, rather than the external electric field used in atomic experiments. The internal field (typically called the 'effective electric field', E_{eff}) depends only on the molecular structure and must be calculated theoretically. This field is directed along the internuclear axis, which is defined by the unit vector $\boldsymbol{n}$, that points, by convention, from the negative ion to positive ion. The EDM interaction in a diatomic molecule is,

$$-d_e E_{\text{eff}} \frac{\boldsymbol{S}\cdot\boldsymbol{n}}{|\boldsymbol{S}|}, \tag{1.4}$$

where $\boldsymbol{S}$ is the spin of the electron.

In the absence of an external electric field, the internuclear axis precesses about the total angular momentum of the molecule, orientating the effective field randomly in space. The role of the applied electric field is to polarise the molecules to a single direction by mixing states of opposite parity. In molecular experiments, it is the rotational levels, rather than the electronic levels in atomic experiments, that are mixed. Mixing these states requires far less field, allowing the molecule to be strongly polarised by relatively small lab fields. If we apply the external electric field $\boldsymbol{E}$ along z-axis, then the dimensionless parameter known as the 'polarisation factor' $\eta(\boldsymbol{E}) = \boldsymbol{n}\cdot\boldsymbol{z}$, quantifies how well we have aligned the internuclear axis of the molecules to the applied field. This factor can be straightforwardly calculated by considering the Stark shift of a rigid rotor [67]. The energy shift due to the EDM interaction

is then written,

$$-d_e \eta E_{\text{eff}}. \tag{1.5}$$

It is this energy shift we try to record in an EDM measurement. The details of how we measure this shift will be discussed in the following chapter.

Aside: Other P, T-odd effects

Paramagnetic molecules are sensitive to more than one T-violating effect. There is also a possible weak interaction between the electron and the nucleus of strength $C_s G_F$, where G_F is the Fermi coupling constant. This adds an additional term to the P, T-odd interaction,

$$-W_s C_s \frac{\boldsymbol{S} \cdot \boldsymbol{n}}{|\boldsymbol{S}|}, \tag{1.6}$$

where W_s is determined by the molecular structure. This means that measurements of the electron EDM also limit the size of the parameter C_s. This parameter restricts BSM theories in the same way as a measurement of d_e. When reporting EDM results, it is customary to set this to zero, with only the value of d_e quoted, which will be the convention throughout the rest of this thesis. For reference, the recent measurement using ThO molecules, with $W_s = -300$ kHz [68], places an upper limit of $|C_s| < 5.9 \times 10^{-9}$ (assuming $d_e = 0$) [24]. In YbF the sensitivity to this parameter is smaller, with $W_s = -33$ kHz [69].

1.2.2 Choice of molecule?

There are many different molecules that could be used to measure the electron's EDM. The first measurement using molecules[2] was performed using TlF [50]. Since then, molecules such as YbF, ThO, PbO, HfF^+, WC and ThF^+ have all been used (or are in preparation to be used) for EDM measurements. Each molecule brings its own advantages and disadvantages to their respective experiments, with there currently seeming to be no 'perfect' choice for an electron EDM measurement.

Typically, a molecule will be chosen for its large enhancement factor. Table 1.1 shows the effective electric field E_{eff}, of these selected molecules. Often, molecules with large enhancements will also be fairly unstudied[3]. This means that a lot of preliminary work is required to develop a reliable source and perform the relevant spectroscopy, before an EDM measurement can begin. Since the 1990s, our group has worked on YbF as their molecule of choice, which has several attractive features for EDM measurements.

Firstly, YbF can be made relatively easily in a supersonic source which allows the experiment to run reliably and consistently throughout data collection. Secondly, the relevant transitions in YbF are directly addressable with convenient laser frequencies, and the energy level structure of the important states are relatively uncomplicated. Finally, YbF has a fairly

[2] In fact, this experiment was originally designed to be sensitive to the proton EDM and Schiff moment, rather than the electron EDM.

[3] The exception to this is ThO, which was researched in the 1960s for its use in nuclear power, see [70].

Molecule	E_{eff}	
YbF	-26 GV/cm	[71]
ThO	84 GV/cm	[68]
PbO	26 GV/cm	[72]
HfF^+	24 GV/cm	[73]
ThF^+	37 GV/cm	[74]
WC	54 GV/cm	[75]

Table 1.1: The effective electric field E_{eff}, of some interesting molecules.

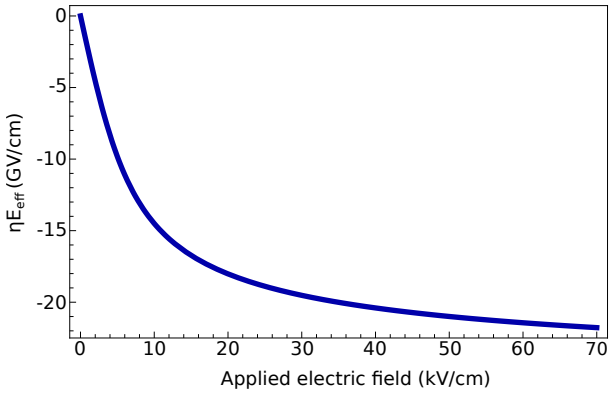


Figure 1.3: ηE_{eff} as a function of applied electric field for the YbF molecule

large enhancement factor of $E_{\text{eff}} = -26$ GV/cm [71] and it can be well polarised in an applied electric field of a few tens of kV/cm, as shown in Figure 1.3. For example, a field of 12.5 kV/cm produces an internal electric field of $\eta E_{\text{eff}} = -15.9$ GV/cm.

YbF also has some good properties that makes it well suited to future EDM experiments. In particular, the measurement is performed in the ground state of the system. Consequently, there is no fundamental limit to the spin precession time of our measurement. Secondly, YbF lends itself well to buffer gas cooling, allowing for slower, more intense sources to be developed and incorporated into the experiment. Finally, YbF is a suitable candidate for laser cooling and slowing. In the future this could enhance interaction time significantly, an idea we will return to in the following section.

It is useful to compare YbF to the ThO molecule. This was used by the Advanced Cold Molecule EDM (ACME) collaboration to set the most recent upper limit on d_e [24]. The excited, metastable level H $^3\Delta_1$ is used as the measurement state. The ThO molecule has one of the largest effective electric fields, $E_{\text{eff}} = 84$ GV/cm [68], and it can be completely polarised ($\eta = 1$) in relatively small applied fields, $\lesssim 100$ V/cm [76]. The rather complicated measurement state has been selected for its ability to reject systematic effects. The direction of the internal electric field can be reversed without changing the external electric field, allowing some of the main systematic effects to be suppressed. In addition, this state also has a tiny magnetic moment $\mu = 0.0085 \times \mu_B$ [77], which also reduces the effects of magnetic noise in the experiment. The significant disadvantage of this system is that the measurement is performed in a metastable state, limiting the interaction period to the 2 ms lifetime of the state [76].

1.2.3 Electron EDM measurements — past, present and future

In 2011, our group at Imperial College London was the first to set a new upper limit on the electron EDM using polar molecules [52]. This experiment performed a spin precession measurement on a pulsed supersonic beam of YbF molecules. The techniques and apparatus used will be described in detail throughout this thesis. The new limit set by this measurement

was $d_e = (2.4 \pm 5.7_{\text{stat}} \pm 1.5_{\text{syst}}) \times 10^{-28}$ e.cm, equivalent to an upper limit of $|d_e| < 10.5 \times 10^{-28}$ e.cm with 90% confidence [52] [78].

In 2014, the ACME collaboration published an improved measurement of $d_e = (-2.1 \pm 3.7_{\text{stat}} \pm 2.5_{\text{syst}}) \times 10^{-29}$ e.cm, equivalent to an upper limit of $|d_e| < 8.7 \times 10^{-29}$ e.cm with 90% confidence [24]. This measurement built upon many of the techniques developed by the YbF experiment, as well as a previous EDM experiment that used a metastable state in PbO [53]. This experiment uses a pulsed, cryogenic buffer gas beam of ThO molecules which travel along the beamline at ∼200 m/s [79]. Once they have left the source, the molecules pass between a pair of electric field plates which are charged to around ±50 V, aligning the internuclear axis of the molecule to the electric field. The ground state population is optically pumped to the H $^3\Delta_1$ measurement state, where a second laser field polarises the spin of the outer electron to be perpendicular to the electric field. As the molecules continue through the experiment, the spin of the electron precesses a tiny amount due to the interaction between the EDM and the electric field. Finally, after 1.1 ms of interaction time, a third laser field reads out this precession angle, which is proportional to d_e. We'll be seeing more of these measurement techniques in later chapters. Currently, the ACME collaboration are improving the statistics of their measurement. A thermochemical source, which uses laser heating of ThO_2 and Th, is expected to produce a larger number of ThO molecules in a continuous beam. In addition, they have improved the efficiency of their state preparation stage by using stimulated Raman adiabatic passage, rather than optical pumping [80]. Along with some other changes, they are expecting to improve their sensitivity by about a factor of 10.

Other molecular EDM experiments include the Cornell group at JILA who use the molecular ion HfF^+, which they trap in an rf Paul trap [54]. This molecule has several $^3\Delta_1$ states which can be used in the same way as the ThO experiment, as well as a relatively large enhancement factor of $E_{\text{eff}} = 24$ GV/cm, and has the benefits associated with the long lifetimes of trapped samples. In 2013, they presented their first, proof-of-principle data set, which constrained the EDM to $|d_e| < 1.5 \times 10^{-25}$ e.cm. However, this very different measurement technique presents its own challenges. In particular, the use of a rotating electric field to align the molecules, which are also rotating inside the trap, has the potential to generate significant geometric phases that can mimic the EDM interaction if not under appropriate control [81]. The group have spent the past few years tracking down possible systematics unique to the experiment, with a second preliminary result of $|d_e| < 4.6 \times 10^{-28}$ e.cm with 90% confidence [82]. To improve their measurement sensitivity, the group are planning on switching to ThF^+ molecular ion [83], which has a higher effective electric field of $E_{\text{eff}} = 37$ GV/cm [74].

Until recently, the WC molecule was used by the Leanhardt group at the University of Michigan. This molecule is almost the perfect candidate for electron EDM searches; the ground state of the system has the favourable $^3\Delta_1$ configuration. This combines systematic error rejection, low magnetic noise and unlimited lifetime, making it an ideal state to work in. Unfortunately, the group had significant difficulty making an intense source of WC molecules, with only a few counts observed per second [84], causing them to abandon the project. If

this problem can be solved, this system has the potential to be a very sensitive measure of the electron EDM.

It is worth mentioning that diamagnetic atoms, such as ^{199}Hg and Xe, are also sensitive to the electron EDM. However, these experiments are typically designed to measure nuclear P, T-odd effects, rather than that of the electron. In addition, solid state searches for the electron EDM also contribute to the field. In recent years, gadolinium gallium garnet (GdGG) [57] and $Eu_{0.5}Ba_{0.5}TiO_3$ [58] have been used in EDM measurements. They detect the EDM by applying a large electric field to the sample, which becomes magnetised if $|d_e| > 0$. The resultant magnetisation of the sample is then recorded using a sensitive SQUID magnetometer. Currently, these measurements are around a factor of 100 worse than molecular techniques, as the magnetic fields produced by the sample are incredibly tiny despite the sample containing a large number of unpaired electrons.

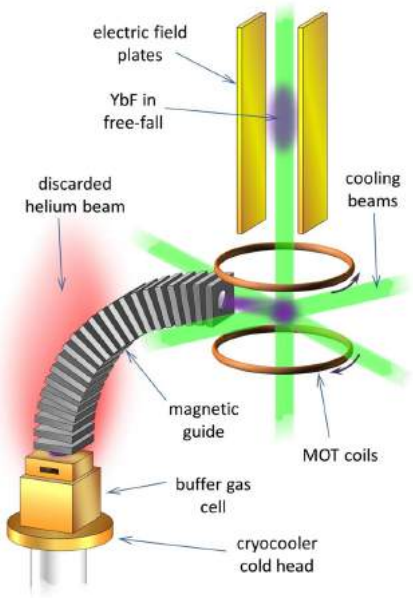


Figure 1.4: Schematic of the YbF fountain experiment. Image courtesy of J. Almond.

Finally, a long term goal of the YbF project is to measure the electron EDM using a fountain of molecules [85]. This work is being conducted by our group, in parallel to the work presented in this thesis. To make this measurement, YbF molecules, travelling at around ~ 200 m/s, will be produced by a cryogenic buffer gas source. As the molecules leave the cell, they will be magnetically guided away from the flow of the buffer gas, into a region of laser slowing, cooling, and eventually trapping. Once enough molecules have accumulated in this region, they will be launched in between a pair of electric field plates where the EDM measurement will be performed. The molecules fly up through the electric field, reach zero velocity, and then begin to fall back down, providing a total interaction time of ~ 250 ms. This is an incredibly ambitious and difficult project, but is predicted to be exceptionally sensitive, with a projected sensitivity of 6×10^{-31} e.cm after 8 hours of integration time. A schematic of this experiment is shown in Figure 1.4.

1.3 Thesis overview

I joined the YbF EDM experiment in October 2013. At this time, the experiment was part way through a new data run that was aiming to improve upon the 2011 result by a factor of three. During the run, it became apparent that a new systematic effect had been created by one of the upgrades. Unfortunately, with the level of sensitivity at the time, it was hard to establish the underlying cause of the systematic shift. At the end of May 2014, the data run was stopped, and we decided to focus on improving the statistical sensitivity of the machine instead. The following chapter (Chapter 2) details the version of the apparatus and experiment technique that was used when I joined the experiment. Chapter 3 details the systematic effects currently associated with the experiment.

During the data run, I was working in parallel on some of the preliminary ideas to improve the statistical sensitivity of the experiment. Since the end of the data run, the upgrades became the main focus of the experiment. During the past three years, almost every aspect of the machine has been changed by these improvements. It is this work that forms the bulk of this thesis. I detail the improvements I have made to the state preparation (Chapter 4), interaction (Chapter 5) and detection (Chapter 6) regions of the machine. Finally, the changes are summarised in Chapter 7 to show that the statistical sensitivity of the machine has been improved by a factor of 11.4 since 2011.

Chapter 2

Overview of the experiment

2.1 Principle of the experiment

The atomic and molecular EDM measurements detailed in Chapter 1 are based on the resonance techniques developed by Rabi and Ramsey in the mid-20th century [86] [87] [88] and always include some form of spin precession measurement. In our case, we are observing the

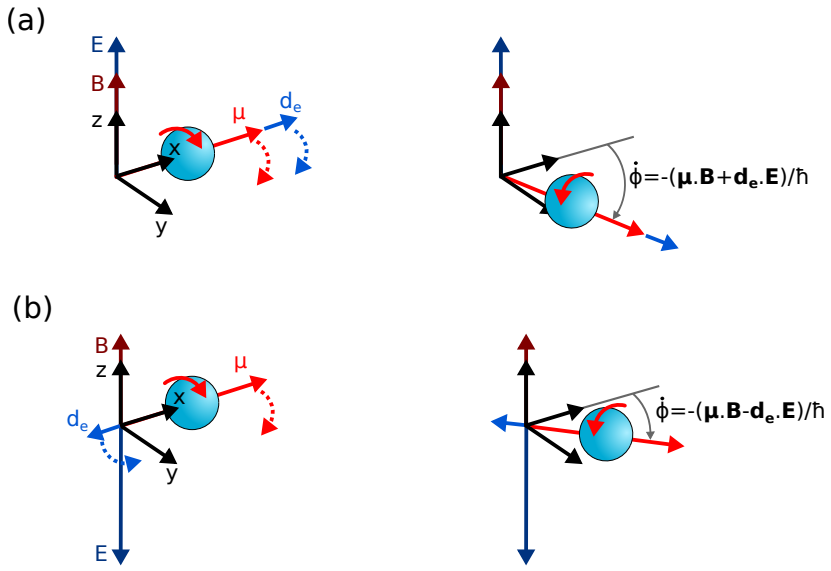


Figure 2.1: An illustration of the spin precession technique used to measure the electron's EDM. We look for the change in precession frequency when the direction of the electric field ($\boldsymbol{E}$) is reversed relative to the magnetic field ($\boldsymbol{B}$), which is proportional to the EDM interaction $-\boldsymbol{d_e} \cdot \boldsymbol{E}$. The dashed lines indicate the direction of the torque experienced by the electron in the presence of an electric and magnetic field. In (a) $\boldsymbol{E}$ and $\boldsymbol{B}$ are both aligned along the $+z$ direction, while in (b) the electric field is aligned along $-z$ direction, pointing in the opposite direction to $\boldsymbol{B}$.

spin of the outermost electron in the YbF molecule as it precesses in a uniform electric and magnetic field. We apply these fields along the $+z$ axis of our system and use rf and laser

fields to align the spin of the electron to the x axis, as shown in Figure 2.1(a). The torque generated by this setup (shown by the dashed lines in Figure 2.1) causes the spin to rotate about the z axis at a rate of $\dot{\phi} = -(\boldsymbol{\mu} \cdot \boldsymbol{B} + \boldsymbol{d_e} \cdot \boldsymbol{E})/\hbar$.

The rotation caused by the electric dipole is incredibly tiny and is difficult to distinguish from the effects of the magnetic dipole. To look for the phase caused directly by the electron EDM, we use a technique that is sensitive to the *difference* in precession frequency when we reverse the direction of the electric field relative to the magnetic field. This is equivalent to moving between Figure 2.1(a) and (b), where the orientation of $\boldsymbol{E}$ has been reversed. This changes the precession frequency by $2\left(\boldsymbol{d_e} \cdot \boldsymbol{E}\right)/\hbar$ to $\dot{\phi} = -(\boldsymbol{\mu} \cdot \boldsymbol{B} - \boldsymbol{d_e} \cdot \boldsymbol{E})/\hbar$. In each configuration, we measure the new orientation of the spin after a known amount of precession time, which allows us to calculate a value for d_e.

This outlines the basic principle behind an EDM measurement, the rest of this chapter details how we carry out the spin precession measurement in practice. Firstly, we need to have an understanding of the YbF molecule and its energy level structure before moving onto decribe the experimental setup, data collection and analysis techniques. The machine described in this chapter was collecting data in the first few months of my PhD. During this time, I was working in parallel on some preliminary tests for the results detailed in the remainder of this thesis. Despite only observing the machine run in this configuration, setting out this measurement technique is helpful to provide context for the work presented in the rest of this thesis. As I have little experience in running this setup, most of my insight into the measurement technique comes from the literature and so this chapter follows closely the work of previous PhD students; J. A. Devlin [89] and I. J. Smallman [90].

2.2 YbF

Diatomic molecules have all the electronic energy level structure and interactions we associate with atoms but with additional degrees of freedom that allow them to vibrate and rotate about the internuclear bond. This greatly increases the complexity of the energy level structure, but for this work these motions can at least be treated as decoupled using the Born-Oppenheimer approximation [91].

To measure the electron EDM we use the polar, paramagnetic diatomic molecule ^{174}YbF. The ^{174}Yb atom forms an ionic bond with ^{19}F to create a closed-shell core with a single electron occupying the outer valence shell [92]. It is the spin precession of this electron we record in our experiment.

To understand how we perform the EDM measurement, we require only a working knowledge of the ground state of YbF and the excited state we use to detect it, detailed in Section 2.2.5. However, to understand the improvements detailed in this thesis, we need to have a more thorough overview of the YbF energy level structure and the allowed transitions. Sections 2.2.1–2.2.4 review these.

2.2.1 Electronic structure

In an atomic system, the electronic states are typically defined by the electronic spin S, orbital angular momentum L and total angular momentum J, along with the principal quantum number. Comparing this to YbF, we find that the system changes from spherical to cylindrical symmetry, where the internuclear axis $\boldsymbol{n}$ defines the internal $\boldsymbol{z}$ axis of the system. Instead of using $\{J,\ L,\ S\}$, it is now the projection of the angular momentum components onto the internuclear axis, labelled $\{\Omega,\ \Lambda,\ \Sigma\}$ respectively, that become the good quantum numbers of the system.

For atoms, we can write down a term symbol to describe the electronic level,

$$^{2S+1}L_J. \tag{2.1}$$

In the same way, we can use an analogous term symbol for diatomic molecules. The electronic states are labelled by letters, with X always labelling the ground state and {A, B, C...} labelling the {first, second, third...} excited states. For molecules, the term symbol describing an electronic state is of the form,

$$\text{letter } ^{2S+1}\Lambda_{\Omega}^{(+/-)} \tag{2.2}$$

where the $+/-$ is only used for states with $\Lambda = 0$ and denotes the reflection symmetry of the wavefunction about an arbitary plane containing the internuclear axis. Similarly to the atomic case where {S, P, D,...} label $L = \{0,\ 1,\ 2, ...\}$, Λ is labelled with the spectroscopic notation $\{\Sigma,\ \Pi,\ \Delta,...\}$ for $\Lambda = \{0,\ 1,\ 2, ...\}$.

In this experiment we are only interested in the ground electronic state X $^2\Sigma^+$ and the first electronic excited state A $^2\Pi_{1/2}$ of YbF. Typically, electronic energy levels will be separated by a few hundred THz and, if you chose your molecule well, are accessible by laser radiation. For YbF the splitting is around 552 nm or ∼542 THz, which we can drive with readily available commercial lasers.

2.2.2 Vibrational, rotational and hyperfine structure of the X $^2\Sigma^+$ state

The next-largest energy scale is caused by the inertial motion of the molecule; the vibrational modes between the two nuclei and the end-over-end rotational modes. To the first approximation, the energies of the low-lying vibrational modes are the harmonic oscillator eigenstates. For YbF, the eigenvalues of the vibrational modes within the X $^2\Sigma^+$ state are,

$$E_v = hf\left(v + \frac{1}{2}\right), \qquad f = 15.1894 \pm 0.0002 \text{ THz [93]}. \tag{2.3}$$

Typically vibrational modes are a few tens of THz, making it awkward to drive these transitions directly. The energy splitting between the $v = 0$ and $v = 1$ modes in the X $^2\Sigma^+$ state is shown by the purple line in Figure 2.2. An important point to note is that the same vibrational modes in different electronic states are not identical. For example, the X $^2\Sigma^+(v = 0)$

state and A $^2\Pi_{1/2}(v' = 0)$ state are not identical. By convention, the quantum numbers of the excited state are labelled with a prime. When the electron is excited to a higher state, the potential in which the nuclei oscillate is changed, making each vibrational potential well different. This in turn, changes the transition probability between vibrational states, discussed further in Section 2.2.4.

Within each vibrational state exists a series of rotational modes, the eigenenergies of which are approximately that of a rigid rotor,

$$E_r = hB_0N(N+1), \qquad B_0 = 7233.8007 \pm 0.001 \text{ MHz [94]} \tag{2.4}$$

In diatomic molecules these are typically split by a few tens of GHz which allows these transitions to be driven by microwave radiation. Figure 2.2 shows a few of the rotational modes, labelled $(N = 0, 1, 2)$ (shown in blue), in the X $^2\Sigma^+(v = 0)$ state. In addition, each rotational level has a defined parity of $(-1)^N$, shown in the brackets of Figure 2.2.

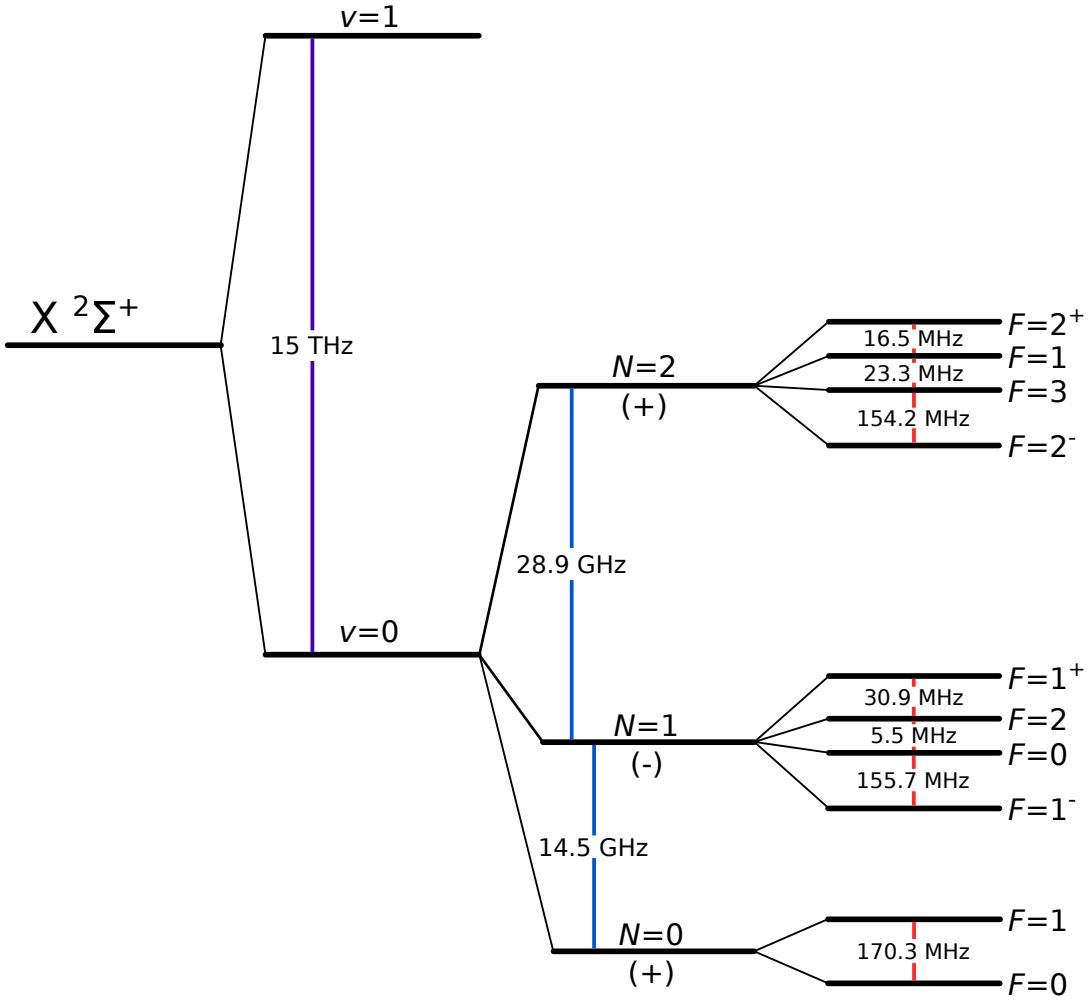


Figure 2.2: The relevant energy levels, and their frequency splittings, in the X $^2\Sigma^+$ ground state of YbF.

The electronic ($\boldsymbol{S}$) and nuclear ($\boldsymbol{I}$) spins also contribute a small amount to the energy

of the state via coupling to the rotational angular momentum $\boldsymbol{N}$ (called the spin-rotation interaction) and also via the hyperfine interaction. The quantity $\boldsymbol{F} = \boldsymbol{N} + \boldsymbol{S} + \boldsymbol{I}$ now defines the total angular momentum operator of the system and F, along with N, become the good quantum numbers of the system. The two interactions are of similar strength and create four possible hyperfine states; $F = N + 1,\ N^+,\ N^-,\ N - 1$ (except in the ground state X $^2\Sigma^+(v = 0,\ N = 0)$ which has only two components $F = 0,\ 1$). Here the +/- superscripts distinguish the hyperfine states with higher/lower energy. Typically these states are separated by a few tens of MHz and are easily coupled by rf radiation. Figure 2.2 shows the hyperfine structure within each rotational state and their transition frequencies shown in red.

It is common to introduce the total electronic angular momentum operator $\boldsymbol{J} = \boldsymbol{N} + \boldsymbol{S}$. However, the spin-rotation interaction that couples $\boldsymbol{N}$ and $\boldsymbol{S}$ is of a similar strength to the hyperfine interaction. This means that J is not a good quantum number of the system for the states where $F = N$, but by convention is typically used to label the states (Hund's case $b_{\beta J}$ [91]). For reference, Table 2.1 shows the composition of the J-mixed states in the $N = 1$ and $N = 2$ rotational states. All other relevant hyperfine levels are of pure J composition.

Label (This work)	Nominal J labelling	Composition
$\lvert N = 1,\ F = 1^- \rangle$	$\lvert N = 1,\ J = 1/2,\ F = 1 \rangle$	$-0.844\,\lvert J = 1/2 \rangle + 0.536\,\lvert J = 3/2 \rangle$
$\lvert N = 1,\ F = 1^+ \rangle$	$\lvert N = 1,\ J = 3/2,\ F = 1 \rangle$	$-0.536\,\lvert J = 1/2 \rangle - 0.844\,\lvert J = 3/2 \rangle$
$\lvert N = 2,\ F = 2^- \rangle$	$\lvert N = 2,\ J = 3/2,\ F = 1 \rangle$	$-0.826\,\lvert J = 3/2 \rangle + 0.564\,\lvert J = 5/2 \rangle$
$\lvert N = 2,\ F = 2^+ \rangle$	$\lvert N = 2,\ J = 5/2,\ F = 1 \rangle$	$-0.564\,\lvert J = 3/2 \rangle - 0.826\,\lvert J = 5/2 \rangle$

Table 2.1: Calculated J composition of each mixed hyperfine state in the $N = 1$ and $N = 2$ rotational states using [94].

The magnetic sub-levels of the hyperfine states, not shown in Figure 2.2 for simplicity, will also play an important role in this experiment. They are labelled from $M_F = -F,\ -F + 1,\ ...,\ +F$. In particular, the magnetic sub-levels of the $F = 0,\ 1$ hyperfine states in the rotational ground state will be frequently referred to and so the labelling system

$$|F,\ M_F\rangle = \mathrm{X}\ ^2\Sigma^+(v = 0,\ N = 0,\ F,\ M_F) \tag{2.5}$$

will be used for simplicity throughout this thesis.

2.2.3 The A $^2\Pi_{1/2}$ state

We can now look at the first excited electronic state in more detail. In this case we are only interested in the ground vibrational state A $^2\Pi_{1/2}(v' = 0,\ J' = 1/2)$. This rotational state is split by 11.9 GHz [93] into a pair of states called an Ω-doublet labelled e/f which have parity of +/- [95].

To understand how this splitting arises, we can consider the reflection of the molecule in a plane containing the internuclear axis. This transformation does not change the energy of the

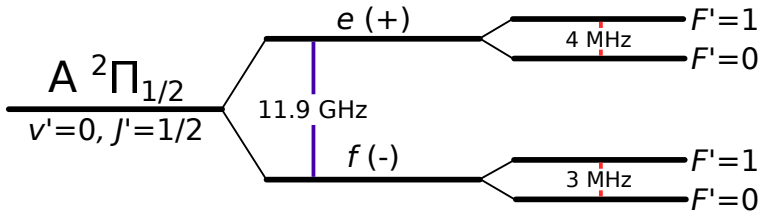


Figure 2.3: Energy level diagram of the first excited electronic state of YbF, A $^2\Pi_{1/2}$.

molecule, but it does reverse the sign of the angular momentum about the axis of reflection. So, for $\Omega > 0$ there are two degenerate states with $\Omega = \pm|\Omega|$ which are related to the electron travelling clockwise and anti-clockwise about the internuclear axis. The symmetric (e) and anti-symmetric (f) combination of the $\Omega = \pm|\Omega|$ wavefunctions are the energy eigenstates of the system which are degenerate in the absence of molecular rotation. This degeneracy is lifted when the electronic angular momentum and the molecular rotation couple together, creating this splitting which is known as Ω-doubling.

As in the ground state, these levels are split further by the hyperfine interaction. As shown in Figure 2.3, the hyperfine splitting is small [95], around 3 MHz for the e state and 4 MHz for the f state, and so the excited state will often be considered as one degenerate state labelled either A $^2\Pi_{1/2}$ (e or f).

2.2.4 Transitions

Now that we understand the structure of YbF, we can look at the relevent transitions referred to throughout this thesis. There are two classes we need to consider; electric dipole transitions, which include transitions between electronic levels X $^2\Sigma^+ \rightarrow$ A $^2\Pi_{1/2}$ and between rotational states X $^2\Sigma^+(v = 0,\ N = 0 \rightarrow 1)$, and magnetic dipole transitions between hyperfine levels within the X $^2\Sigma^+(v = 0,\ N = 0, 1, 2)$ states. The important transitions are shown in Figure 2.4 with the selection rules for each type of transition briefly reviewed below.

Electric dipole transitions

The X $^2\Sigma^+$ state can be optically excited to the A $^2\Pi_{1/2}$ and similarly, the A $^2\Pi_{1/2}$ can spontaneously decay back down to the X $^2\Sigma^+$ state. In YbF, these transitions are in the green region of the visible spectrum, shown in green on Figure 2.4. In particular, X $^2\Sigma^+(v = 0) \rightarrow$ A $^2\Pi_{1/2}(v' = 0)$ is around 552nm. The selection rules that govern these transitions are;

$$\text{Parity must change} \tag{2.6}$$

$$\Delta F = 0, \pm 1 \tag{2.7}$$

$$\Delta M_F = 0, \pm 1 \text{ but not } \Delta M_F = 0 \text{ when } \Delta F = 0 \tag{2.8}$$

In general, these rules group transitions into six different categories, or branches. These, like other spectroscopic notation, are historical labels and related to the change in rotational

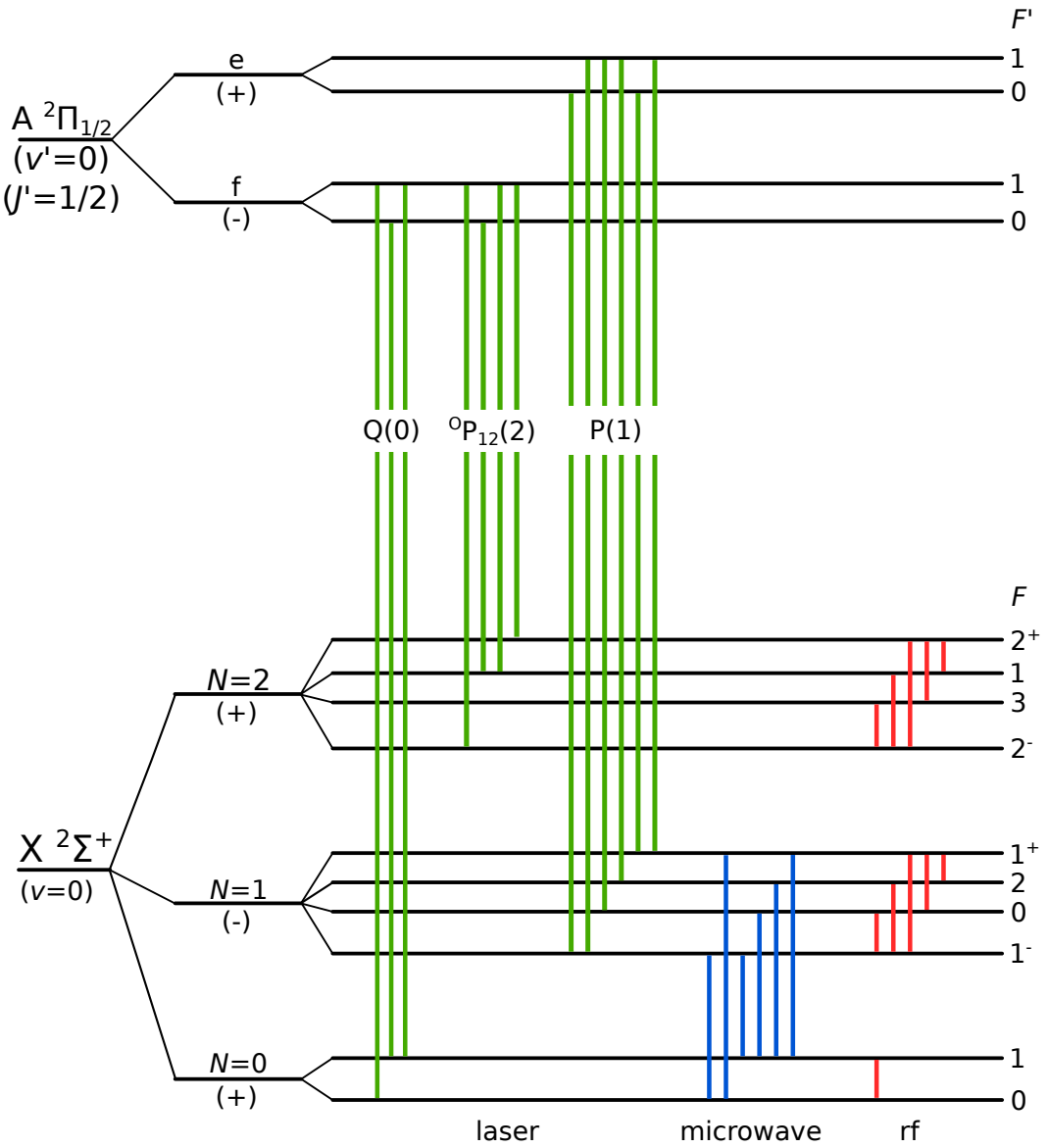


Figure 2.4: A diagram showing the relevant allowed transitions in YbF. Optical transitions are shown in green, microwave transitions in blue and rf transitions in red. Optical transitions are labelled using spectroscopic notation.

quantum number ΔN and the intermediate quantum number ΔJ. Even though the YbF structure doesn't strictly follow the rules of this notation, we use these labels for simplicity. Figure 2.4 shows the relevant branches; Q(0) at 542 811 GHz, $^{O}P_{12}(2)$ at 542 767 GHz and P(1) at 542 808 GHz.

Once excited to the A $^2\Pi_{1/2}(v' = 0,\ J' = 1/2)$ upper state, the population decays to the ground state with a lifetime of 28 ± 2 ns [96], giving a decay rate of $\Gamma = 2\pi \times (5.7 \pm 0.4)$ MHz.

As discussed in Section 2.2.2 above, the wavefunctions of the $v' = 0$ and $v = 0$ states are not identical and so the vibrational quantum number can change in an electronic transition, with a probability determined by the overlap of each state. In YbF, the square

of the wavefunction overlap (often called the Franck-Condon factor) is strongly diagonal, $f_{00} = |\langle v'=0|v=0\rangle|^2 = 0.928 \pm 0.005$, $f_{01} = |\langle v'=0|v=1\rangle|^2 = 0.069 \pm 0.005$ and $f_{02} = |\langle v'=0|v=2\rangle|^2 = (3 \pm 0.5) \times 10^{-3}$ [96]. In this case, we need only consider this as a loss mechanism; for every excitation to A $^2\Pi_{1/2}(v'=0)$, 93% of the time the population is kept within the $v=0$ ground state, while 7% is lost to higher vibrational modes. The decays also follow the rules (2.6)–(2.8) above, with the excited state f decaying to $N=0$ or $N=2$ and the e state decaying only to $N=1$.

The branching ratios to each individual hyperfine state can be calculated from the Clebsch-Gordon coefficients. J. A. Devlin's thesis [89] has a comprehensive list of the branching ratios and includes the explicit form used for calculating transition probabilities for the microwave and rf transitions discussed below.

The electric dipole transitions between the X $^2\Sigma^+(v=0,\ N=0 \rightarrow 1)$ rotational levels are not introduced until later but will play a crucial role in the updates discussed in the following chapters. The important microwave transitions are shown in blue on Figure 2.4 and range from 14.3 to 14.7 GHz.

Magnetic dipole transitions

Transitions between hyperfine states, within a single electronic, vibrational and rotational level are driven using rf. These oscillating magnetic fields manipulate the electronic and nuclear spins to drive magnetic dipole transitions. The selection rules for these are

$$\text{Parity cannot change} \tag{2.9}$$

$$\Delta F = 0, \pm 1 \tag{2.10}$$

$$\Delta M_F = 0, \pm 1 \text{ but not } \Delta M_F = 0 \text{ when } \Delta F = 0 \tag{2.11}$$

The allowed transitions are shown in red on Figure 2.4 and range from 30–200 MHz.

Dark states

When driving population from a lower state with total angular momentum F, to an excited state with total angular momentum $F' = F-1$, there are always sublevels in the ground state that can't be addressed by the radiation [97]. A specific example we will encounter in later chapters is the transition $F=2 \rightarrow F'=1$, as shown in Figure 2.5. Driving this transition with a fixed polarisation will always leave two sublevels in the ground state unaddressed. For example, using linearly polarised radiation to drive this transition will leave the $M_F = \pm 2$ states unaddressed, as shown in Figure 2.5(b). Similarly, using $\sigma^{\pm}$ polarisation will leave the $M_F = \pm 1,\ \pm 2$ states unaddressed, as shown in Figure 2.5(a) and (c). In addition, if the light is a fixed mixture of these three polarisations, two unaddressed levels will still exist, in this case as a coherent superposition of different ground state sublevels. It is these unaddressed levels we call 'dark states', with the pumped levels often being called 'bright states'.

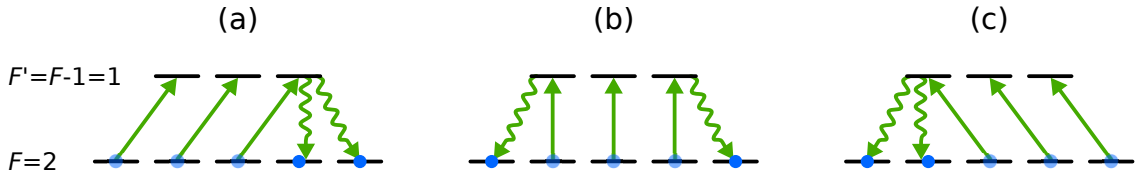


Figure 2.5: Dark states created when pumping from a state of total angular momentum $F = 2$ to a state with total angular momentum $F' = F - 1 = 1$ using (a) σ^+ polarised light, (b) linear polarised light and (c) σ^- polarised light.

If the dark states are stationary then the population of the system will eventually accumulate in these levels, becoming trapped. This type of 'angular momentum dark state' occurs in the new pumping and detection schemes presented in Chapter 4 and 6. If we do nothing to address the dark states then population leaks out of the system at a rate proportional to the Rabi frequency of the transition [89]. This effect will seriously compromise the amount of population we can prepare in the pump region, as well as the total number of fluorescence photons emitted in the new detection scheme.

The simplest way to solve this problem is to apply a static magnetic field at an angle to the polarisation of the radiation. The spin will precess, causing the population to rotate between magnetic sublevels at a rate proportional to the Lamor frequency, and so destabilising the dark states. In some cases this may not be the best option, either when a magnetic field is not wanted in a certain region of the experiment, or if the ground state has a small g-factor. Alternatively, the polarisation can be modulated between σ^+ and σ^- light (or between vertical and horizontal polarisation) at a rate proportional to the Rabi frequency [89]. In this case, no individual state is left unaddressed as the population is transferred from the positive to negative M_F sublevels (or from high $|M_F|$ to low $|M_F|$). This is the option we choose to utilise in the new pumping and new detection scheme, discussed in more detail in Chapters 4 and 6.

A more general type of dark state can occur in a multi-level system driven by coherent radiation; know as 'coherent population trapping' [98]. Often these dark states can be destabilised by detuning the radiation by some small amount. However, when considering the new pump and probe schemes for YbF, there are over 30 magnetic sublevels to keep track of, as well as many different sources of radiation. It becomes incredibly complicated to ensure that no population trapping is occuring and that we are operating each scheme at its optimal efficiency. This will be discussed in later chapters.

2.2.5 Simplified energy level structure

To introduce the measurement of the EDM we only need to consider the $F = 0,\ 1$ levels of the ^{174}YbF X $^2\Sigma^+(v = 0,\ N = 0)$ ground state, and its excited state partner A $^2\Pi_{1/2}(v' = 0,\ J' = 1/2,\ f)$. All other higher vibrational and rotational states are considered as a single loss mechanism.

Figure 2.6 shows the states we care about and the relevant splittings. Throughout this

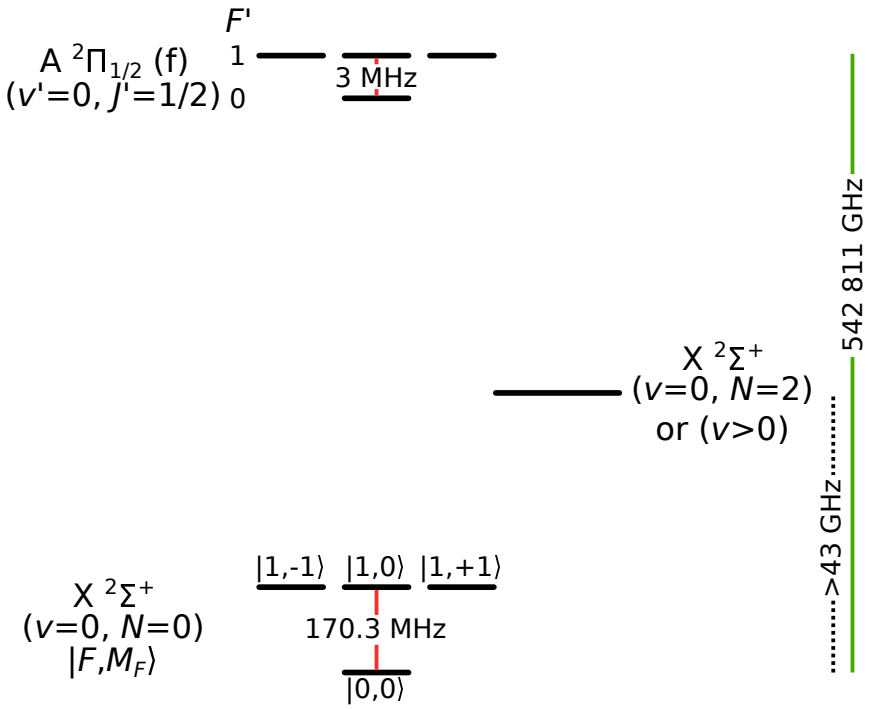


Figure 2.6: Simplified energy level scheme of YbF used for understanding the measurement technique outlined in this chapter.

thesis the ground state hyperfine sublevels will often be refered to using the label $|F,\ M_F\rangle$.

2.3 Experimental setup

Now that we have a good understanding of the YbF molecule, we can now look at how we manipulate it. This section begins with a discussion of the main YbF beam machine before detailing the equipment used to control the experiment.

2.3.1 Beam machine overview

Figure 2.7 shows a front and side cross-section of the machine, showing the main components required for taking EDM data. This set up is described in more detail in I. J. Smallman's thesis [90].

The heart of the experiment consists of a 2 m tall, 200 mm diameter vacuum chamber which is typically held at a pressure of $\sim 1\times10^{-7}$ mbar. Figure 2.7 shows the beamline divided into six regions, labelled (1) – (6), which will help us to best explain the experimental setup and sequence. During normal data taking, the chamber is also surrounded by two additional layers of mu metal shielding, not shown in Figure 2.7.

At the bottom of the machine (1) is the supersonic YbF source. A pulsed solenoid valve releases a supersonically expanding pulse of 2% SF_6+98% Ar gas mixture into the vacuum for 180 μs. After a 350 μs delay relative to the pulse that triggers the solenoid valve, a Nd:YAG laser ablates an Yb target in the presence of this gas mixture to create YbF.

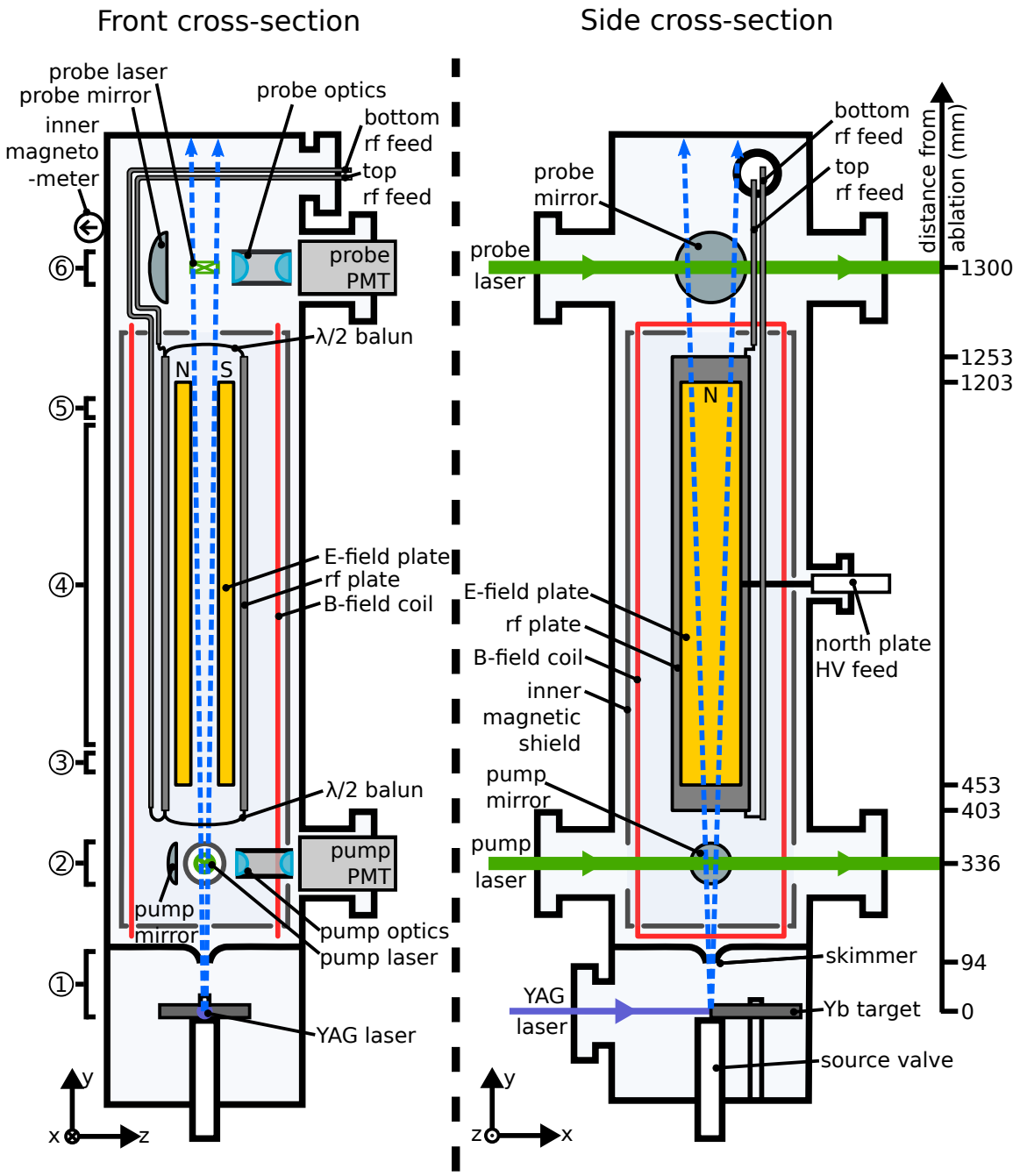


Figure 2.7: Front and side cross-section of the main vacuum chamber.

The molecules are then entrained in the carrier gas to be rapidly cooled to a translational temperature of 3–15 K and a rotational temperature of 1–5 K. This reliably produces $\sim 3\times10^9$ X $^2\Sigma^+(v = 0, N = 0)$ ground state YbF molecules per steradian per pulse, which travel vertically (along the y-direction) at 590±40 m/s. Other products, including other YbF isotopes and ^{174}YbF molecules in higher lying states, are also produced but do not interfere with our measurement so for now, we can ignore them.

The molecular packet then passes through a 2 mm diameter skimmer, placed 94 mm from the ablation point, which collimates the molecular beam as it enters the main chamber.

This gives a transverse extent to the beam of 2% of its position along the beamline, unless otherwise restricted by apertures, as shown by the blue dashed line in Figure 2.7.

The next section of interest (2), is the pump region. The molecules fly through a pump laser where the fluoresence is collected and imaged onto the face of the pump PMT.

The molecules then fly into the interaction region, labelled (3) – (5). Here, the molecules fly through static electric and magnetic fields as well as two time-dependent pulses of rf. The interaction region is fully enclosed in a mu-metal magnetic shield (diameter 170 mm, height 985 mm, plus end caps). A YbF molecule travelling at 590 m/s will be in this region for approximately 1 ms.

The interaction region contains two pairs of parallel plates. Closest to the centre line is a pair of electric field plates. These electric field plates are made from aluminium, coated in a 1 μm layer of copper and 5 μm layer of gold (dimensions 750 mm $\times$ 70 mm $\times$ 12.7 mm) and are separated by 12 mm. A precisely engineered support structure and two ceramic rods slotted through the plates keep this separation as uniform as possible across the entire interaction region. They can support up to $\pm$7.5 kV, equivalent to 12.5 kV/cm. The field points in the $+z$ direction if the north plate (labelled N) is positively charged and the south plate (labelled S) is negatively charged. The field points in the $-z$ direction if reversed.

Moving away from the centre line, the next structure is the parallel plate rf transmission line. This supports 170 MHz rf in the TEM mode, with the rf magnetic field polarised in the x direction. The rf plates (dimensions 850 mm $\times$ 56 mm $\times$ 2mm) are separated by 50 mm. The rf can be coupled onto these plates either at the top or bottom with a semi-rigid coax, allowing the rf to flow either from the top of the machine to the bottom or from bottom to top.

Finally, a magnetic field coil produces a small, static magnetic field in the z direction. These loops are simply glued onto the inner magnetic shield with vacuum epoxy.

Once the molecules have left the interaction region, they reach the final section of interest (6), the probe region, where molecules are detected via laser induced fluoresence. This is collected and imaged onto the face of the probe PMT. This optical setup has a collection efficiency of around 5% and when combined with the PMT quantum efficiency of 10% gives an overall collection efficiency of 0.5% [99].

Figure 2.8 gives an overview of the hardware used to control the experiment. The next sections describe the individual components used for each system in reference to this figure.

2.3.2 Laser beam generation

Both the pump and probe beams are derived from the same solid state laser, a *Menlo Orange One* with NTT doubler head. The laser is tuned to Q(0)($F = 1$) at 542 811 GHz with the internal temperature control and piezo. A small portion of light is picked off and sent to the transfer cavity lock setup [100]. Using the internal piezo, we can actively stabilise the frequency of the *Menlo* over long periods of time by referencing to a stable HeNe laser.

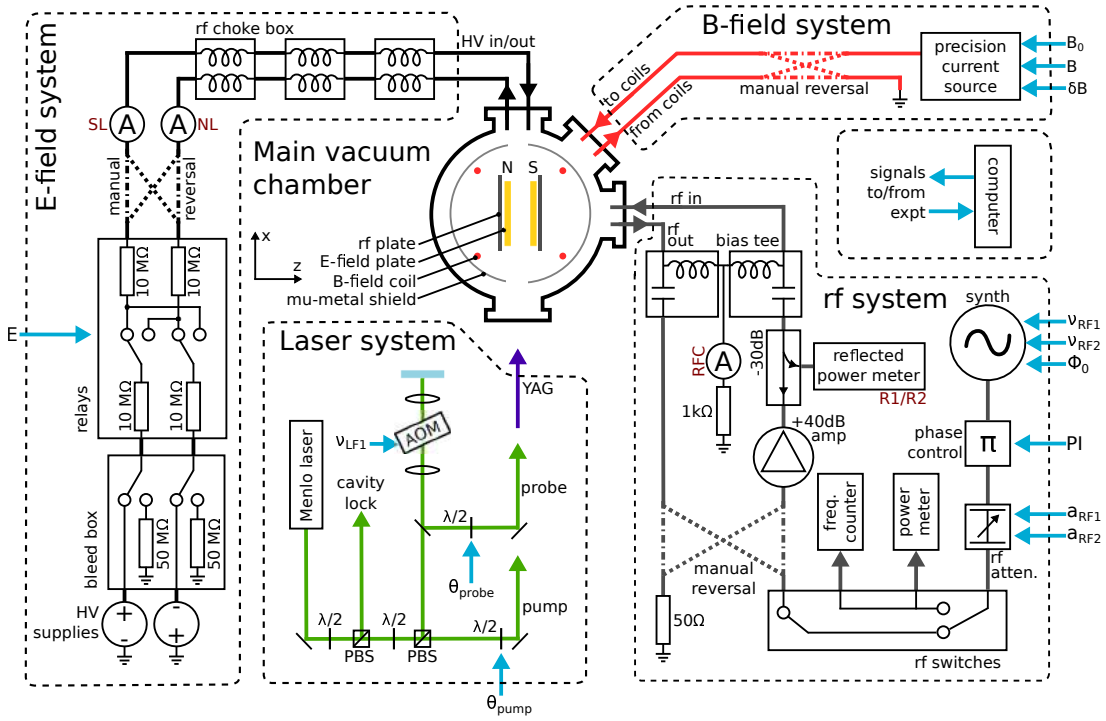


Figure 2.8: Schematic overview of the hardware used to control the experiment. Blue arrows label some of the important parameters controlled by the computer during the experimental sequence, the relevance of these are listed in Tables 2.2 and 2.3. Detector names are written in red and detailed in Tables 2.4 and 2.5

The main output of the *Menlo* is used as the pump laser source, with a part of this light being picked off and double passed through an AOM to blue shift the light to Q(0)($F = 0$) by 170.3 MHz. This light provides the probe beam for the experiment. The frequency of the probe light is controlled and optimised by the ν_{LF1} voltage signal sent from the computer.

Before entering the machine, both pump and probe beams are linearly polarised to a random orientation about the x axis by a pair of Glan-Taylor polarisers[1]. At the beginning of a set of measurements, the voltages θ_{pump} and θ_{probe} that control the independent orientations of the polarisers are chosen and set by the computer. Before being sent to the machine, the beams are shaped; the pump beam to 5 mm $1/e^2$ diameter gaussian beam and the probe to a 5×2 mm rectangular top hat. Typically, these beams have a total power of around 5 mW and 1 mW respectively.

2.3.3 Electric field generation

The high voltage used to create the electric field is generated by a pair of *Applied Kilovolts* supplies which can produce up to ±12 kV, but are set to ±9 kV for normal data taking, generating a field of 7.5 kV/cm. This is limited by the ability of the plates to support the voltage before break down occurs. The direction of the electric field (E) can be reversed

[1]In reality, a short train of optics is used to allow us to monitor the power of each beam and ensure the input power is constant for every polarisation orientation

automatically by a set of relays, described in [101]. This allows either positive or negative charge to be applied to either the *North* or *South* plate, labelled N and S in Figure 2.8. Between switches, the bleed box grounds the plates. The electric field can also be reversed manually by changing which relay each plate is plugged into. We label the different states of the cables as *true* or *false* indicated by the vertical and diagonal dashed lines on Figure 2.8.

Leakage currents that reverse with the direction of the electric field have the potential to provide a systematic error. Each cable is installed with a floating nanoammeter [102] that monitors the leakage currents flowing from the machine. The leakage is logged in real time during data acquisition and is typically <5 nA. They can also be used to monitor charging currents as the plates change polarity.

The cables then run through three ferrite choke boxes which isolate the rf system from the relay state of the electric field system, described in [89]. The cables then attach to the plates with a pair of spring loaded ceramic feedthroughs that press onto the side of the electric field plates, approximately half way along the length of the plates.

2.3.4 rf generation

The two pulses of 170 MHz rf are generated by the same *HP 8657A* rf synthesizer which is directed to the machine by a pair of *ZASWA-2-50DR+* switches. When not being pulsed to the machine, the rf is directed to a *HP 53131A* frequency counter and a *HP 438A* power meter, which are logged by the computer. We can independently control the phase, frequency, amplitude and duration of each rf pulse; the frequency of the rf pulses (ν_{RF1} and ν_{RF2}) is tuned directly by the DCFM of the synthesizer while the amplitude (a_{RF1} and a_{RF2}) is modulated by a *Mini-Circuits ZX73-2500* voltage controlled rf attenuator. The relative phases between the pulses (Φ_0) can be controlled by adjusting the DCFM voltage between rf pulses and an optional π phase shift (PI) can also be added to the second pulse by *Mini-Circuits PAS-1* bi-phase modulator.

Once the correct rf pulse has been generated it is amplified by *CPC MRI Plus* +40 dB amplifier and is sent into the vacuum chamber. The cables can be connected in different states labelled *true*/*false* depending on whether the rf is flowing from bottom to top/top to bottom respectively. In either case, the rf flowing out of the machine is dumped into a 50 Ω load. The efficiency of the coupling onto the parallel plate transmission line can be monitored by the reflected power meter.

2.3.5 Magnetic field generation

The magnetic fields are generated by a home built precision current supply, described in [90]. This can produce a few milliamperes of current with a fractional stability of 5×10^{-3}. The precision source controls the size and direction of the magnetic field and also minimises the ambient magnetic field. In addition to the automatic reversal, the direction of the magnetic field can also be changed by manual reversal of the cables running to the machine. This is

also labelled *true/false* depending on the connections to the machine. This manual reversal is represented by the dashed lines in Figure 2.8.

2.4 Experimental sequence

We can now begin to look at the experimental sequence used to measure the electron's EDM. To understand the heirarchy of data taking we need to know a bit of jargon before moving on to the details at each level.

A single pulse of YbF molecules travelling through the machine is called a *shot*. The machine produces a shot every 40 ms, which is phase locked to half the mains frequency (25 Hz). From beginning to end the shot lasts only 2.6 ms.

In between shots, several of the machine parameters can be varied between two states. For example, the direction of the $\boldsymbol{E}$ field, the direction and/or the size of the $\boldsymbol{B}$ field could be changed. Section 2.4.2 discusses this example in more detail to show how we can extract a value for the EDM. In the experiment, we collect data in *blocks* of 4096 shots, which switch many more parameters than this to create distinct *machine states*. A block contains 512 distinct states with each state visited eight times per block.

Finally, many blocks of data create a data set, with an uninterrupted series of blocks being called a *cluster*. This section discusses the experimental sequence from the individual shot up to the overview of a full data set.

2.4.1 A shot

To begin, let's follow the sequence of events for a single molecular packet travelling through the machine. The sequence can be divided into six events, with the regions in which they occur, as shown in Figure 2.7.

(1) Make some YbF

Every 40 ms, the supersonic source produces YbF molecules that travel vertically upwards at 590 m/s. Although lots of products are created, only the molecules thermalised to the X $^2\Sigma^+(v = 0,\ N = 0)$ ground state take part in the experiment. We define $t = 0$ as the moment the YAG fires, creating YbF.

(2) Prepare

At $t = 570$ μs, the molecules pass through a linearly polarised pump laser beam propagating along the x direction. It is tuned to the Q(0)($F = 1$) line which removes all the population from the $F = 1$ state. About 30% of the $F = 1$ population decays into the $F = 0$ ground state. The rest is lost to the X $^2\Sigma^+(v = 0,\ N = 2)$ state, or to higher vibrational states in X $^2\Sigma^+$ where it no longer participates in the experiment. Efficient optical pumping, shown in Figure 2.9, approximately doubles the original population of $F = 0$ and empties $F = 1$.

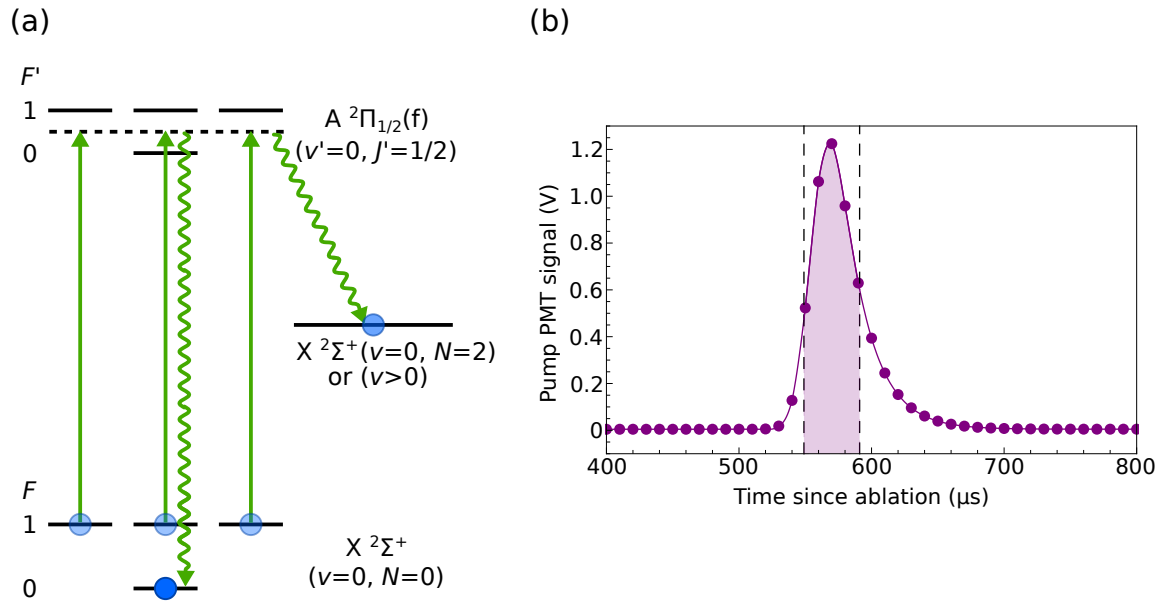


Figure 2.9: (a) Optical pumping on Q(0)($F = 1$) cleans out the thermal population in $F = 1$. This decays into the $F = 0$ ground state, or is lost to higher vibrational and rotational states in X $^2\Sigma^+$. (b) The fluorescence signal detected by the pump PMT. The shaded region, bounded by the times t'_1 and t'_2, shows the typical velocity class of molecules selected for data analysis in Section 2.5.2.

The fluorescence from these decays is collected by a PMT and is used to normalise out source fluctuations. A typical signal is shown in Figure 2.9(b).

Once the molecules have passed through the pump laser they are intialised in the state

$$|F = 0,\ M_F = 0\rangle \tag{2.12}$$

(3) Create a superposition

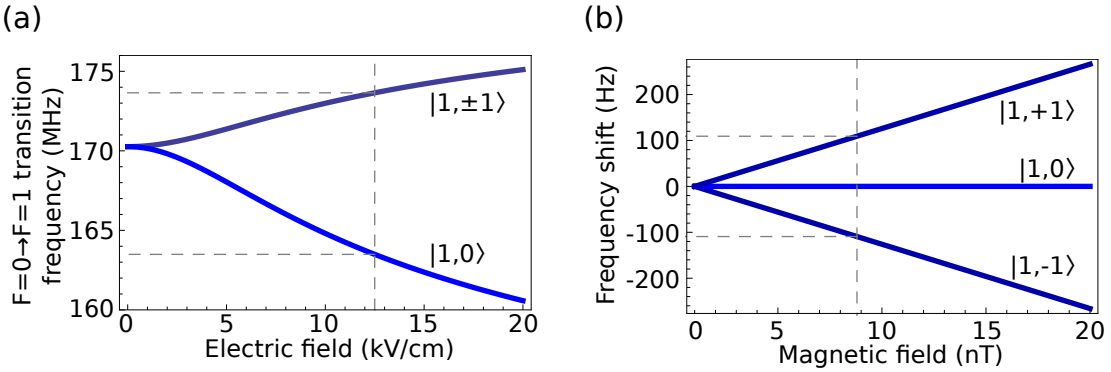


Figure 2.10: (a) The Stark shifts and (b) Zeeman shifts of the magnetic sublevels in X $^2\Sigma^+(v = 0,\ N = 0)\,|F = 1\rangle$ state. The grey dashed lines indicate operating values.

The molecules then move into the interaction region. The electric field increases from

0 kV/cm to 7.5 kV/cm across the $\sim$ 1 cm fringe field (where the length scale is set by the plate separation). Since the rotational constant is much larger than the energy provided by the electric field, the internuclear axis adiabatically follows the field, without any population transferring between rotational states. Once inside the plates, the electric field polarises the YbF molecules, aligning their internuclear axis $\boldsymbol{n}$ to the z-axis of the experiment. At this field ($|E_z| = 7.5$ kV/cm), the molecules have a polarisation factor of $\eta = \langle \boldsymbol{n}.\hat{\boldsymbol{z}} \rangle = 0.61$ where $\hat{\boldsymbol{z}}$ is a unit vector along z. This electric field creates a Stark shift between the magnetic sublevels in the $F = 1$ state, shown in Figure 2.10(a). A small magnetic field of $|B_z| = 8.8$ nT is also applied. This creates a Zeeman shift of around ± 125 Hz, breaking the degeneracy of the $M_F = \pm 1$ states in the $F = 1$ state, shown in Figure 2.10(b). The explicit energy level structure of the X $^2\Sigma^+(v = 0,\ N = 0)$ state within the interaction region (the grey dashed lines in Figures 2.10) is shown in Figure 2.11.

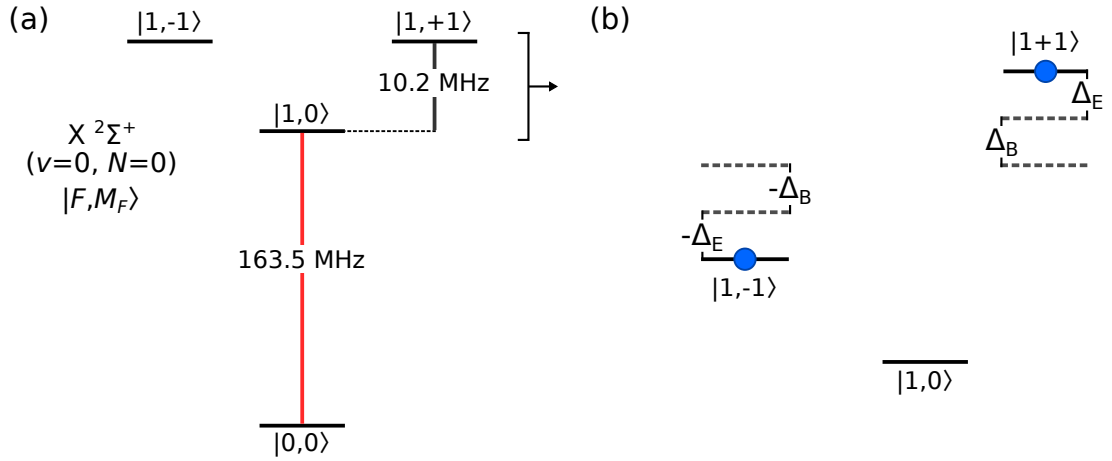


Figure 2.11: Energy level structure of the X $^2\Sigma^+(v = 0,\ N = 0)$ hyperfine states in the interaction region where $|E_z| = 12.5$ kV/cm and $|B_z| = 8.8$ nT. (a) The Stark shifted energy level structure of the ground state in the electric field and (b) the energy level splitting of the $F = 1$ sublevels caused by the Zeeman and electron EDM interactions; $\Delta_B = B\mu_B$ and $\Delta_E = d_e \eta E_{\text{eff}}$. This gives splittings of $|\Delta_B/\hbar| = 2\pi \times 125$ Hz and $|\Delta_E/\hbar| < 2\pi \times 0.3$ mHz.

Once inside this region a 9 μs pulse of $\omega_{\text{rf}} = 2\pi \times 173.6$ MHz rf is sent through the TEM transmission line. The geometry of the rf plates ensures that the rf is polarised in the x direction, which drives $\sigma^{\pm}$ transitions in the z-basis. This drives the $|0, 0\rangle$ state into a superposition of the $|1, \pm 1\rangle$ states. The amplitude of the pulse is tuned to ensure all the population of the $F = 0$ ground state is coherently transferred to the $F = 1$ state — otherwise known as a π-pulse. This is shown in Figure 2.12.

After the pulse of rf the population is in the superposition,

$$|0, 0\rangle \rightarrow \frac{i}{\sqrt{2}} \left(|1, +1\rangle - |1, -1\rangle \right). \tag{2.13}$$

In this example, the energy scale is defined such that the $|1, \pm 1\rangle$ superposition has zero energy.

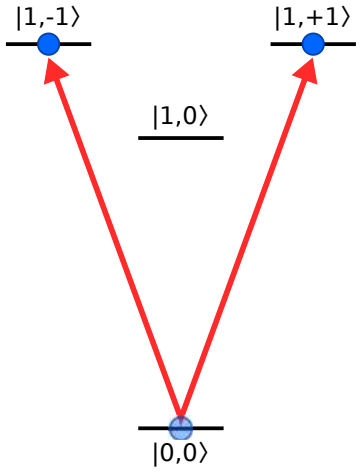


Figure 2.12: A pulse of $\omega_{\mathrm{rf}} = 2\pi \times 173.6$ MHz x-polarised rf couples the $|0,0\rangle \leftrightarrow i(|1,+1\rangle - |1,-1\rangle)/\sqrt{2}$ states. The amplitude of the pulse is tuned so that all the population from the $|0,0\rangle$ state is coherently transferred to the $F = 1$ upper state.

This removes some global phase factors that multiply the equations that follow.

(4) Evolve

This superposition of the population is then allowed to evolve in the static electric and magnetic fields for time $\tau = 980$ μs. The Zeeman and electron EDM interactions create opposite energy shifts between the $|1,\pm1\rangle$ states. For electric and magnetic fields applied in the $+z$ direction, the energy shifts of the $|1,\pm1\rangle$ states are $\pm(\Delta_B - \Delta_E) = \pm(B\mu_B - \eta E_{\mathrm{eff}} d_e)$. In this case, the typical energy level splittings are $|\Delta_B/\hbar| = 2\pi \times 125$ Hz and $|\Delta_E/\hbar| < 2\pi \times 0.3$ mHz [24].

As they fly through these fields, the superposition in Equation (2.13) evolves to

$$\frac{i}{\sqrt{2}}\left(|1,+1\rangle - |1,-1\rangle\right) \rightarrow \frac{i}{\sqrt{2}}\left(e^{i(\phi_B+\phi_E)}\,|1,+1\rangle - e^{-i(\phi_B+\phi_E)}\,|1,-1\rangle\right) \tag{2.14}$$

where $\phi_B = \Delta_B\tau/\hbar$ and $\phi_E = \Delta_E\tau/\hbar$. Equivalently, the system's angular momentum precesses about the z axis of the system under the torque of the electric and magnetic fields at a rate of $(\Delta_B \pm \Delta_E)/\hbar$, depending on the orientation of the applied electric field to the magnetic field. Any decoherence between these levels is small; the lifetime of the $F = 1$ state is much longer than the time it takes for the molecular packet to travel through the machine, and a vacuum of $< 10^{-6}$ mbar ensures hyperfine-state changing collisions are negligible [67].

(5) Recombine the superposition

After the free evolution period, a second 9 μs, π-pulse of rf is applied. This maps the state $\left(|1,+1\rangle - |1,-1\rangle\right)/\sqrt{2}$ coherently onto the state $ie^{i\phi_{\mathrm{rf}}}\,|0,0\rangle$. Here, $\phi_{\mathrm{rf}} = \omega_{\mathrm{rf}} \times 9$ μs. The final

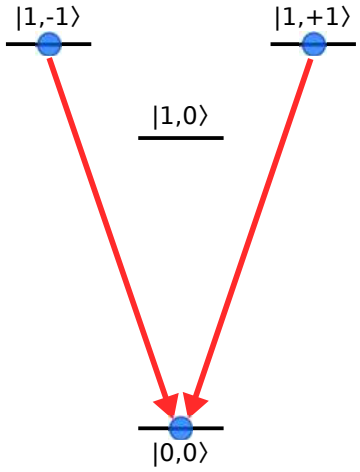


Figure 2.13: A second π pulse of rf recombines the superposition. Since the system has a different phase after the evolution period, about half the population is transferred to $|0,0\rangle$ and half is left in $|1,\pm1\rangle$.

distribution of states after the π-pulse is,

$$\frac{i}{\sqrt{2}}\left(e^{i(\phi_B+\phi_E)}\,|1,+1\rangle - e^{-i(\phi_B+\phi_E)}\,|1,-1\rangle\right)$$
$$\rightarrow -e^{i\phi_{\rm rf}}\cos\left(\phi_B+\phi_E\right)|0,0\rangle - \sin\left(\phi_B+\phi_E\right)\left\{\frac{1}{\sqrt{2}}\left(|1,+1\rangle + |1,-1\rangle\right)\right\}. \quad (2.15)$$

(6) Probe

The molecules leave the interaction region and fly through the probe laser beam. This is tuned to the Q(0)($F=0$) transition and counts the number of molecules in the $|0,0\rangle$ state, as shown in Figure 2.14. Typically, one photon per molecule is produced before the population is lost from the probe state. The fluorescence emitted by the decays is collected and imaged onto the face of the probe PMT. A typical time of flight profile is shown in Figure 2.14(b). The PMT signal is

$$S(t) = S_b(t) + S_0(t)\cos^2\left(\phi_B+\phi_E\right) \quad (2.16)$$

where $S_B(t)$ is any background light from scatter inside the chamber and $S_0(t)$ is proportional to the number of molecules taking part in the experiment. By considering how this signal $S(t)$ changes between different switch states of the machine we can extract an EDM value. In a typical shot, around 1000 photons are detected during the gate window [99].

2.4.2 The simplest block

With the knowledge of a single shot we can now start to measure the EDM by taking many shots of the experiment. Firstly, we can consider fixing both the electric field and magnetic field along the $+z$ direction. In this example, we fix the magnitude of the electric field but scan the magnitude of the magnetic field across a few nT. As we adjust the magnetic field we begin to scan out the $\cos^2$ interference curve described in Equation (2.16). If we then

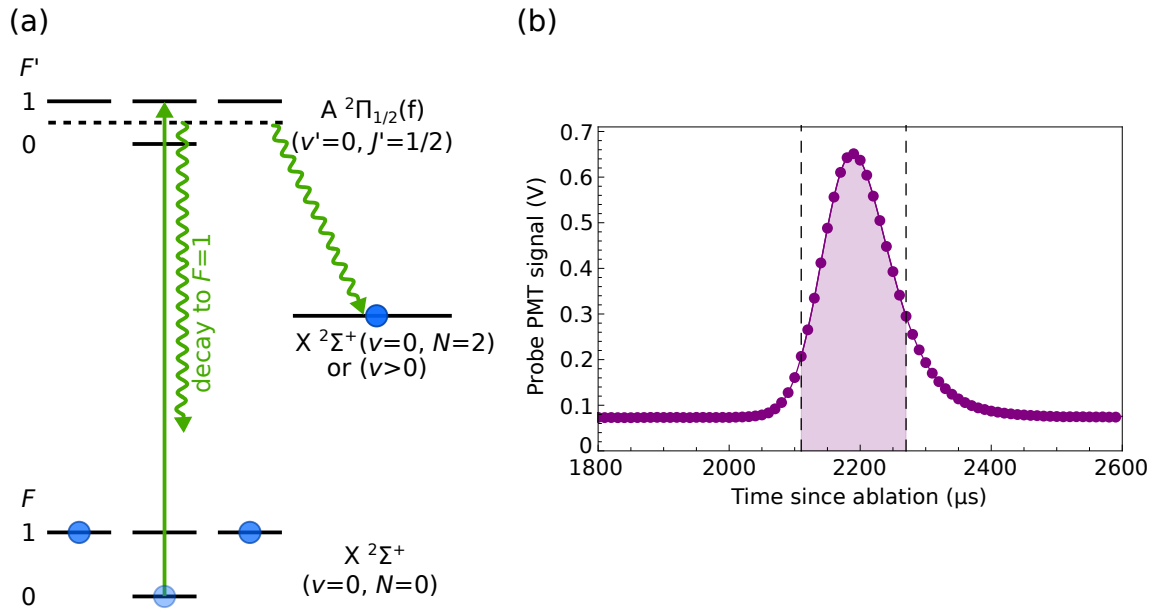


Figure 2.14: (a) The population in the $|0,0\rangle$ state is measured using the probe beam which is tuned to Q(0)($F=0$). Typically one photon/molecule is produced before the population is lost from the probe state. (b) Typical fluorescence signal detected by the probe PMT. The shaded region, bounded by times t_1 and t_2 shows the typical gate window used for analysis.

reverse the direction of the electric field and rescan the magnitude of the magnetic field we see a second interference curve described by

$$S(t) = S_b(t) + S_0(t)\cos^2\left(\phi_B - \phi_E\right). \tag{2.17}$$

The phase difference between these fringes, shown greatly exaggerated in Figure 2.15, is directly proportional to the size of the EDM.

The most efficient way to look for this phase shift is to sample each curve at four different points, where the change in signal caused by a non-zero EDM is maximised. The signals labelled {A, B, C, D} are recorded for the electric field pointing in one direction, and {A', B', C', D'} for the opposite direction. Four magnetic field values are chosen to apply phase shifts of $\phi_B = \{-\pi/4 - \pi/32,\ -\pi/4 + \pi/32,\ \pi/4 - \pi/32,\ \pi/4 + \pi/32\}$ at each point respectively. Using just these eight points we can extract a value of d_e [78],

$$d_e = \frac{(\pi/32)}{\eta E_{\text{eff}} \tau}\left(\frac{A + B - C - D - A' - B' + C' + D'}{-A + B + C - D - A' + B' + C' - D'}\right), \tag{2.18}$$

where the expression in brackets is the change in signal caused by an EDM normalised to the small step in magnetic field; $\phi_E/(\pi/32)$ and the prefactor converts from ϕ_E to a value of d_e.

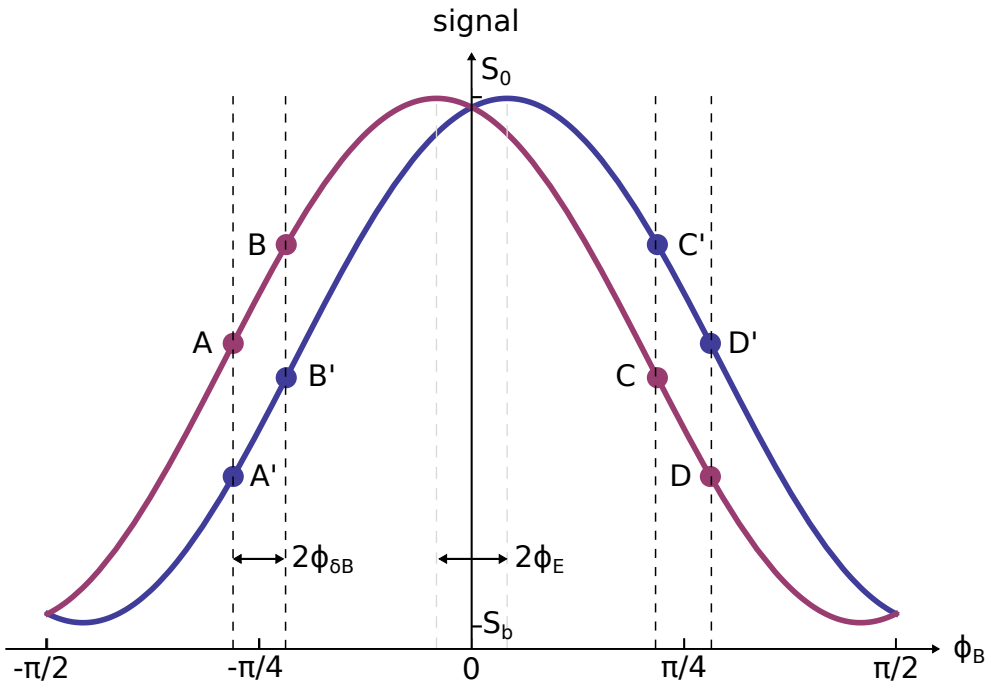


Figure 2.15: A pair of interferometer fringes scanned out by the magnetic field for different directions of electric field along z. The effect of the electron's EDM, shown greatly exaggerated here, generates a phase shift of the entire fringe by $2\phi_E$. The eight points show how we sample the curve to extract a value of the EDM.

2.4.3 A real block

The example in Section 2.4.2 shows that an EDM value can be extracted by recording just eight shots. We can think of this as switching three distinct parameters; the direction of the applied electric field (labelled E), the direction of the magnetic field (labelled B) such that it steps between $\phi_B = \pm\pi/4$ and the direction of the smaller magnetic field (labelled δB) which steps between $\phi_{\delta B} = \pm\pi/32$.

In addition to E, B and δB, several other parameters are switched during a full block. A real data set switches nine parameters, listed in Table 2.3, creating $2^9 = 512$ unique combinations which we call machine states. A block of data contains 4096 shots, which allows each machine state to be visited eight times. Switching parameters in this way allows us to look for correlations between the signal and any switched parameters, or even any combination of parameters. In addition, this switching technique allows us to look for small signal changes in the presence of background noise, to lock and optimise parameters as well as providing information on systematic effects [103] [104].

The parameter X is modulated by a unique waveform W_X which specifies how the parameter is switched during a block. The waveform is simply a list of 4096 numbers with values of $+1$ or -1. Each element of the waveform defines the state of parameter X for each shot within the block. Every waveform has an equal number of $+1$ and -1 values and all waveforms used within the block are orthogonal to each other. At the beginning of a block, the computer will

randomly generate a list of waveforms, using the technique described in [104]. The waveforms are chosen to modulate parameters at high frequencies, which suppresses low frequency noise, and to be strongly aperiodic, which suppresses long term signal drifts. Hardware restrictions must also be considered, for example, every electric field modulation incurs several seconds of dead time making frequent reversal impractical.

Parameter name	Description	Value
ν_{rf1}	Centre frequency of the first rf pulse.	173.6 MHz
ν_{rf2}	Centre frequency of the second rf pulse.	173.6 MHz
ν_{LF1}	Centre frequency of the probe AOM.	170.25 MHz
a_{rf1}	Centre amplitude of the first rf pulse.	0 dBm (+40 dB)
a_{rf2}	Centre amplitude of the second rf pulse.	-1.5 dBm (+40 dB)
B_0	Bias z magnetic field to cancel stray fields.	<2 nT
θ_{probe}	Probe polarisation angle.	0–360°
θ_{pump}	Pump polarisation angle.	0–360°
Φ_0	Relative phase between rf pulses.	0–10π rad

Table 2.2: Parameters held constant during a block.

Parameter name	Description	Step
E	Direction of electric field, $\pm E_z$.	$\pm$12.5 kV/cm
B	Direction of magnetic field.	$B_0 \pm 8.8$ nT
δB	Small step in magnetic field.	1.1 nT
RF1F	Frequency of the first rf pulse.	$\nu_{\mathrm{rf1}} \pm 2$ kHz
RF2F	Frequency of the second rf pulse.	$\nu_{\mathrm{rf2}} \pm 2$ kHz
RF1A	Amplitude of the first rf pulse.	$a_{\mathrm{rf1}} \pm 5\%$
RF2A	Amplitude of the second rf pulse.	$a_{\mathrm{rf2}} \pm 5\%$
LF1	Frequency of the probe laser AOM.	$\nu_{\mathrm{LF1}} \pm 300$ kHz
PI	Fixed phase between rf pulses.	$\Phi_0 \pm \pi/2$ rad

Table 2.3: Parameters that are switched between two different states during a block.

The block begins with the computer generating a new set of random waveforms. Once this is complete, the computer randomly sets θ_{pump} and θ_{probe}, the polarisation angle of the pump and probe beams, as well as Φ_0, the phase difference between the two rf pulses. These parameters, along with others listed in Table 2.2, are fixed throughout a block. It also records several of the experimental parameters including: the electric field, the magnetic field steps B and δB, the bias field B_0, the rf frequency steps, RF1F and RF2F, and their central values ν_{rf1} and ν_{rf2}, and amplitudes a_{rf1} and a_{rf2} as well as the laser frequency step LF1 and its

central value ν_{LF1}. This takes around 40 s to complete.

Once this is complete the machine then begins to fire its 4096 shots, switching parameters in between according to the generated waveforms. A shot is fired every 40 ms, with the molecular beam lasting only 2.6 ms. This allows for plenty of time to switch all the parameters, except for the electric field. This is switched deliberately slowly (16 s) to ensure charging currents are limited to a few μA which avoids the shields being magnetised.

Once the shots are finished the block is automatically analysed and the fixed parameters are adjusted based on these results. In this way the rf and laser frequencies stay on resonance and any changes in the stray magnetic field are trimmed away by the bias field. Once this is complete the machine is now ready to take another block. This whole process takes around six minutes to complete.

2.4.4 A cluster

A collection of blocks is called a cluster. These are taken autonomously by the computer without human intervention over the course of a day. In between clusters we realign laser beams, demagnetise magnetic shields and every 10 or so clusters we skim the Yb target. We also change the manual state of the machine by reversing the cable connections. Each cluster is labelled by the manual state of the electric field system, magnetic field system and the rf system, each of which can be in state true or false depending on which way round the cabels are connected. For example, a cluster will be labelled {E, B, rf}={T, T, T} to indicate the manual state of the machine in that cluster. Understanding how different signals change with manual state is important for distinguishing potential systematic effects.

2.5 Detectors and data analysis

The level of detail used in this section is not necessary to understand the results presented in the remaining chapters, but is presented for completeness.

2.5.1 Detectors

Two types of detectors are used to collect data during a shot. A single point detector records one value per shot, typically at the end of the molecular pulse. Time dependent detectors record several points during a gated time interval within a shot, taking points every few μs depending on the resolution of the detector. We have already come across two time dependent detectors in this chapter; the pump and probe PMTs. The remaining detectors are listed in Tables 2.4 and 2.5.

Many of the additional detectors will be discussed later on. However, it is worth briefly mentioning the *short* and *9 V battery* detectors. These are plugged directly into the analogue-to-digital converter card which samples the time dependent detector signals. These dummy inputs provide a useful diagnostic for the data acquisition electronics and analysis algorithms by checking the detectors produce the expected results from these well defined inputs.

Detector	Name	Measures
Pump photodiode	NPD	Power of the pump laser beam.
Probe photodiode	TPD	Power of the probe laser beam.
MiniFlux 1 magnetometer	M1	Magnetic field along z axis close to HV supplies of the electric field system.
MiniFlux 2 magnetometer	M2	Magnetic field along z axis over the optical table (between M1 and M3).
MiniFlux 3 magnetometer	M3	Magnetic field along z axis on top of the computer control rack.
North leakage monitor	NL	Leakage current on the HV cable connected to the North plate.
South leakage monitor	SL	Leakage current on the HV cable connected to the South plate.
rf1 reflected power	R1	Power of rf reflected out of the machine during the first rf pulse.
rf2 reflected power	R2	Power of rf reflected out of the machine during the second rf pulse.
Pi flip monitor	PF	Phase of the second rf pulse with respect to the first.

Table 2.4: List of single point detectors which record one value per shot. See Figure 2.8 for location of NL, SL, R1 and R2.

Detector	Name	Measures	Records (μs)	Resolution (μs)	Typical gate
Pump PMT	NORM	Laser induced fluorescence from the pump beam.	400–780	10	549–591
Probe PMT	TOP	Laser induced fluorescence from the probe beam.	1800–2590	10	2110–2270
Inner magnetometer	MAG	Magnetic field along z axis, next to the vacuum chamber.	400–2400	200	400–2400
Short	GND	Voltage across a 50 Ω resistor; dummy input.	400–2400	200	400–2400
9 V battery	BAT	Voltage across a 9 V battery; dummy input.	1800–2590	10	1800–2590
rf ammeter	RFC	DC current flowing onto the rf plates.	400–2400	100	400–2400

Table 2.5: List of time dependent detectors which record several values over a shot. See Figure 2.7 for location of MAG and Figure 2.8 for location of RFC.

2.5.2 Extracting signals from detectors

Once a block is complete, a set of signals has been recorded for every one of the 4096 shots by the detectors listed in Tables 2.4 and 2.5. During a block, each shot will visit one of the 512 machine states which correspond to the nine switch parameters being in either a +1 or −1 state. When performing the EDM measurement, it is important to determine how these signals are correlated with specific parameters, or even parameter combinations.

Let $S_D(i;\ t)$ label the (possibly time dependent) signal from detector D on the ith shot of the block. The signal which is correlated with the parameter X is called a *channel*, which we label $\{X\}$. To evaluate the signal change caused by switching X (while effectively averaging over all other parameters) we apply the equation,

$$\{X\}_D(t) = \frac{1}{N}\sum_{i=1}^{N} W_X(i) S_D(i;\ t), \tag{2.19}$$

where $W_X(i)$ is the ith element of the waveform for parameter X and $N = 4096$, the number of shots in a block. The waveforms used for analysis are not necessarily restricted to those used to modulate the switched parameters during a block, as described in Section 2.4.3. For example, the analysis waveform that consists of 4096 +1's (called W_{SIG}) gives the average signal at time t for detector D, $\{\mathrm{SIG}\}_D(t)$. Other frequently used waveforms are the product of two or more modulation waveforms. This has the notation,

$$W_{X\cdot Y}(i) = W_X(i) \times W_Y(i). \tag{2.20}$$

This channel combination compares the signal when X and Y are in the same switch state, to when they are in opposing switch states.

In terms of detectors, we most often consider the signal from the probe PMT detector which has been normalised to the pump PMT signal. We call this the *top-normed* detector signal. This normalisation removes any common sources of noise e.g from source fluctuations. This combination of detectors modifies Equation (2.19) to,

$$\{X\}(t) = \frac{1}{N}\sum_{i=1}^{N} W_X(i)\frac{\tilde{\mathcal{N}}}{\mathcal{N}(i)} S_{\mathrm{TOP}}(i;\ t), \tag{2.21}$$

where $\mathcal{N}(i)$ is the integrated pump PMT signal for the ith shot in the block

$$\mathcal{N}(i) = \int_{t_1'}^{t_2'} S_{\mathrm{NORM}}(i;\ t)\ dt. \tag{2.22}$$

The integral bounds t_1' and t_2' are the beginning and end of the time interval over which the pump PMT signal is integrated, as shown by the shaded region in Figure 2.9(b). This gate window selects which molecules take part in the experiment in order to minimise the statistical uncertainty of the measurement. Too narrow a window and the number of molecules participating in the experiment is reduced, increasing statistical uncertainty. Too wide an

interval and the long pulse of molecules experiences increased inhomogeneity in the rf, electric and magnetic fields, also increasing measurement uncertainty. Equation (2.21) also allows us to look at any temporal variation within anlysis channels which could indicate problems in the machine. Finally, $\tilde{\mathcal{N}}$ is the mean of all the integrated pump signals in the entire block,

$$\tilde{\mathcal{N}} = \frac{1}{N}\sum_{j=1}^{N}\int_{t_1'}^{t_2'} S_{\mathrm{NORM}}(j;\ t)\ dt, \tag{2.23}$$

which keeps the top-normed signal in units of V.μs and ensures the common sources of noise are rejected while keeping the central value the same.

A few of the interesting channels and their interpretations are listed in Table 2.6. If no detector label, the reader should assume the signal from the top-normed detector was analysed.

Channel	Description
$\{\mathrm{SIG}\}$	The average signal in the probe PMT.
$\{\delta B\}$	Proportional to the amplitude of the interference curve. Typically used to calibrate analysis channels.
$\frac{\{B\}}{\{\delta B\}}$	The average interferometer phase, normalised by the amplitude of the interferometer. This is non-zero in the presence of an uncancelled background magnetic field. This channel is used to optimise B_0 and cancel any stray field.
$\{E\cdot\delta B\}$	Correlation between electric field reversal and amplitude of interference curve.
$\frac{\{E\cdot B\}}{\{\delta B\}}$	Leading term in EDM expansion. See Equation (2.24).
$\{RF1F\}$	Average detuning of first rf pulse.
$\{E\cdot RF1F\}$	The detuning of the first rf pulse correlated with reversal of electric field. If this is non-zero it indicates an imperfect field reversal causing a change in Stark shift, contributing to rf detuning.
$\{E\}_{\mathrm{NL}}$	Leakage current on the cable connected to the North plate correlated with the direction of electric field. A non-zero value could mimic an EDM signal.
$\{LF1\cdot\delta B\}$	Correlation between laser frequency detuning and amplitude of interference curve. Used to optimise the frequency of the probe beam towards the Q(0)($F=0$) peak.

Table 2.6: Some interesting analysis channels and their meanings.

More complicated channel combinations than those listed in Table 2.6 are denoted by square brackets. The most important example being the [EDM] channel. In the case of an imperfect experiment where there is an uncancelled background magnetic field as well as imperfect electric and magnetic field reversals the expression for the channel is [78],

$$[\text{EDM}] = \frac{g_F \mu_B B_{\delta B}}{\eta E_{\text{eff}}} \left[\frac{\{E \cdot B\}}{\{\delta B\}} - \frac{\{B\}\{E \cdot \delta B\}}{\{\delta B\}\{\delta B\}} + \frac{\{SIG\}}{\{\delta B\}} \left(\frac{\{B \cdot \delta B\}\{E \cdot \delta B\}}{\{\delta B\}\{\delta B\}} - \frac{\{E \cdot B \cdot \delta B\}}{\{\delta B\}} \right) \right], \tag{2.24}$$

where $B_{\delta B}$ is the difference in magnetic field caused by the small step δB, chosen such that $g_F \mu_B B_{\delta B} \tau / \hbar = \pi/32$. The first term in Equation (2.24) is the expression in the case of an ideal experiment and is equivalent to Equation (2.18). The second and third terms remove the effects of these imperfections from the EDM channel.

Often, we may want to calculate a single value for each channel by integrating over all the arrival times of the molecules during a gated time interval for any detector signal

$$\langle \{X\}_D \rangle = \int_{t_1}^{t_2} \{X\}_D(t)\ dt. \tag{2.25}$$

If the detector is top-normed then we relate $t_1 = \kappa t_1'$ and $t_2 = \kappa t_2'$ so that the same velocity class of molecules is selected, shown in Figure 2.14(b). For a ratio of channels such as $\{X\}\{Y\}/\{Z\}$ the integrated quantity is $\langle \{X\}\{Y\}/\{Z\} \rangle$ where the integral has been applied last, rather than $\langle \{X\} \rangle \langle \{Y\} \rangle / \langle \{Z\} \rangle$.

2.5.3 Analysis techniques

Statistics

The channel values taken over several blocks then need to be combined together to produce an average value with an associated confidence interval. The distribution of channel values often deviates from normal, meaning the usual mean and standard error are not robust measures of the channel. Instead, to calculate the central value, the 5% trimmed mean is used. This method drops the smallest and largest 5% of values and calculates the mean of the remaining data.

To estimate the error on the mean we use the bootstrap method [105]. To implement this we begin with the real experimental (untrimmed) data set. This contains n blocks of data with n measurements of the channel $\{X\}$ creating a set of channel values $\boldsymbol{X} = \{x_1,\ x_2, ...,\ x_n\}$. Next, we randomly select n samples with replacement from $\boldsymbol{X}$ to create a replicate data set $\boldsymbol{X}^{*1}$. This process is repeated m times (usually $m = 5000$) to generate many replicate data sets $\{\boldsymbol{X}^{*1},\ \boldsymbol{X}^{*2}, ..., \boldsymbol{X}^{*m}\}$. The 5% trimmed mean of each replicate is then calculated to create a set of trimmed mean values $\boldsymbol{\nu} = \{\nu^1,\ \nu^2, ..., \nu^m\}$. We use the cumulative distribution function of the set of trimmed means CDF(ν), to calculate symmetric confidence intervals which provide us with an error for the central value.

The advantage of the bootstrap method is that it assumes nothing about the underlying distribution. By resampling we are modelling how we have sampled the distribution through measurements, rather than modelling the underlying distribution. The final set of trimmed means $\boldsymbol{\nu}$ is well approximated by a Gaussian and has a standard deviation of $s/\sqrt{n}$, where n is the total number of blocks and s is the sensitivity of the machine, this is explained further in Chapter 3.

Blind

To ensure we do not bias the results through our analysis, a hidden artificial offset is added to the EDM channel $\{E{\cdot}B\}$ by the computer during data anlysis. The value of the blind is chosen randomly by the computer from a normal distribution with zero mean and 5×10^{-27} e.cm standard deviation. Once the blind is removed no more data analysis is allowed.

Chapter 3

Sensitivity and systematics

3.1 Sensitivity

3.1.1 Shot noise limit

There is a fundamental limit on the statistical sensitivity of the EDM measurement. The output of the detection system gives a series of pulses, corresponding to photons arriving at the face of the PMT. This is a poissonian process where on average, p photons are counted during a shot. The fluctuations in the number of photons detected by the PMT is simply,

$$\sigma = \sqrt{p} \tag{3.1}$$

which scales as $\sigma\sqrt{N}$ for N measurements. This is called the *shot noise*. In an ideal experiment this will be the only source of noise and the sensitivity of the machine will simply follow this limit. In reality there are many additional sources of noise that can reduce the measurement sensitivity, some of which are discussed in the following sections. To operate the machine as efficiently as possible, the contributions from these noise sources should be under control below the level of the shot noise. To ensure this is the case, we first need to estimate the shot noise of our experiment and compare it to real experimental data to diagnose any suspected sources of noise. We can also use the shot noise limit to investigate how we might improve the sensitivity of our machine.

To begin, consider the simplest possible EDM measurement, presented in Figure 3.1. In this technique we simply sit at $\phi_B = \pi/4$ and reverse the direction of the electric field from $+E$ to $-E$, shown by the markers in the Figure 3.1. The signal at each point ($S_{\pm E}$), which is proportional to the number of photons counted by the probe PMT, is

$$S_{\pm E} = S_b + S_0 \cos^2(\phi_B \pm \phi_E) \simeq S_b + S_0 \left(\frac{1}{2} \mp d_e \eta E_{\text{eff}} \tau/\hbar\right) \tag{3.2}$$

where the signal has been expanded about $\phi_B = \pi/4$ and ϕ_E is assumed to be small. Let's assume we take $N/2$ measurements at point $+E$ and N/2 measurements at $-E$. The total signal difference between these two points after N measurements, which we attribute to the

EDM interaction, is,

$$\frac{N}{2}(S_{-E} - S_{+E}) = NS_0 d_e \eta E_{\text{eff}} \tau/\hbar \tag{3.3}$$

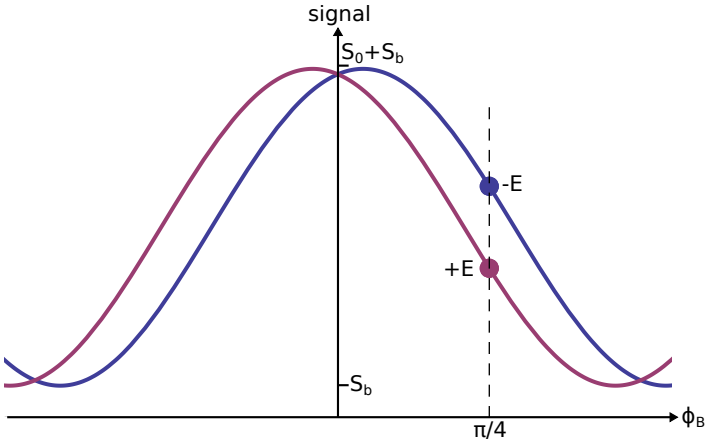


Figure 3.1: A simple EDM experiment used to estimate the shot noise limit.

The probe PMT records an average signal of $S_0/2+S_b$ per shot. This gives an uncertainty in the total recorded signal of,

$$\sigma = \sqrt{N(S_0/2 + S_b)}. \tag{3.4}$$

By equating the signal uncertainty σ, to Equation (3.3), we find the minimum value of d_e the experiment would be able to distinguish with 1-σ uncertainty after N measurements,

$$\sigma_{d_e} = \frac{\hbar}{S_0 \eta E_{\text{eff}} \tau} \sqrt{\frac{S_b + S_0/2}{N}}. \tag{3.5}$$

Defining the contrast of the interference curve as the amplitude of the curve divided by the average signal,

$$\mathcal{C} = \frac{S_0/2}{S_0/2 + S_b}, \tag{3.6}$$

gives a very simple experession for the EDM shot noise sensitivity,

$$\sigma_{d_e} = \frac{\hbar}{\eta E_{\text{eff}} \tau 2\mathcal{C}} \frac{1}{\sqrt{N\,(S_0/2 + S_b)}}, \tag{3.7}$$

where the expression under the square-root is proportional to the average number of photons we detect for N measurements.

This simple example gives us the shot noise limit of our experiment and also provides a useful comparison when considering a more comprehensive EDM experiment. In reality, we extract the shot noise from a block of data using the analysis channels, described in Section 2.5.2. For reference, we can rewrite Equations (3.3), (3.4) and (3.6) using the analysis channels

by following the derivations presented in [89] [90],

$$\langle\{E \cdot B\}\rangle \simeq \frac{1}{\hbar}\frac{32}{\pi}\langle\{\delta B\}\rangle N d_e \eta E_{\text{eff}} \tau \tag{3.8}$$

$$\sigma \simeq \langle\{\text{SIG}\}\rangle \sqrt{N\left(\frac{1}{P_{\text{TOP}}} + \frac{1}{P_{\text{NORM}}}\right)} \tag{3.9}$$

$$\mathcal{C} \simeq \frac{\frac{16}{\pi}\langle\{\delta B\}\rangle}{\langle\{\text{SIG}\}\rangle} \tag{3.10}$$

where $\langle\{E \cdot B\}\rangle$ is the signal attributed to the EDM interaction averaged over all molecular arrival times, and P_{NORM} and P_{TOP} are the number of photons detected by the pump and probe PMTs during their detection gate,

$$P_{\text{TOP}} = \frac{\langle\{\text{SIG}\}\rangle}{0.1} \qquad P_{\text{NORM}} = \frac{\langle\{\text{SIG}\}_{\text{NORM}}\rangle}{0.02} \tag{3.11}$$

where the experimentally determined factors 0.1 and 0.02 convert the PMT signals from V.μs into photon counts. Following the idea presented in the simple example, we can equate the signal change caused by the EDM interaction, Equation (3.8), to the statistical fluctuations in the total number of photon counts, Equation (3.9). This gives us a final expression of the 1-σ statistical sensitivity of the machine,

$$\sigma_{d_e} = \frac{\hbar}{\eta E_{\text{eff}} \tau 2\mathcal{C}\sqrt{N}} \sqrt{\frac{1}{P_{\text{TOP}}} + \frac{1}{P_{\text{NORM}}}} \tag{3.12}$$

which is equivalent to Equation (3.7) if $P_{\text{NORM}} \ll P_{\text{TOP}}$. Typically, we quote the sensitivity of the machine in units of $(x/\sqrt{N_b})$ e.cm, such that $N = 4096 \times N_b$ where N_b is the number of blocks we record. For a data run this would be of the order $N_b \sim 10^5$.

During the last YbF EDM data set, the statistical sensitivity of the machine was [90],

$$\sigma_{d_e}^{(2011)} = \left(5.7 \times 10^{-26}/\sqrt{N_b}\right) \ e.\text{cm}. \tag{3.13}$$

When I joined the experiment in 2013, the statistical sensitivity of the machine had been improved by a factor of 2.7 to [89],

$$\sigma_{d_e}^{(2013)} = \left(2.1 \times 10^{-26}/\sqrt{N_b}\right) \ e.\text{cm}, \tag{3.14}$$

with the machine typically recording data slightly above the predicted limit at $\left(2.56 \times 10^{-26}/\sqrt{N_b}\right)$ e.cm. With the improvements presented in this thesis, the predicted shot noise limit has been improved by an additional factor of 4.2 to give,

$$\sigma_{d_e}^{(2016)} = \left(0.5 \times 10^{-26}/\sqrt{N_b}\right) \ e.\text{cm}. \tag{3.15}$$

The following section examines Equation (3.12) in more detail to show how we can improve the shot noise limit to make a more sensitive measurement of the electron EDM.

3.1.2 Increasing sensitivity

The statistical uncertainty of the EDM measurement should follow the shot noise limit, shown in Equation (3.12). Now we can investigate how we reduce this quantity to make an improved measurement. The effective electric field $E_{\text{eff}} = -26$ GV/cm is a fixed quantity for the X $^2\Sigma^+$ state in YbF. However, we do have control over the molecule's polarisation factor, η. By applying a larger electric field we can better align the YbF molecule to the z axis of the experiment, and so increasing η. To date, the new electric field plates, detailed in Chapter 5, are able to support up to ± 5 kV [106]. However, it is expected that as the machine collects data the plates will naturally condition themselves to withstand higher voltages. The HV supplies and cable improvements detailed in [89] are capable of increasing the supplied voltage to ± 12 kV. This would increase η from 0.51 to 0.69, a modest yet helpful increase in σ_{d_e} which could be easily attainable over the course of the next data run.

Increasing the interaction time τ is a long term goal of the project. The first step of which is to develop a buffer gas source of YbF that produces an intense beam of slow molecules. Our group has already developed such a source that reliably produces $\sim 1 \times 10^{10}$ ground state molecules per steradian per pulse at a rate of 2 Hz [107] [108]. A typical molecular packet has a peak forward velocity of 180 m/s. The next major challenge for the buffer gas source is to increase the repetition rate, ensuring the gain in interaction time isn't compromised by the loss in the number of molecules per second. Once this is ready, the source will be installed. In the future, ultracold YbF will be used to measure the EDM. The group is currently developing a laser-cooled fountain of molecules which will increase interaction time by a factor of 300 [85], as discussed in the Section 1.2.3.

The contrast $\mathcal{C}$ of the interferometer can also be increased by reducing the length of the rf pulses. Shorter rf pulses means that the molecular packet will sample less of the electric field inhomogeneity, creating a more uniform rf detuning across the entire pulse, and so a more efficient π-pulse. With the upgrades detailed in Chapter 5 we can now apply much shorter rf pulses, reducing the length of the pulse from 9 μs to 2 μs. However, preliminary data taken using the new detection scheme, detailed in Chapter 6, suggests that the contrast has been slightly reduced from 0.76 to $\sim$0.5. It is hoped that future work will improve upon this.

The main goal of my PhD has been to dramatically increase the factor P_{TOP}. This is achieved by pumping more molecules into the X $^2\Sigma^+(v = 0,\ N = 0,\ F = 0)$ ground state at the start of the experiment, and by detecting these molecules more efficiently at the end of the measurement. We have also included a way to detect both the $(F = 0)$ and $(F = 1)$ components of the measurement, which will further increase the EDM sensitivity. The following chapters present a detailed description of all the upgrades we have made over the past few years, with an overview presented in Chapter 7. With all these improvements, the sensitivity has been increased by 11.4 since 2011.

3.1.3 Noise

The EDM experiment can suffer from many different sources of noise, all of which can increase measurement uncertainty. Magnetic field noise, electrical noise, source noise and laser intensity fluctuations are just a few we need to consider. It has previously been shown [109], that the experiment suffers from a significant low frequency $1/f$ noise component and a white noise component which dominates above 5 Hz. There are also some small magnetic field noise peaks at 5.5 Hz, 10.75 Hz and 11.75 Hz [109]. If any of these noise sources are of a similar size (or bigger than) the shot noise, then measurement sensitivity will be reduced. We need to ensure that all noise sources are under control below the shot noise limit.

We use multiple techniques to reduce the noise present in the experiment. Sometimes, incorporating simple measurements into the experimental sequence can be very effective. For example, a significant proportion of the noise from the YbF supersonic source is removed by normalising the LIF signal in the TOP PMT to the signal in the NORM PMT. Modulating experimental parameters also helps to reject noise. In this case, only the noise around the modulation frequency will contribute to the noise on that parameter [104]. Through careful choice of waveforms, see Section 2.4.3, we can reject a significant fraction of the noise on a parameter. In particular, almost all the switched parameters are modulated at high frequencies (> 5 Hz) to reject the $1/f$ low frequency components of the noise.

Ambient magnetic noise can create significant problems for any EDM measurement [110]. In general, all frequencies up to about 10 kHz can cause problems. Low frequency noise is rejected by switching techniques and by the three layers of mu metal magnetic shielding we place around the interaction region, while higher frequencies are suppressed by phase locking the experiment to the 50 Hz mains frequency. We also have three *Miniflux* magnetometers placed strategically around the lab as well as a *Bartington* magnetometer in between the *inner* and *middle* magnetic shields to record the magnetic fields in the lab. J. A. Devlin's thesis shows that the typical magnetic field noise on the EDM channel, recorded by the Bartington magnetometer, is $\sigma_B = \left((6.0 \pm 0.2) \times 10^{-27}/\sqrt{N_b}\right)$ e.cm [89]. When compared to the shot noise limit of $\left(2.1 \times 10^{-26}/\sqrt{N_b}\right)$ e.cm presented in the previous section this is insignificant. However, as sensitivity of the experiment improves, new types of magnetic noise become important. In Chapter 5 we will see that magnetic Johnson noise, caused by the molecular beam being in such close proximity to the aluminium electric field plates, begins to dominate the magnetic field fluctuations in the experiment.

In addition to random magnetic field fluctuations, we are also particularly susceptible to magnetic fields that are correlated with the direction of the electric field as there is no way to distinguish them from the EDM interaction. This, along with other systematic effects, is the subject of the following section.

3.2 Systematic effects

3.2.1 Introduction

Every EDM experiment must ensure that systematic effects are under control. Of particular concern are magnetic fields that depend on the applied electric field. The energy shifts caused by the magnetic dipole interaction $-\boldsymbol{\mu}\cdot\boldsymbol{B}$ exactly mimic the EDM interaction $-\boldsymbol{d_e}\cdot\boldsymbol{E}$ if the magnetic field $\boldsymbol{B}$ is correlated with the electric field $\boldsymbol{E}$.

One of the attractive properties of diatomic molecules is that when they align themselves to the electric field, their interaction with perpendicular magnetic fields is highly suppressed by the tensor Stark effect [51]. Unlike atomic EDM experiments, where every magnetic field can effect the measurement [110], only magnetic fields that point along the direction of the electric field are of concern.

In the prescence of an electric and magnetic field, the states X $^2\Sigma^+(v=0,\ N=0)\,|F=1,\ M_F=\pm1\rangle$ will shift in opposite directions by an amount $\pm\Delta_E$ due to the EDM interaction and $\pm\Delta_B = \pm\left(\Delta_{B_z}+\Delta_{B_x}\right)$ due to the magnetic dipole interaction, where Δ_{B_z} is the shift due to the magnetic field aligned to the electric field, and Δ_{B_x} is perpendicular to the electric field. Figure 3.2(a) shows the energy shifts for each magnetic sublevel in $F=1$. Figure 3.2(b) shows how the Zeeman splittings depend on the size of the magnetic field. The energy shifts caused by perpendicular magnetic field are significantly suppressed, at around $\sim 10^{-7}$ times smaller. They also have a non-linear response to the applied magnetic field, making the effect distinguishable from the EDM interaction. For typical running conditions, these splittings are $|\Delta_{B_z}/\hbar| = 2\pi\times 125$ Hz and $|\Delta_{B_x}/\hbar| < 2\pi\times 0.04$ mHz.

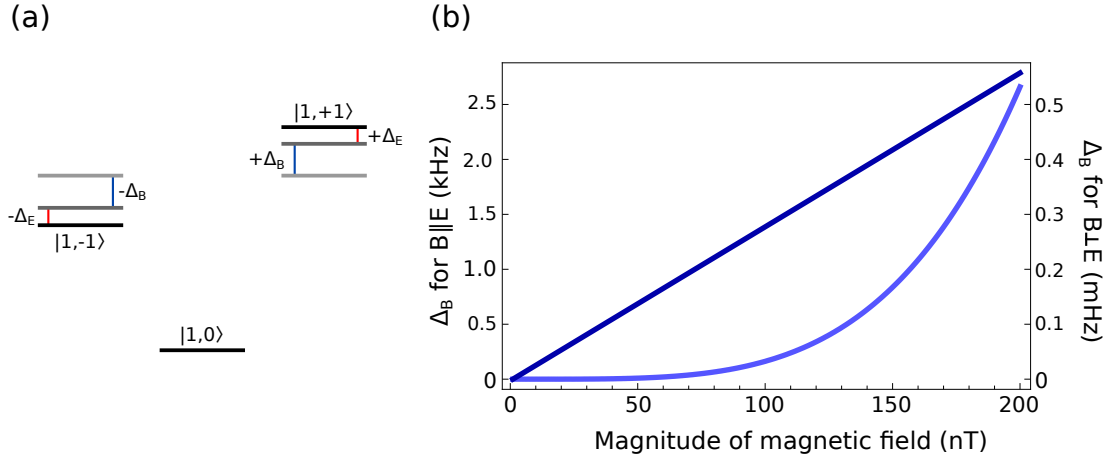


Figure 3.2: (a) X $^2\Sigma^+(v=0,\ N=0)\,|F=1,\ M_F\rangle$ energy levels. The $M_F=\pm1$ states shift by $\pm\Delta_E$ in an electric field and by $\pm\Delta_B=\pm(\Delta_{B_z}+\Delta_{B_x})$ in a magnetic field, where Δ_{B_z} is the shift due to the magnetic field aligned with the electric field, and Δ_{B_x} the shift due to the perpendicular magnetic field. (b) The splittings Δ_{B_z} (dark blue) and Δ_{B_x} (light blue) as a function of applied magnetic field. Note the different scales on the two vertical axes. Splittings calculated for $|E_z|$ =12.5 kV/cm.

In terms of systematic effects, this feature is hugely beneficial. The most sensitive measurement of the electron EDM using atoms, was plagued by the systematic effects associated with perpendicular magnetic fields. In particular, the 'motional magnetic field' effect was one of the eventual limitations for these measurements. The movement of the atom through the electric field generates a magnetic field $\boldsymbol{B} = \boldsymbol{E} \times \boldsymbol{v}/c^2$, which is exactly correlated with the electric field. In the YbF measurement, this systematic error is a factor of 1000 times smaller than the other contributions, because the magnetic field is perpendicular to the applied electric field.

However, magnetic fields along z are more problematic. For example, if a 1 pT magnetic field along the z-axis is correlated with the electric field, it will produce a systematic error of 3.6×10^{-27} e.cm; two orders of magnitude larger than the current upper limit. The following section details some of the existing systematics and how we deal with them.

3.2.2 Current systematic effects

Although this thesis does not focus on systematic errors, they are an important part of any EDM experiment. Most of the measurement time is taken up with diagnosing, quantifying and controlling these effects. Typically, a systematic effect will be quantified by exaggerating the imperfection and taking data in this non-ideal setup. The effect is then extrapolated back to normal running conditions. If it is not possible to do this then we have to decide on a likely model of how the systematic is generated and consider the worst-case scenario shift. Table 3.1 presents the current contribution of each known systematic effect, which are described in more detail below.

The first term in the table, the uncorrected E-asymmetry, is generated by an imperfect electric field reversal, where the magnitude of the electric field changes by a small amount δE, upon reversal. Typically, this asymmetry will be around 0.1 V across the whole interaction region [90]. This imperfection will generate a different Stark shift between the $|0,0\rangle$ and $|1,\pm1\rangle$ states for each direction of the electric field. This generates an rf detuning which is correlated with the state of E. The rf detuning has a known effect on the phase of the interferometer, which is corrected for in the analysis [78]. However, to account for any additional effects that may occur due to an imperfect reversal, δE is increased or decreased by ± 10 V to estimate the size of the EDM shift for normal running conditions. A null gradient of $(2.1 \pm 2.9) \times 10^{-28}$ e.cm/(V/cm) was recorded [90], which is consistent with the EDM having no dependence on δE. However, since there is a known mechanism that can generate the shift, we associate an error using the worst case gradient with the typical size of this imperfection, giving the value in the table above.

Ideally, the electric field plates will support equal voltages ($\pm V$) relative to ground. However, the plates may become offset from ground by some amount $\bar{V}$ such that the voltages are now $\pm V + \bar{V}$. Although it is hard to see how this generates a shift of the EDM, it is suspected that the fringe fields change in a way that is dependent on the state of E, effecting the pump and probe efficiency [90]. To place a value on this effect, we enhance it by taking data with

Systematic error	Current upper limit (10^{-28} e.cm)	Ref.
Uncorrected E-asymmetry*	0.5	[90]
Voltage offset	0.063	[90]
Residual rf1 detuning*	0.6	[90]
dc anf rf leakage currents	0.2	[89]
dc shield magnetisation**	0.5 (1.6)	[89]
ac shield magnetisation**	0.05 (0.14)	[89]
rf rotation	0.084†	[89]
Geometric phase	0.01	[78]
Motional magnetic field	0.0005	[78]
Sum in quadrature	0.96 (1.80)	

Table 3.1: Table of of current systematic errors and their contributions. *Indicates an upper limit determined by the statistical sensitivity of the machine. **Taken using auxilliary offline measurements using two high voltage supplies: *Bertan* (*Applied Kilovolts*). Discussed further in the text below. †This is a projected value.

$\bar{V} = +500$ V and $\bar{V} = -500$ V. This produces a measurable shift of $(6.3 \pm 2.0) \times 10^{-30}$ e.cm/V [90]. When combined with the measured offset $|\bar{V}| < 1$ V, recorded with HV probes, we find the error listed in the table.

In addition to the voltage offset systematic described above, it was also discovered that there is a strong systematic shift caused by the detuning of the first rf pulse when combined with a voltage offset [90]. However, when $\bar{V}$ is carefully zeroed there is no dependence on this detuning, producing a null gradient of $(2.3 \pm 2.8) \times 10^{-28}$ e.cm/kHz. When combined with the average detuning of 0.1 kHz to give the residual rf1 detuning error in the table.

Leakage currents are a common problem for every EDM experiment. It is particularly difficult in the YbF experiment as, although we can record the leakage currents, we can't easily record the magnetic fields they produce. We also have no handle to enhance these currents, forcing us to model the systematic. Although the Bartington magnetometer outside the chamber does not record any magnetic fields correlated with the direction of the electric field, we still need to be conservative and consider the worst case scenario model in which all the leakage will generate a magnetic field along z. In addition, the rf can produce a leakage current which also needs to be considered [89]. Using the approach detailed in [89], we find the currents produce a false EDM as detailed in the table.

The dc and ac shield magnetisation are also hard to exaggerate and so these tests have to be performed outside the machine. The values presented in the table were quantified by measuring the magnetic field produced at the centre of a duplicate shield when high charging currents were deliberately passed through the holes in the shield, and then extrapolated back

to the actual charging currents used in the experiment. The results of these offline tests are shown in the table.

In 2013 it was discovered that the rf was coupling onto the HV lines, being reflected at the relays and re-radiated into the machine, creating a rotation of the rf field. In the case of the true rf manual state (rf propagating from bottom to top), the amount of rf reflected back into the machine was dependent on the state of the relays, creating a rotation of the rf field that was dependent on the direction of the electric field. This effect has been suppressed by the installation of rf ferrite chokes [89] but further tests need to be performed before assigning a value to this systematic. The predicted value presented in the table assumes that we can restrict the amount of reflected rf to one part in a million, and the ratio of 'bad' polarisation to 'good' polarisation in the interaction region to below 0.1 [89]. This seems realistic with the new ferrite chokes and some comprehensive rf field maps.

Warping of the plates creates a distortion of the electric field. The molecules adiabatically follow the direction of the field, generating a geometric phase [111]. The rotation of the electric field about the x and y axes is restricted to below ± 0.5 mrad. Fortunately, this phase alone is not enough to produce a systematic effect as it does not change when the electric field is reversed. However, when combined with a non-reversing patch potential on the plates, the geometric phase does become a problem. This effect is difficult to enhance and so we have to model a worse case scenario of a 1 V patch covering a quarter of the plate and average over the interaction region. This gives the number in the table.

The motional magnetic field is a very tiny effect for molecular beam experiments. However, this is included for comparison as it severely limits the measurement capabilities of atomic beam measurements.

Adding these systematic errors together in quadrature gives a total known systematic error of 0.96×10^{-28} e.cm. It is worth noting that the largest sources of error in this table either come from systematics that scale with the sensitivity of the machine, or from offline measurements that can also be improved with longer integration time.

In addition, there is still an unknown systematic effect, discovered in late 2013, which is generated by the high voltage supplies [89]. After the 2011 measurement, the HV supplies were upgraded from an unmatched positive and negative supply (*Bertan 602B-150N/P*), to a pair of *Applied Kiolovolts HP010* 10 kV supplies, making the system electrically matched in each E-field state. The *Applied Kilovolts* power supplies have some different properties to the *Bertan* power supplies which seem to generate a systematic effect, the mechanism of which is still unknown. Since the discovery, there has been some progress towards understanding this effect, but at the time it took a week of integration to see an inconclusive 3-σ result. In March 2014, the focus shifted towards upgrading the sensitivity of the experiment, in the hope that we will be able to quickly and efficiently diagnose the underlying cause of this systematic error.

Chapter 4

The new pump scheme

4.1 Introduction

Measurement sensitivity can be improved by increasing the number of molecules that take part in the experiment. This can be achieved in two ways; by changing the molecular source to produce a higher flux of ^{174}YbF, or by making more efficient use of the molecules already available with an improved pump scheme.

Eventually, both these techniques will be used to enhance sensitivity. The buffer gas source being developed by the group is expected to produce $\sim$3 times more molecules per steradian per pulse [107], alongside the significant gain in interaction time. However, during my PhD I have developed a new optical pumping scheme which collects approximately six times more molecules from higher lying rotational levels than the previous setup. This chapter concentrates on the development, experimental setup and results of this pump scheme.

Before diving into the details, it is worth discussing our requirements of the new pump scheme, in order to make a successful EDM measurement. Firstly, and most importantly, the pumping should completely empty out the X $^2\Sigma^+(v = 0,\ N = 0,\ F = 1)$ state. Any left over population in this level will create an unwanted background, reducing the contrast of our measurement. Secondly, for the new detection scheme to work well, we require all the hyperfine components of X $^2\Sigma^+(v = 0,\ N = 1)$ to also be emptied (see Chapter 6). Left over population in these states will similarly reduce the measurement contrast. Finally, this pump scheme should be easily adapted to work with the buffer gas source. In the current EDM measurement we use both 'pulsed' fields (rf pulses) and 'not-pulsed' fields (electric field, magnetic field, pump and probe laser beams). The molecular packets produced by a buffer gas source are very extended (with pulses taking $\sim$1 ms to leave the cell) and contain a broad range of velocities. This property makes it hard to use pulsed fields effectively and so the changes we make to the pump region must only use static fields and not rely on any velocity or time-dependent effects. With these criteria in mind, we can begin to look at the new pump scheme, presented below.

4.1.1 The new pump scheme

The main goal of the new pump scheme is to collect as much of the thermal population in the X $^2\Sigma^+(v = 0,\ N = 0, 1, 2)$ states and transfer it to the $F = 0$ ground state using optical pumping, ready for the EDM experiment to begin. With the original scheme, presented in

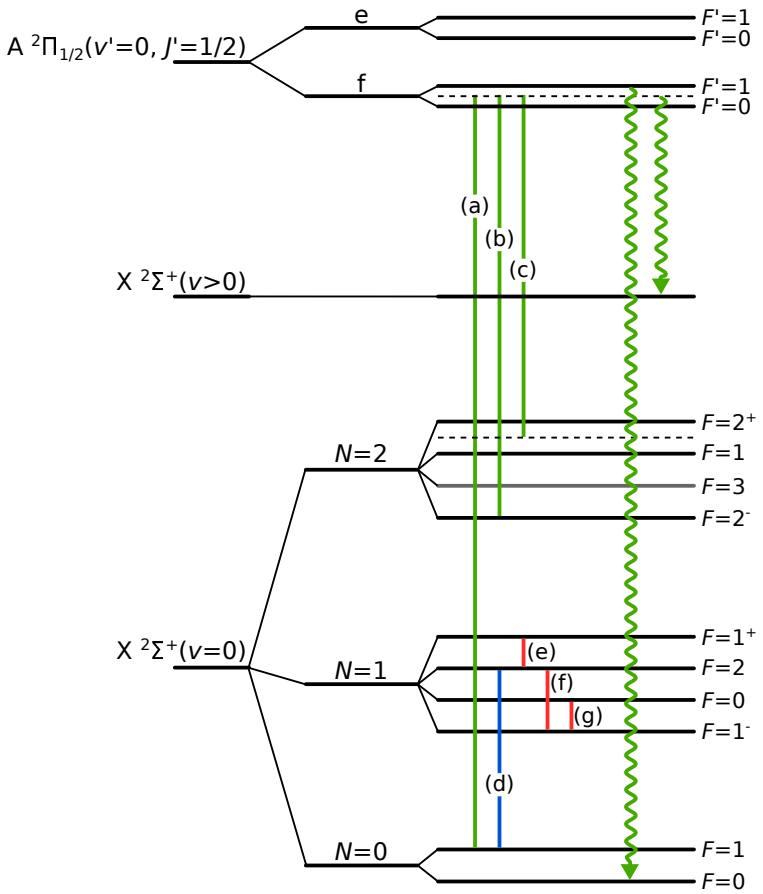


Figure 4.1: Transitions driven in the improved pump scheme. Microwave radiation (d) and rf radiation (e)–(g) mix the thermal population in $N = 1$ into $(N = 0,\ F = 1)$. This is then optically pumped, along with the intial $(N = 0,\ F = 1)$ population, into the ground state $|0, 0\rangle$ by (a). Any decays into the $N = 2$ rotational state are repumped (b)–(c). The thermal population in the $N = 2$ rotational state is also collected by these laser frequencies. The excited state can decay along any of the optically addressed states (a)–(c), into the ground state $|0, 0\rangle$ or to higher vibrational levels in X $^2\Sigma^+(v > 0)$ shown by the wiggly lines.

Section 2.4.1, we already transfer about 1/3 of the $F = 1$ population into $F = 0$ by pumping on Q(0)$(F = 1)$ transition, labelled (a) in Figure 4.1. The remaining 2/3 decays to $N = 2$ (or $v > 0$) and is lost from the experiment. Closing this decay route is the natural first step towards a more efficient pump scheme. To do this we apply two additional laser beams; $^{O}P_{12}(2)(F = 2^-)$ and $^{O}P_{12}(2)(F = 1,\ 2^+)$, labelled (b) and (c) in Figure 4.1. This final sideband is equally detuned between the $F = 1$ and $F = 2^+$ hyperfine states which are separated by 5.5 MHz. To ensure there are no dark states as we pump from $F = 2 \rightarrow F' = 1$,

the polarisation is modulated between left- and right-handed circularly polarised light at a rate of ∼1 MHz. As an additional gain, these lasers also collect the thermal population in the $N = 2$ states.

To drive population from $N = 1$ into $N = 0$, a combination of microwave and rf fields are applied to the molecules. A single microwave frequency is tuned to the X $^2\Sigma^+(v = 0,\ N = 0,\ F = 1) \rightarrow (N = 1,\ F = 2)$ transition at 14 458 087 kHz, labelled (d) in Figure 4.1. Three rf fields drive magnetic dipole transitions within the X $^2\Sigma^+(v = 0,\ N = 1)$ state; $F = 2 \rightarrow F = 1^+$ (30.9 MHz, (e)), $F = 1^- \rightarrow F = 2$ (161.2 MHz, (f)) and $F = 1^- \rightarrow F = 0$ (155.7 MHz, (g)). This radiation mixes the population in $N = 1$ and connects it to the optical pumping transitions.

Together, the laser, microwave and rf fields collect the population from the $N = 1$ and $N = 2$ states and, in addition to the original $(N = 0,\ F = 1)$ population, this population is optically pumped into $(N = 0,\ F = 0)$, with some loss to higher vibrational states.

4.1.2 How much population is available?

In this new scheme, the population in higher lying rotational states will now play a role in the measurement. This means that the gain we expect from the pumping is dependent on the rotational temperature of the molecules. For a beam of temperature T the probability of occupying a state X $^2\Sigma^+(v = 0,\ N)$ is governed by the Boltzmann distribution,

$$P(N,\ T) = S(T)\ (2N + 1)\ e^{-N(N+1)B_0 h/k_B T} \tag{4.1}$$

where $S(T)$ is the normalising constant and $B_0 = 7.234$ GHz is the rotational constant from Equation (2.4). A plot of this probability for different temperatures is shown in Figure 4.2. On average, our YbF molecular beam is thermalised to 2 K (shown by the dark blue line and markers in Figure 4.2), but can vary between 1–5 K (shown by the light blue, dashed lines in Figure 4.2), depending on the source parameters. Figure 4.2 shows that even at 1 K there is a significant proportion of the population in higher rotational states, providing strong motivation for adding in these additional frequencies to the pump scheme. Using T =2 K as an example, the probability of occupying a rotational level is $P(N,\ 2\ \text{K}) = \{0.16,\ 0.35,\ 0.29\}$ for $N = \{0,\ 1,\ 2\}$.

Typically, we normalise these probabilities such that the Zeeman sublevels in the ground state X $^2\Sigma^+(v = 0,\ N = 0)$ each contain one unit of population. Using this definition, the fractional population in a single Zeeman sublevel within a rotational state is,

$$P_z(N,\ T) = \frac{1}{2N + 1}\frac{P(N,\ T)}{P(0,\ T)}. \tag{4.2}$$

To find the number of 'units' of population we simply multiply this quantity by the number of Zeeman sublevels accessible to the new scheme. At 2 K there are $\{4\times1,\ 12\times0.71,\ 13\times0.35\}$[1]

[1]Remember, the state $(N = 2,\ F = 3)$ cannot be excited to the upper state due to the selection rules, which lowers the total population accessible by the scheme.

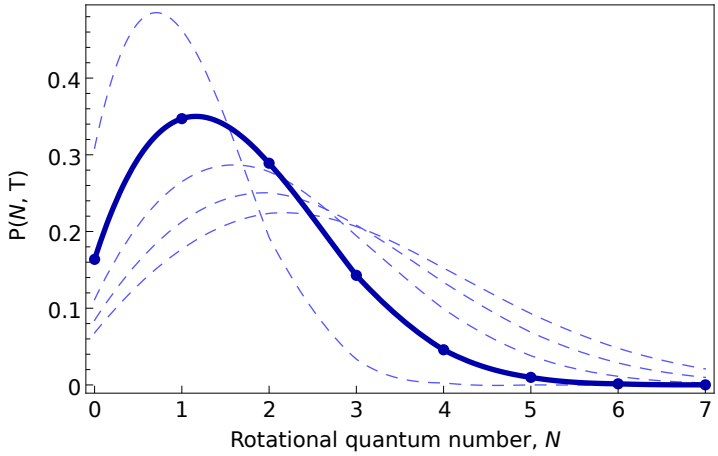


Figure 4.2: Probability of occupying a state X $^2\Sigma^+(v = 0,\ N)$ for a given rotational temperature T; $P(N,\ T)$. The dark blue markers show the population distribution for $T = 2$ K, the average rotational temperature of the beam. The dashed light blue lines show the variation in the population distribution as the rotational temperature changes between 1–5 K, depending on the source parameters.

units of population in each of the rotational levels we address, giving a maximum available population of 17.1. Previously, the maximum population was 4, but we only ever saw the population increase from one unit to two units, equivalent to observing the $F = 0$ signal double. The next section explains why this is the case, and compares the two pump schemes using a basic model to predict the proportion of this population we can realistically expect to add to the measurement.

4.1.3 How much population do we expect?

To collect these extra molecules, ideally all the population from the higher rotational levels will eventually be excited to the upper A $^2\Pi_{1/2}(f)$ state. Once excited, a molecule can decay to either: the ground state, back into the pumped levels, or to X $^2\Sigma^+(v > 0)$ where it is lost from the measurement. The maximum possible increase will be when no population is left in the addressed states after pumping. The fraction of the excited state population that ends up in $|0, 0\rangle$ is,

$$\frac{\sum_{F',M'_F} \mathrm{P}\left(|F', M'_F\rangle \rightarrow |0,0\rangle\right)}{\sum_{F',M'_F} \left[\mathrm{P}\left(|F', M'_F\rangle \rightarrow |0,0\rangle\right) + \mathrm{P}\left(|F', M'_F\rangle \rightarrow v > 0\right)\right]} \simeq 0.69, \tag{4.3}$$

where $\mathrm{P}\left(|F', M'_F\rangle \rightarrow \mathrm{X}\right)$ is the probability of decaying from the excited state A $^2\Pi_{1/2}(f)\,|F',\ M'_F\rangle$ to the lower state X, where the sum is over the four M'_F sublevels of the excited state. This result is evaluated using the branching ratios of these transitions from Table B.1 in [89]. Equation (4.3) shows that if we can drive all the population to the excited state, 69% of it will decay into the ground state, with the remaining 31% being lost to the higher vibrational levels. A similar calculation for the original pump scheme shows that only 29% of the pop-

ulation from ($N = 0,\ F = 1$) is pumped into ($N = 0,\ F = 0$). Taking into account the fact the $F = 1$ level has three time the $F = 0$ population, this last result suggests that the original pump scheme should increase the ($N = 0,\ F = 0$) population by a factor of 1.9, in good agreement with what is observed experimentally.

Combining this Equation (4.3) with the available population in the X $^2\Sigma^+(v = 0,\ N = 0,\ F = 1)$, X $^2\Sigma^+(v = 0,\ N = 1,\ F = 0, 1^-, 1^+, 2)$ and X $^2\Sigma^+(v = 0,\ N = 2,\ F = 1, 2^-, 2^+)$ states, we can work out the gain we would expect from the new pump scheme when compared to the original pump setup. For a molecular beam of temperature T, the fractional increase in molecular signal will be,

$$f(T) = \frac{P_z(0,T) + 0.69 \times [3\ P_z(0,T) + 12\ P_z(1,T) + 13\ P_z(2,T)]}{P_z(0,T) + 0.29 \times [3\ P_z(0,T)]} \tag{4.4}$$

where $P_z(N,\ T)$ is the probability of occupying a Zeeman sublevel when compared to the ground state, Equation (4.2), which is multiplied by the number of Zeeman sublevels accessible to the new pump scheme. The factor $f(T)$ is plotted as a function of temperature in Figure 4.3. This shows that we could expect a significant enhancement, between a factor of 5–9, depending on the rotational temperature of the beam. At 2 K the fractional gain in signal is 6.4.

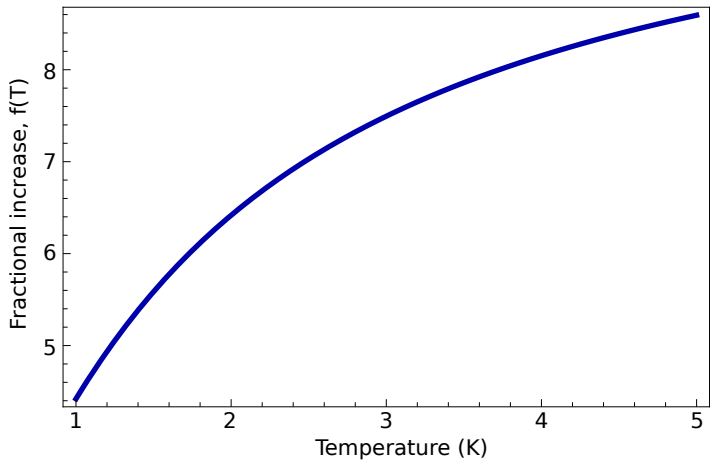


Figure 4.3: Predicted fractional increase of the $|0, 0\rangle$ signal using the new pump scheme as a function of temperature T, see Equation (4.4).

This simple model shows that the new pump scheme is potentially very promising, increasing the number of molecules by up to a factor of 9 is a very significant gain. However, this is the upper limit to what we can achieve and this model tells us nothing about the experimental parameters we can control to optimise the pumping efficiency. A full model of the system requires numerical simulations of the optical Bloch equations (OBEs) that include all the energy levels involved, and their interactions with the electromagnetic fields each with their own detunings, polarisations and powers, as well as the Doppler broadening effects of the molecular beam. That work was done by J. Devlin and is reported in his thesis [89]. Here, I summarize the results of these simulations.

The OBE simulations suggested that by applying the laser, microwave and rf fields shown in Figure 4.1, we can increase the number of molecules that take part in the experiment by a factor of 5.6. To achieve this we require a total laser intensity of $8I_{\text{sat}}$, or 35.2 mW/cm^2, with the power in the sidebands $\{\text{Q}(0)(F = 0),\ ^{\text{O}}\text{P}_{12}(2)(F = 1, 2^+),\ ^{\text{O}}\text{P}_{12}(2)(F = 2^-)\}$ roughly divided into the proportions $\{20\%, 50\%, 30\%\}$[2]. Also, a microwave electric field of $(\mu_e|E|)/\hbar = \Omega_{\text{mw}} = 2\pi \times 1.5$ MHz is required. This is equivalent to ∼8 dBm of microwave power. Finally, we require an oscillating magnetic field of $(\mu_B|B|)/\hbar = \Omega_{\text{rf}} = 2\pi \times 1$ MHz for each of the rf sidebands. This is a considerable amount of power, at around 55 dBm per sideband. The next section explains how we apply each of these fields to the molecules and compares the lab parameters to the simulation requirements.

4.2 Equipment

This section discusses the new equipment required to create the optical pumping fields with the correct frequency, power and duration. An overview of the equipment is shown in Figure 4.4. Much of this hardware is also used for the new detection scheme. To show how they relate to each other, the hardware used for the new detection scheme is shown faded out in Figure 4.4, but will be discussed in more detail in Chapter 6.

4.2.1 Lasers

In the new pump scheme shown in Figure 4.1, we need to drive the three laser transitions, labelled (a), (b) and (c). This is done using two lasers and an AOM. The first laser system is the *Menlo Orange One* fibre laser with NTT doubler head. As before this is tuned to $\text{Q}(0)(F = 1)$ at 542 811 GHz using the internal temperature control and piezo. A small portion of light is picked off and sent to the transfer cavity lock setup. Using the internal piezo we actively stabilise the frequency of the *Menlo* over long periods of time to the 780 nm reference. The reference laser has been updated from a stabilised HeNe to a sub-Doppler polarisation spectroscopy feature in ^{87}Rb, to create a strong dispersion-like signal with a zero crossing, the design of which is based on [112]. We lock to the $F = 2 \rightarrow F' = 3$ D2 line, the width of which is less than 7 MHz. The reference is now stable to < 0.5 MHz per hour and ~ 1.5 MHz per day, providing us with both better short term and day-to-day stability than the HeNe reference used previously.

The second laser system uses a *Coherent 899-21* ring cavity dye laser, which is pumped by an Ar^+ laser at 3–6 W of light (depending on age of dye) on all visible lines. Typically, this will produce around 200 mW of green light which is tuned to the $^{\text{O}}\text{P}_{12}(2)(F = 1,\ 2^+)$ transition at 542 767 GHz which is equally detuned from two hyperfine states, $F = 1$ and $F = 2^+$ (separated by 16.5 MHz), in the $N = 2$ rotational manifold. Typically, the linewidth

[2] I_{sat} is the saturation intensity of a two level system. In this case, we use this parameter as a unit to normalise the intensities applied in the lab despite being far from the two-level case. For the A→X transition $I_{\text{sat}} = \pi hc\Gamma/(3\lambda^3) = 4.4$ mW/cm^2. In the multilevel case, the condition for saturation (population is distributed equally across all levels) occurs at a higher intensity, which typically scales as the ratio between the number of driven ground states to the total number of states of the system. See [89] for details.

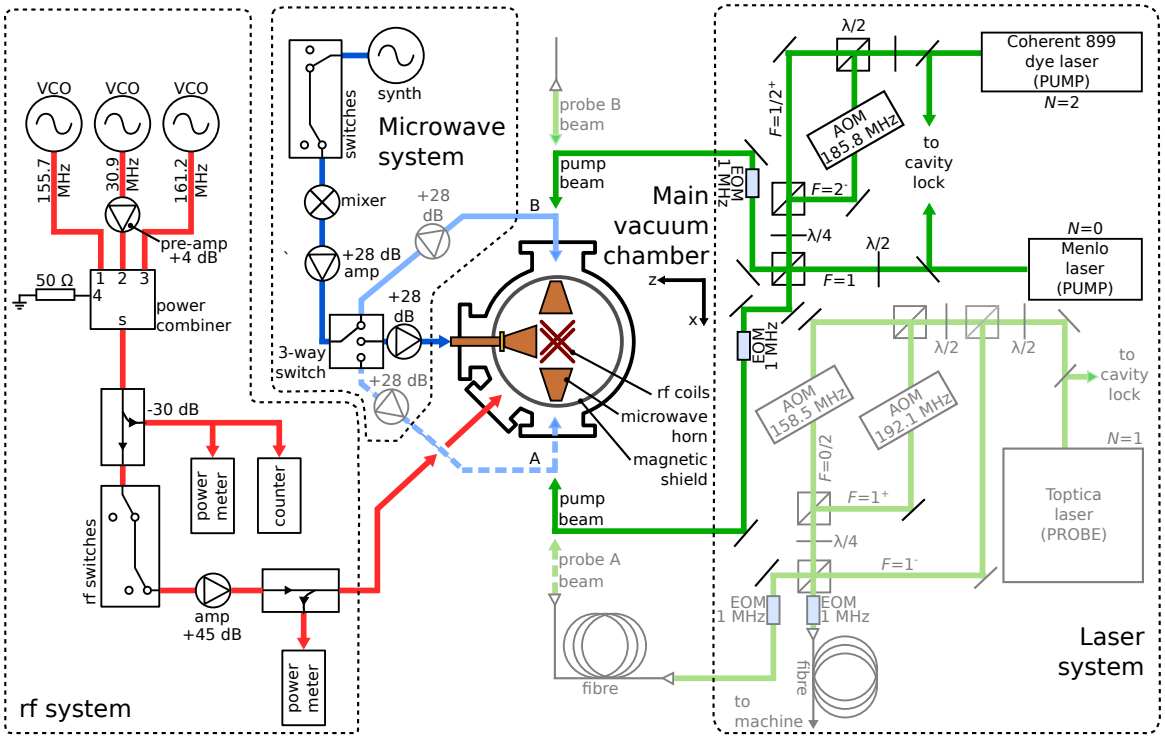


Figure 4.4: Schematic overview of the hardware used to control the new pump scheme. New laser, microwave and rf systems have been added, shown in green, blue and red respectively. The hardware required for the new detection scheme (described in Chapter 6) is shown by the faded regions to show how they relate together, but will be referred to in later discussions.

of the dye laser will be locked to around 1 MHz by its own external reference cavity but the centre can drift by up to 10 MHz/hour [113] and so a small portion of the output light is sent to the transfer cavity setup. The frequency is actively stabilised by feeding back a voltage to the dye laser's own reference cavity. Some of the output light is picked-off and single-passed through an AOM to blue shift the light to the ${}^{O}P_{12}(F = 2^{-})$ transition by 185.5 MHz.

These three laser frequencies $\{Q_1(0)(F = 1), {}^{O}P_{12}(2)(F = 1,\ 2^{+})$ and ${}^{O}P_{12}(2)(F = 2^{-})\}$ are then combined and overlapped on two polarising beam splitters, as shown in Figure 4.4. This produces two output laser beams with equally distributed power in each sideband. These are passed through two optically active lithium niobate crystals that are electrically modulated (EOM) by a resonant circuit to switch the polarisation between left- and right-handed circular at a rate of ~ 1 MHz.

Each output is then shaped into an elongated gaussian beam which has a $1/e^2$ dimension of $w_z \times w_y = 2.2 \times 23.5$ mm. These beams are then sent into either side of the pump region, propagating along the $\pm x$ directions, doubling the laser power applied to the molecules. Since all fields need to be on together, it is the w_y dimension that sets the interaction time available for the optical pumping. For molecules travelling at 590 m/s, the interaction time is 40 μs, slightly below the time suggested by the simulations (50 μs).

The powers in each sideband can be varied to optimise the pumping efficiency. Typical powers in each pump beam ($\pm x$) are 8 mW in the Q(0) sideband, 22 mW in the ${}^{O}P_{12}(F = 2^{-})$ sideband and 55 mW in the ${}^{O}P_{12}(F = 1,\ 2^{+})$ sideband. This gives a total combined power of 170 mW, equivalent to $75I_{\text{sat}}$, with the powers in each sideband distributed by {9%, 65%, 26%}. The laser power available far exceeds that of the $8I_{\text{sat}}$ suggested by the OBE simulations.

4.2.2 Microwaves & rf

To apply the microwave field to the molecules we use a small horn (aperture dimensions 21 × 25 mm), which sits only a few millimetres away from the beamline. It is rotated about the z axis to produce linearly polarised microwaves in the x, y plane at 50.5° to the y axis. A set of four resonant rf coils create linearly polarised oscilating magnetic fields at 45° to the x axis[3]. This setup is shown in the illustration and in the photos of Figure 4.5.

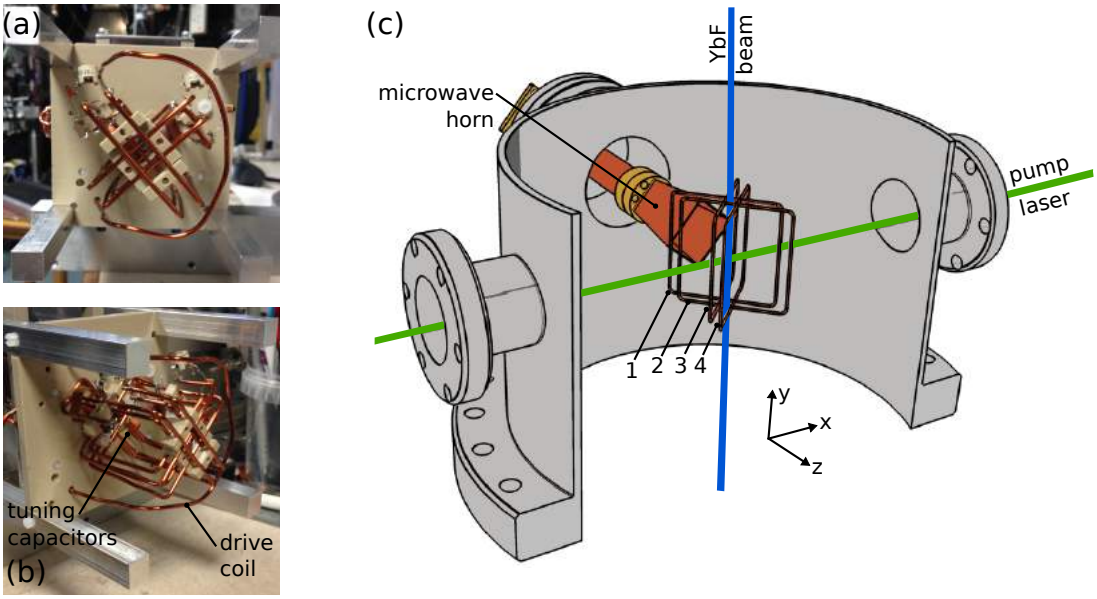


Figure 4.5: (a)-(b) Two views of the rf coils mounted on the support structure (c) Schematic view of the new pump region, including the four resonant rf coils, microwave horn, centre line of the laser beam and molecular beam. The self resonances of each coil are (1) 36.4 MHz, (2) 155.7 MHz, (3) 161.2 MHz and (4) 30.9 MHz.

The ∼14 GHz microwaves are generated by an *Anapico APSYN420* microwave synthesizer. The frequency of the microwaves is controlled by the internal DCFM of the synth and the amplitude by a *Pasternack PE8552* mixer. The *Pasternack PE7117* switch controls the start time and duration of the microwaves being sent to the machine[4]. The microwave pulse with the correct frequency, amplitude and duration is then amplified by a *Mini-Circuits*

[3]Although this is the intention, it is more than likely that the microwaves and rf scatter off everything inside the chamber, creating a complicated pattern of polarisations and standing waves.

[4]The fields are fixed at a constant amplitude as the molecules fly through the region, but need to be turned off during the remainder of the shot to avoid interference with any other process.

ZX60-183A-S+ (+28 dB) amplifier. This is then sent to a *AMC SW-218-3A* three-way switch which controls the region the microwaves are directed to; the pump region or either detection region, see Chapter 6. On the air side, the microwaves are launched into a waveguide. They propagate through a pressure window into the vacuum where they are radiated by the microwave horn.

The rf frequencies are generated by three individual voltage controlled oscillators (VCOs). The frequency and amplitude of the rf can be controlled directly by each VCO. The 30.9 MHz VCO is pre-amplified to boost the output using a *Mini-Circuits ZFL500HLN* amplifier. The three frequencies are then combined by a *Mini-Circuits ZFL-4-37* power combiner. A small amount of the power (−30 dB) is picked off and sent to a *HP 53131A* frequency counter and *HP 438A* power meter for diagnostics. The rf is then sent through two *Mini-Circuits ZASWA-2-50DR* switches which select the start time and duration of the rf pulse that is sent to the pump region. This is then amplified by *AR worldwide KAW1050* (+45 dB) rf amplifier before being connected to the feedthrough where it propagates down to the drive coil, labelled in Figure 4.5(b), where it couples onto the resonant coils.

During the development of the pump scheme, it was originally suspected that up to four rf frequencies would be needed to completely clear the dark states in $N = 1$. The rf coil setup, designed by B. E. Sauer, reflects this, with two low frequency coils, which are tuned outside the vacuum with fixed capacitors, and two high frequency coils, which are tuned in-situ with tunable capacitors. Figure 4.5(c) highlights the positions of the different coils. We can measure how well the rf couples onto the resonant coils by recording the back-reflected rf power. When the coil is on resonance, the reflected power drops as the rf is coupled onto the coil and radiated in the pump region, as shown in Figure 4.6. The red line shows a Lorentzian fit to the resonances of each coil. Using this fit, the Q-factor of each coil is calculated to be; (a) Q=400, (b) Q=210, (c) Q=470 and (d) Q=420, which shows that the three coils required for the pump scheme all have similar Q-factors, despite the wide range of frequencies.

The final piece of the puzzle is to check that the power we can generate in the lab is sufficient to drive the molecules at the Rabi rates suggested as optimum by the OBE simulation; $\Omega = 2\pi \times 1.5$ MHz for the microwave field and $\Omega = 2\pi \times 1$ MHz for each of the rf sidebands. To do this we empty out one of the levels connected to the transition we are interested in driving and repopulate it using a short pulse of radiation of length τ. If the field is homogeneous then we observe Rabi flopping — the population transfers back and forth between the two driven levels — as we scan the power sent to the machine. When all the population is transferred to the depleted state, $\Omega\tau = \pi$. Since the fields in the pump region are not very homogeneous, short pulses of radiation need to be applied to see this effect. In the following discussion, we reduce the length of the rf and microwave pulses purely to find the Rabi rate of the system. In the real experimental sequence, these fields will be on for the entire period the molecules fly through the pump region.

A $\tau = 1$ μs pulse of microwaves was used to drive the $(N = 0,\ F = 1) \leftrightarrow (N = 1,\ F = 2)$ electric dipole transition. We observed a π-pulse when 16.5 dBm of microwave power was recorded at the feedthrough. To perform a π-pulse in 1 μs requires a Rabi rate of $\Omega = 2\pi \times 0.5$

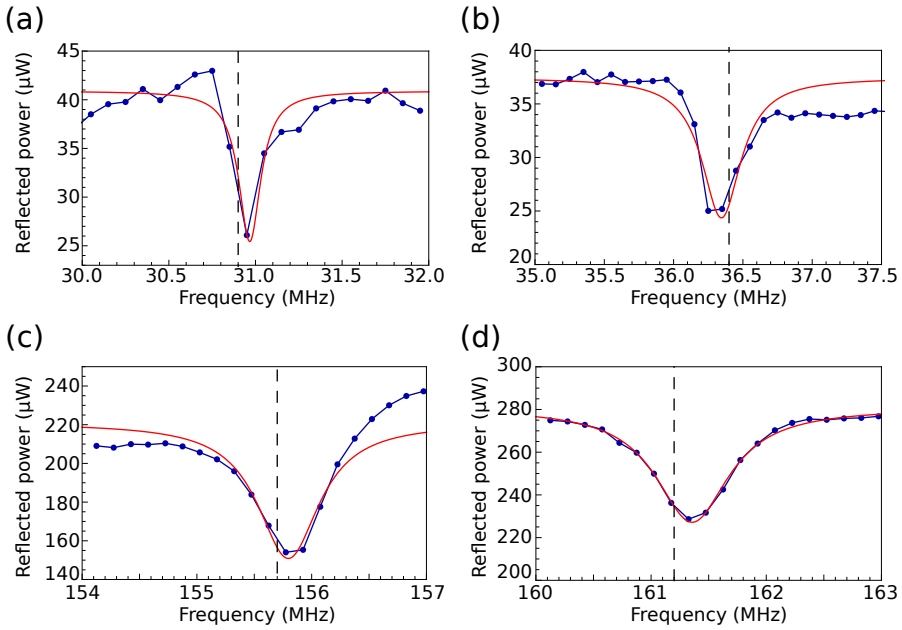


Figure 4.6: Back reflected power as a function of frequency for the resonant rf pump coils. Red line: Lorentzian fit to data. Black dashed line: frequency of transition in $N = 1$ state to drive (a) $F = 1^+ \leftrightarrow F = 2$ at 30.9 MHz, (b) $F = 1^+ \leftrightarrow F = 0$ at 36.4 MHz, (c) $F = 0 \leftrightarrow F = 1^-$ at 155.7 MHz and (d) $F = 2 \leftrightarrow F = 1^-$ at 161.2 MHz.

MHz. The suggested Rabi rate, which is three times faster, will require nine times more power, equivalent to ∼26 dBm of microwaves at the feedthrough. Using $\Omega = (\mu_e|E|)/\hbar$ suggested that to create this Rabi rate only required around 8 dBm of electric field at the molecular beam. This indicates that there are some losses inside the chamber, most likely from reflections off the rf coils and chamber, or possibly from launching of the microwaves from the feedthrough into the vacuum via the pressure window. Currently, we can only apply a maximum of 19 dBm at the feedthrough, limiting the Rabi rate to $\Omega = 2\pi \times 0.7$ MHz. This power could be easily boosted to the suggested level using a small microwave amplifier, positioned just before the feedthrough.

Similarly, each of the rf sidebands were used to drive a π-pulse in $\tau = 20$ μs. The recorded power at the feedthrough for the {30.9 MHz, 155.7 MHz, 161.2 MHz} sideband was {9 dBm, 32.5 dBm, 24.5 dBm}. This drives the magnetic dipole transitions at a Rabi rate of $\Omega = 2\pi \times 0.05$ MHz. To increase the Rabi rate by a factor of 20 requires 400 times more power, equivalent to recording {35 dBm, 58.5 dBm, 50.5 dBm} at the feedthrough for each sideband. Currently, the maximum power available at the feedthrough is {62 dBm, 57 dBm, 64 dBm}, which is sufficient, or close to, the required power to drive these transitions at the suggested Rabi rate.

4.2.3 Summary

To summarise, the setup used for the pump scheme can effectively apply laser, microwave and rf fields to the molecules. The powers available for each field exceed, or are approaching, the requirements suggested by the OBE simulations. A comparison of the suggested parameters and the experimental setup is presented in Table 4.1.

Parameter		Simulation requirement	Experiment	Notes
Interaction time		50 μs	40 μs	Set by the dimensions of the laser; 23.5 mm long.
Lasers	Total	$8I_{\text{sat}}$ 18 mW	$75I_{\text{sat}}$ 170 mW	The available laser power far exceeds the requirements suggested by the OBE simulations.
	Q(0)($F = 1$)	$1.6I_{\text{sat}}$ 3.6 mW	$6.8I_{\text{sat}}$ 16 mW	
	$^{\text{O}}\text{P}_{12}(F = 1, 2^{+})$	$4I_{\text{sat}}$ 9.1 mW	$48.8I_{\text{sat}}$ 111 mW	
	$^{\text{O}}\text{P}_{12}(F = 2^{-})$	$2.4I_{\text{sat}}$ 5.5 mW	$19.5I_{\text{sat}}$ 44 mW	
Microwaves	14 458 087 kHz	$\Omega = 2\pi \times 1.5$ MHz $\rightarrow$ 8 dBm	$\Omega_{\text{max}} = 2\pi \times 0.7$ MHz 19 dBm max	$\Omega = 2\pi \times 1.5$ MHz requires 26 dBm.
rf	30.9 MHz	$\Omega = 2\pi \times 1$ MHz $\rightarrow$ 57 dBm	$\Omega_{\text{max}} = 2\pi \times 22$ MHz 62 dBm max	The rf powers also have to be balanced to optimise pumping efficiency, see Section 4.3 for more details.
	155.7 MHz		$\Omega_{\text{max}} = 2\pi \times 0.8$ MHz 57 dBm max	
	161.2 MHz		$\Omega_{\text{max}} = 2\pi \times 5$ MHz 64 dBm max	

Table 4.1: Comparison of available experimental powers and interaction time with J. A. Devlin's suggested requirements from OBE simulations [89].

4.3 Results

4.3.1 Introduction

To test the effectiveness of the new pump scheme we perform spectroscopy on ^{174}YbF in the detection region, while pumping in the pump region. By scanning across the Q(0), Q(1) and Q(2) lines[5], which are only a few GHz apart, we can observe population disappear from the driven states and reappear in the ground state when the pump fields are applied to the molecules.

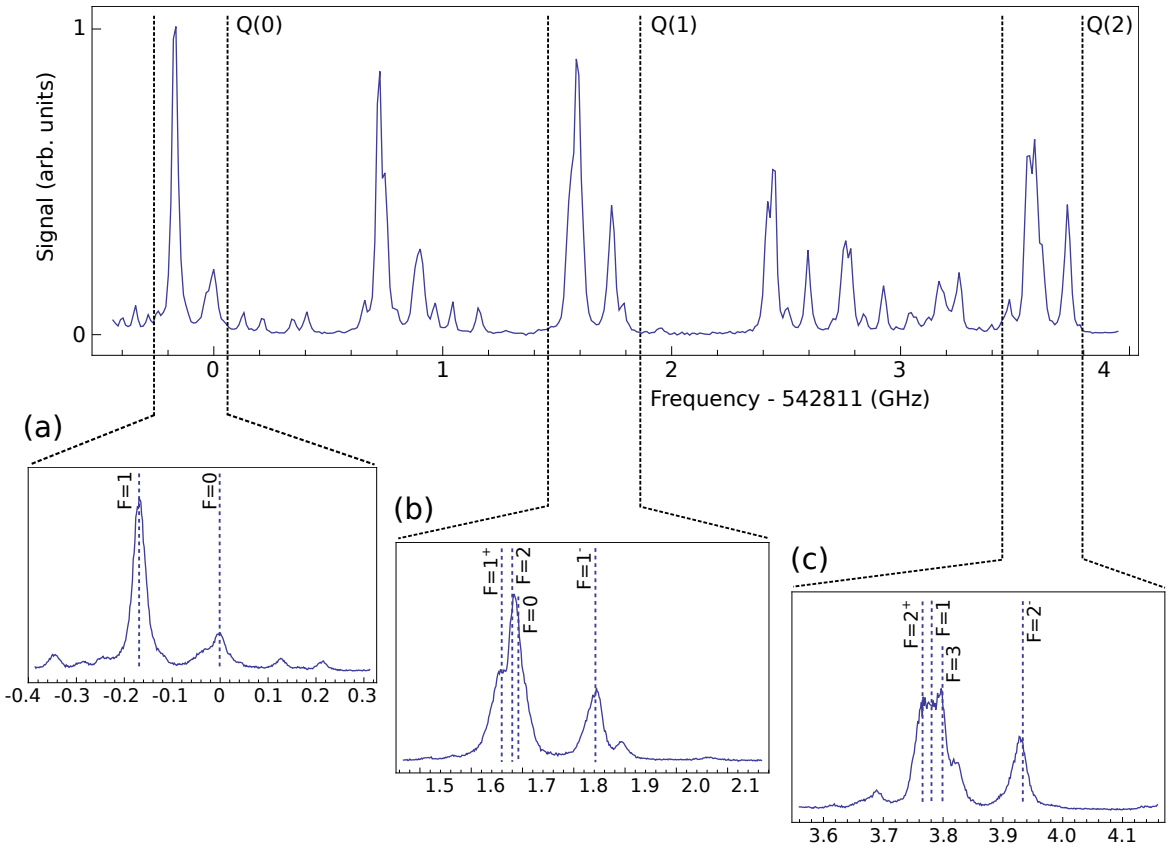


Figure 4.7: A spectrum of the YbF molecular beam, centred at Q(0)($F = 0$), 542811 GHz. There are many different transitions observed in this spectrum, but we only need to pick out the relevant ^{174}YbF peaks. For the following results we will use the (a) Q(0), (b) Q(1) and (c) Q(2) transitions to diagnose the efficiency of the pumping scheme.

The spectrum of the YbF molecules in this spectral region is relatively clear. Figure 4.7 shows a typical scan across these lines from 542810.5 – 542815 GHz. The Q lines we use to test the pump scheme are fairly prominent features and are relatively well isolated, making the effects of the pump scheme straightforward to interpret, when compared to other regions of the spectrum. Figure 4.7(a)–(c) highlights Q(0)–Q(2) and shows the positions of

[5]Q(N) labels a $\Delta J = 0$ transition from ground state X $^2\Sigma^+(v = 0,\ N)$, see Section 2.2.4.

the hyperfine components of each rotational level within the peaks.

However, the supersonic source uses Yb metal which contains many isotopes in their natural abundances; 31.83% (^{174}YbF), 21.83% (^{172}YbF), 16.13% (^{173}YbF), 14.82% (^{171}YbF) and 12.76% (^{176}YbF), along with many other unknown products which contaminate the spectrum, creating underlying peaks. These make it harder to estimate the true effect of the pumping, allowing us to only place an upper limit on the efficiency of the new pump scheme and in particular, how well we can remove population from the $N = 1$ and $N = 2$ rotational states.

4.3.2 Spectroscopy: Looking at leftover population

In this section, we look in detail at how well population is removed by each component of the pump scheme. Firstly, the effects of the original pumping on Q(0)($F = 1$) are presented, before the additional laser frequencies, microwaves and rf are included in turn.

Unless otherwise stated, the data presented here were taken using the 'typical' experimental setup presented in Section 4.2. Two pump lasers, propagating along the $\pm x$ directions contain a total power of ~ 170 mW or $75 I_{\mathrm{sat}}$. The sidebands $\{\mathrm{Q}(0)(F = 1), {}^{\mathrm{O}}\mathrm{P}_{12}(F = 1, 2^{+}), {}^{\mathrm{O}}\mathrm{P}_{12}(F = 2^{-})\}$ are divided into the proportions {9%, 65%, 26%} with each pump beam containing roughly equal power. The microwave frequency, which is tuned to resonance at 14 458 087 kHz, has 16 dBm at the feedthrough. The rf frequencies are slightly detuned to {30.5 MHz, 161.0 MHz} with powers {35.8 dBm, 41.2 dBm} at the feedthrough. So far, it seems as though the 151.7 MHz rf sideband has very little effect on the pumping signal and so is not included in these results — this is discussed in more detail below. The probe beam used to take these data sets has a $1/e^2$ radius of 5 mm, with a power of only 300 μW ($0.09 I_{\mathrm{sat}}$). This low intensity beam minimises power broadening effects and provides good resolution of the peaks in the spectrum.

For these results, an analysis gate of 150 μs was used, selecting molecules with speeds between ∼590–630 m/s to contribute to the total signal. Background laser scatter is removed from the data by integrating the signal from the PMT when no molecules are present in the detection region, using the same analysis gate. The integrated background is then subtracted from the integrated time-of-flight so that any signal can be attributed to YbF in the molecular beam.

Original pumping: ($N = 0$, $F = 1$)

Figure 4.8 shows two scans over the Q(0) transitions. The black data shows the unpumped spectrum and the coloured data shows the results of pumping on Q(0)($F = 1$), labelled transition (a) in Figure 4.1.

Figure 4.8(a) shows the effect of the original scheme. Using a small pump beam with a $1/e^2$ radius of 5 mm, containing around 5 mW of pump light, completely empties the $F = 1$ level, $\lesssim 5\%$ of the population is left behind, and the height of the $F = 0$ peak is doubled.

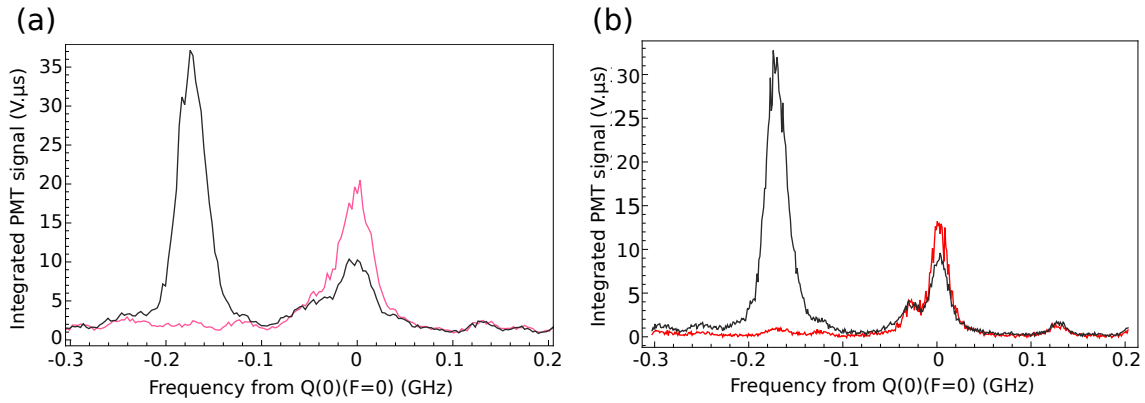


Figure 4.8: Comparison of the unpumped Q(0) spectrum (black) with the pumped spectrum (coloured) using (a) $1.4I_{\mathrm{sat}}$ and (b) $6.8I_{\mathrm{sat}}$ of Q(0)($F = 1$) pump light.

Figure 4.8(b) shows the effects of the same transition being driven by the pump light, but containing a total of 16 mW in the $\pm x$ elongated beams. This is the first component of the new pump scheme. In this case, the Q(0)($F = 1$) transition is power broadened by the high intensity laser field and off-resonantly couples to the ground state, removing population from $F = 0$, and pumping it into $N = 2$. This amount of power in the Q(0)($F = 1$) sideband is required to balance out the high powers of the $N = 2$ beams. Even with the addition of these extra lasers, which create complicated interactions, it may still be possible that there is some off-resonant coupling to $F = 0$ which lowers the total signal gain we achieve. Some preliminary observations have shown that the fractional increase in $F = 0$ signal is sensitive to the detuning of the Q(0)($F = 1$) sideband. This may indicate that off-resonant coupling is still occuring but further tests are required to confirm this is the case.

Add in ($N = 2$) sidebands

The next step is to add in the repump lasers that collect the lost population from ($N = 0,\ F = 1$), as well as the thermal population in $N = 2$. These are labelled (b)–(c) in Figure 4.1, which are applied to the molecules in addition to (a) so that all laser fields are now illuminating the molecules. Figure 4.9 shows scans over (a) Q(0), and (b) Q(2). The black data shows the unpumped spectrum, the blue data shows the effects of pumping with all three laser sidebands, including polarisation modulation.

At each stage, before adding more levels to the scheme, all the states we address should be as empty as possible. To place a number on the fraction of population we pump out from $N = 2$, we record the height of the peak at a single point in the spectrum both before and after pumping. Figure 4.9(b) is a good example of how underlying peaks can limit our ability to place a true number on the fraction of population we remove from a level. The $F = 2^-$ peak on the right hand side of this plot has pumped out asymmetrically, indicating there is an additional small peak sitting below $F = 2^-$, at a slightly lower frequency. This unknown line will contribute to our final estimate of the left over population.

Taking the ratio of the peak heights at the dashed lines in Figure 4.9(b), indicates $\lesssim 15\%$

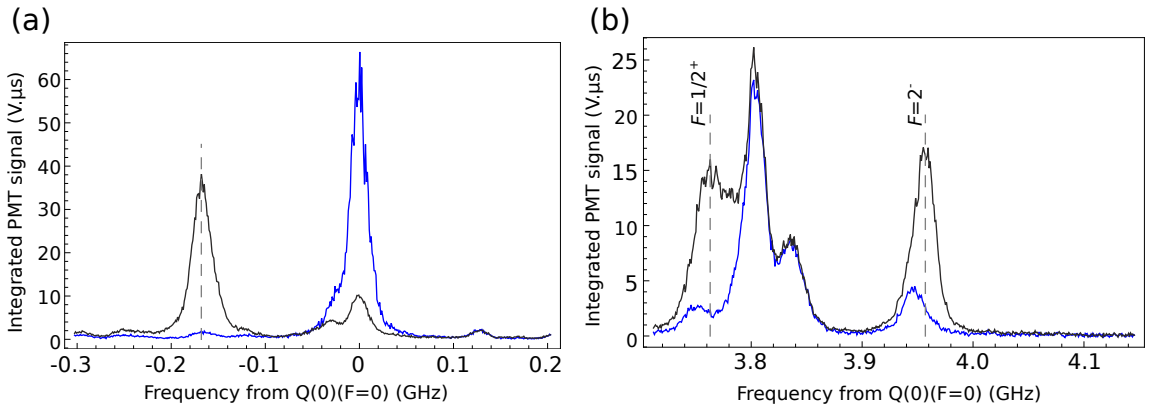


Figure 4.9: Scans across (a) Q(0) lines and (b) Q(2) lines showing the effects of pumping with all laser fields (blue) compared to unpumped spectrum (black). Dashed lines show the position at which we record the change in height both before and after pumping.

of the population remains across the three hyperfine components of $N = 2$ that are addressed by the pump light. Performing the same analysis on the $(N = 0,\ F = 1)$ peak shows us that none of this population has leaked into this state, the population is still <5%.

Aside: Polarisation modulation

Using just a single frequency pump beam tuned to ${}^{O}P_{12}(2)(F = 2^{-})$ allows us to clearly see how pumping from an $F = 2 \rightarrow F' = 1$ state can create dark states. We destabilise $M_F = \pm 2$ dark states by modulating the polarisation between left- and right-handed circularly polarised light. Figure 4.10(a) shows a scan across the Q(2) lines, using only a single pump beam propagating along $+x$, where the black data shows the unpumped spectrum, the purple data shows pumping without polarisation modulation and the blue data shows pumping with the modulation. This plot shows a clear difference between the three, with the left over population being reduced by an extra 15% when the polarisation modulation is applied to the laser field.

Figure 4.10(b) shows the effects of adding the polarisation modulation when both pump beams are on, propagating along $\pm x$. Interestingly, in this case the polarisation seems to have a very small effect on the pumping efficiency. It is suspected that some instability between the pump beams changes on a faster timescale than that of the molecules flying through the pump region, destabilising the dark states for us. Since the beams have different polarisations, the changing phase difference between them will mix the dark states for us. However this effect is occuring, it doesn't really matter, as long as the dark states are destabilised during the pumping.

Add in microwaves

The next stage is to add in the single microwave frequency, labelled (d) in Figure 4.1. This should deplete population from the $(N = 1,\ F = 2)$ level, ideally without adding any

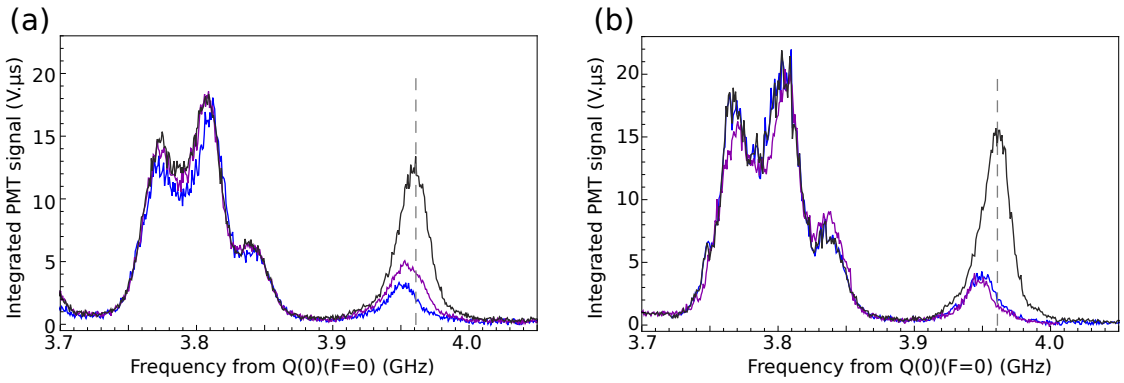


Figure 4.10: Optical pumping using a single frequency laser tuned to ${}^{O}P_{12}(2)(F = 2^{-})$, both with (blue) and without (purple) polarisation modulation and propagating along (a) only $+x$ and (b) both $\pm x$. The unpumped spectrum is shown in black.

additional population into the $N = 2$ and $(N = 0,\ F = 1)$ states. Figure 4.11 shows scans across (a) Q(0), (b) Q(1) and (c) Q(2), the black data shows the unpumped spectrum and the light blue data showing the effect of adding the microwave field. In the Q(1) spectrum,

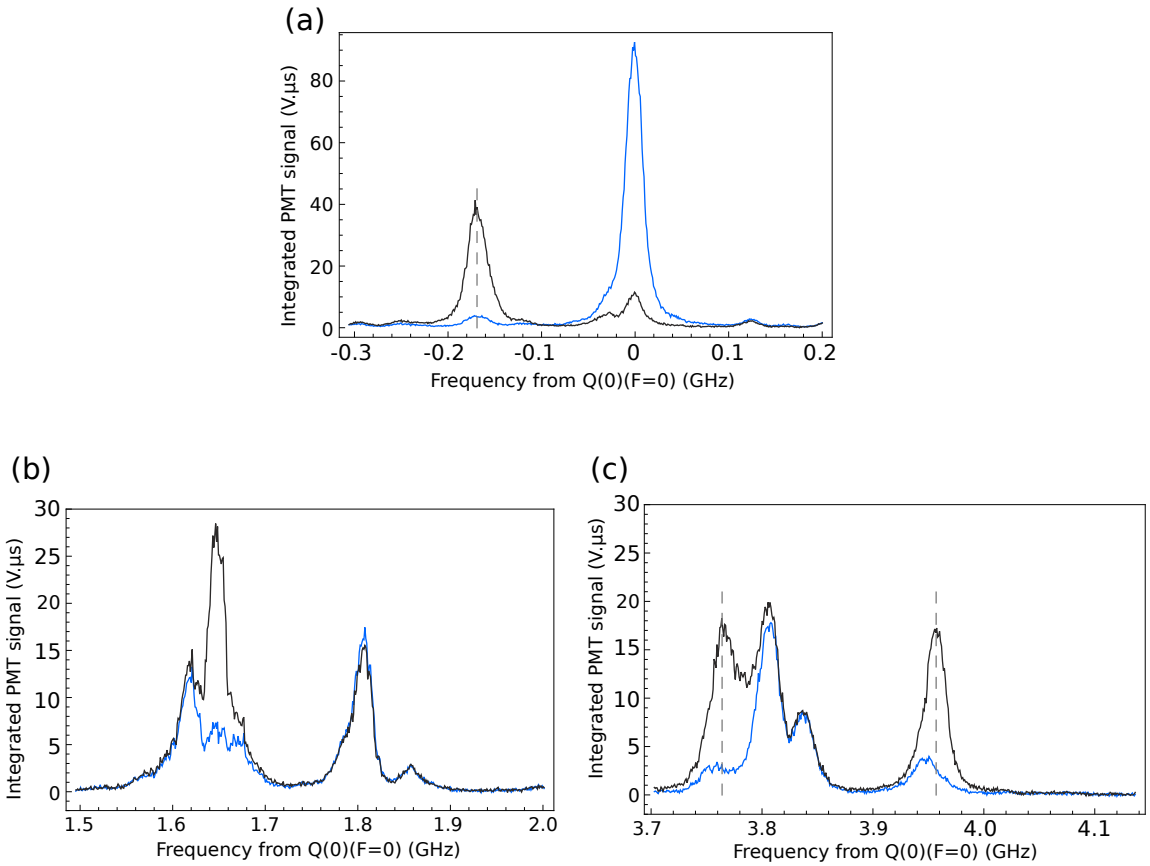


Figure 4.11: Scans across (a) Q(0), (b) Q(1) and (c) Q(2) showing the effects of pumping with lasers and microwave field (light blue) compared to the unpumped spectrum (black). The dashed lines show the peak heights used for analysis.

the $(F = 0,\ 2)$ lines sit very close together, making it tricky to distinguish how well we are

removing population from the individual ($F = 2$) state. So for now, we'll ignore this and assume that it is working well. However, we can see that the population left behind in $N = 0$ has increased slightly to ∼10% and in $N = 2$ is $\lesssim 15\%$ across all the hyperfine components. This result shows that when we add the microwave frequency, the population removed from the $N = 0$ and $N = 2$ states is almost unchanged, with perhaps a very small additional piece of population not being pumped from ($N = 0, F = 0$).

Add in RF

At this stage we are now ready to add in the final rf fields. Using only two rf frequencies; the 30.9 MHz and 161.2 MHz sidebands, detuned to 30.5 MHz and 161.0 MHz respectively, seem to be sufficient to empty the $N = 1$ states. To date, adding in the 151.7 MHz sideband, or the 36.4 MHz sideband, has very little effect on the pumping of these levels. It is suspected that the rf, which contains a substantial amount of power, broadens the 161 MHz transition into the adjacent level, which is only 6 MHz away, making the addition of the 151 MHz frequency somewhat redunadant. Figure 4.12 shows the effects of these two rf fields being applied to the molecules, in addition to the laser and microwave fields.

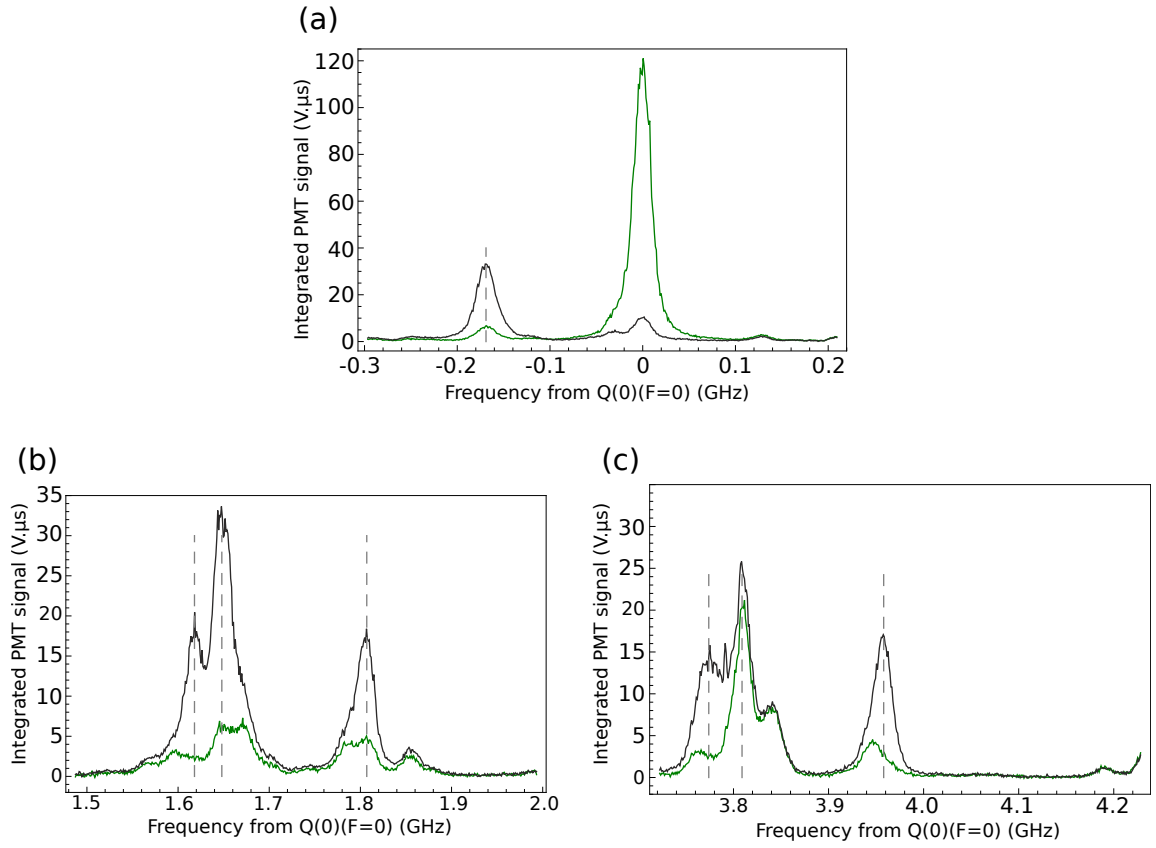


Figure 4.12: Scans across (a) Q(0), (b) Q(1) and (c) Q(2) showing the effects of the new pump scheme (green) compared to the unpumped spectrum (black).

Looking at the left over population; the ($N = 0, F = 1$) population has increased again to about ∼20%. In the $N = 2$ levels, the left over population has also increased slightly to

18% across all the hyperfine states. In $N = 1$, we leave behind {13%, 19%, 27%} of the population in the $\{F = 1^+, (F = 0, 2), F = 1^-\}$ levels. As a ball-park figure, we seem to be able to remove $\sim 80\%$ of the population from the $(N = 0,\ F = 1)$, $(N = 1,\ F = 0, 1^{\pm}, 2)$ and $(N = 2,\ F = 1, 2^{\pm})$ states using the new pump scheme. In addition, we can also see some off-resonant pumping from the $(N = 2,\ F = 3)$ level in Figure 4.12(c) which is 31.8 MHz away from the $^{O}P_{12}(2)(F = 1, 2^+)$ laser sideband. The high power rf seems to be providing us with an unexpected gain, about 20% of the population from this level is pumped out, hopefully into the ground state.

4.3.3 Spectroscopy: Signal gains

The results presented in the previous section show that the pumping is successfully removing most of the population from the higher levels. However, the main goal of this upgrade is to significantly increase the population in $(N = 0,\ F = 0)$. To check this is the case, we select the Q(0)$(F = 0)$ peaks from Figures 4.8 – 4.12 and look at the signal increase, which is normalised to the unpumped Q(0)$(F = 0)$ line. This is shown in Figure 4.13.

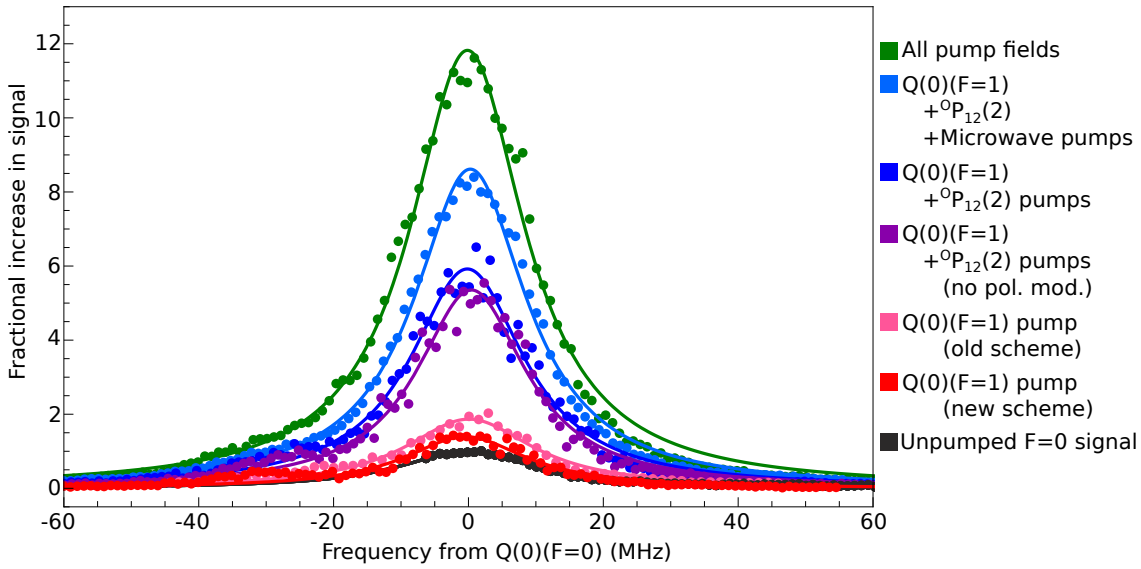


Figure 4.13: Increase in Q(0)$(F = 0)$ population for each applied field combination. The solid line shows a Lorentzian fit to the data points. The new pump scheme, shown in green, increases the population by a factor of 11.8 ± 0.8, equivalent to a factor of 6.2 ± 0.4 gain above the previous pumping scheme.

In each case, we can compare the gain in $F = 0$ population to the previous pump setup. The results of each data set in Figure 4.13 are presented in Table 4.2 below. For the full pump scheme, shown in green, 11.8 ± 0.8 units of population have been added to the ground state. This is an increase in signal of 6.2 ± 0.4 when compared to the previous pump scheme.

It is also of interest to see if the fractional gain $f(T)$ has any dependence on rotational

Pump fields	Increase in $F = 0$ population	Signal gain, $f(T)$
Q(0)($F = 1$) (new scheme)	1.4 ± 0.1	0.7 ± 0.1
Q(0)($F = 1$) (old scheme)	1.9 ± 0.2	1.0 ± 0.1
Q(0)($F = 1$) + $^{O}P_{12}(2)$ (no pol. mod.)	5.4 ± 0.5	2.8 ± 0.3
Q(0)($F = 1$) + $^{O}P_{12}(2)$	5.9 ± 0.4	3.1 ± 0.2
Q(0)($F = 1$) + $^{O}P_{12}(2)$ + microwaves	8.5 ± 0.5	4.5 ± 0.2
All pump fields	11.8 ± 0.8	6.2 ± 0.4

Table 4.2: Peak heights of each data set from Figure 4.13 comparing population increase in $F = 0$ to the fractional signal gain $f(T)$, as defined in Equation (4.4).

temperature, as suggested by Equation (4.4). The rotational temperature of the source is calculated by fitting the intensities of the Q(0)($F = 0$), Q(1)($F = 1^-$) and Q(2)($F = 2^-$) lines to the Boltzmann distribution, which is modified by the rotational line strengths of these transitions [107]. In this case, the probe beam is of sufficiently low intensity to neglect any cycling effects of the levels, which will artificially enhance the signal of a level. The only experimental control we have over the rotational temperature is to step the target wheel and try to enhance the population in a higher or lower Q line. When it seems like the temperature has changed, we repeat the scans presented in Figure 4.12 using the same experimental setup, and calculate the new rotational temperature and fractional signal gain. Figure 4.14 presents a small set of these experiments. The red data point is from the data presented above.

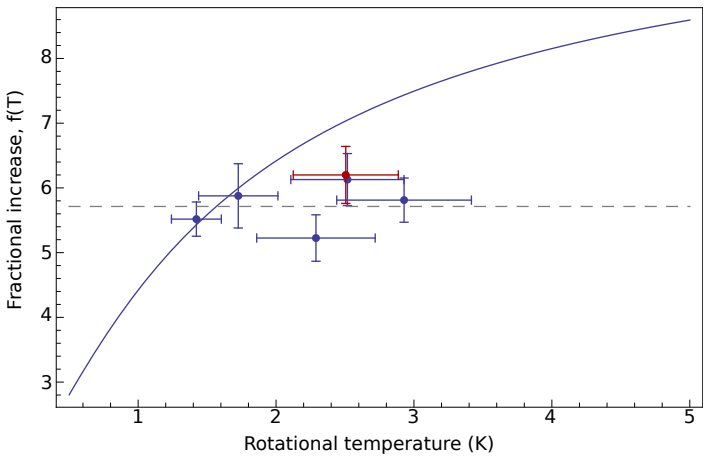


Figure 4.14: Rotational temperature dependence of the fractional signal increase $f(T)$, the solid line plots Equation (4.4). From this small sample set, there seems to be no dependence on the rotational temperature. The weighted mean of this data is shown by the dashed line.

From Figure 4.14 there seems to be very little dependence on rotational temperature. It's a shame this data doesn't follow the predicted model — there may be some inefficiency in the pump scheme that is stopping us reaching the entire gain we would expect. If we assume there is no rotational temperature dependence, the weighted mean and standard deviation of these points suggest we can expect a gain of 5.7 ± 0.4. This value is very close to the gain of 5.6 predicted by the OBE simulations.

4.3.4 Conclusion

At the beginning of this chapter, I introduced the requirements of the new pump scheme. Firstly, the ($N = 0,\ F = 1$) level needs to be emptied by the pumping. The old pump scheme left behind $< 5\%$ of the original $F = 1$ population. In comparison, the new pump scheme leaves a little bit more, $< 20\%$. It is expected that the reduction in contrast due to this extra population will be negligible when compared to the gain in signal we have achieved with the new pump scheme, and other additional upgrades detailed in this thesis. If, in the future this does present a problem, a small clean-up laser could be added to the very end of the pump region (with minimal effort) to ensure this state is completely clear.

Secondly, for the new probe scheme to work well, the levels in $N = 1$ should also be emptied. Figure 4.12(b) shows that $\sim$20% of the total $N = 1$ population has been left behind across all the hyperfine levels which can also reduce measurement contrast. Again, if this presents a problem in the future, it can also be solved by recycling the probe laser (which detects on the P(1) transition) to an earlier port in the vacuum chamber, and use it as an initial clean out beam before detection. This is discussed in more detail in Chapters 6 and 7.

Overall, the pump scheme has increased the number of molecules taking part in the experiment by a factor of 6.2 ± 0.4. Using the weighted average, presented in Figure 4.14, the factor is 5.7 ± 0.4, improving measurement sensitivity by a factor of $\sqrt{5.7} = 2.4$. Some preliminary observations have indicated that certain parameters seem to play an important role in increasing the gain and/or reducing the amount of leftover population. In particular, the distribution of power between the two rf sidebands and the Q(0)($F = 1$) detuning seem to be more significant than others. The whole parameter space of the pumping, which includes the detuning of each field as well as the total and relative powers of each laser, microwave and rf sideband, has yet to be explored experimentally. This is a mammoth task and really emphasises why the OBE simulations have been so helpful towards achieving these results and also how they could be used to push towards a more efficient scheme.

Chapter 5

The new interaction region

5.1 Introduction

As the sensitivity of the machine improves, systematic effects will also need to be under control at the same level. It becomes increasingly important to show that the magnetic fields inside the chamber are well behaved. Previous EDM measurements using YbF have had to infer the magnetic field generated inside the vacuum chamber using external magnetometers or from measurements of other properties such as the leakage currents [78]. Using these techniques, any magnetic field which is correlated with the electric field reversal is particularly difficult to distinguish from an EDM signal. This is a common systematic effect that needs to be carefully considered by every EDM experiment, independent of the magnetic field measurement technique. For example, a correlated magnetic field of only 3 fT along z would mask an EDM signal of $d_e = 10^{-29}$ e.cm using YbF. To try and measure these fields directly, we began discussions with *Twinleaf*, a company who have developed optical SERF (spin-exchange-relaxation-free) magnetometers with a sensitivity of a few fT/$\sqrt{\text{Hz}}$, the design of which is based on [114]. This magnetometer will be small enough to sit inside the inner magnetic shield, behind the electric field and rf plate structure and will be able to record low frequency (<25 Hz) magnetic field noise along the z axis with high sensitivity. Using the normal running conditions of the machine (e.g. a 9.1 nT magnetic field that is modulated at 25 Hz) we are expecting this magnetometer to have a sensitivity of around 270 fT/$\sqrt{\text{Hz}}$, significantly improving our ability to search for systematic effects inside the machine.

During discussions with *Twinleaf* in early 2015, they suggested that the magnetometer could be limited by magnetic Johnson noise. Thermal fluctuations of the electrons inside conducting objects can contribute to the uncertainty in the measurement of the magnetic field, depending on the magnetometer's position inside the vacuum chamber. With this suggestion, we realised that magnetic Johnson noise can also effect the EDM measurement sensitivity [115] [116], and so we began a thorough analysis of the conductors in our chamber and the contributions they would make to both the magnetometer and the molecules.

The analysis showed that the *Twinleaf* magnetometer recording data at a sensitivity of 270 fT/$\sqrt{\text{Hz}}$ would not be limited by Johnson noise. However, with the sensitivity gains we

are expecting with the improvements presented in this thesis and in [89], we found that the Johnson noise from the electric field plates would contribute to our measurement uncertainty, with the noise being comparable to the predicted shot noise limit. The following section outlines the theoretical analysis we made on the conductors inside our vacuum chamber in the context of magnetic noise on the EDM measurement [117].

Following this discovery, we designed and built a new pair of electric field plates which have reduced their contribution to the magnetic Johnson noise by a factor of 100. Sections 5.3 to 5.4 present the design and performance of these new electric field plates. This work is also summarised in [106], a paper I co-authored on the content of this chapter. Some small changes were also made to the rf TEM transmission line to incorporate this new design and to improve the coupling, these changes are outlined in Section 5.5. The SERF magnetometer is still in the development stage at *Twinleaf* but is expected to be installed during the next round of data taking. This should provide a tighter limit on the systematic effects caused by magnetic fields correlated with the electric field direction.

5.2 Magnetic Johnson noise

5.2.1 Magnetic noise introduction

As we found in Chapter 2, to measure d_e we record the phase change of the valence electron in YbF as its spin precesses in an applied electric field and magnetic field. The phase shift has an electric part $\phi_E = d_e \eta E_{\text{eff}} \tau / \hbar$ and a magnetic part,

$$\phi_B = \frac{\mu}{\hbar} \int_0^\tau B_z(t)\ dt \tag{5.1}$$

which is now time-dependent due to a fluctuating magnetic field. Here, μ is the magnetic moment of the hyperfine state (in this case it is simply the Bohr magneton, μ_B) and B_z is the component of the magnetic field parallel to the electric field. If the fluctuations in the magnetic phase become comparable to the shot noise limit then the efficiency of our data taking is reduced. In this case, the current fluctuations caused by the thermal motion of the electrons in the surrounding conductors are the source of magnetic noise we consider.

Let the time-dependent noise in B_z be $B_{n,z}(t)$. The spectral density of the noise power $B_{n,z}^2(f)$, is defined by the correlation function between the magnetic field at the same point in space at different times,

$$\langle B_{n,z}(t_0) B_{n,z}(t_0 + t) \rangle = \int_0^\infty B_{n,z}^2(f) \cos(2\pi f t)\ df, \tag{5.2}$$

where $B_{n,z}(f)$ has units of $\mathrm{T}/\sqrt{\mathrm{Hz}}$. The rms phase uncertainty in ϕ_B after the interaction time τ is

$$\sigma_{\phi_B}(\tau) = \frac{\mu}{\hbar} \left\langle \left(\int_{t_0}^{t_0+\tau} B_{n,z}(t)\ dt \right)^2 \right\rangle^{1/2}, \tag{5.3}$$

where we take the mean of the expression inside the angled brackets. Following [115], we can rewrite Equation (5.3) using Equation (5.2) to give,

$$\sigma_{\phi_B}(\tau) = \frac{\mu\tau}{\hbar}\left(\int_0^\infty B_{n,z}^2(f)\frac{\sin^2(\pi f\tau)}{(\pi f\tau)^2}\,df\right)^{1/2}. \tag{5.4}$$

Equation (38) of [117] provides a formula for $B_{n,z}(f)$ at a distance z from an infinite slab of conducting material at temperature T, having a thickness d and resistivity ρ. The molecules pass between a pair of electric field plates which each contribute to the magnetic field noise, so we multiply Equation (38) of [117] by a factor of $\sqrt{2}$ to give,

$$B_{n,z}(f) = \sqrt{2}\times\mu\sqrt{\frac{2k_BT}{\pi\rho}}\left(\int_0^\infty R(\xi,t)e^{-2\xi z}\xi\,d\xi\right)^{1/2}, \tag{5.5}$$

where $R(\xi,t)$ is a complicated expression given in Equation (39) of [117], repeated here for completeness,

$$R(\xi,\ t) = \frac{\frac{\gamma}{2\alpha}(1-e^{-4\alpha t})(1+\gamma)+\frac{\gamma}{\beta}\sin(2\beta t)e^{-2\alpha t}(1-\gamma)+\frac{\gamma^2}{\xi}(1+e^{-4\alpha t}-2\cos(2\beta t)e^{-2\alpha t})}{\left[1+\gamma\left(1+\frac{2\alpha}{\xi}\right)\right]^2+e^{-4\alpha t}\left[1+\gamma\left(1-\frac{2\alpha}{\xi}\right)\right]^2-2e^{-2\alpha t}\left\{\cos(2\beta t)\left[(1-\gamma)^2-4\left(\frac{\beta\gamma}{\xi}\right)^2\right]+\sin(2\beta t)\frac{4\beta\gamma}{\xi}(1-\gamma)\right\}}. \tag{5.6}$$

The variables α, β and γ are defined as,

$$\alpha = \frac{1}{\sqrt{2}}\left(\xi^2+\sqrt{\xi^4+\left(\frac{2\pi\mu f}{\rho}\right)^2}\right)^{1/2}, \tag{5.7}$$

$$\beta = \frac{\mu\pi f}{\rho\alpha}, \tag{5.8}$$

$$\gamma = \frac{\xi^2}{\alpha^2+\beta^2}. \tag{5.9}$$

The variable ξ also contains frequency dependence which is encoded via Fourier integrals, detailed in [117]. Using this theoretical setup we can begin to investigate the magnetic noise in the experiment.

Aside: Are we sensitive to any other frequencies?

In the derivation presented above, we are considering an interferometer that measures for a period τ and then stops; where the $\mathrm{sinc}(\pi f\tau)$ component of Equation (5.3) is the Fourier transform over this measurement period. The disadvantage of this approach is that it does not capture the full noise spectrum we may be susceptible to. For example, the machine fires a shot every 25 Hz and we reverse the electric field between the plates roughly every 20 s with 14 s of dead time after each switch. These features contain many more frequency components than that of the Fourier transform of a single shot, which may change how the magnetic noise effects the experiment.

If we encode these additional features into the frequency dependence, we find that over a

large frequency range, the spectrum is approximately that of a $\text{sinc}(\pi f\tau)$ function, but with strong additional contributions at low frequencies. Figure 5.1 shows the how the sensitivity of the machine changes when you incorporate this more complex switching model, and compares it to the $|\text{sinc}(\pi f\tau)|$ function. This shows that the switching makes us more sensitive to low frequency components of the noise. Luckily, the magnetic Johnson noise power spectrum $B_{n,z}(f)$, has a flat response at these lower frequencies, see Figure 5.3, and so adding these components will not drastically change the result of this calculation. This allows us to hide all these additional complexities, and use the simple $\text{sinc}(\pi f\tau)$ function as representative of the whole experiment. Note, that this would not be the case if the magnetic Johnson noise power spectrum behaved differently at low frequency. For example, if it had $1/f$ behaviour then we would need to take these additional components into account, greatly increasing the complexity of this calculation.

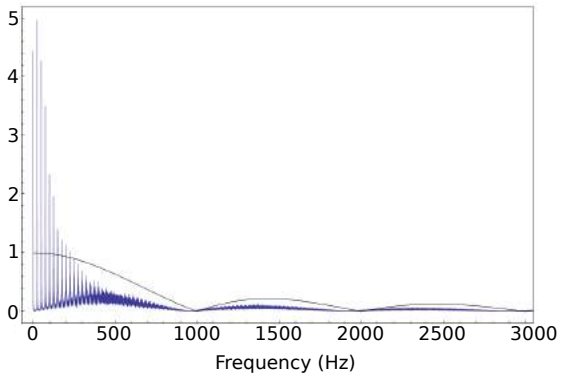


Figure 5.1: Frequency sensitivity of a simplified EDM experiment, compared to the function $|\text{sinc}(\pi f\tau)|$, shown in black.

5.2.2 Magnetic noise in the experiment

In the previous generation [52] [78], the experiment used aluminium field plates ($\rho = 2.7 \times 10^{-8}$ Ω.m) of thickness $d = 12.7$ mm. The gap between the plates was 12 mm, so the distance from the molecular beam to the surface was $z = 6$ mm. A cross-section of this design is shown in Figure 5.2(a). The magnetic noise spectrum for this set of electric field plates, given by Equation (5.5), is plotted by the blue line in Figure 5.3.

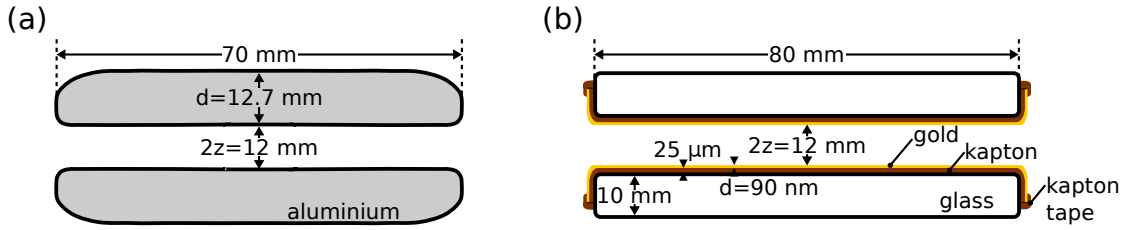


Figure 5.2: Schematic cross-sections of (a) the aluminium plate design and (b) the gold tape on glass plate design.

The integrand in Equation (5.4) also contains the function $\text{sinc}(2\pi f\tau)$, shown in green in

Figure 5.3 where an interaction time of $\tau = 1$ ms was used. This shows us that frequencies above 10^4 Hz have minimal contribtuion to the magnetic noise. After squaring and multiplying these two functions, numerical integration of Equation (5.4) gives the phase noise caused by these plates as $\sigma_{\phi_B} = 1.5$ mrad. This is equivalent to an uncertainty in the EDM of $\sigma_{d_e} = \sigma_{\phi_B}\hbar/(\tau\eta E_{\text{eff}}) = \left(1.2 \times 10^{-27}/\sqrt{N_b}\right)$ e.cm. The work presented in this thesis has improved the statistical sensitivity of the machine to $\left(5 \times 10^{-27}/\sqrt{N_b}\right)$ e.cm. If the aluminium plates remain unchanged then they will reduce measurement sensitivity by about 15%.

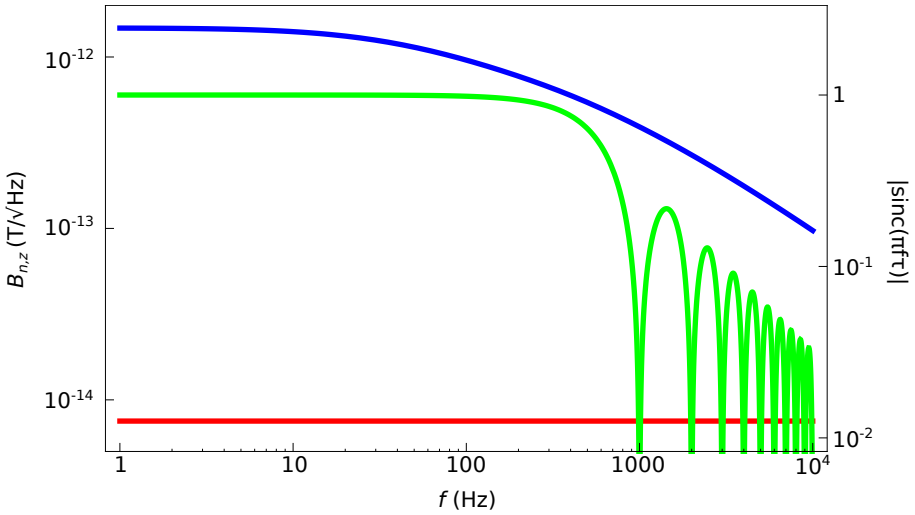


Figure 5.3: Quantities to be integrated to find σ_{ϕ_B} using Equation (5.4). Blue: magnetic field noise power spectrum $B_{n,z}(f)$ of the aluminium plate pair ($\rho = 2.7 \times 10^{-8}$ Ω.m), of thickness d =12.7 mm and separation $z = 6$ mm, calculated using Equation (5.5) at $T = 300$ K. Green: the function $|\text{sinc}(\pi f\tau)|$, using an interaction time of $\tau = 1$ ms. Red: $B_{n,z}(f)$ of the gold film electric field plates ($\rho = 2.3 \times 10^{-8}$ Ω.m), with thickness $d = 90$ nm.

At low frequency, $B_{n,z}$ tends to a constant value of,

$$B_{n,z}(0) = \mu\sqrt{\frac{k_B T}{4\pi\rho}\frac{d}{z(z+d)}}, \tag{5.10}$$

where the factor $\sqrt{d\,(k_B T/\rho)}$ can be attributed to the rms noise from fluctuating current dipoles, averaged over thickness d. Many different physical factors and regimes contribute to the z-dependence of this result, and even in the extremal cases, there (unfortunately) seems to be no simple, intuitive explanation for this form.

Equation 5.10 suggests four ways to reduce the magnetic noise: reduce T, increase z, increase ρ, and reduce d. The temperature does not offer significant improvement without cooling the plates to liquid nitrogen temperatures or below. This is rather complicated and impractical for the experiment, considering the relatively small gain it would provide. Increasing z is also not feasible for this experiment because a large electric field is required

to align YbF and it becomes challenging to support such a large potential difference across an increased plate separation.

One option to increase the resistivity of the plates is to use ITO coated glass, which has $\rho = 7.2 \times 10^{-4}$ Ω.m. This type of electrode is used in many other atomic and molecular experiments, including other EDM measurements [118] [119], because of its good vacuum properties and its transparency to visible light. However, previous unpublished work from our group found that ITO coated electric field plates were prone to discharge at high voltages, with each breakdown damaging the surface of the ITO coating. This is also reported by [119], who tried to avoid this using expensive custom coatings, in particular by coating around the edge of the field plates.

Instead, the approach we chose was to reduce d. To do this we have made the electrodes from *Sheldahl* gold-coated polyimide (Kapton) tape, on which the conducting gold layer is only 90 nm thick. This is roughly 10^{-4} of the previous conductor thickness with the resistivity relatively unchanged $\rho = 2.3 \times 10^{-8}$ Ω.m. Numerical integration of Equation (5.5), plotted in red on Figure 5.3, confirms that the magnetic Johnson noise has been reduced by a factor of roughly 100. The phase uncertainty of this new design is $\sigma_{\phi_B} = 15$ μrad with a corresponding EDM uncertainty of $\sigma_{d_e} = \left(1.1 \times 10^{-29}/\sqrt{N_b}\right)$ e.cm. A cross-section of the new design is shown in Figure 5.2(b). A summary of the magnetic Johnson noise analysis is presented in Table 5.1 below.

Plates	ρ (Ω.m)	d (mm)	σ_{ϕ_B} (mrads)	$\sigma_{d_e}/\sqrt{N_b}$ (e.cm)
Aluminium	2.7×10^{-8}	12.7	1.54	1.2×10^{-27}
Gold film	2.3×10^{-8}	90×10^{-6}	1.47×10^{-4}	1.1×10^{-29}

Table 5.1: Summary of the Johnson noise analysis for the two electric field plate designs, both with equal plate separation $z = 6$ mm and operating at a temperature of $T = 300$ K. The interaction time is set to $\tau = 1$ ms.

Using this analysis, we can also calculate the magnetic Johnson noise contributions from other conducting structures close to the beamline, these are summarised in Table 5.2 below. Together, the significant sources of Johnson noise, including the new electric field plates, will contribute $\sigma_{d_e} = \left(2.1 \times 10^{-28}/\sqrt{N_b}\right)$ e.cm to the EDM sensitivity. This is well below the new predicted shot noise limit of the experiment. Certain structures, in particular the rf plates, may need to be revisited during the next round of sensitivity upgrades.

5.3 Design

5.3.1 Construction of gold film plates

The thin film electrodes are built on slabs of untempered float glass, with dimensions 835 × 80 × 10 mm, chamfered on the edges at 45° by a few mm, and rounded by hand using silicon carbide abrasive paper. The thickness of each glass slab increases linearly along its

Structure	ρ (Ω.m)	d (mm)	z (mm)	$\sigma_{d_e}/\sqrt{N_b}$ (e.cm)
rf plates	2.7×10^{-8}	2	25	2.0×10^{-28}
Support structure	2.7×10^{-8}	8.5	51	7.8×10^{-29}
Inner shield	6.0×10^{-7}	1	85	1.5×10^{-29}
E-field plates	2.3×10^{-8}	90×10^{-6}	6	1.1×10^{-29}
Sum in quadrature				2.1×10^{-28}

Table 5.2: Summary of magnetic Johnson noise contributions from other conductors close to the molecular beamline. Calculated at a temperature of $T = 300$ K and an interaction time of $\tau = 1$ ms.

length, with one end ~ 400 μm thicker than the other, and with one plate on average slightly thicker than the other. Although not an immediate concern, the way we chose to mount the plates in the support structure, discussed in the following section, means that the variation in thickness relates directly to a change in plate separation of at least 400 μm, equivalent to a 3% variation in the electric field strength across the interaction region. To put this in context, the separation of the aluminium field plates was shown to vary by ± 110 μm [120], equivalent to less than ± 1% variation in electric field strength. To correct for the different thicknesses of each plate, we simply sanded a small region of the back face on one of the plates where the support structure is attached. The sanded region can be seen in Figure 5.4(b).

Once the glass slabs were prepared they were cleaned using detergent and water before being rinsed in distilled water and isopropanol. The entire front face of the glass was then coated in a single piece of *Sheldahl* self-adhesive, 6 inch wide, gold-coated kapton tape using a cold-roll laminator. A photo of the front face is shown in Figure 5.4(a). Excess tape was folded around the edges and trimmed away so that the edge of the tape sits roughly half-way around the side and bottom faces, as shown by the cross-section in Figure 5.2(b) and highlighted by the dashed line in Figure 5.4(a).

On the top edge, the tape is folded over to the back face where it is cut to form a small tab of 5×15 mm, with the long axis parallel to the top edge. A small aluminium block, with dimensions $20 \times 4 \times 4$ mm, which is tapped to accept an M2 thread for the high voltage connector, is glued onto this tab using conductive epoxy. This landing pad is shown in Figure 5.4(b).

The edges of the gold tape tend to discharge at high voltage. This is suppressed by covering the edges in self-adhesive, uncoated kapton tape, highlighted by the shaded region in Figure 5.4(a). The top edge of the tape and the four corners are covered with *Torr Seal* epoxy, to avoid awkward edges.

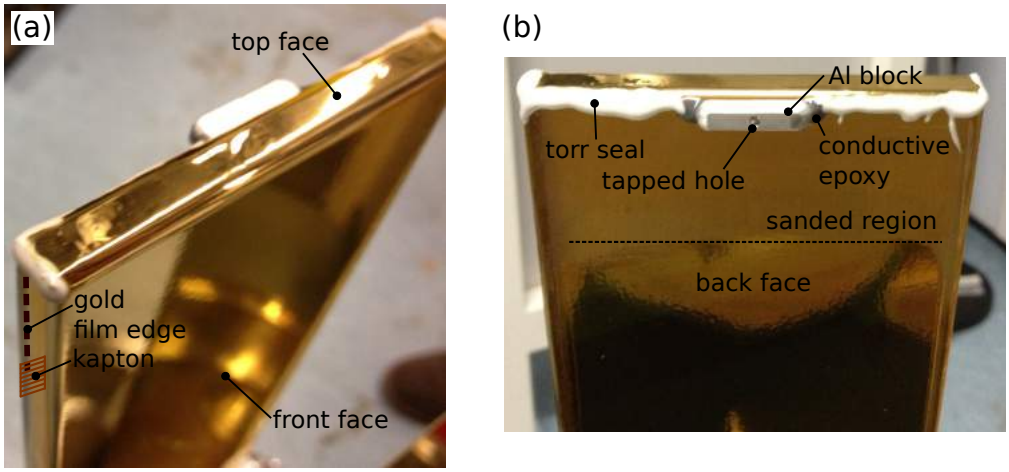


Figure 5.4: Photos of the finished plates showing (a) the front view and (b) back view.

5.3.2 Mounting the field plates

Inside the vacuum chamber, the plates need to be mounted vertically along the beamline. The plates are held by two horizontal alumina rods, glued with *ScotchWeld* structural epoxy to the back face at the top and bottom of the plate. These ceramic rods then plug into a pair of precisely machined aluminium side plates which ensure the separation is fixed to 12 mm. This is shown in the photos in Figure 5.5.

The construction of this setup was done in situ by lifting the plates between the support structure to the correct vertical position, and then pulling them tightly against the ceramic rods using elastic bands before gluing them into place. Using the field map measurements presented in Section 5.4.1, Figure 5.7, the plate spacing is shown to be uniform to within ± 100 μm, with an average separation of 12.4 mm. This is very similar to the previous setup.

Once assembled and placed inside the vacuum chamber the entire apparatus was baked at 80°C for three days to speed up any outgassing. After cooling to room temperature the base pressure of the vacuum falls to 4×10^{-7} mbar, which is the same as the base pressure of the chamber without the field plates. From this, we can conclude that the outgassing rate of the electric field plates is below 5×10^{-5} mbar.l/s.

5.3.3 High voltage

The electric field plates are connected to high voltage using coaxial cable with the outer plastic jacket stripped away. The core of this cable is non-magnetic and is soldered into a short piece of M2 threaded tube. This is then screwed into the landing pad on the back of each plate, making the electrical connection. The braid of the cable, which is grounded to the support structure, is trimmed away from this region to reduce the chance of electrical breakdown. The ends of the braid are tidied up with a copper crimp. A close up of this is shown in Figure 5.6(c).

The cables are held to the support structure using a PEEK mounting block, shown in Figure 5.6(b). The molecular beam is shielded from the dielectric by a pair of ground planes

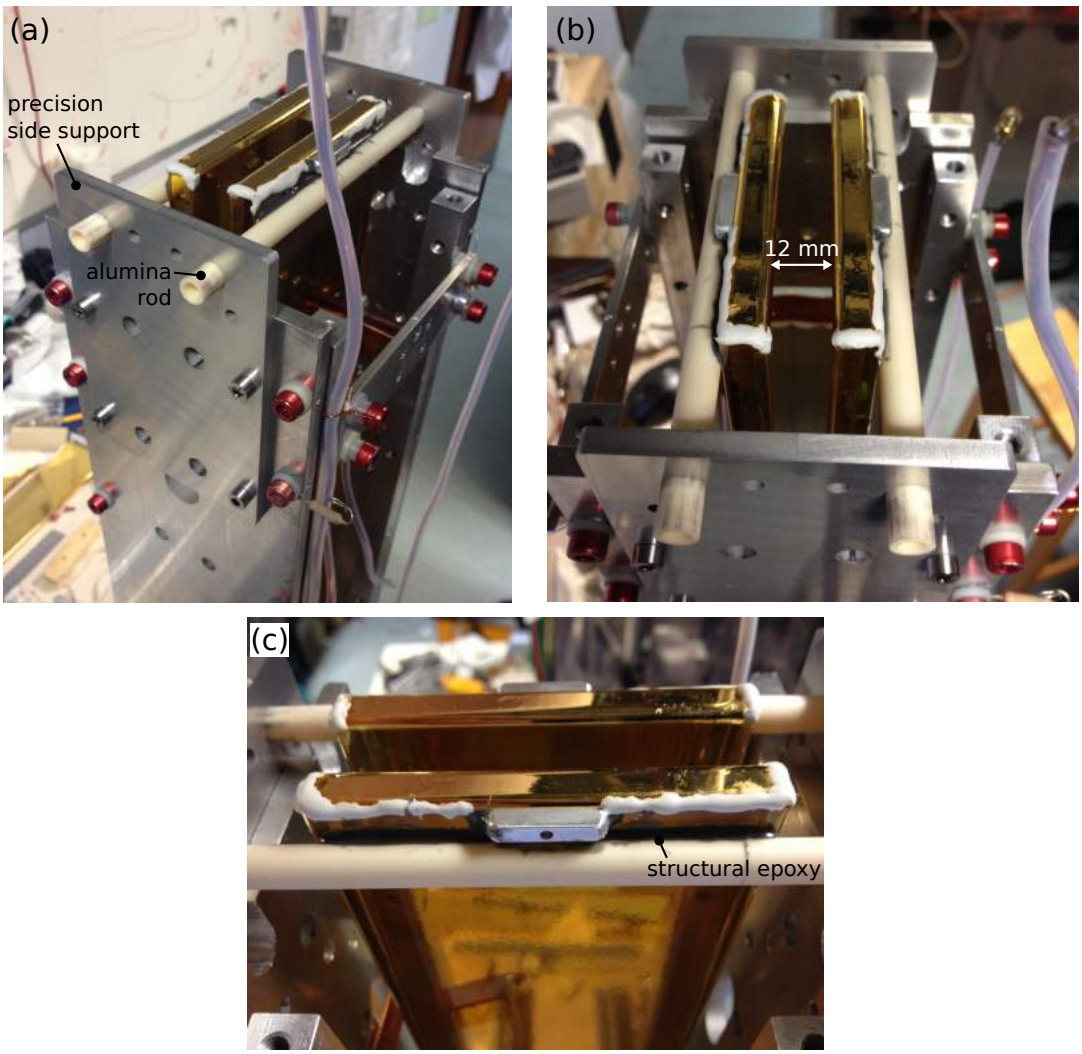


Figure 5.5: Photos of the mounted electric field plates. Alumina rods are glued to the back of the plates at the top and bottom (not shown). These then plug into precisely machined side supports which set the plate separation. The rf plates are not installed in these pictures.

which ensures the molecules always see a well defined field as they leave the interaction region. The cables are then fed up through a single hole in the inner shield end cap, minimising the chance of magnetising the inner shield by the high voltage charging currents. These cables are connectorised at the end to push onto a 20 kV coaxial feedthrough.

Next, the plates need to be conditioned to support the large electric field without excessive leakage currents. This is done by applying a voltage and switching its polarity with a one minute period. While monitoring the leakage currents, we raise the voltage in 100 V steps until current spikes of 10-100 nA appear. At this point the voltage is held constant, while continuing to switch the polarity, until the spikes disappear. This can typically take between a few minutes to a few hours after which the voltage can be stepped up again. If the leakage current becomes continuous at > 10 nA the voltage is reduced for a time. If leakage currents > 1 μA are observed then the voltage is reduced to zero and conditioning begins again.

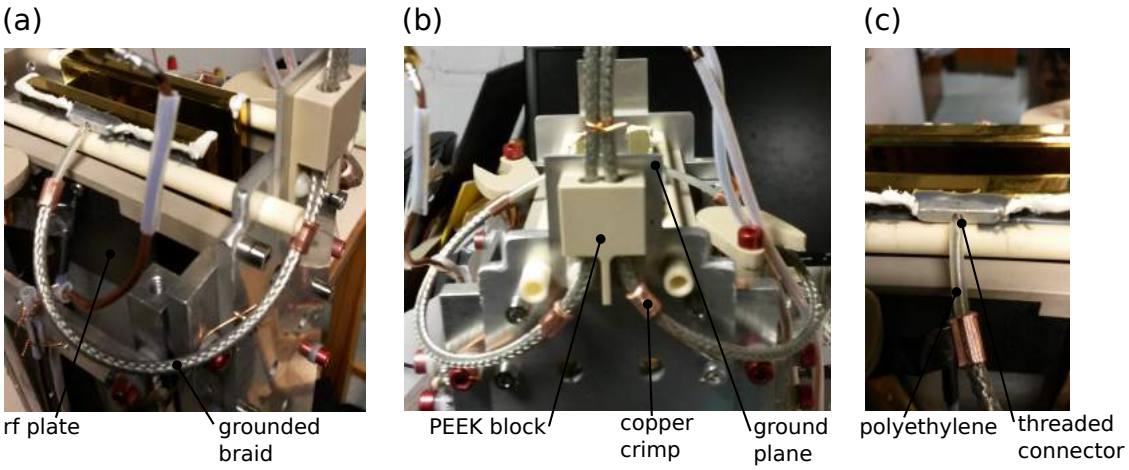


Figure 5.6: Photos of the high voltage connection to the electric field plates.

These current spikes do not seem to damage the gold film. After several days conditioning, the plates can comfortably support ±5 kV, equivalent to an electric field of 8.3 kV/cm. At this field strength, the polarisation factor is $\eta = 0.51$, slightly reduced from the $\eta = 0.61$ we had in the previous setup. Unfortunately, this reduces the statistical sensitivity by a factor of 0.85. However, it is hoped that as we begin to take data the plates will naturally condition themselves and the electric field could be increased back up to 12.5 kV/cm or more.

5.4 Performance

5.4.1 Electric field uniformity

It is important for the EDM experiment that the molecules experience a homogeneous electric field between the plates [78] [111]. Using the technique described in [120], we have mapped the electric field uniformity of the new plates at $|E_z| = 4$ kV/cm. This method uses the molecules themselves to sense the electric field variation using the Stark shift of the hyperfine structure, see Figure 2.10. The red, triangular points in Figure 5.7 shows the fractional variation of the field as a function of position along the length of the plates. This is within ±0.8 %, which provides a sufficiently uniform Stark shift for the EDM measurement. For comparison, the fractional field variation of the old plates is also shown by the blue, circular points, which is very similar.

Rotation of the electric field can be undesirable when it introduces a geometric phase that changes with electric field reversal [78] [111]. As a function of y the field rotates about x by less than ±0.5 mrads across the entire length due to the warping of the mounted glass slabs. From the geometry we expect this rotation in the x axis to be similar. This small electric field rotation is not enough to produce a systematic error alone as the phase does not change when the electric field is reversed [90]. However, this can create a systematic effect when combined with a reversing patch potential on the surface of one of the plates [78]. The new electric field plates provide us with an additional safe-guard against these patch potentials: the home-built plates can be easily re-laminated in fresh tape for a relatively small cost.

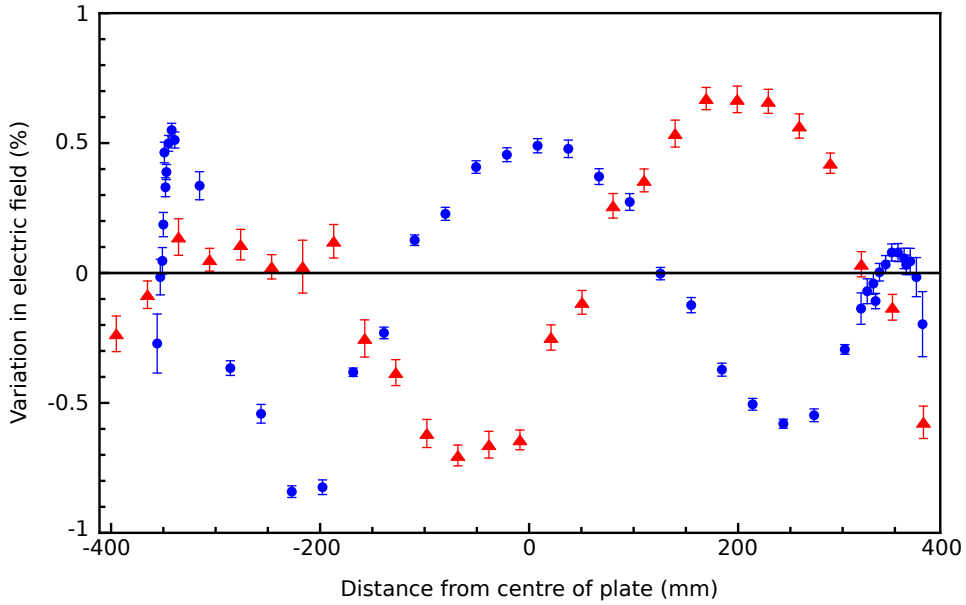


Figure 5.7: Fractional variation of the electric field as a function of distance along the interaction region, as measured by the Stark shift of the hyperfine structure in YbF. Blue circles: aluminium plates. Red triangles: gold film plates.

Although not eliminating patch potentials, this would change their position and/or reduce the amount of surface contamination, allowing us to place tighter constraints on possible systematic uncertainties. Even without this additional protection, the geometric phase is small even for the worst case scenario [78] [90] with $\sigma_g < 1 \times 10^{-30}$ e.cm.

5.4.2 Leakage currents

The leakage current from the entire high voltage system, including the plates, operating at ± 5 kV is 0.4 ± 0.1 nA. This is dominated by the leakage from the external 10m-long coaxial connecting cables and high voltage switching equipment. The leakage current from the plates and high voltage connections under vacuum is less than 300 pA, when removing the leakage currents caused by the unconnected HV cables. The shortest leakage path from the gold film to the grounded support structure is 21 mm.

The leakage currents that flow during data taking can generate a magnetic field that is correlated with the direction of the electric field. For example, a current flowing between the plates would certainly generate such a correlation and if the total leakage path generates a magnetic field along z, then a systematic effect is created. Until we are able to directly measure these magnetic fields we can only assume the worst case scenario: a leakage current that generates a magnetic field entirely in the z direction. Figure 5.8(a) shows the worst-case model that we used for the aluminium plates, where the feedthroughs were positioned in the middle of the plates, and Figure 5.8(b) the model for the new plates.

The previous EDM measurement recorded a leakage current correlated with the electric

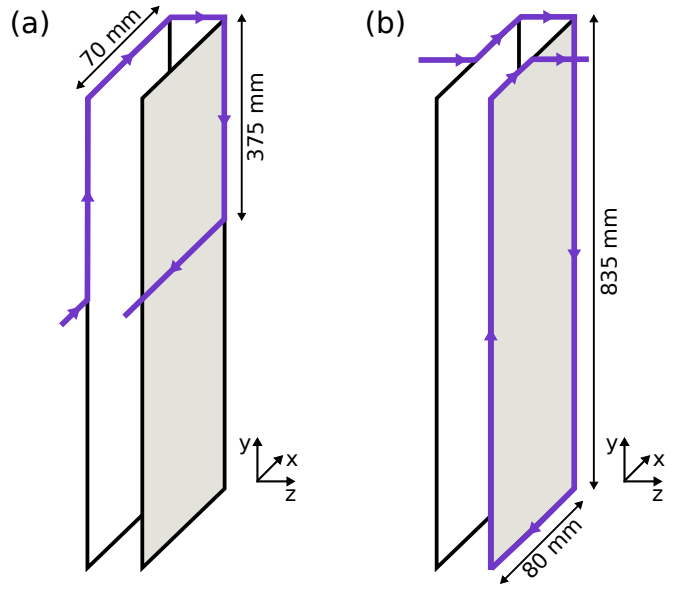


Figure 5.8: Illustration of the leakage current path used to model the magnetic field generated by the leakage currents (a) Aluminium electric field plates and feethroughs and (b) new gold foil plates with feedthrough connections.

field reversal of < 1 nA when averaged over the main dataset [78] [52]. Using the path shown in Figure 5.8(a) this generates a 5 fT magnetic field that is correlated with the electric field, when averaged over the entire interaction region. The systematic shift caused by this field was limited to $\sigma_{\text{leakage}} < 2 \times 10^{-29}$ e.cm [52] [78]. With the improvements predicted in [89] and presented in this thesis, this was expected to be one of the biggest contributors to the systematic uncertainty, see Table 3.1. However, with a leakage current of 300 pA associated with the plates and high voltage connections inside the vacuum, and assuming this will entirely contribute to the correlated magnetic field, gives a worst case magnetic field of 2 fT with an associated systematic effect of

$$\sigma_{\text{leakage}} < 1.3 \times 10^{-29}\ e.\text{cm}. \tag{5.11}$$

With the installation of the SERF magnetometer we will be able to further restrict this, giving us a direct measurement of the magnetic field along the z direction which is correlated with electric field reversal.

5.5 Improvements to the rf system

After the last published measurement [52], a new rf amplifier was installed to drive shorter, higher power rf π-pulses, reducing the pulse length from 18 μs to 2 μs [90]. Broadening the rf linewidth desensitizes the experiment from systematic errors associated with the rf detuning. This also increases the contrast of the interferometer, and hence measurement sensitivity, by ensuring the π-pulse is more efficient across a larger velocity class of molecules. Unfortunately, when operating the experiment with rf pulses shorter than 9 μs, some strange

behaviour was observed by the rf and high voltage ammeters [89]. After some investigation, the behaviour was connected to rf *multipactor discharges* occuring in the machine [121]. The process generating these discharges is as follows: a charged particle strikes a metal or dielectric surface in an rf field which releases secondary electrons. These electrons are then accelerated by the rf field into a second surface, where more secondary electrons are emitted. Since the rf is continually changing direction this process can avalanche, creating a significant amount of current, the magnitude of which could be correlated with the direction of the electric field.

Several measures were taken to try and reduce the number of multipactor discharges [89], but it was found that only by increasing the pulse length to 9 μs, thereby reducing the amount of rf power in the machine, could the discharges be stopped entirely. As we began to upgrade the electric field plates, it was decided that we should also improve the rf system so that it can support the shorter rf pulses. Analysis showed that for the rf field required to drive a 2 μs pulse, a gap of only 3 mm can support a multipactor discharge [89]. A photo of the rf structure in Figure 5.9(a) highlights some of the suspected areas causing the discharges.

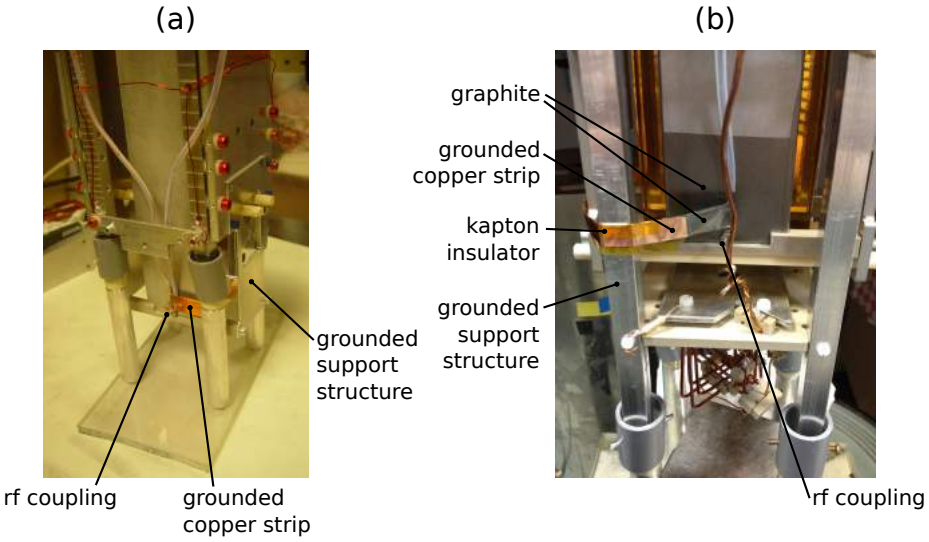


Figure 5.9: Changes made to the rf system to reduce multipactor discharges. (a) Previous rf TEM transmission line and coupling. The suspected ground planes responsible for the mulitpactor discharges are indicated. (b) Upgraded transmission line. Graphite is used to supress potential secondary electron emission. The grounded copper strip used to balance the TEM transmission line has been pulled away from the rf structure.

The generation of an avalanche of electrons is determined by the secondary electron yield (SEY) of a surface which varies significantly between types of materials (conductor or dielectric) and depends on incident electron energy, flux and angle as well as surface temperature and roughness. SEY is defined as the ratio of secondary electrons to incident electrons. A material with SEY ≤ 1 will suppress multipactor discharges. We discovered that graphite has this property across a broad range of incident electron energies [122] [123] and so we coated many of the suspected surfaces with self-adhesive graphite sheet. The covered

areas can be seen in the photo in Figure 5.9(b). In addition, the grounded copper strip used to balance the TEM transmission line, was extended away from the rf plates to increase the distance between these structures, also shown in Figure 5.9(b). With these changes to the interaction region, we can now successfully drive 2 μs long rf π-pulses without mulitpactor discharges occurring.

The rf coupling has also significantly improved since the last rebuild (Feb 2012). Either because of the changes made to the rf coupling, or the fact that the electric field plates are now made of glass, we can now drive rf pulses with on average 40 times less power across the whole interaction region. In some areas of the transmission line this is as much as a factor of 120. A plot of the rf power required to drive a π-pulse in 10 μs, as a function of distance along the interaction region is shown in Figure 5.10. The dashed lines show the field map from the last rebuild while the solid lines show the results from the most recent build, for different directions of rf flowing in the machine.

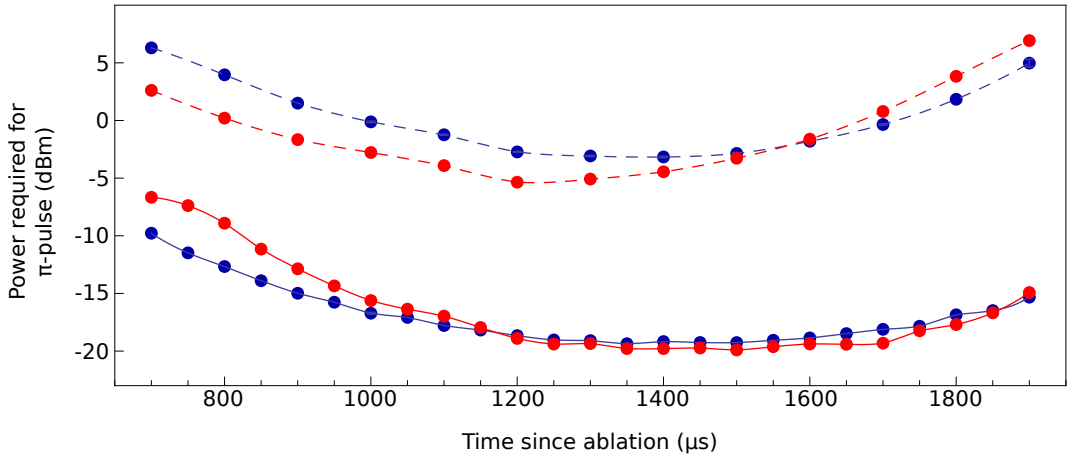


Figure 5.10: A plot of the rf power required for a π-pulse in 10 μs as a function of distance along the interaction region. Dashed lines indicate the power required in Feb 2012, solid lines indicate power required after the final rebuild in Nov 2015. Blue: rf is flowing up the transmission line. Red: rf flowing down the transmission line.

With the ability to drive 2 μs rf pulses, the contrast has been increased from 0.61 ± 0.01 to 0.76 ± 0.02 [89]. This gives a fractional improvement in statistical sensitivity of 1.25, in addition to being desensitised from certain systematic errors caused by rf detuning across the molecular packet. Once the machine is acquiring data we will be able to place an empirical value on these systematic effects.

5.5.1 Conclusion

Since 2015 we have made several successful improvements to the interaction region. We are able to apply $|E_z| = 8.3$ kV/cm to the molecules using the new, low magnetic Johnson noise electric field plates. Despite taking a small hit in sensitivity due to the reduced polarisation

factor, the leakage currents from inside the vacuum are below 300 pA. The contrast of the interferometer will also be improved by shortening the rf pulses from 9 μs to 2 μs. Together, these improvements put the experiment in a good position to restrict systematic uncertainties and record EDM data without being limited by magnetic Johnson noise.

Chapter 6

The new probe region

6.1 Introduction

Measurement sensitivity can be improved by increasing the number of molecules that take part in the experiment. Using the new pump scheme, sensitivity has already been improved by directly preparing more molecules into the initial measurement state. This gain in sensitivity can be enhanced even further by detecting the molecules more efficiently at the end of the experiment.

Previously, a single molecule participating in the measurement would scatter 1.2 photons on average before going dark to the probe light. Preliminary results using the new probe scheme, indicate that this has increased up to 13.8 photons per molecule. In addition, the new probe scheme incorporates a second detector that allows us to record both arms of the EDM interferometer output. In the second detector, we record an additional set of molecules that were not previously accessible, improving the statistics of our measurement even further. Together, these gains are expected to increase measurement sensitvity by a factor of 4.9.

It is worth briefly outlining the requirements we place on a new detection scheme, before beginning the in depth discussion. Firstly, the detection must be state selective and should be able to pick out the population exclusively from either the $F = 0$ or $F = 1$ hyperfine component of X $^2\Sigma^+(v = 0,\ N = 0)$. Any contamination between the levels will decrease the contrast of our measurement and reduce sensitivity. Secondly, if we want each molecule to scatter more photons than the current scheme, we must use a method that cycles population around several levels before decaying to a dark state. In addition, an ideal technique would also allow us to detect both $F = 0$ and $F = 1$ components of the interferometer output[1]. This would instantly gives us access to twice as many molecules, improving measurement sensitivity by a factor of $\sqrt{2}$. It could also provide us with an additional handle on systematic tests, as well as a way to normalise the molecular signal against source fluctuations and any other common noise sources. Finally, as with the pump scheme, the new probe scheme must only use fields that the molecules fly through (rather than fields that pulse on and off during a

[1]The two quadratures of the interferometer are encoded into the quantum state of the ^{174}YbF molecules and not spatially separated. The reader may find it useful to refer to Figure 7.1.

shot) so that these techniques can be easily transferred when the buffer gas source is included into the experiment.

The following sections discuss the development, experimental setup and results of the new probe scheme which is based on optical pumping techniques. Section 6.5 presents an alternative detection scheme that also fullfills these criteria, but requires coherent control of the population using a microwave field.

6.1.1 The new detection scheme

In the new detection scheme we cycle population within the rotationally closed P(1) transition. This system is typically used for laser cooling molecules to create a quasi-closed cycling scheme, reducing the number of repump wavelengths required [124]. Using this transition, the population can only decay back into the pumped levels, or to higher vibrational levels, after which the molecule is lost from the detection. Three laser sidebands are used to address all the states in $N = 1$; P(1)($F = 1^-$), P(1)($F = 0, 2$) and P(1)($F = 1^+$), labelled (a)–(c) on Figure 6.1. The sideband P(1)($F = 0, 2$) is equally detuned between these hyperfine states, which are separated by 5.5 MHz. In addition, the polarisation is modulated between left- and right-handed circularly polarised light to remove the dark states created by pumping from $F = 2 \rightarrow F' = 1$.

However, the P(1) cycling scheme does not address either of the EDM measurement states in $N = 0$ and so a single microwave frequency is also applied. This field connects one of the hyperfine components in $N = 0$ to the optically pumped levels in $N = 1$, allowing the population from the state to be collected. In the first detection region (6A), the microwave field is tuned to the X $^2\Sigma^+(v = 0,\ N = 0,\ F = 1) \rightarrow (N = 1,\ F = 2)$ transition at 14 458 087 kHz, labelled (d) on Figure 6.1. The population from the $F = 1$ state is then cycled around by the P(1) lasers until it decays to X $^2\Sigma^+(v > 0)$. The fluorescence emitted by the decays is collected and imaged onto the face of the *probe A* PMT. This produces a signal,

$$S^A(t) = S_b^A(t) + S_0^A(t)\sin^2(\phi_B + \phi_E), \tag{6.1}$$

where $S_b^A(t)$ includes background laser scatter, background signal from other YbF isotopes that sit beneath the P(1) lines, as well as any leftover population in $N = 1$ not removed by the pumping scheme, and $S_0^A(t)$ is directly proportional to the number of molecules in $(N = 0,\ F = 1)$.

The second region (6B), uses identical cycling lasers but selects the population in $(N = 0,\ F = 0)$ by driving the X $^2\Sigma^+(v = 0,\ N = 0,\ F = 0) \rightarrow (N = 1,\ F = 1^-)$ transition at 14 467 242 kHz, labelled (e) on Figure 6.1. As in the first detection region, the fluorescence from the decays is collected and imaged onto the face of the *probe B* PMT. This produces a signal,

$$S^B(t) = S_b^B(t) + S_0^B(t)\cos^2(\phi_B + \phi_E), \tag{6.2}$$

where $S_b^B(t)$ now contains background laser scatter, any signal from the unpumped lines

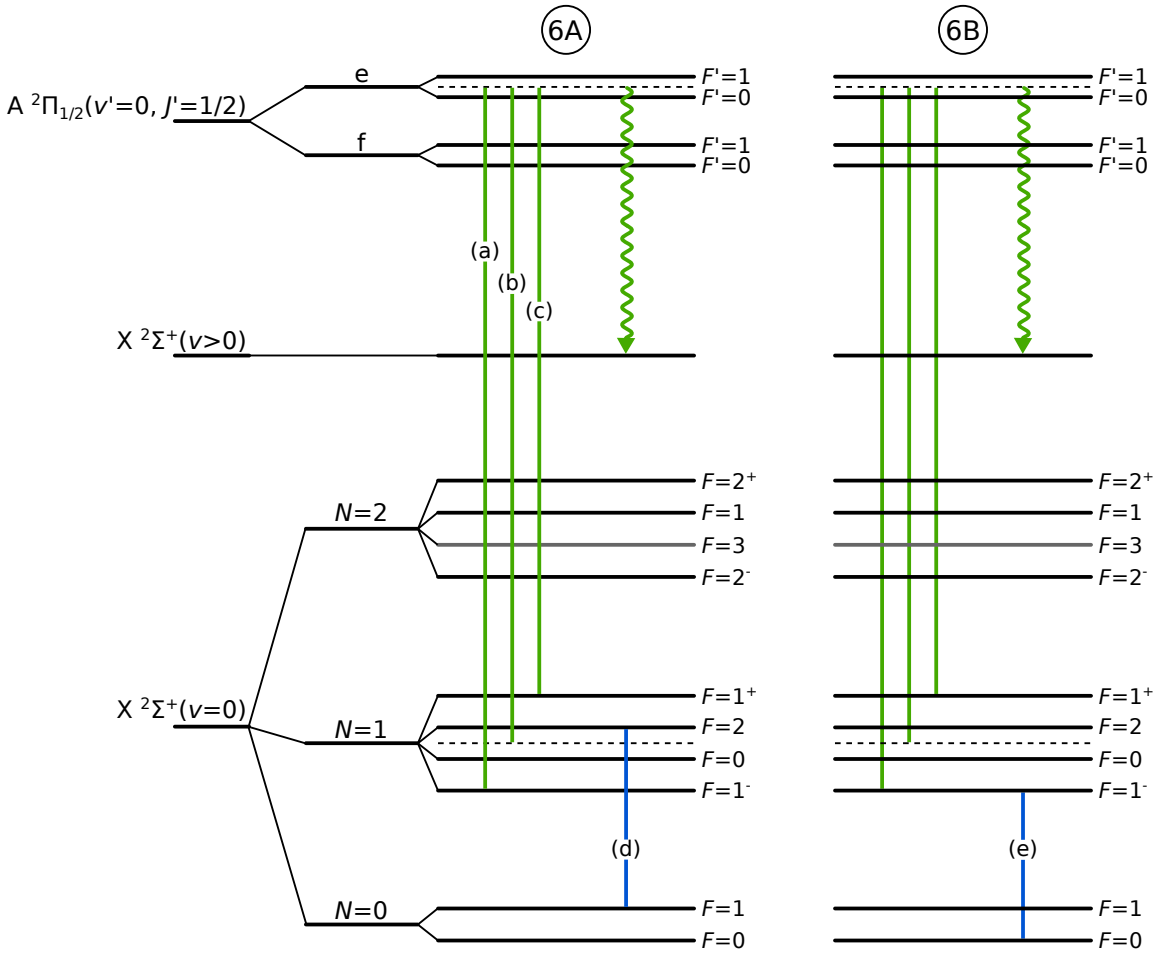


Figure 6.1: Transitions driven in the new detection scheme. A single hyperfine state in $N = 0$ is selected by microwave radiation, transition (e) selects ($N = 0$, $F = 0$) and transition (d) selects ($N = 0$, $F = 1$). The population in the selected state is then cycled around the $N = 1$ rotational level by the P(1) optical transitions (a)–(c), before decaying to higher vibrational states.

beneath the P(1) transition and any leftover population in $N = 1$ after the first detection region, and $S_0^B(t)$ is directly proportional to the number of molecules in the $(N = 0, F = 0)$ state.

This detection scheme allows the population from a single hyperfine level to be cycled within $v = 0$, scattering multiple photons in the process, before decaying to a higher vibrational state. In addition, both quadratures of the EDM measurement can be recorded by the different detection regions.

6.1.2 How many photons can we scatter?

If the new scheme works optimally, every piece of population from the selected state will be excited to the upper A $^2\Pi_{1/2}(e)$ level. From here, it can decay either back into the pumped levels or to the higher vibrational states. The maximum number of photons we would expect

from this scheme is equivalent to the number of times we can excite the population to this upper level, before it decays out of the cycling transition. The probability of this decay is $1-f_{00}$ where $f_{00} = 0.928$ is the branching ratio to $v = 0$ [96]. The average number of photons a molecule will scatter with sufficient power and interaction time is,

$$\langle N_{\text{photons}} \rangle_{\text{max}} = \frac{1}{1 - f_{00}} = 13.9 \text{ photons}. \tag{6.3}$$

A similar analysis on the current probe scheme, which uses a single sideband tuned to Q(0)($F = 0$) (see Figure 2.14), shows that a molecule will produce, on average, 1.2 photons before going dark to the probe light. This is potentially a very significant gain, with the signal being increased by a factor of 11.7. In addition, this scheme allows us to detect both arms of the interferometer, by counting the population in both hyperfine states. If both regions perform perfectly, then this enhancement increases even further to a factor of 23.5 above the current detection scheme.

6.1.3 How many photons do we expect to scatter?

Using the new detection scheme, a molecule can now scatter up to 14 photons if it is exposed to microwave and laser fields with sufficient power and interaction time. We now need to quantify what the phrase 'sufficient' means.

For the new pump scheme, OBE simulations directed us towards the optimal experimental setup. For the detection scheme, we would like to have a similar comparison between simulation and experiment, to guide us in the lab. For a simple system with a small fraction of dark states, the solutions to the OBE equations will closely follow the solutions to a linear rate equation model [89]. This simple model will provide us with an estimate for the number of photons we would expect to scatter for given powers and interaction times. The following discussion is based on [89].

In the model of our molecular system, there are N_g ground states, N_e excited states and N_L 'leak' states to which population can be lost. The system has the normalisation condition, $N_g n_g(t) + N_e n_e(t) + N_L n_L(t) = 1$, where n_g is the probability of occupying a single ground state of the system, and n_e and n_L the probability of occupying an excited and leak state respectively. Each excited state decays at a rate γ_g to the collection of ground states, and γ_L to the collection of leak states, such that the total decay rate is $\gamma_g + \gamma_L = \Gamma$. In addition, pairs of ground and excited states are linked by a classical radiation field which drives population between the levels at a rate $R_{g,e,i}$. Here, the index i labels the individual field driving population between states g and e, and the sum of the rates $R_{\text{tot}} = \Sigma_i R_{g,e,i}$. In this model, any mechanism that mixes ground states together, for example the polarisation modulation or microwave fields we use in the detection scheme, is assumed to have no effect on the rates at which population is driven to the excited state by the laser fields.

Using the derivation presented in [89], the probability of occupying the leak states grows

over time according to,

$$N_L n_L(t) = 1 - \exp\left[\frac{-\gamma_L N_e t}{(\Gamma N_e N_g)/R_{\text{tot}} + N_e + N_g}\right]. \tag{6.4}$$

The average number of photons scattered by the system is simply

$$\langle N_{\text{photons}} \rangle = \langle N_{\text{photons}} \rangle_{\text{max}} \times f_{v>0}, \tag{6.5}$$

where $f_{v>0}$ is the fraction pumped into X $^2\Sigma^+(v > 0)$. This can now be calculated from Equations (6.3) and (6.4).

It is helpful to rewrite the pumping rates $R_{g,e,i}$, in terms of more convenient quantities we can control in the lab. In particular, the rate of driving a transition on resonance is $R_{g,e,i} = |\Omega_{g,e,i}|^2/\Gamma$. The Rabi rate $\Omega_{g,e,i}$, can be related to the strengths of individual transitions $f_{g,e,i}s_i = 2|\Omega_{g,e,i}|^2/\Gamma^2$, where $s_i = I_i/I_{\text{sat}}$ is the saturation parameter, I_i the intensity of the radiation driving the transition and $I_{\text{sat}} = \pi hc\Gamma/3\lambda^3 = 4.4$ mW/cm^2 is the saturation intensity. The transition strength $f_{g,e,i}$, can be calculated from the Clebsch-Gordon coefficients shown in Appendix B of [89].

Plugging in the relevant parameters for the first detection region, $\{N_g = 15,\ N_e = 4,$ N_L=1, $\gamma_L = 0.07 \times \Gamma$, $\Gamma = 2\pi \times 5.7$ MHz$\}$, we can calculate the number of scattered photons for realistic lab parameters. Figure 6.2 shows the average number of scattered photons as a function of interaction time for different laser intensities. In this very simplistic model, I have assumed we drive each hyperfine state in $N = 1$ on resonance, with each of the four sidebands containing equal intensities I, equivalent to a total power of $4I$. Although this is not strictly the setup we use in the lab, the powers in the sidebands are typically redistributed to account for this.

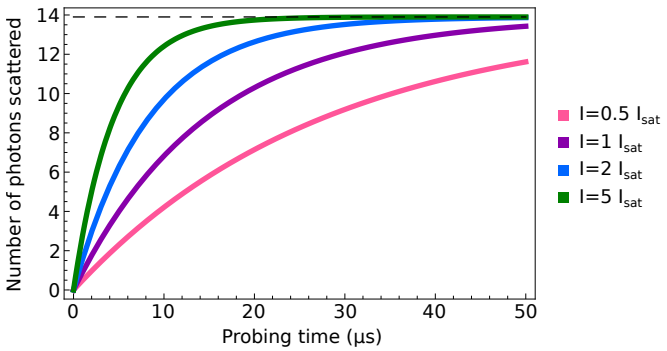


Figure 6.2: Average number of photons scattered by a molecule as a function of interaction time for the new detection scheme, as predicted by the simple rate equation model.

In the detection region, a molecule travelling at 590 m/s will have 17 μs of interaction time (see Section 6.2.2 for details). Figure 6.2 shows that if each laser sideband contains $I = I_{\text{sat}}$ (or equivalently a total of $4I_{\text{sat}}$), then a molecule will scatter on average 9 or 10

photons in this time. Increasing the laser intensity to $I > 5I_{\text{sat}}$ (or $> 20I_{\text{sat}}$ in total), then a molecule will scatter almost all of the possible 14 photons in 17 μs.

Unfortunately, the rate model does not tell us anything about power required for the microwave field. However, we can make the safe assumption that this field will need to have a comparable Rabi rate to the laser fields. For $I = I_{\text{sat}}$, this is around $\Omega_{\text{mw}} = (\mu_e|E|)/\hbar \sim 2\pi \times 1.5$ MHz which is approximately 0 dBm of microwave power at the molecular beam. For $I = 5I_{\text{sat}}$, this increases to about $\Omega_{\text{mw}} \sim 2\pi \times 3.5$ MHz, equivalent to 7 dBm of microwave power at the molecules.

The results from the rate equation model indicate we should aim for a total of 90 mW/cm^2 in each of the probe beams, across a 17 μs interaction time. If we can achieve this, along with 5 dBm of microwave power at the molecules, we can expect to transfer almost all the population into the higher vibrational levels, scattering a significant fraction of the available photons. The next section details how we achieve each of these probe fields in the lab, before comparing them to the requirements suggested by the rate equation model.

6.2 Equipment

Figure 6.3 shows an overview of the new hardware required to control the frequency, power and timings of the detection fields. Each system is discussed in more detail in the following sections.

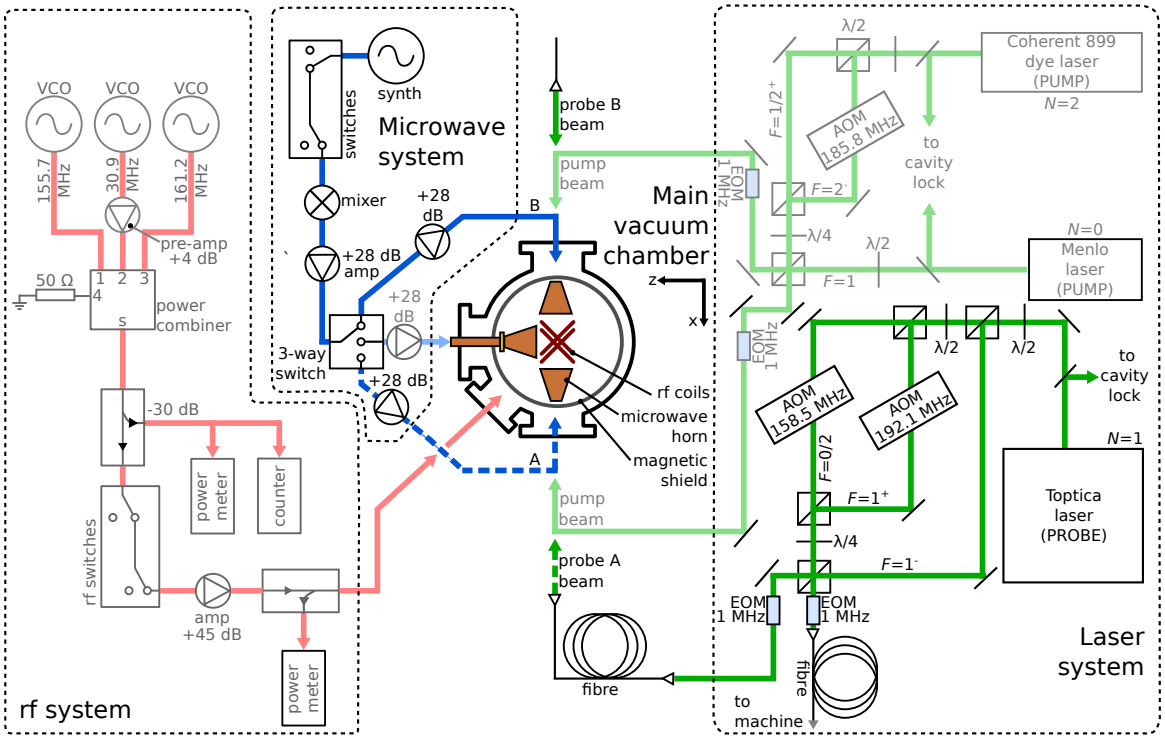


Figure 6.3: Schematic overview of the new hardware required to control the probe scheme fields.

6.2.1 Microwaves

The microwave fields are applied to a detection region by a pair of small microwave horns (aperture dimensions 21 × 25 mm), which are angled towards the detection volume, as shown in Figure 6.4. As the horns are fed into the vaccuum chamber, they are free to rotate about their pivot, shown in Figure 6.4(a), but are gently supported horizontally by the microwave coaxial cable. As they slide through the ports into the main body of the chamber, the support structures also slide against each other. Eventually, the pivot of each horn will be caught by a groove in the opposing side support, shown in Figure 6.4(b). Finally, the horn is locked into its angled position by the opposite support, where the flange then seals onto the port of the vacuum chamber, securing everything in place. This is then replicated exactly above in the second detection region.

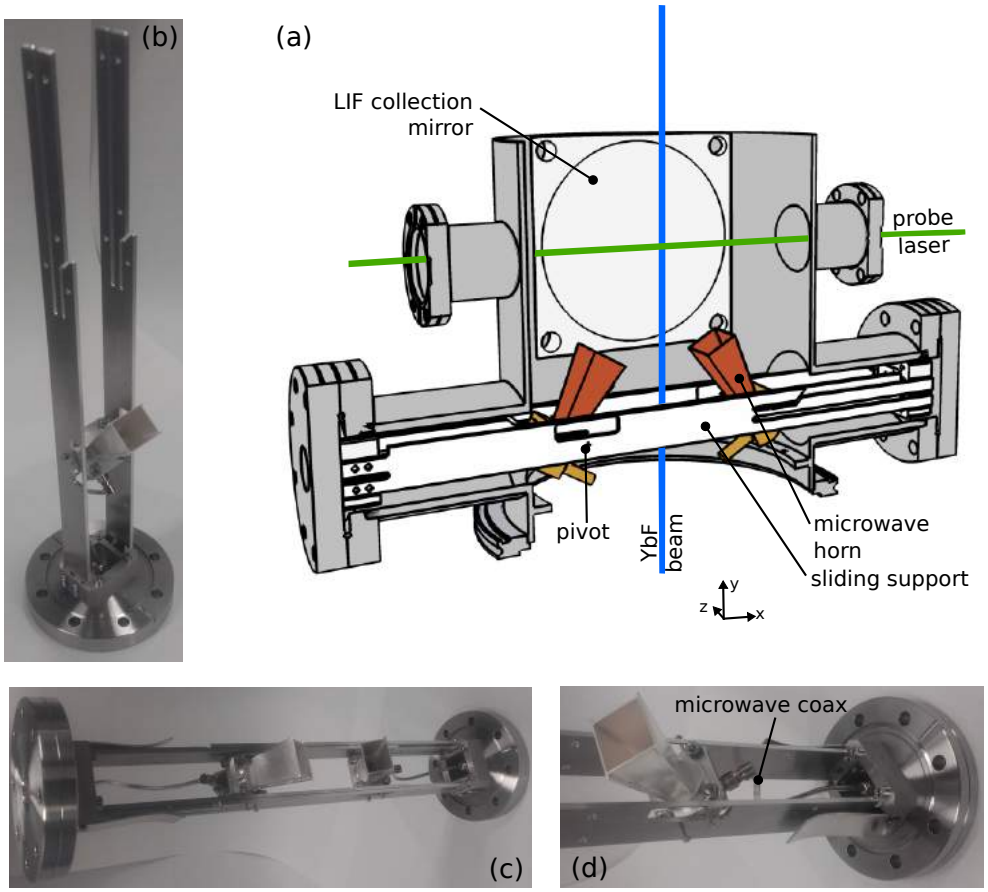


Figure 6.4: (a) Schematic of a single probe region showing the position of the microwave horns inside the chamber with the large solid angle collection mirror. (b)–(d) Some views of the microwave horn assembly, designed by J. A. Devlin. An outer and an inner component (as shown in (b)) slide into each other inside the vacuum chamber, catching the pivot of each horn and locking them into the angled position. A braided microwave coaxial cable connects each horn to the vacuum feedthroughs.

The microwave field is fed to the horns by a braided coaxial cable. Outside the chamber,

the microwaves are generated by the ANAPICO synthesizer. This setup is also used for the pump region and so the reader should refer to Section 4.2.2 for more details on this. An *AMC SW-218-3A* three-way switch directs microwaves towards the pump region, or to either detection region. Before being connected to the feedthrough, the power is boosted by a *Mini-Circuits ZX60-183A-S+* (+28 dB) amplifier so that the maximum power available at the feedthrough is +19 dBm. Typically, we feed the microwaves to the horn directed along $+x$, although we can easily feed into either, or even both, of the horns during the detection period. This feature allows us to have control over the standing wave pattern created inside the chamber, just in case this becomes important either for diagnostics or for an unforseen systematic effect.

To check the amplitude of the microwave field at the molecules, we use the same technique described in Section 4.2.2. We pump out the population from one of the levels connected to the microwave field we are interested in, and then repopulate it with a short pulse of radiation of length τ. When all the population is transferred from one state to the other, $\Omega_{\mathrm{mw}}\tau = \pi$. Using a $\tau = 3$ μs pulse of radiation, tuned to the $(N = 0,\ F = 1) \rightarrow (N = 1,\ F = 2)$ transition, we can drive a π-pulse between these states with 0.9 dBm of power recorded at the feedthrough. The required Rabi rate to produce this π-pulse is $\Omega_{\mathrm{mw}} = 2\pi \times 0.2$ MHz. Increasing the power up to 19 dBm also increases the Rabi rate up to $\Omega_{\mathrm{mw}} = 2\pi \times 1.6$ MHz. This Rabi rate is perhaps a little low when compared to the suggestions made by the rate model. However, we will see later that it seems to not really be a problem when it comes to our ability to scatter photons.

6.2.2 Lasers

A *Toptica TA-SHG pro* supplies the probe light for the new scheme. This is an integrated laser system, consisting of a tunable infra-red diode laser, a high-power tapered amplifier and a frequency doubling stage which contains a non-linear crystal inside an external bow-tie cavity. Typically, 45 mW of 1104 nm IR is amplified to 1.8 W by the TA which is doubled into around 1 W of green light at 552 nm.

The output of the *Toptica* is locked to P(1)($F = 1^-$) transition at 542 808 GHz and is split into three lines; an unshifted line and two single-passed AOM lines. One AOM shifts the light by 192.1 MHz to the P(1)($F = 1^+$) transition. The other by 158.5 MHz, to between two hyperfine states, separated by 5.5 MHz, which we label the P(1)($F = 0, 2$) transition. These beams are them combined and overlapped on two polarising beam splitters which produces two ouputs of equal power, containing all three frequencies, as shown in Figure 4.4. These outputs are sent through two resonant EOM crystals which modulate the polarisation between left- and right-handed circular at $\sim$1 MHz before being coupled into fibres. The output of the fibres is collimated and shaped into gaussian beams with a $1/e^2$ radius of 5 mm. The beams are sent along the $+x$ direction into each of the detection regions. The size of the probe beam sets the interaction time available for the detection. For a molecule travelling at 590 m/s, this beam size limits the interaction time to 17 μs.

Typically, each probe beam contains a total of 150 mW of power distributed approximately {25%, 40%, 35%} across the three {P(1)($F = 1^+$), P(1)($F = 0, 2$), P(1)($F = 1^-$)} sidebands, equivalent to $43I_{\text{sat}}$ total. Plugging these numbers into the rate equation model, Equation (6.4), we would expect each molecule to scatter almost all the possible photons, with 98% of the maximum available population being transferred into the higher vibrational levels.

6.2.3 Collection optics

The fluorescence from the molecules is collected by a large spherical mirror and imaged onto the face of the PMT by a pair of spherical lenses, as shown by the setup in Figure 6.5(a). During the upgrades to the probe region, we decided to test a different optical configuration, shown in Figure 6.5(b). To collect a larger fraction of the solid angle emitted by the molecules, the main collection mirror (diameter 130 mm and radius of curvature $R = 75$ mm) can be set up in an elliptical configuration. The centre of the detection volume sits at one focus of the elipse ($R - f/2$), and the face of the PMT sits at the other ($R + f/2$). This focusses a large fraction of the solid angle onto the face of the PMT. Furthermore, an identical back-reflector, at position R away from the centre of the detection volume, allows for an additional fraction to be collected.

Unfortunately, we were not able to get this configuration to successfully collect the molecular signal without significant background scatter hitting the PMT. The optical setup was returned to the traditional imaging configuration, using the large spherical mirrors, shown in Figure 6.5(a). The mirrors are made from diamond turned aluminium, and have been hand-polished to a reflectivity of ∼80%. The back-reflector mirror is bolted onto the re-entrant flange containing the lenses and PMT, while the main LIF collection mirror is supported off it by aluminium rods, shown in Figure 6.5(c).

Previously, the imaging setup used a smaller collection mirror with diameter 90 mm and radius of curvature of $R = 50$ mm. There was also an additional pressure window between the vacuum and first imaging lens, which we have removed, instead making the vacuum seal directly with the first spherical lens. The collection efficiency of this setup was calculated to be around 5% [99]. Despite the mirrors being larger, the same fraction of solid angle is still collected. There may be a small gain by the fact the vacuum seal is now made by removing the pressure window, but overall it is very similar. This allows us to assume that the collection efficiency is still $\sim 5\%$. However, one thing that has changed is the detection volume. The shape of the probe beam has changed from 2 mm × 5 mm top hat beam to a 5 mm ($1/e^2$) radius gaussian beam. Figure 6.5(a) compares the previous detection volume (shown in purple), to the new volume (shown in red), which is around a factor of two wider. It is tricky to disentangle the effect of the increased detection volume from the effects of the laser cycling, increased laser intensity, and the number of molecules being produced by the source but, preliminary results show that the larger detection volume is directly increasing the number of photons we count by around a factor of four in detector A, and between 2–3 in detector B.

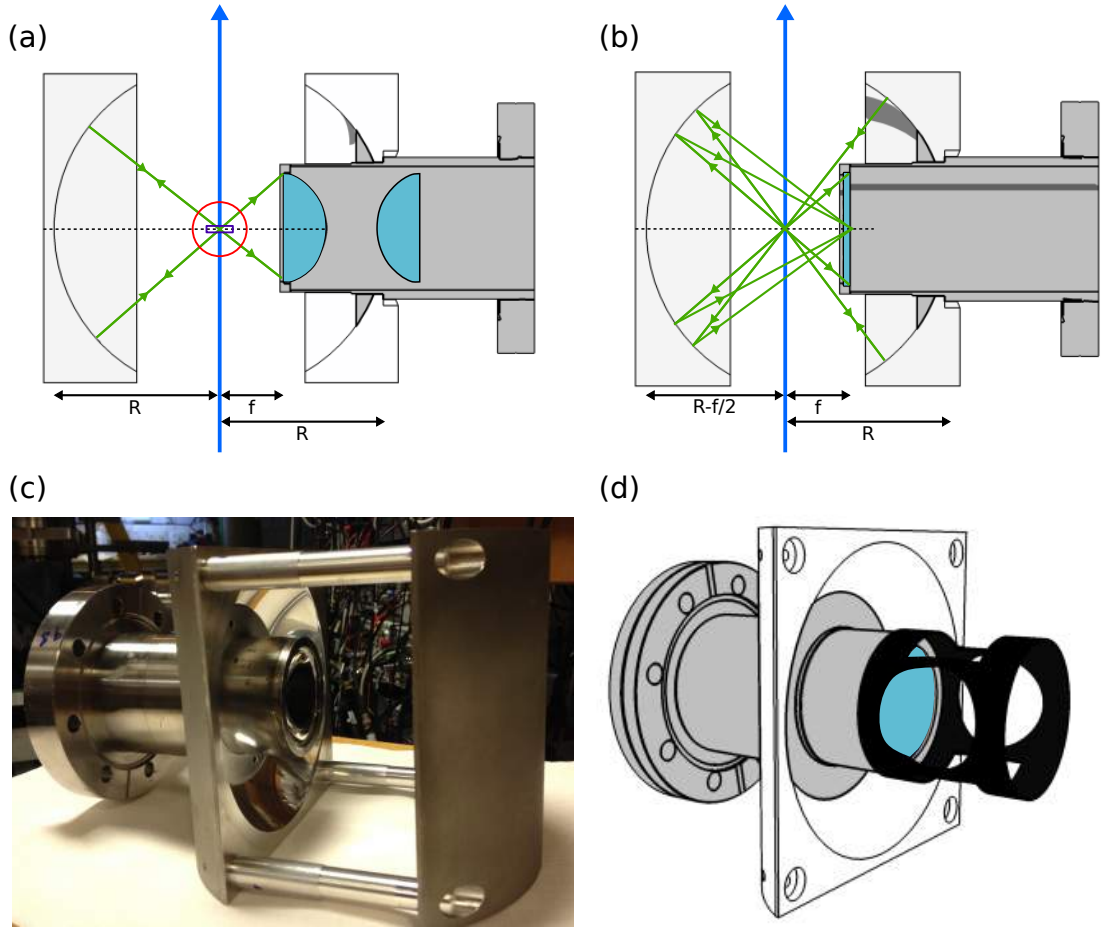


Figure 6.5: (a) Collection optics in the imaging configuration where the old detection volume is shown in purple and the new volume in red. In the new setup, the mirrors have a radius of curvature $R = 75$ mm and diameter 130 mm, the back focal length of the lens is $f = 32$ mm. (b) Collection optics in the elliptical configuration where the PMT sits directly behind the vacuum window. The molecular beam sits at one focus of the elipse $(R - f/2)$ and the face of the PMT sits at the other focus $(R+f/2)$. (c) Photo of the re-entrant flange and mirror assembly. (d) Illustration of re-entrant flange and back-reflector mirror with scatter blocking shield.

Finally, with such a high amount of power required for the probe scheme, we had to take a number of measures to reduce the background scatter into the PMT. The input and output arms of the laser ports have been extended 30 cm away from the body of the vacuum chamber and have been completely blackened inside using soot. Despite the window being AR coated, we still see some 'halo' effect as the beam passes through and so in addition, there are several 1 inch apertures inside the arms to reduce the scatter caused by the vacuum windows. The output window is also tilted by 10° to avoid back-reflection into the chamber from both of the polarisations. Inside the chamber, we tried to reduce as much of the off-axis light as possible using a blackened cylindrical shield with holes cut in it for the laser and molecular beams, shown in Figure 6.5(d). With all these measures, the scatter is below 50 photons/μs

in both regions when more than 150 mW of probe light is sent into the detection region.

6.3 Results

6.3.1 Introduction

To test the effectiveness of the new probe scheme, a combination of spectroscopy and molecular time-of-flight profiles will be used. Of particular interest are the P(1) transitions, which sit in the bandhead of the YbF spectrum. Figure 6.6 shows the positioning of the P(1) lines (and P(2) lines, for reference), in relation to the Q(0), Q(1) and Q(2) lines used in Chapter 4 to test the new pump scheme. For the results presented in this section, we will always be applying the new optical pumping which empties population from the higher rotational states and transfers it to the $F = 0$ ground state, see Chapter 4 for more details. The optical pumping changes the YbF spectrum in Figure 6.6 from the original, unpumped spectrum (shown in black) to the pumped spectrum (shown in blue).

Figure 6.7 shows the P(1) lines in more detail. Typically, we perform spectroscopy using a low power probe beam which provides good resolution of all the line features in the spectrum. Here, a 300 μW beam was used to record the unpumped spectrum (shown in black) and a pumped spectrum (shown in dark blue). However, in the new detection scheme we'll be applying much more power to the molecules (up to $\sim$150 mW), which broadens these features together, making them harder to distinguish. A spectrum of the pumped P(1) lines was taken using 15 mW probe beam and is shown by the light blue line in Figure 6.7 for comparison. Throughout this section we'll be looking at how this broadened spectrum responds to the microwave and laser fields we apply to the molecules.

Figure 6.7 also shows how underlying spectral lines will contribute to the overall signal we see in the detector. It is clear that even after pumping there is still a significant amount of background signal which, despite not being caused by ^{174}YbF, will still contribute to the number of photons scattered by the molecular beam. The effect this has on the measurement sensitivity will be presented in Chapter 7.

Microwave transitions

The new probe scheme requires a different microwave frequency for each detection region. One frequency selects the $F = 0$ population and connects it to the P(1) cycling lasers acting on $N = 1$, the other frequency selects the $F = 1$ population. In Section 6.1.1 I showed that the new probe scheme uses the $(N = 0,\ F = 1) \leftrightarrow (N = 1,\ F = 2)$ and $(N = 0,\ F = 0) \leftrightarrow (N = 1,\ F = 1^-)$ electric dipole transitions to connect these states together. However, there are six allowed transitions between $N = 0$ and $N = 1$, which are shown in Figure 6.8. Four of the six frequencies have a similar transition strength (shown in grey, red and dark blue), while the remaining two have a much weaker transition strength (shown in pink and light blue). For reference, the Clebsch-Gordon coefficients of these transitions are shown in Table 6.1, which have been calculated using the method presented in Appendix B of [89].

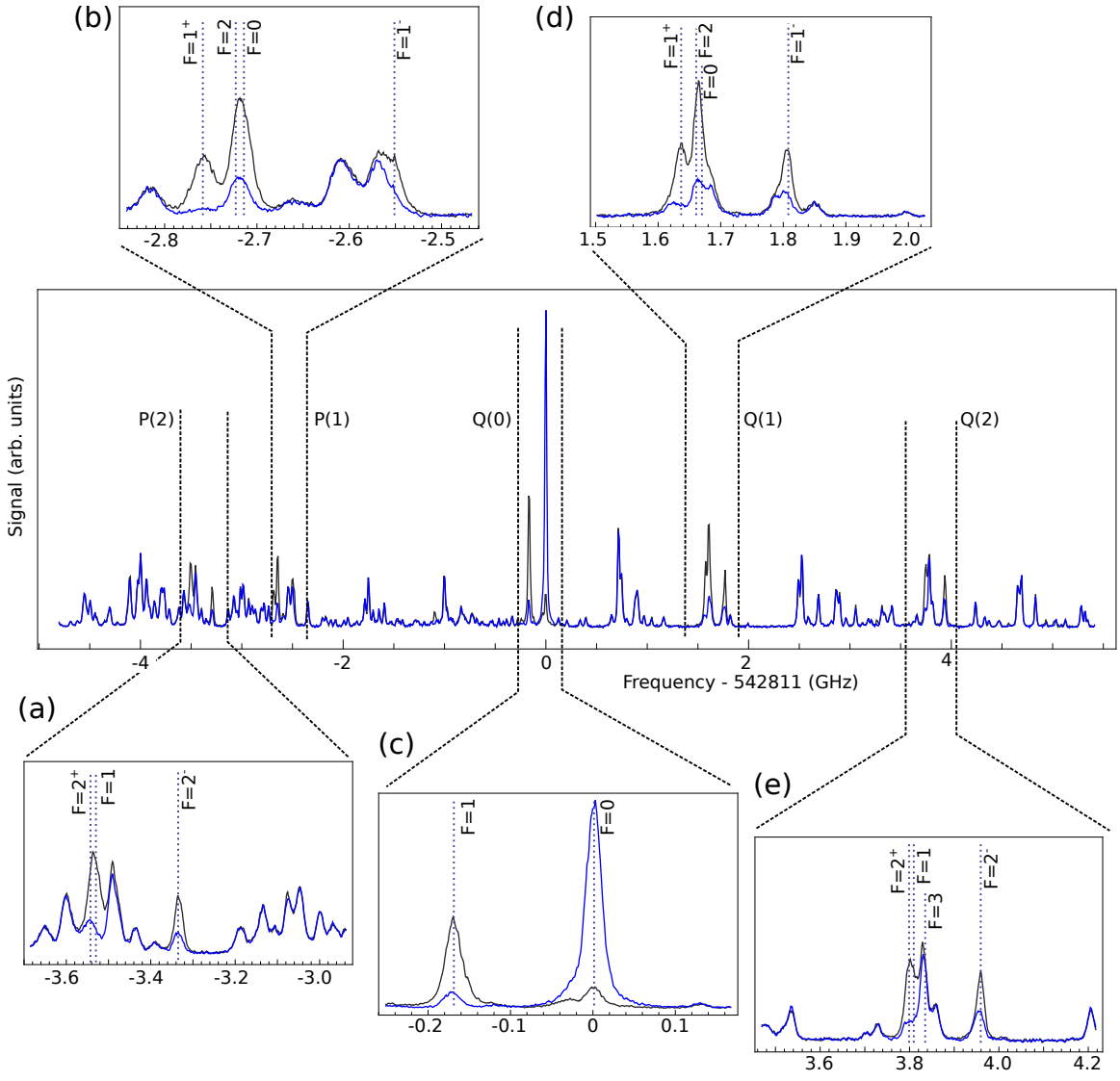


Figure 6.6: YbF spectrum from 542 806 GHz to 542 816 GHz. Some interesting ^{174}YbF lines are shown in (a) P(2), (b) P(1), (c) Q(0), (d) Q(1) and (e) Q(2) which highlight the positions of each hyperfine component. Black: Unpumped spectrum. Blue: Spectrum after applying the new pump scheme.

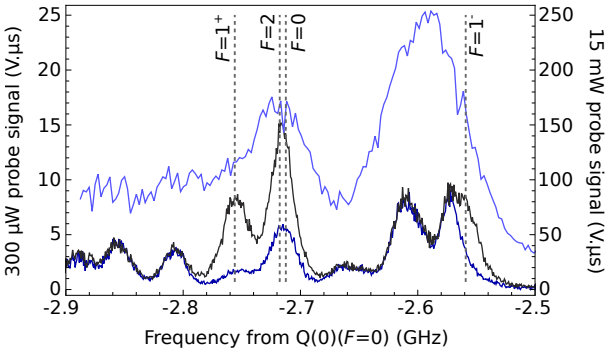


Figure 6.7: Black: P(1) spectrum recorded using 300 μW of probe light. Dark blue: P(1) spectrum after pumping, recorded using 300 μW of probe light. Light blue: Broadened P(1) spectrum after pumping, recorded using 15 mW of probe light.

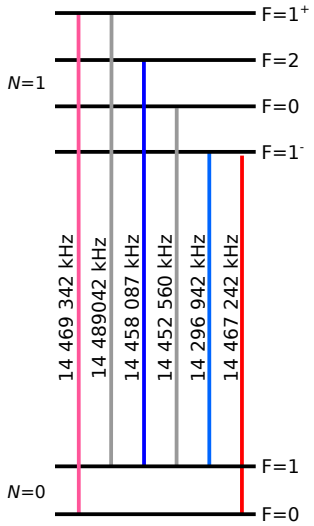


Figure 6.8: Relevant microwave transitions and their frequencies.

		X $^2\Sigma^+(v=0,\ N=0)(F,\ M_F)$			
		(0, 0)	(1, -1)	(1, 0)	(1, +1)
X $^2\Sigma^+(v=0,\ N=1)(F,\ M_F)$	$(1^+, -1)$	−0.029	0.408	−0.408	0
	$(1^+, 0)$	−0.029	0.408	0	−0.408
	$(1^+, +1)$	−0.029	0	0.408	−0.408
	$(2, -2)$	0	0.577	0	0
	$(2, -1)$	0	0.408	0.408	0
	$(2, 0)$	0	0.236	0.471	0.236
	$(2, +1)$	0	0	0.408	0.408
	$(2, +2)$	0	0	0	0.577
	$(0, 0)$	0	0.333	0.333	0.333
	$(1^-, -1)$	0.577	0.020	−0.020	0
	$(1^-, 0)$	0.577	0.020	0	−0.020
	$(1^-, -1)$	0.577	0	0.020	−0.020

Table 6.1: Table of microwave Clebsch-Gordon coefficients, calculated from [89].

The following sections compare the efficiency of the probe scheme when using a strong or weak microwave transition to select the population from either the $F = 0$ or $F = 1$ state, to explain how we decided on which of the microwave transitions to use. The transitions we compare are; $(N = 0,\ F = 0) \leftrightarrow (N = 1,\ F = 1^-)$, $(N = 0,\ F = 0) \leftrightarrow (N = 1,\ F = 1^+)$, $(N = 0,\ F = 1) \leftrightarrow (N = 1,\ F = 2)$ and $(N = 0,\ F = 1) \leftrightarrow (N = 1,\ F = 1^-)$, shown by the coloured lines in Figure 6.8. For brevity, these will be labelled $\{F = 0 \leftrightarrow 1^-,\ F = 0 \leftrightarrow 1^+,\ F = 1 \leftrightarrow 2,\ F = 1 \leftrightarrow 1^-\}$ in the following discussions. The next section details the preliminary experiments we perform to test the microwave fields are reaching the detection volume, and addressing the correct transitions.

6.3.2 Spectroscopy: Single laser sideband

To confirm microwaves are reaching the detection region, we perform spectroscopy across the P(1) lines both with and without the presence of a microwave field, equivalent to turning the detection on and off. Figure 6.9 shows a schematic of the steps in the experiment. In the first stage, the population from higher lying levels is pumped into the X $^2\Sigma^+(v = 0,\ N = 0,\ F = 0)$ state, shown in (a). The molecules then enter the interaction region of the experiment, where a small electric field is applied, $|E_z| = 3.3$ kV/cm, to define the z-axis of the experiment. A $\pi/2$ pulse of x-polarised rf is applied, which transfers half the population from $|0,0\rangle$ to $(|1,+1\rangle - |1,-1\rangle)/\sqrt{2}$, shown in (b). This mimics the population difference we would expect to see at the end of the interaction time during normal EDM data. Finally, the molecules enter detection region A, where a single 15 mW laser sideband is scanned across the P(1) transitions in the prescence of a microwave field, shown in (c). For all this data, 19 dBm of power was recorded at the feedthrough. When the microwave and laser fields are on resonance with the same hyperfine state in $N = 1$, the fluorescence signal will increase as the population from the ground state can be excited up to A $^2\Pi_{1/2}(e)$, scattering additional photons.

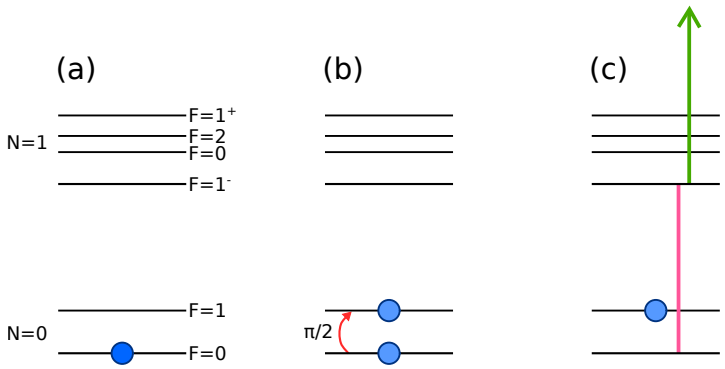


Figure 6.9: Schematic of single frequency laser spectroscopy experiment. (a) All the population in the higher rotational states is pumped into X $^2\Sigma^+(v = 0,\ N = 0,\ F = 0)$. (b) A $\pi/2$ pulse of x-polarised rf transfers half the population into the $(|1,+1\rangle + |1,-1\rangle)/\sqrt{2}$ state. (c) The molecules enter the detection region where they experience a single frequency laser sideband that scans across the P(1) transitions, and a microwave field that is switched on and off. When the two fields are in resonance with the same state, the fluorescence signal will increase.

Figure 6.10 shows the resulting spectra from each of the microwave transitions we are interested in testing, see Figure 6.8 as reference. Figure 6.10 (a) shows the change in the spectrum caused by the $F = 1 \leftrightarrow 2$ field. When the single laser frequency hits the $F = 2$ hyperfine state, the fluorescence signal increases as the population from $(N = 0,\ F = 1)$ is driven to the excited state. Similar results are seen in Figure 6.10 (b) for the $F = 1 \leftrightarrow 1^-$ transition, Figure 6.10 (c) for the $F = 0 \leftrightarrow 1^-$ transition and Figure 6.10 (d) for the $F = 0 \leftrightarrow 1^+$ transition. These spectra show that the microwave fields are reaching the detection volume and are addressing each of the transitions correctly.

In Figure 6.10 (c), there is also evidence of an increase in the laser-induced fluorescence

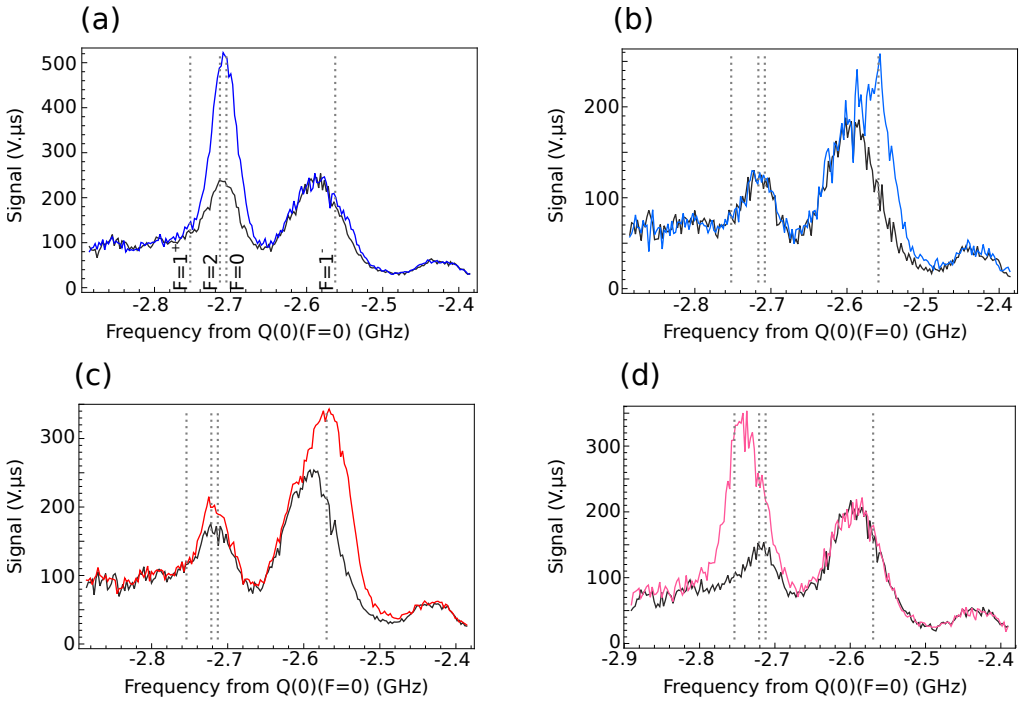


Figure 6.10: Results of single frequency spectroscopy. Here, a single laser frequency scans across the P(1) lines in the prescence of a fixed microwave frequency field which drives population between one hyperfine state in $N = 0$ and one hyperfine state in $N = 1$. The fluorescence signal is increased when the laser field is on resonance with the level in $N = 1$. (a) $F = 1 \leftrightarrow 2$, (b) $F = 1 \leftrightarrow 1^-$, (c) $F = 0 \leftrightarrow 1^-$ and (d) $F = 0 \leftrightarrow 1^+$. The coloured/grey lines show the spectrum with/without a microwave field.

around the $F = 2$ peak. To explain this, we notice that the $F = 0 \leftrightarrow 1^-$ and $F = 1 \leftrightarrow 2$ transitions are separated by ~ 9 MHz. The high power probe fields are broadening these two features together, allowing a small portion of the ($N = 0$, $F = 1$) population to be off-resonantly pumped by the $F = 0 \leftrightarrow 1^-$ microwaves[2]. This effect could become a concern when we move to the full detection scheme, as any population from the 'wrong' state will reduce the contrast of our measurement. The following experiment investigates how much of an effect this off-resonant pumping has on the ground state population.

6.3.3 Detecting in region A

We can now move on to investigate the details of the full probe scheme acting in detection region A only. There are two aspects of the detection to consider. Firstly, how the probe fields effect the population of each of the hyperfine states in $N = 0$. Secondly, how the change in population is converted to a number of detected photons.

To perform these tests, we extend upon the method presented in the previous section.

[2]There is also evidence of off-resonant pumping occuring in Figure 6.10 (a) for the $F = 1 \leftrightarrow 2$ transition, although it is not as obvious.

A schematic of the experiment is shown in Figure 6.11. As before, we pump the population into the ground X $^2\Sigma^+(v = 0,\ N = 0,\ F = 0)$ state using the new pump scheme, shown in (a). The population is then divided equally between the $|0,0\rangle$ and $(|1,+1\rangle - |1,-1\rangle)/\sqrt{2}$ levels by a short $\pi/2$ pulse of rf, imitating the result of normal EDM sequence, shown in (b). The molecules enter the first detection region (A) where they travel through the optical and microwave fields. In this case, the microwave frequency is still fixed to one of the four transitions, and the three optical sidebands {P(1)($F = 1^+$), P(1)($F = 0, 2$) and P(1)($F = 1^-$)} are all scanning simultaneously across the P(1) lines, shown in (c). In this region, we apply a total of 130 mW of laser power, which is balanced in the proportions {25%, 40%, 35%} across the three sidebands. The maximum available microwave power is applied to the molecules, which we record as 19 dBm at the feedthrough. Finally, the molecules enter the second detection region (B), where we apply a lower power (400 μW) probe beam tuned to either the Q(0)($F = 0$) or Q(0)($F = 1$) transition, shown in (d). This allows us to look at the leftover population in these levels after the detection.

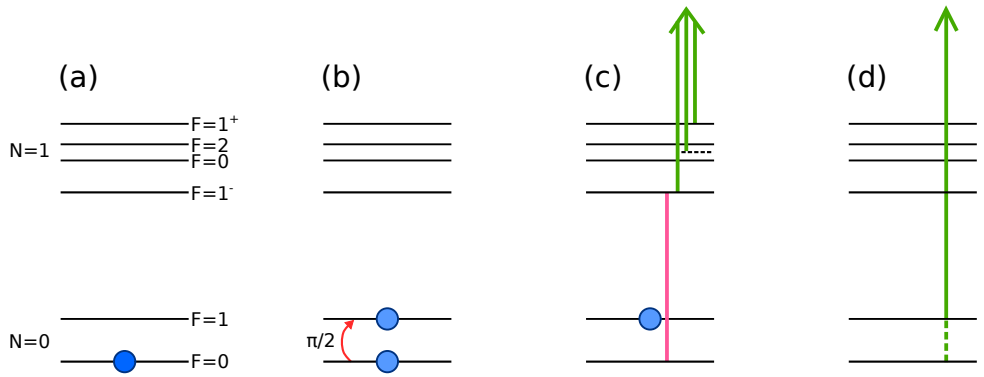


Figure 6.11: Experiment used to test the new detection scheme. (a) Firstly we prepare the population in the ground state using the new pump scheme. (b) A single $\pi/2$ pulse of rf transfers half the population to $(|1,+1\rangle - |1,-1\rangle)/\sqrt{2}$. (c) The new probe scheme is applied in detector A. (d) Look for leftover population in the ground state using the Q(0) transitions in detector B.

As the P(1) lasers scan across the transition, we expect to see a single point in the spectrum where they all come onto resonance. The signal should increase due to the addition of the microwaves, as in the single sideband spectroscopy, but will be enhanced even further by the cycling effects. Ideally, in the second detection region, we will see the population disappear entirely from the selected state and leave the other hyperfine level unchanged. Since we will only ever be working on resonance, i.e. the condition for cycling is fulfilled, much of the spectrum is unimportant. Instead, we look specifically at how the time-of-flight (TOF) profile of the molecular beam changes on resonance both with and without the microwave field present.

Figure 6.12 presents the data from this experiment for each of the microwave frequencies we are interested in; (a)–(d) $F = 1 \leftrightarrow 2$, (e)–(h) $F = 1 \leftrightarrow 1^-$, (i)–(l) $F = 0 \leftrightarrow 1^-$ and (m)–(p) $F = 0 \leftrightarrow 1^+$. Each set of four images includes, from left to right: (l) a spectrum

of the P(1) lines, (II) the TOF profile in detection region A due to the new probe scheme, (III) the TOF profile in detection region B recorded using Q(0)($F = 0$) light and (IV) using Q(0)($F = 1$) light. In each figure, the black spectrum (or TOF) shows the effect of applying the cycling lasers, with no microwaves linking the $N = 0$ and $N = 1$ states, while the coloured spectrum (or TOF) shows the signal change caused by the addition of the microwave field, effectively turning on the detection. The grey dashed lines on the spectra, Figures 6.12(a), (e), (i) and (m), indicate the resonance position we would lock to for normal running. The TOFs presented in the remaining figures are all recorded at this point.

Before beginning the in-depth discussion of this data, there are a few things to point out. Firstly, the population has been equally divided between the $F = 0$ and $F = 1$ hyperfine levels, even though the Q(0)($F = 1$) TOF appears much larger. This is caused by the small cycling effect of this transition, which scatters around twice as many photons as the Q(0)($F = 0$) transition, before going dark to the probe light. This is directly reflected in the height of the TOF. Secondly, the comparison between TOFs from detector A and TOFs from detector B should be treated with caution due to the vastly different probe beam intensities (150 mW compared to 400 μW). It is certainly likely that off-axis molecules are detected in region A but not in region B. Instead, this data should indicate to us which microwave transition scatters the most photons, and also point to any problems across the ground state hyperfine components.

Firstly, let us compare how we can detect the population in the ($N = 0,\ F = 1$) level with Figures 6.12(a)–(h). The first immediate difference we see is that the use of the strong microwave transition ($F = 1 \leftrightarrow 2$, shown in dark blue) yields many more photons than use of the weak transition ($F = 1 \leftrightarrow 1^-$, shown in light blue). To measure the number of photons produced in each case, we select the central 150 μs slice of the TOF in detector A, and the central 173 μs slice of the TOF in detector B, both of which correspond to molecules with speeds in the range 590 ± 18 m/s. We find that the strong microwave transition produces an additional ∼300 000 photons above the background, while the weak microwave transition only ∼150 000 photons above the background. The spectra corresponding to this gating of the TOF profile, for these two microwave transitions, are shown in Figure 6.12(a) and (e). This difference is also reflected in the Q(0)($F = 1$) TOFs in Figure 6.12(d) and (h); around 83% of the population has been removed from $F = 1$ using the strong transitions (d), and slightly less 77% by the weak transition (h). Comparing the two transitions, the change in population depletion is far less than the change in the number of scattered photons. This is caused by the vastly different probe beam intensities (400 μW vs. 130 mW), making it hard to compare these numbers directly. However, overall the strong microwave transition performs better in each case. In Figure 6.12 (c) we can see some evidence of off-resonant pumping, with a small fraction of the population removed from $F = 0$ by the strong microwave transition. However, at $< 10\%$, any effect this has on the contrast is cancelled out by the significant signal increase[3].

[3]A more significant problem regarding the contrast of the measurement is the background signal which is also enhanced on resonance due to left over population in $N = 1$ after the pumping stage. This is discussed

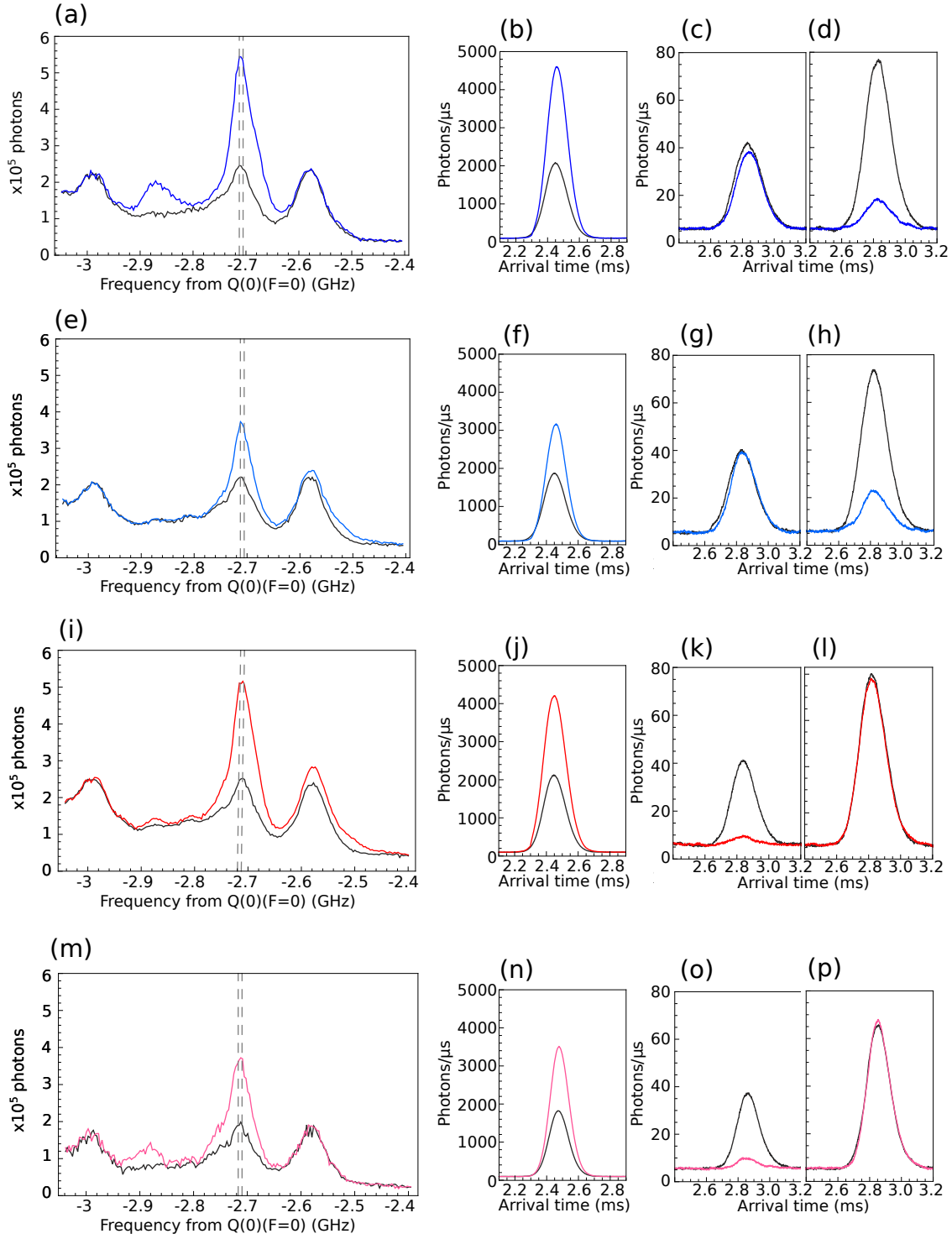


Figure 6.12: Detecting with the full probe scheme in region A, looking for leftover population in region B. Here, we investigate each of the microwave frequencies; (a)–(d) $F = 1 \leftrightarrow 2$, (e)–(h) $F = 1 \leftrightarrow 1^-$, (i)–(l) $F = 0 \leftrightarrow 1^-$, and (m)–(p) $F = 0 \leftrightarrow 1^+$. Each set of four images contain (I) a spectrum of the P(1) lines, (II) the TOF profile in detection region A, (III) the TOF profile in detection region B using Q(0)($F = 0$) light and (IV) using Q(0)(F=1) light. Black spectrum (or TOF): no microwaves. Coloured spectrum (or TOF): with microwaves.

Similarly, we can compare the microwave fields that select the $F = 0$ population, Figures 6.12(i)–(p). This data shows a very similar trend, with the strong transition ($F = 0 \leftrightarrow 1^-$, shown in red) producing more photons than the weak transition ($F = 0 \leftrightarrow 1^+$, shown in pink). On resonance, the central velocity class of molecules scatters around $\sim$ 270 000 photons, and $\sim$190 000 photons respectively, above the background. This is also reflected in the Q(0)($F = 0$) TOFs, where 91% has been removed by the strong transition and 87% by the weak transition. In both cases, there has been very little effect on the $F = 1$ population.

Overall, these results show that using the new detection scheme, we are removing almost all the population from the $F = 0$ state, and a significant fraction from the $F = 1$ state. In addition, the detection has negligible effect on the state we are not trying to probe, fulfilling the criterion of state-selectivity. The data also shows that by using the stronger microwave transitions, we can scatter many more photons. In the following section, we move on to look at the detection in both regions, using the scheme presented in Section 6.1.1, to place a final number on the enhancement in photon number we achieve with this scheme.

6.3.4 Detecting in both regions

This section presents the first results using the full, two detector detection scheme. In this case, we will only consider the detection that uses the $F = 1 \leftrightarrow 2$ microwave field in region A, and $F = 0 \leftrightarrow 1^-$ microwave field in region B, as shown in Section 6.1.1.

For this final discussion, we would like to place a number on the overall improvement the new probe scheme brings to the measurement, when compared to the original detection method. In an attempt to compare the two schemes, we record a series of interferometer curves in each region using the two methods, to try and isolate the improvement due to the detection scheme.

A schematic of the experiment used to record this data is shown in Figure 6.13. Firstly, the molecules are pumped from higher rotational levels into the X $^2\Sigma^+(v = 0,\ N = 0,\ F = 0)$ ground state by the new pump scheme, as shown in (a). The molecules continue through the machine, where they enter the interaction region of the experiment. In this region, a small magnetic field B_z is applied, in addition to an electric field $|E_z| = 3.3$ kV/cm, which defines the z-axis of the system. Once the molecules are inside this region, a 5 μs π-pulse of x-polarised rf is applied. This transfers all the population from $|0, 0\rangle$ state into the $(|1, +1\rangle - |1, -1\rangle)/\sqrt{2}$ superposition, as shown in (b). The molecules continue to propagate through the interaction region, where the states collect a phase proportional to the magnetic and electric fields (c); $\left(e^{i(\phi_B+\phi_E)}|1, +1\rangle - e^{-i(\phi_B+\phi_E)}|1, -1\rangle\right)/\sqrt{2}$. After 1 ms of interaction time, a second 5 μs π-pulse of rf is applied to recombine the states into two quadratures; $\cos(\phi_B + \phi_E)|0, 0\rangle + \sin(\phi_B + \phi_E)(|1, +1\rangle + |1, -1\rangle)/\sqrt{2}$, as shown in (d). The molecules leave the interaction region and enter detection region A, where the $F = 1$ component is probed using the new detection scheme, with the microwave field tuned to the $F = 1 \leftrightarrow 2$ transition, (e). Finally, the molecules continue into the detection region B, where the $F = 0$

in more detail in the final chapter of this thesis.

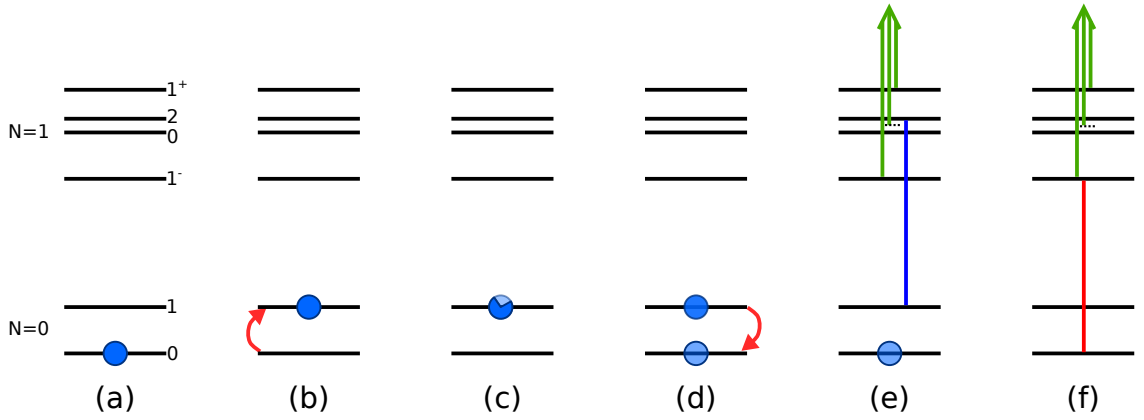


Figure 6.13: Schematic of the experiment used to test the new detection scheme. (a) Molecules are prepared in the ground state using the new pump scheme. (b) Molecules enter the interaction region where an electric and magnetic field is applied to the molecules. A π-pulse of rf transfers the $|0,0\rangle$ into a superposition of $|1,\pm1\rangle$. (c) The $|1,\pm1\rangle$ states evolve in the magnetic field, collecting a phase proportional to the magnetic field. (d) A second pulse of rf recombines the population, to create a distribution across the $F=0$ and $F=1$ levels. (e) Probe the $F=1$ level in region A, and (f) $F=0$ in region B.

component is probed using the $F=0 \leftrightarrow 1^-$ transition, (f).

This experiment should sound very familiar to the reader, as it is identical to a single shot of the EDM experiment. However, instead of stepping between fixed values and directions of the magnetic and electric field to measure the EDM interaction, we scan out the interference curve by ramping the applied magnetic field by a few nT. In this case, the EDM phase is completely negligible and we expect to record signals in each detector of,

$$S^A = S_b^A + S_0^A \sin^2(\phi_B) \tag{6.6}$$

$$S^B = S_b^B + S_0^B \cos^2(\phi_B) \tag{6.7}$$

where S_b is the background signal caused by underlying molecules, any leftover population in $N=1$ after pumping, and any laser scatter, and S_0 is directly proportional to the population in the selected state.

To make the comparison to the previous detection scheme, we simply replace the laser and microwave fields with a single, low power (2 mW) Q(0)($F=0$) laser beam, which probes either in region A or in region B. Unlike the previous probe setup, the beam is now shaped to the same 5 mm $1/e^2$ radius gaussian beam to try and remove the effect of the increased detection volume. The signal enhancement due to the cycling detection is then simply the ratio between the amplitudes of the two interference curves.

Figure 6.14 shows the results of this experiment. These tests were performed without the middle and outer magnetic shields installed onto the machine. This means that across the interaction region, there is a significant magnetic field gradient which washes out the contrast

of the interference curve and reduces the signal-to-noise of the data. To try and counteract this, a small analysis gate of 20 μs is used (which is scaled to 22.8 μs for the second detector so that the same velocity class of molecules is always selected).

Figure 6.14(a) shows the interference curves recorded using the new detection scheme. Both quadratures of the interferometer have been detected in a single shot, with the blue curve showing the $F = 1$ population recorded in detector A, and the red curve showing the $F = 0$ population recorded in detector B. For comparison, Figure 6.14(b) and (c) shows the $F = 0$ population recorded using the old detection method in region A and B respectively.

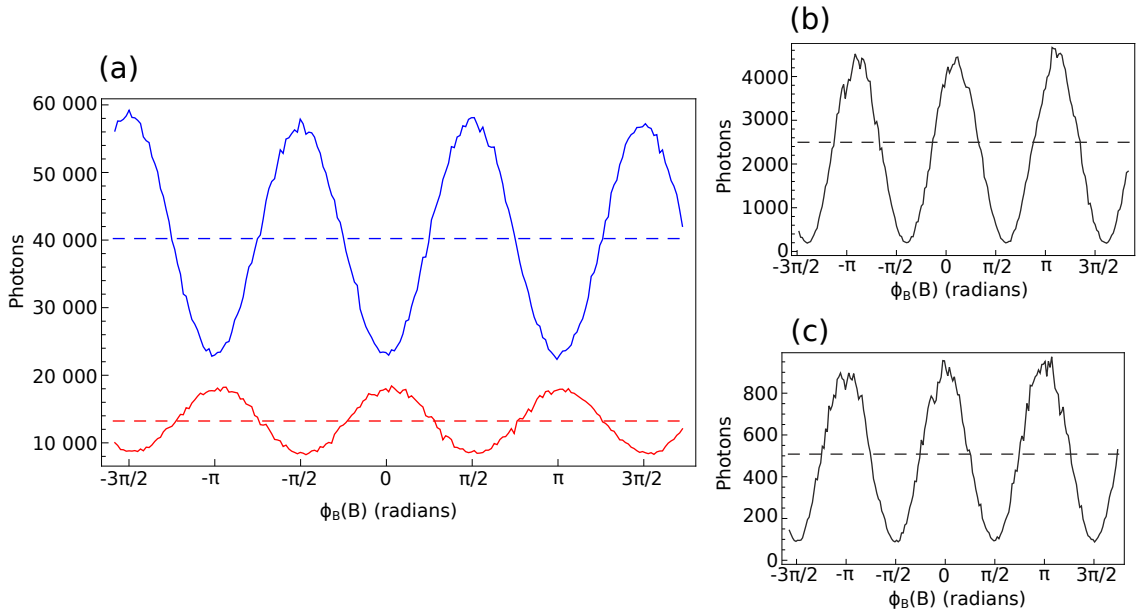


Figure 6.14: (a) Interference curve of the $F = 1$ population recorded in detector A (blue) and $F = 0$ population recorded in detector B (red) using the new probe scheme. (b) $F = 0$ interference curve using the old detection scheme, recorded in detector A and (c) in detector B.

The signal increase caused by the new detection scheme is the ratio of the amplitudes of these curves recorded in each detection region e.g. $S_0^A(\text{new})/S_0^A(\text{old})$, with the caveat that the source intensity has not significantly changed between these data sets. In detection region A, the amplitude of the interference curve has increased by a factor of 8.2 and in region B by a factor of 11.5.

6.4 Conclusions

This first set of data shows promising results for the new detection scheme. If we assume that this is at least a repeatable result, and is achievable across the whole moelcular packet once the magnetic shields are installed, then the number of photons scattered per molecule has increased dramatically. In the previous scheme, a single molecule would scatter 1.2 photons on average before going dark to the probe light. This has now increased to 13.8 photons

per molecule in the $F = 0$ detector, very close to the maximum number we would expect to achieve. In addition, the $F = 1$ population can be detected, which scatters around 9.8 photons per molecule. If these results can be extended, we can expect to achieve an increase in sensitivity of

$$\sqrt{\frac{13.8 + 9.8}{1.2}} = 4.4 \tag{6.8}$$

with this new scheme.

These interference curves can also be used to work out the contrast of the new measurement technique. We will be returning to this idea in the following Chapter where we estimate the final sensitivity of the upgraded experiment.

6.5 Alternative scheme

6.5.1 Introduction

With all these upgrades, there has been a big jump in the amount of equipment required for the day-to-day running of the experiment. In particular, the number of lasers now needed to take data has increased from one to three. There is always a risk when adding more lasers to a setup, that the amount of effort and experimental down-time will also increase. Although, (so far) we seem to be running fairly consistently and reliably, despite using a dye laser in the pump scheme, there is always a risk that one of these sytems will stop working to specification, causing us to waste very valuable time. Originally, we were reluctant to include this third laser into the setup and the alternative detection scheme described in this section reflects this.

Instead of cycling population on the P(1) transition, we choose to recycle the pump lasers up to the probe region (along with an additional sideband) to cycle population between the $N = 0$ and $N = 2$ levels. The sidebands Q(0)($F = 0$), Q(0)($F = 1$), ${}^{O}P_{12}(2)(F = 2^{-})$ and ${}^{O}P_{12}(2)(F = 1, 2^{+})$, labelled (b)–(e) in Figure 6.15, cycle population inside $v = 0$ until it is lost to higher vibrational states.

However, these laser sidebands would completely destroy the measurement contrast by detecting both hyperfine components at once. So to achieve the state selectivity, we first apply a microwave π-pulse in region (6a), using 14 467 242 kHz microwave field. This transfers population from $(N = 0,\ F = 0) \rightarrow (N = 1,\ F = 1^{+})$ where it is protected from the cycling lasers that are applied in region (6b). The shelved population is then brought back to $(N = 0,\ F = 0)$ with a second microwave π-pulse in (6c) to detect the second quadrature with the same laser sidebands in (6d).

6.5.2 The lasers

Cycling the population amongst the $N = 0$ and $N = 2$ levels into X ${}^{2}\Sigma^{+}(v > 0)$ is relatively straightforward. While developing the pump scheme we have already performed an almost identical experiment. In fact, Section 4.3.2, shows that we can pump out all the relevant

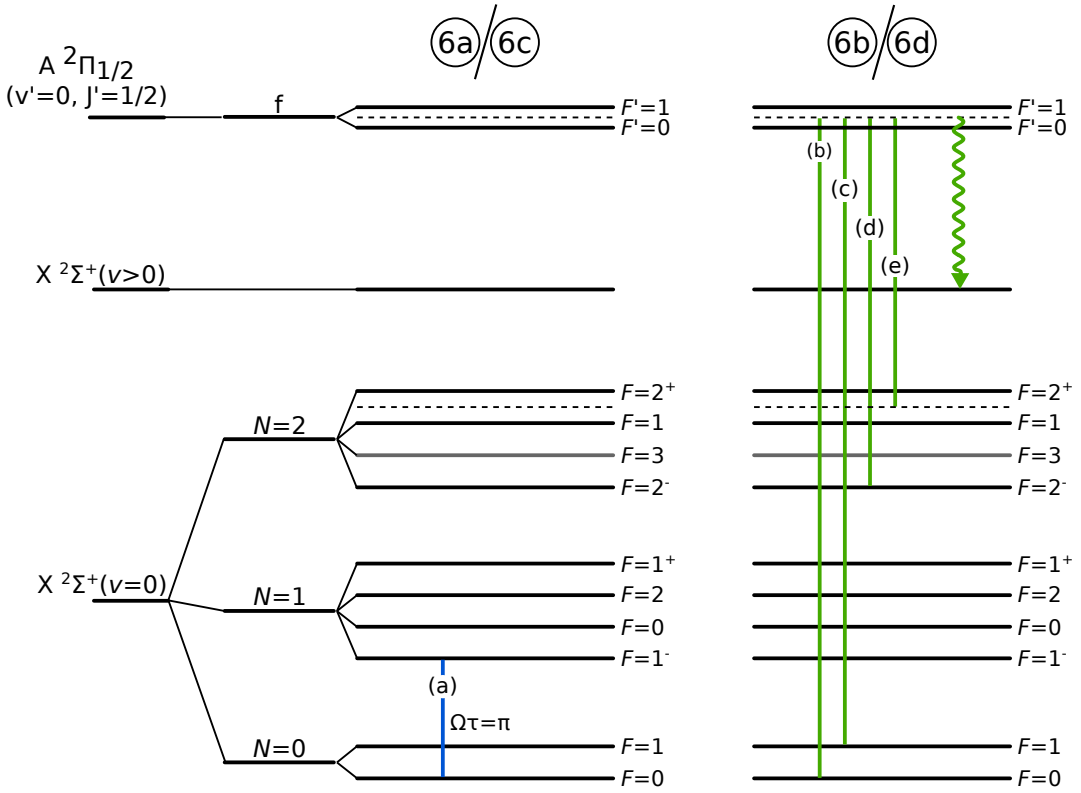


Figure 6.15: In the first region, microwaves shelve the $(N = 0,\ F = 0)$ hyperfine component into $(N = 1,\ F = 1^-)$ using a microwave $\pi-$pulse, labelled transition (a). The molecules continue to fly through to the laser cycling region, where the population in $(N = 0,\ F = 1)$ is counted using laser sidebands on $\mathrm{Q}(0)(F = 0)$, $\mathrm{Q}(0)(F = 1)$, $^{\mathrm{O}}\mathrm{P}_{12}(2)(F = 2^-)$ and $^{\mathrm{O}}\mathrm{P}_{12}(2)(F = 1, 2^+)$, labelled (b)–(e). The next stage is to bring the shelved population back from $N = 1$ using an identical microwave $\pi-$pulse and count the population in the $F = 0$ state with the same lasers in the final region.

levels (except for the $(N = 0,\ F = 0)$ ground state) with less than 15% of the population remaining in these states. Adding the final sideband on $\mathrm{Q}(0)(F = 0)$ should have little effect on the drive rates, and so we would easily achieve $> 85\%$ of the possible photons. In this case, each molecule would scatter around 12 photons on average.

6.5.3 The microwaves

Performing a robust and efficient transfer of population from $N = 0$ to $N = 1$, without blocking a significant portion of the molecular signal, proved to be much more challenging then we originally expected. We spent many months trying to to find an appropriate solution to the problem, with success in some areas, but never fullfilling all the requirements. In this section I briefly review the progress we made in this area, as a testament to the amount of time and effort we spent on the project.

The probability of finding a molecule in the upper state after interacting for time τ with

the microwave field which has Rabi frequency Ω and detuning δ is [16],

$$\frac{\Omega^2}{\Omega^2+\delta^2}\sin^2\left(\frac{\sqrt{\Omega^2+\delta^2}}{2}\tau\right). \tag{6.9}$$

The probability is unity when the microwave field is on resonance ($\delta = 0$) and when $\Omega\tau = \pi$. These conditions cannot be achieved simaltaneously for all molecules due to the spread in velocities across the molecular packet. In addition, the microwave field may be inhomogeneous, leading to different molecules experiencing different values of Ω. To find the overall performance of the system, we need to consider both these effects, as well as the fraction of molecules that execute this π-pulse.

The spread of velocities within the molecular packet leads to the faster molecules spending less time in the microwave field, and so will receive slightly less than a π-pulse, while slower molecules will receive slightly more than a π-pulse. Typically, we sample molecules which have velocities between around 560 m/s up to 620 m/s. Despite the product $\Omega\tau/2$ varying by $\pm 5\%$ about $\pi/2$, the average π-pulse efficiency across this velocity distribution is $> 99\%$ due to quadratic behaviour of the $\sin^2$ about $\pi/2$. So, in this case, we can negelct the effects caused by the velocity distribution of the molecular packet.

In this project, the limiting factor for performing a microwave π-pulse was ultimately caused by the inhomogeneity of the microwave electric field. Typically, a waveguide or transmission line that supports a microwave field will have one dimension of the order $\lambda/2$. This parameter also defines the positions of the nodes and anti-nodes of the field if a standing wave is created in the line. For a microwave field at 14 GHz, $\lambda/2 = 1$ cm. When we compare this dimension to the size of the molecular packet in the detection region, we begin to see how electric field uniformity was such a big problem for this system. Figure 6.16 illustrates this point.

The transverse extent of the molecular beam is defined by the skimmer, which sets the expansion to 2 mm for every 94 mm the molecules have propagated along the beamline, unless otherwise restricted by apertures. In the z-axis the beam is unrestricted and is already larger than $3(\lambda/2)$ when it reaches the first microwave region. In the x-axis, the beam is apertured by the electric field plate separation, making it only slightly wider than $\lambda/2$ throughout the detection region. This means, that for an efficient π-pulse to occur, the electric field must contain almost no standing wave component as the field propagates along x. In addition, any standard, 'off-the-shelf' microwave component may aperture the molecules in the z-axis, which could effect the overall performance of the setup.

Figure 6.17 shows a few of the hardware design iterations we attempted during this project. Using a waveguide-based design, shown in Figure 6.17(a), we were able to perform an efficient π-pulse but found that it significantly restricted the molecular signal. With this, the design evolved towards a transmission line which adiabatically flared out to surround the entire molecular beam, shown in Figure 6.17(b)–(c). For this design to perform an efficient population transfer, it relies strongly on our ability to terminate the line correctly.

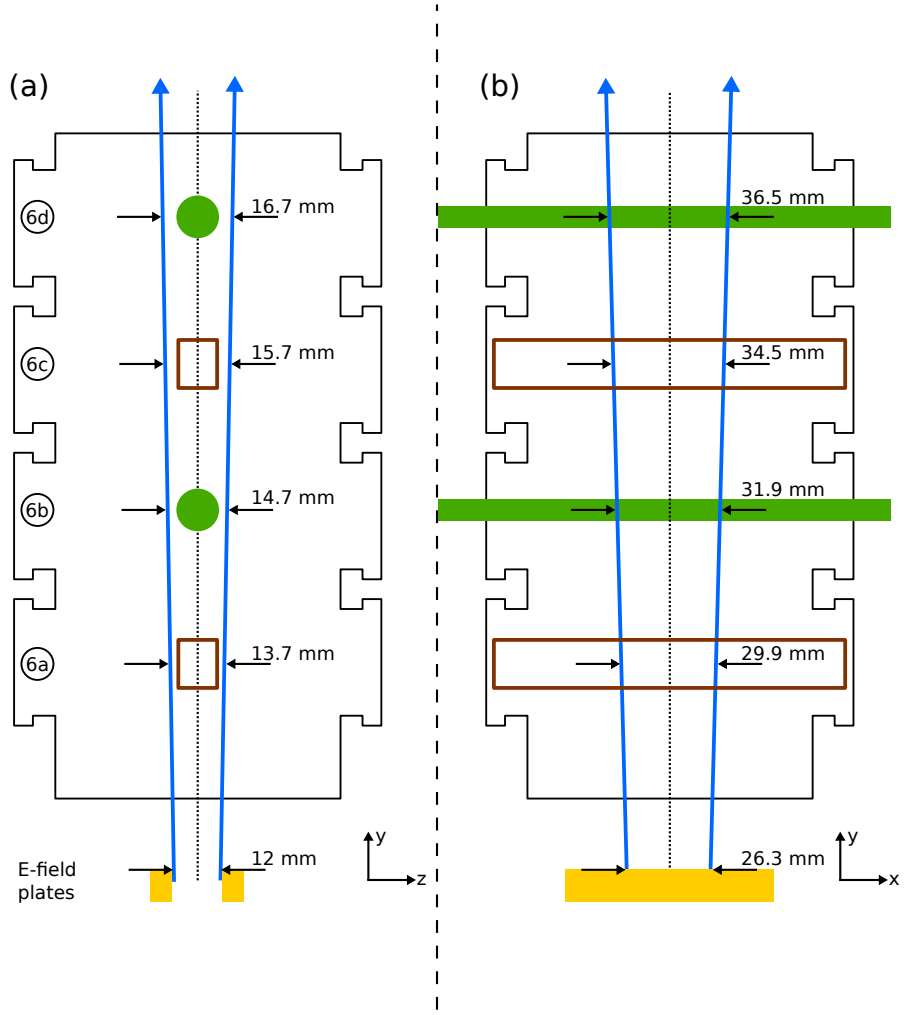


Figure 6.16: Illustration of the transverse extent of the molecular beam in the detection region compared to typical dimensions of waveguide/transmission line that supports the 14 GHz microwave field. Copper regions represent the microwave structure and green the laser cycling regions.

Unfortunately, we were not able to achieve this and the design suffered from significant standing waves, creating poor electric field uniformity. The results of each of these designs are discussed briefly in the sections below.

Waveguide design

In this design, the microwave field is supported inside a standard microwave waveguide (WR75, dimensions 9.5×19.1 mm), which supports frequencies from 10–15 GHz. To expose the molecules to the electric field, an aperture is cut across the short side of the waveguide (aperture dimensions 9×30 mm), which allows them to fly through the field, shown in Figure 6.17(d). To keep the electric field relatively well confined inside the waveguide, four 1 mm wide strips are left behind. These carry the surface currents that support the electric field across the gap. A commercial terminator ensures that most of the electric field is a homo-

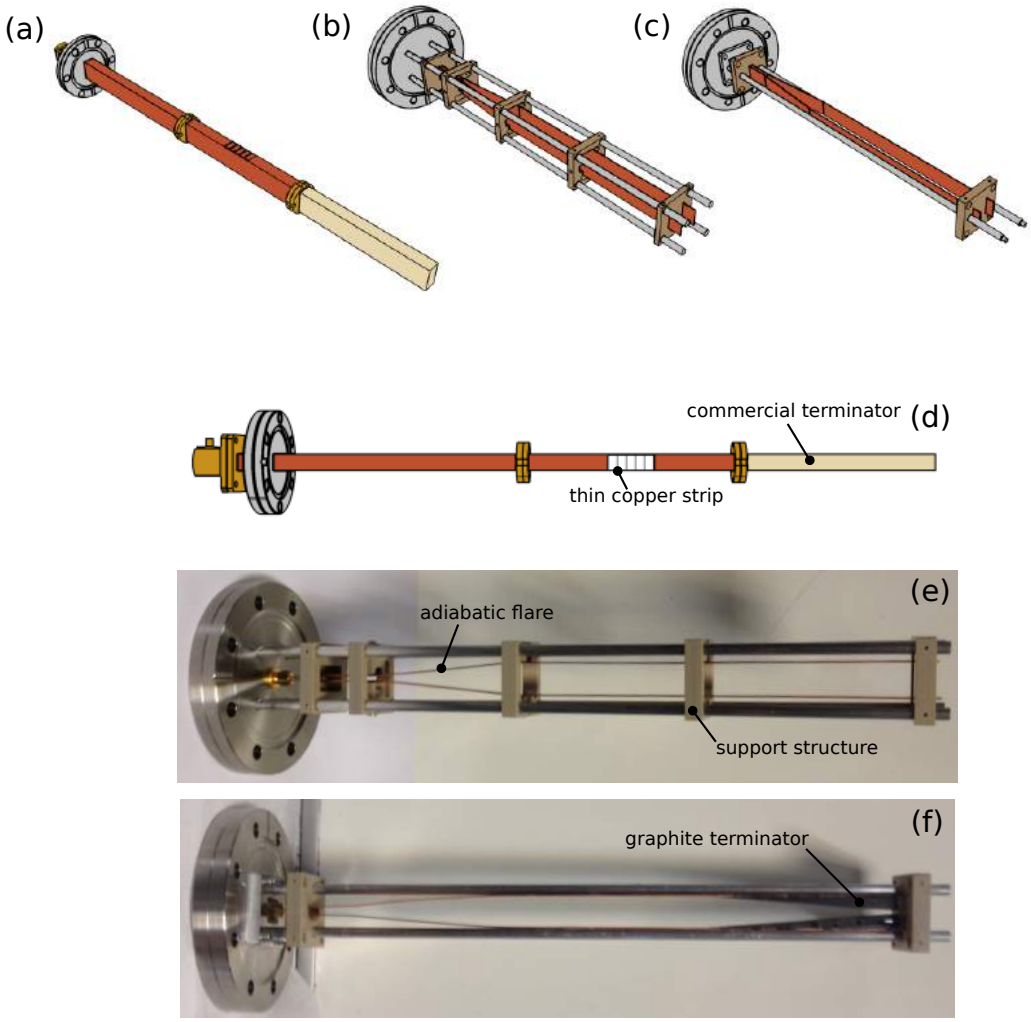


Figure 6.17: Designs of microwave π-pulse devices. (a) & (d) Waveguide design; an aperture is cut into the short side of the waveguide to allow the molecules pass through the field. Four 1 mm strips are left behind to contain the electric field inside the waveguide and maintain electric field homogeneity, in addition a commercial terminator prevents back reflections that would set up a standing wave. (b) & (e) Flared transmission line, version one and (c) & (f) version two. The input of the transmission line is impedance matched to 50 Ω where it then adiabatically flares out to surround the molecular beam, while maintaining the TEM mode. One version of the graphite absorber we used to terminate the line can be seen in (f).

geneous travelling wave, with some small standing wave component due to reflections at the aperture.

The schematic in Figure 6.18(a) shows the experiment we performed to test the efficiency of the microwave π-pulse. Fistly, we remove population from $(N = 0,\ F = 0)$ and $(N = 1, F = 1^-)$ using two laser frequencies tuned to Q(0) and Q(1), we then refill the ground state with population from $(N = 0,\ F = 1)$ using an rf π-pulse, and finally we remove this

population to ($N = 1,\ F = 1^-$) using the microwave π-pulse. At each stage, we look for the change in signal using a weak probe beam tuned to Q(0)($F = 0$).

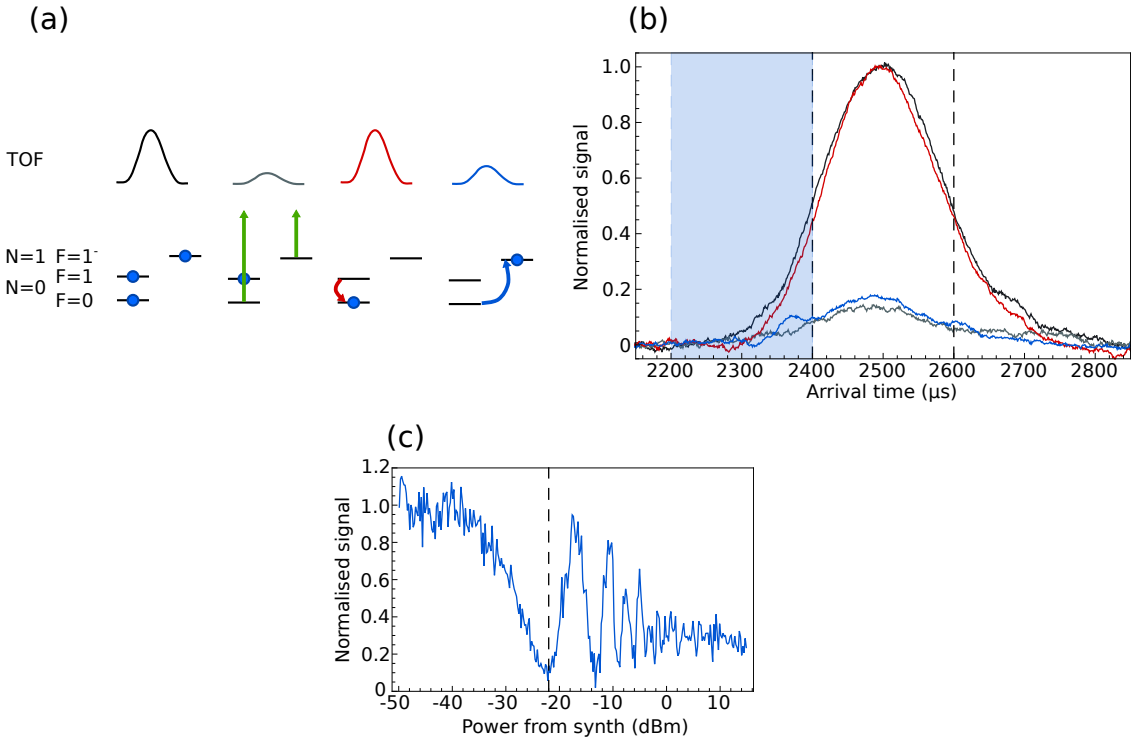


Figure 6.18: (a) Schematic of the experiment to quantify the π-pulse efficiency of the waveguide. (b) Results of the experiment, a microwave π-pulse has been achieved with 94% efficiency. (c) Rabi flopping between the ($N = 0,\ F = 0$) and ($N = 1,\ F = 1^-$) states using the microwave field produced by the waveguide design.

The results of this experiment are shown by Figure 6.18(b), where the shaded region shows the position of the microwave field in relation to the detection, and the region indicated by the dashed line shows the selection of molecules we consider in the analysis. In the first step of this experiment, we safely assume that all the population has been removed from both states, where any remaining signal is attributed to underlying lines in Q(0). The black and gray time-of-flight profiles (TOFs) show that the underlying lines contribute to 12% of the original signal. In the next stage we refill, back up to the level indicated by the red TOF, which shows that the rf π-pulse efficiency is $> 99\%$. Finally, removing the population with the microwave π-pulse, depletes the signal to 18%. This is slightly above the background signal, but gives an overall π-pulse efficiency of 94%. In addition, Figure 6.18(c) shows the population Rabi flopping between the states due to the microwave field created by the waveguide design, where the dashed line indicates the position of the π-pulse.

Unfortunately, this is not the only factor determining the overall performance of this system. We need to also consider the fraction of molecules that will execute the π-pulse. From the geometry of the setup, we would expect around 57% of the molecules to make it through a waveguide in the first region, and 43% to make it through a waveguide in the

second region. This was confirmed experimentally by looking at the signal ratio between the two detectors, both with and without a waveguide in region (6c). Doing this showed that only 45% of the molecular beam made it through the waveguide to the second detection region. With this much loss, only 37% of the total molecules would contribute to a complete measurement. Although there would still be a small gain in sensitivity (around a factor of 2), we thought we could achieve better overall efficiency with a different design, described below.

Microwave transmission line

This design is based on a parallel plate transmission line setup. The first section of the line launches the TEM mode of the microwave field in a 50 Ω impedance matched transmission line. The parallel plates then adiabatically flare out from a 2 mm separation to 16 mm separation over 50 mm. This adiabatic flare maintains the TEM mode without exciting any higher orders that can now be supported by the parallel plates. In addition, the plates are also designed to minimise any lossy modes caused by reflections off the edge of the plates.

In version one of the transmission line model, shown in Figure 6.17(b) and (e), we found that the PEEK supports interfered with the electric field that radiated out from the line, creating standing waves across the plates. These were removed, creating version two of the transmission line, shown in Figure 6.17(c) and (f), which is much more open, with minimal support around the parallel plate structure.

Simulations of this design, performed by J. A. Devlin [89], suggested the π-pulse could be up to 97% efficient, with the caveat that we could terminate the line effectively. This proved to be incredibly challenging and we spent a lot of time trying to get both home-built and commercial aborbers to work. One design can be seen in Figure 6.17(f). This is a home-built absorber which uses flaked graphite, shown to have good absorbant properties at 14 GHz [125], that has been cast into vacuum epoxy and moulded into a wedge shape. Throughout this project we tried many different vacuum epoxies, different proportions of graphite, different wedge designs and even many different commercial absorbers.

The biggest challenge with these absorbers was trying to get the bench tests, where we probed the electric field with an antenna and power meter, and the tests in vacuum using the molecules to tie up. A typical bench test result is shown in Figure 6.19(a), where the light blue line shows the power in the electric field without the absorber, and the dark blue line the power in the field with the absorber. We can see that some absorption is occurring, and the standing wave across the central region has been reduced by about 5%. Figure 6.19(b) shows the π-pulse efficiency we would expect to achieve if the field measured by the bench test is simply this standing wave pattern. This shows we would expect the central molecules to experience a very homogeneous field. However, every time we would move the transmission line from the bench to the machine, we would always see the same result which we now affectionately call a 'Rabi splat', instead of Rabi flopping. A typical Rabi splat is shown in Figure 6.19(c). The inhomogeneity of the electric field means that we would only

ever achieve a 50% population transfer. The loss of contrast due to the leftover population completely removes the gain from the photon scatters, leaving you with the same sensitivity as before

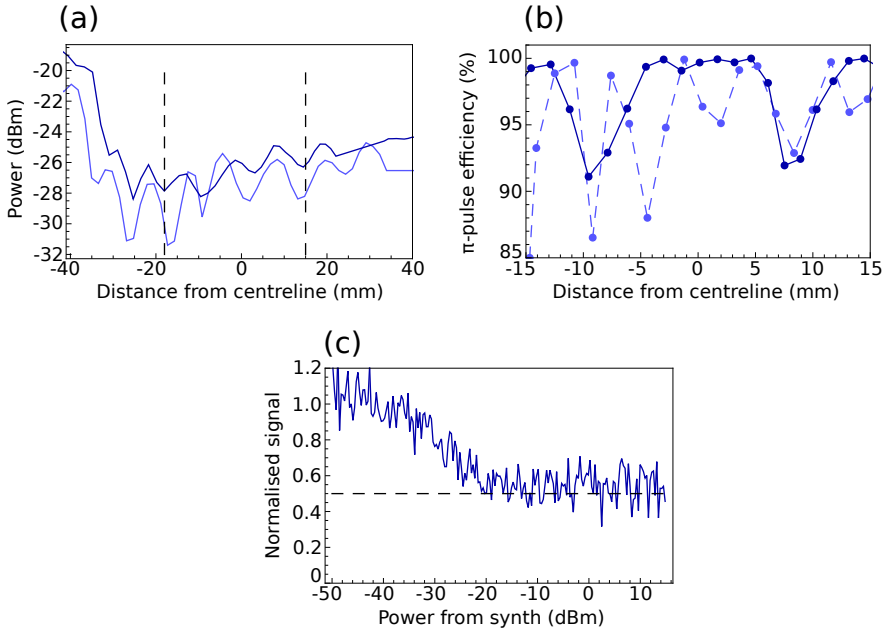


Figure 6.19: (a) A typical bench test result showing the standing wave in the transmission line both with (dark blue) and without (light blue) an absorber. (b) The calculated π-pulse efficiency for the results from this bench test. (c) A typical Rabi splat recorded by the molecules using the microwave transmission line design. The electric field inhomogeneity limits the population transfer to 50%.

Ultimately, the ability to achieve an efficient microwave π-pulse across the whole molecular packet was a very difficult challenge to overcome. After many attempts, we gave up on this technique and focus our efforts towards the optical pumping probe scheme.

Chapter 7

Conclusions and Outlook

7.1 Overview of improvements

This thesis has discussed in detail all the upgrades we have made to the YbF EDM experiment since 2013. Together these changes have improved upon the statistical sensitivity. This final chapter reviews all the upgrades in the context of collecting EDM data, and places a final value on the predicted shot noise limit of our next measurement.

7.1.1 Experimental setup

Figure 7.1 shows a front and side cross-section of the new beam machine. Two new vacuum chambers were built to accommodate the changes to the detection region and to simplify the electrical connections inside the machine. Once assembled, the machine is now over two metres tall. Two separate inner magnetic shields surround the interaction and detection region. In addition, the chamber is surrounded by two layers of mu-metal magnetic shielding, also redesigned to fit the new chamber, which are not shown in Figure 7.1. As in Chapter 2, we divide the chamber into six regions, labelled (1) – (6), which help to explain the new setup. The supersonic source (1) is the only region to remain unchanged by these upgrades, and so the reader can refer to Section 2.3.1 if necessary.

In the pump region (2), three resonant rf coils and a microwave horn have been added to deliver additional fields to the molecules. Alongside these fields, the pump laser beam has been elongated and now includes several frequencies. These changes have significantly increased the number of molecules pumped into the intial X $^2\Sigma^+(v = 0,\ N = 0)\,|0,0\rangle$ measurement state.

In the interaction region (3) – (5) the electric field plates have been redesigned to minimise magnetic Johnson noise. The electric field plates are constructed from float glass (dimensions 835 × 80 × 10 mm) and have been laminated in gold coated self-adhesive polyimide (Kapton) tape. To date, they can support up to $|E_z| = 8.3$ kV/cm across a separation of 12 mm. The rf plates have been shortened by 50 mm to accommodate this new design.

The detection region has been redesigned to incorporate a combination of microwaves and multiple laser frequencies to scatter many more photons per molecule. A set of large

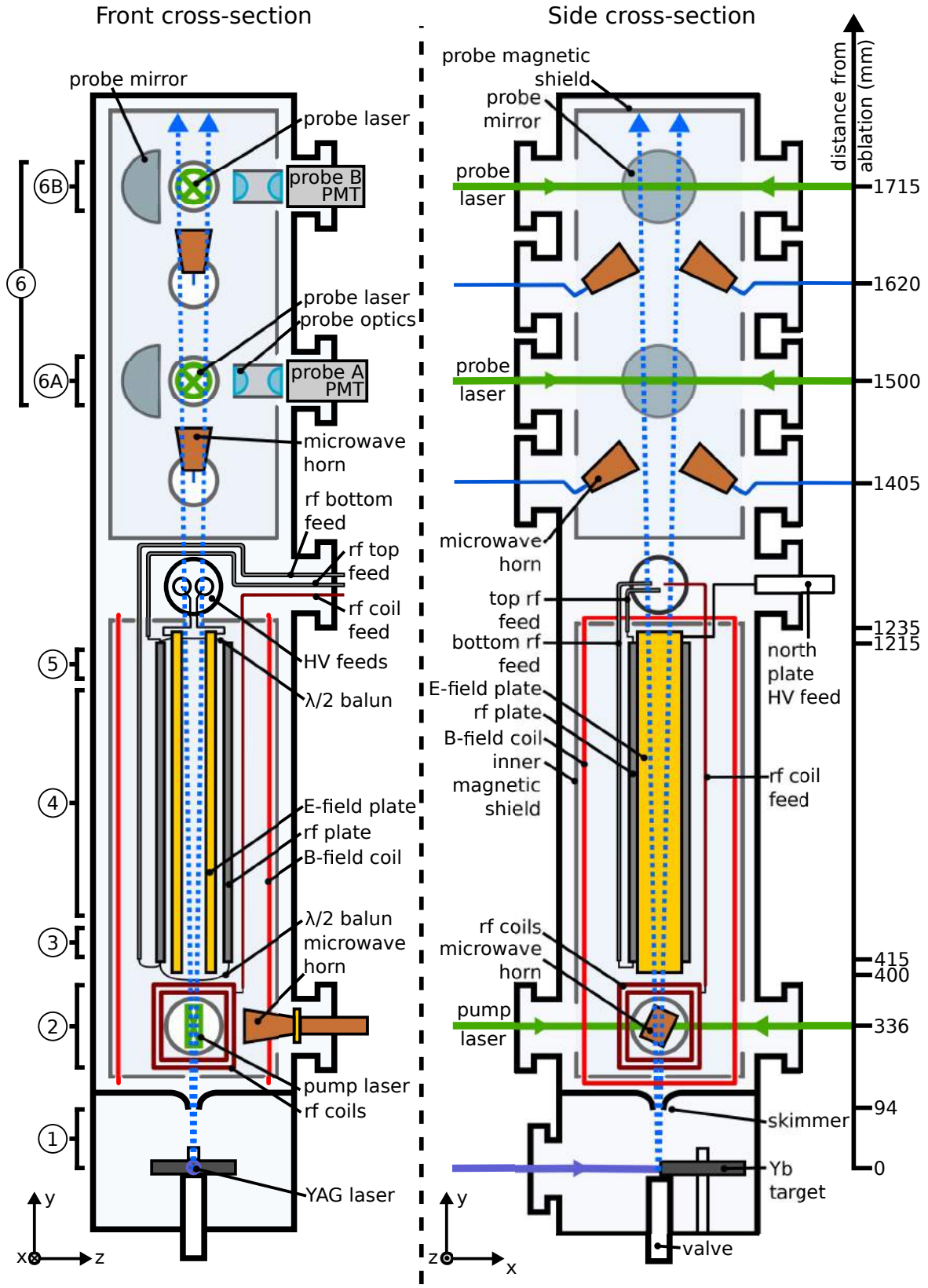


Figure 7.1: Front and side cross-sections of the new beamline vacuum chamber showing the improvements made to the pump, interaction and detection regions.

hemispherical mirrors have also been designed to collect as many of these photons as possible. The fluorescence from the YbF molecular packet is imaged onto the face of the PMT. The setup in (6A) is replicated in (6B) to create a second detection region, allowing us to detect both quadratures of the EDM interferometer output.

Outside the vacuum chamber, a whole host of new equipment has been added to control the new laser, microwave and rf fields. A schematic of the new equipment is shown in Figures 4.4 and 6.3. The reader should refer to the specific chapters for more details on these components.

7.1.2 New experimental sequence: A shot

In general, regions (1), (3) – (5) remain unchanged and so the reader can refer to Section 2.4.1 for additional details on these steps.

(1) Make some YbF

The supersonic source produces a pulse of YbF that travels through the machine at 590 m/s. We define $t = 0$ as the moment the YAG fires. The ^{174}YbF molecules that thermalise to the X $^2\Sigma^+(v = 0,\ N = 0, 1, 2)$ states will contribute to the measurement.

(2) Prepare

Using a combination of laser, microwave and rf fields, the population from X $^2\Sigma^+(v = 0,\ N = 0,\ F = 1)$, $(N = 1,\ F = 0, 1^{\pm}, 2)$ and $(N = 2, F = 1, 2^{\pm})$ levels, is collected and optically pumped into the X $^2\Sigma^+(v = 0,\ N = 0,\ F = 0)$, ground state. A schematic of the new pump scheme is shown in Figure 7.2(a). The original thermal population in $|0, 0\rangle$ is increased by a factor of 12, as shown by the time-of-flight profiles in Figure 7.2(b). This improves on the previous pumping technique by a factor of 6. Approximately ∼20% of the original population is left behind in each of the pumped levels.

(3) Create a superposition

The molecules enter the interaction region. An electric field of 8.3 kV/cm polarises the YbF molecules, aligning them to the internuclear axis. The polarisation factor is $\eta = 0.51$, as shown in Figure 7.3(b). The electric field also creates a Stark shift between the magnetic sublevels in $F = 1$, as shown in Figure 7.3(a). In addition, a small magnetic field $B_z = \pm 8.8$ nT, removes the degeneracy of the $|1, \pm 1\rangle$ sublevels, splitting them by about ± 125 Hz.

Once inside the transmission line, a 2 μs pulse of $\omega_{\mathrm{rf}} = 2\pi \times 172.5$ MHz rf is applied which transfers the population from $|0, 0\rangle$ into a superposition of the $|1, \pm 1\rangle$ levels. The population is now in the superposition,

$$|0, 0\rangle \rightarrow \frac{i}{\sqrt{2}} \left(|1, +1\rangle - |1, -1\rangle \right). \tag{7.1}$$

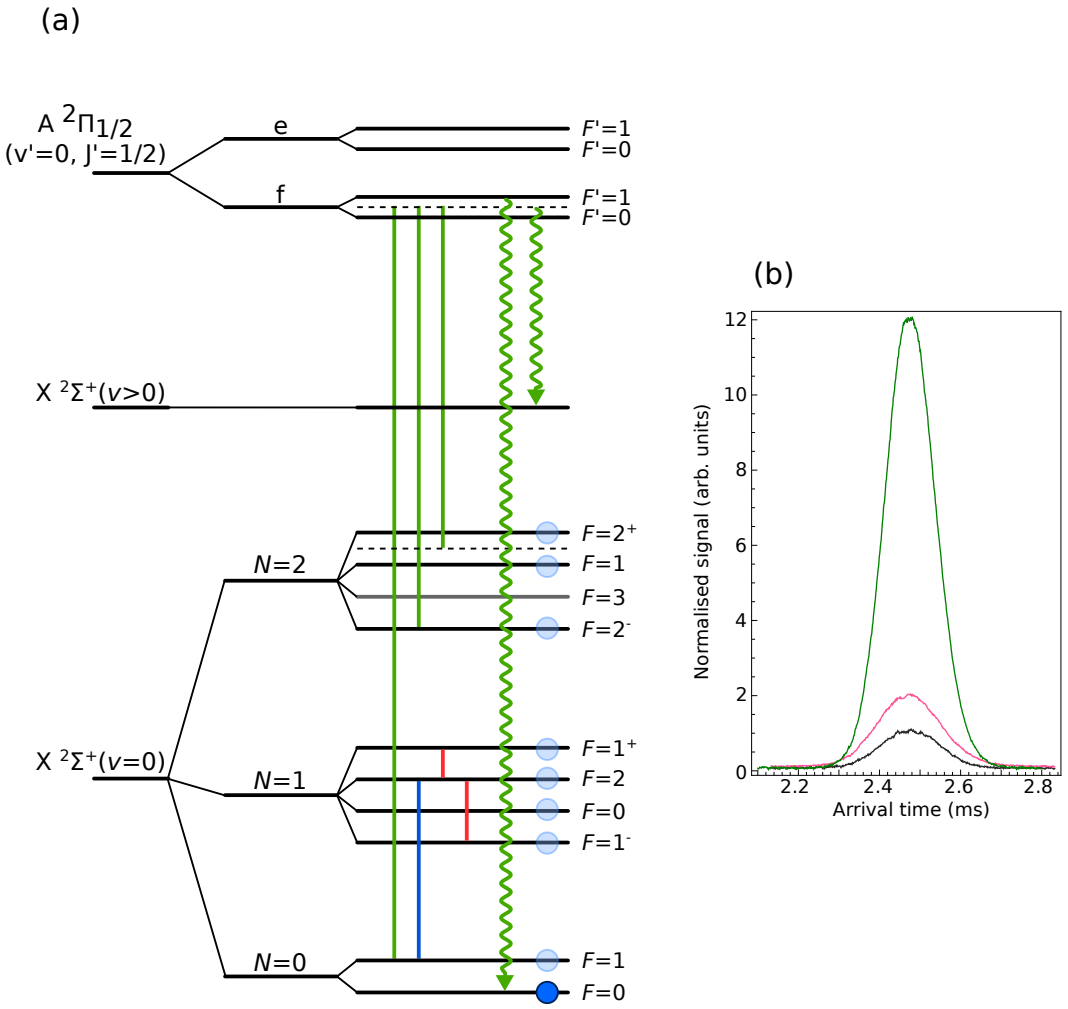


Figure 7.2: (a) Schematic of the new pump scheme which uses a combination of laser, microwave and rf fields to optically pump the population from higher rotational levels into the ground state. (b) Normalised signal increase due to the pump scheme. Black TOF shows the thermal $F = 0$ population, which is doubled to the pink profile using the old pump scheme (a single laser tuned to Q(0)($F = 1$)). This is increased by a further factor 6, to 12 times the thermal population, using the new pump scheme, shown by the green TOF profile.

(4) Evolve

As before, the superposition evolves inside the static electric and magnetic fields for time $\tau = 980\ \mu$s. The Zeeman and electron EDM interactions create opposite energy shifts between the $|1, \pm 1\rangle$ states. As they fly through these fields, the superposition evolves to,

$$\frac{i}{\sqrt{2}}\left(|1,+1\rangle - |1,-1\rangle\right) \rightarrow \frac{1}{\sqrt{2}}\left(e^{i(\phi_B+\phi_E)}\,|1,+1\rangle - e^{-i(\phi_B+\phi_E)}\,|1,-1\rangle\right), \tag{7.2}$$

where $\phi_B = \mu_B B\tau/\hbar$ and $\phi_E = d_e \eta E_{\text{eff}}\tau/\hbar$.

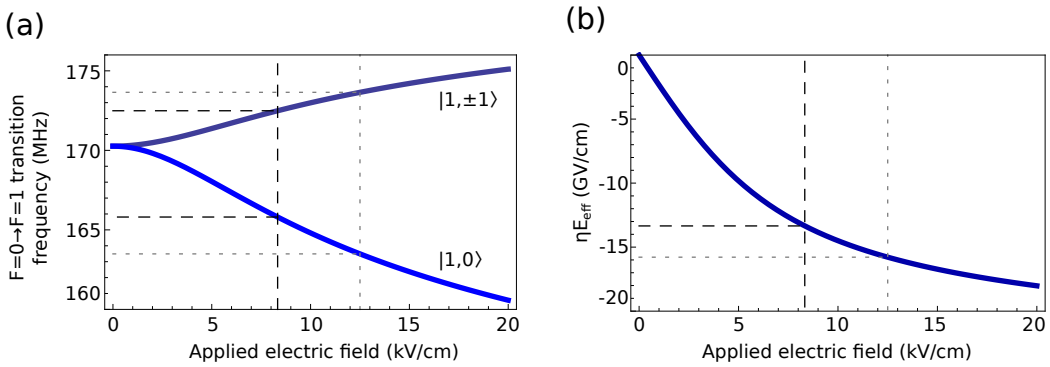


Figure 7.3: Stark shift of the magnetic sublevels in $F = 1$. (a) Stark shift as a function of applied electric field, gray dotted lines showing the Stark shift in the previous setup, black dashed lines show the Stark shift in the current electric field. (b) ηE_{eff} as a function of applied electric field. Gray dotted line shows the previous polarisation factor, and black dashed shows the new polarisation factor with the electric field of $|E_z| = 8.3$ kV/cm.

(5) Recombine the superposition

After the free evolution period, a second 2 μs pulse of rf recombines the superposition. This maps the state $(|1,+1\rangle - |1,-1\rangle)/\sqrt{2}$ coherently onto the state $ie^{i\phi_{\text{rf}}}|0,0\rangle$, where $\phi_{\text{rf}} = \omega_{\text{rf}} \times 2\ \mu$s. After the second π-pulse the state is,

$$\frac{i}{\sqrt{2}}\left(e^{i(\phi_B+\phi_E)}|1,+1\rangle - e^{-i(\phi_B+\phi_E)}|1,-1\rangle\right)$$
$$\rightarrow -e^{i\phi_{\text{rf}}}\cos(\phi_B+\phi_E)|0,0\rangle - \sin(\phi_B+\phi_E)\left\{\frac{1}{\sqrt{2}}(|1,+1\rangle + |1,-1\rangle)\right\}. \quad (7.3)$$

(6A) Probe $N = 0$, $F = 1$

The molecules leave the interaction region and enter the first detection region. They fly through a large probe laser beam which contains multiple frequencies. A microwave field is also applied to the molecules to selectively couple a single hyperfine level into the optical cycling system. A schematic of the detection used in region A is shown in Figure 7.4(a). The $F = 1$ population is cycled by the P(1) transition, causing the molecule to scatter many photons. In this detection region, preliminary results show that a single molecule scatters on average around 9.8 photons, before going dark to the probe light. This has increased the number of photons per molecule by a factor of 8.2. A typical time-of-flight profile using the old and new detection schemes is shown in Figure 7.4(b).

The signal recorded by the *probe A* PMT is,

$$S^A(t) = S_b^A(t) + S_0^A(t)\sin^2(\phi_B+\phi_E), \quad (7.4)$$

where S_0^A is proportional to the population in the $F = 1$ state, and S_b^A is the background signal caused by any population leftover in $N = 1$ after pumping, background molecular

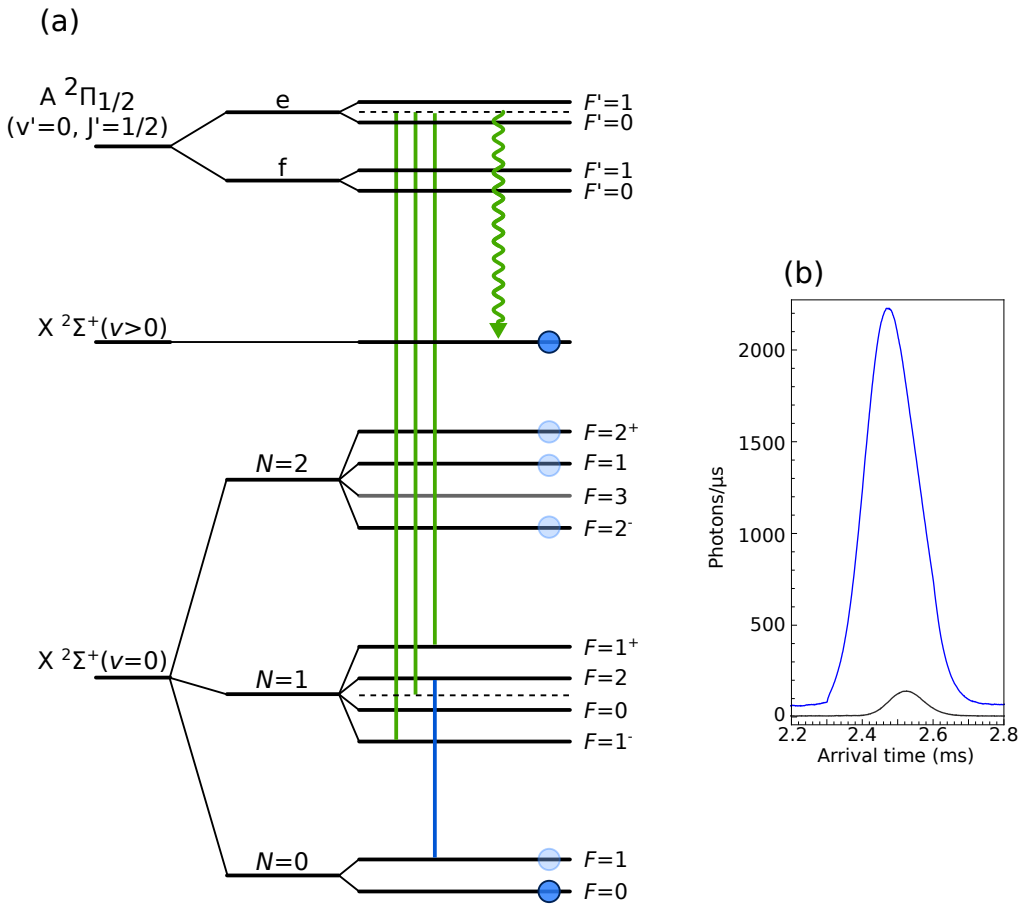


Figure 7.4: (a) Schematic of the microwave and laser fields used to detect the $F = 1$ population in region A. (b) A typical time-of-flight profile recorded by the *probe A* PMT. Black TOF shows previous detector signal, blue TOF shows the signal using the improved detection scheme.

signal beneath P(1), as well as laser scatter.

(6B) Probe $N = 0$, $F = 0$

About 400 μs later, the molecules enter the final detection region. The molecules experience the same laser frequencies, this time with a microwave field that selects the population in $F = 0$. A schematic of the detection scheme used in region B is shown in Figure 7.5(a). This time, a single molecule is found to scatter 13.8 photons on average, increasing the scattered photons by a factor of 11.5. A typical time-of-flight profile in the region is shown in Figure 7.5(b).

The signal recorded by the *probe B* PMT is,

$$S^B(t) = S_b^B(t) + S_0^B(t)\cos^2(\phi_B + \phi_E), \tag{7.5}$$

where S_0^B is proportional to the number of molecules in the state $F = 0$, and S_b is the background molecular signal after the first detection region, as well as any laser scatter.

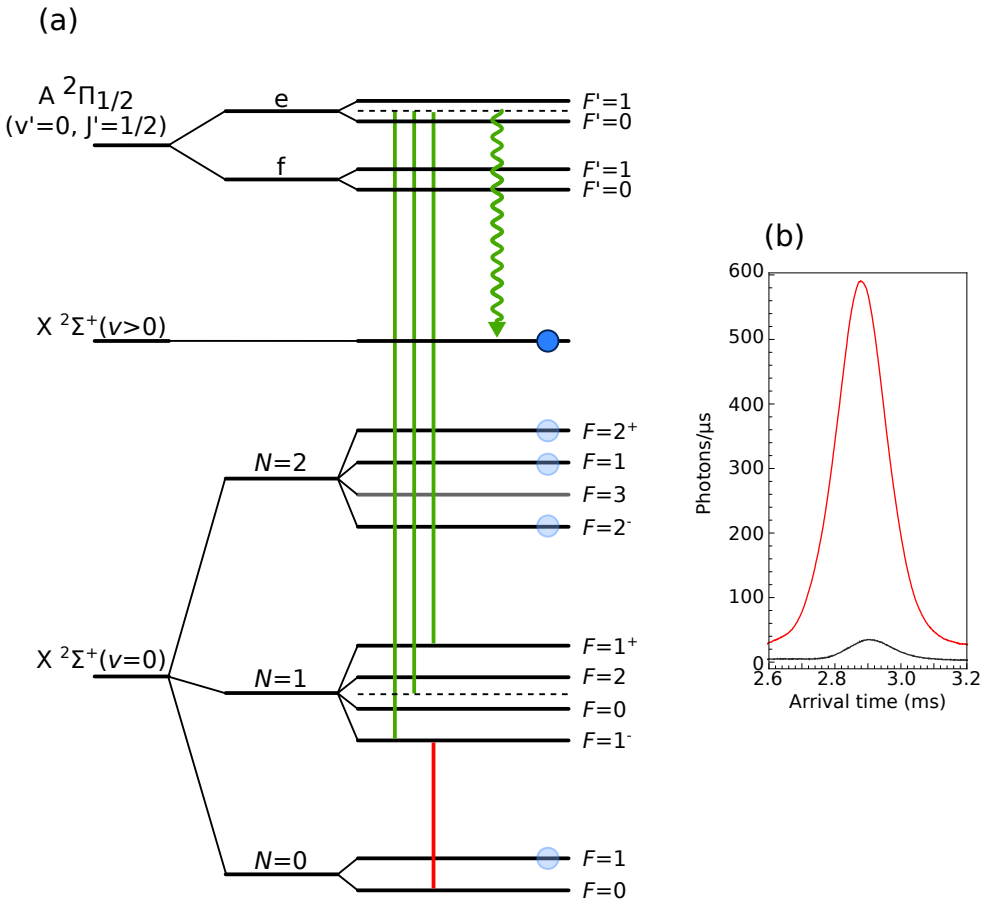


Figure 7.5: (a) Schematic of the microwave and laser fields used to detect the $F = 0$ population in region B. (b) A typical time-of-flight profile recorded by the *probe B* PMT. The red TOF shows the improved detection scheme, compared to the old scheme, shown in black.

By considering how the signals, $S^A(t)$ and $S^B(t)$, change between different switch states of the machine, we can extract an EDM value from each detection region.

7.1.3 New experimental sequence: A block

Previously, the simplest block used only eight shots to extract a single value of d_e, see Section 2.4.2 for details. With the improvements to the detection system, the same eight shots will now provide two independent measurements of d_e by using both quadratures of the interferometer. We can consider each detector as a measure of d_e, with its own value and uncertainty. However, it will also be useful to consider the signals together as they can help to reject common noise sources such as laser intensity fluctuations and source fluctuations. It is likely that the composite signal,

$$S^C(t) = \frac{S^B(t) - S^A(t)}{S^B(t) + S^A(t)}, \tag{7.6}$$

will be the new signal of interest, and replace the top-normed detector signal from Section 2.5. However, this relies on the background signal in each detector being small compared to the amplitude of the interference curve, $S_b \ll S_0$, and on the two curves being of similar size, $S_0^A \simeq S_0^B$. Currently, neither of these conditions are fullfilled, which makes analysis much more complicated. Some of the differences between the detectors can be quantified and accounted for. For example, understanding the collection efficiency of each detection region, as well as improving the efficiency of detecting the $F = 1$ population, will help to achieve $S_0^A \simeq S_0^B$.

A bigger concern is the significant background ($S_B \simeq S_0$) that is currently present in both of the detector signals. It seems as though the background is largely due to signal from other YbF isotopes in the bandhead, rather than laser scatter or leftover $N = 1$ population. There are also additional subtleties, in particular that the background of detector B depends on how efficiently we detect in detector A, which is dependent on how well we pump in the first stage of the experiment. Firstly, this is a concern for measurement sensitivity; a large background reduces the contrast of the measurement (see Section 7.2.2). However, a large background could be more of a concern regarding potential systematic effects. A significant fraction of the background signal is due to other YbF isotopes in the bandhead which, by the time they reach the detection region, have been through the same laser, microwave, rf and electric fields as the ^{174}YbF. Of particular concern are the even isotopes ^{172}YbF and ^{176}YbF, which have almost identical hyperfine structure [92] and so are likely to respond to the 170 MHz rf in some way. If this response is at all correlated with the electric field direction, then the background signal will produce a systematic effect. If we have no handle on reducing the background (ideally such that $S_B \ll S_0$), then it becomes difficult to track down and suppress the mechanism of the possible systematic shift.

To acquire a more comprehensive block of data, we switch many parameters in the experiment. The software that runs the EDM machine allows us to modulate as many experiment parameters as required. However, increasing the number of switch parameters will also increase the time it takes to collect a block of data. With these upgrades, 22 new parameters have been added to the experiment; the frequency and amplitude of each rf and microwave field, as well as the frequency and relative power of each laser sideband. Over the next few months, as the measurement technique is developed further, we will decide which parameters will need to be modulated, and which will stay fixed during a block. So far, the efficiency of the pump and probe schemes seem to be more sensitive to a few parameters over others. In particular, the Q(0)($F = 1$) detuning and the relative rf powers, have more influence over the pumping efficiency, while the relative laser power in each of the P(1) probe beams seems to also be important. Regardless of which of these parameters are switched, they will all need to be recorded at least once a block.

7.2 Sensitivity

We can now consider how each of the changes we have made to the machine has increased or decreased measurement sensitivity. After N shots of the experiment, each detector A and B, will record its own value of d_e, with its own shot noise uncertainty $\sigma_{d_e}^A$ and $\sigma_{d_e}^B$ respectively, which are defined as,

$$\sigma_{d_e}^{A/B} = \frac{\hbar}{\eta E_{\text{eff}} \tau 2\mathcal{C}^{A/B}\sqrt{N}} \sqrt{\frac{1}{P^{A/B}}}, \tag{7.7}$$

where P^A, P^B are the number of photons detected per shot in region A and B, and $\mathcal{C}^A$, $\mathcal{C}^B$ is the contrast in each detector. During the last data set recorded by the YbF EDM experiment, the shot noise limit was [90],

$$\sigma_{d_e}^{(2011)} = (5.7 \times 10^{-26}/\sqrt{N_b})\ e.\text{cm}, \tag{7.8}$$

where $N_b = N/4096$, the number of blocks recorded in the measurement.

Between 2011 and 2013, several small improvements were made to the machine to improve sensitivity by a factor of 2.7. These improvements included upgrades to the rf transmission line, an additional layer of magnetic shielding and new electric field supplies. With these upgrades, the predicted shot noise limit in 2013 was [89],

$$\sigma_{d_e}^{(2013)} = (2.1 \times 10^{-26}/\sqrt{N_b})\ e.\text{cm}. \tag{7.9}$$

Since 2013, we have made significant changes to the machine, which have been discussed comprehensively throughout this thesis. Each of these changes contribute to the new shot noise limit of the YbF EDM experiment. The individual improvements will now be discussed in turn, in the context of measurement sensitivity.

7.2.1 Polarisation factor, η

In 2013, the aluminium electric field plates could be comfortably charged to $|E_z| = 12.5$ kV/cm [89], producing a polarisation factor of $\eta^{(2013)} = 0.61$. The new gold film plates, detailed in Chapter 5, have been shown to support up to $|E_z| = 8.3$ kV/cm, which has slightly reduced the polarisation factor to $\eta^{(2016)} = 0.51$. Overall, this will reduce the statistical sensitivity by a small factor of

$$f_\eta = \frac{\eta^{(2016)}}{\eta^{(2013)}} = \frac{0.51}{0.61} = 0.84. \tag{7.10}$$

However, it is expected that as the EDM machine continues to run, the plates will naturally condition themselves to support higher voltages, increasing this factor up to, or above, 1.

7.2.2 Contrast, $\mathcal{C}$

Figure 7.6 compares (a) a typical interference curve recorded in 2014, to (b) the preliminary interference fringes presented in Chapter 5. Both data sets have been analysed using a 20 μs gate to allow direct comparison between the two.

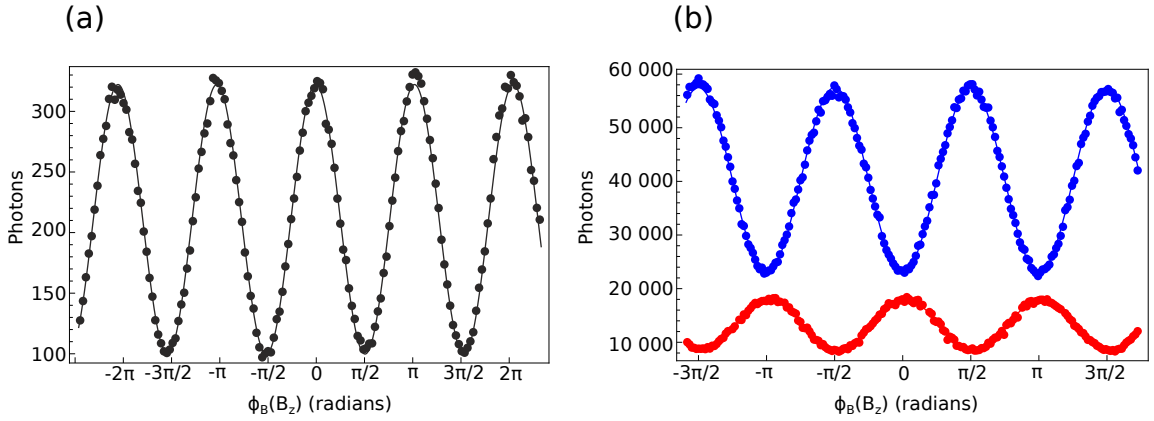


Figure 7.6: (a) Typical interference fringe recorded in 2014 using the previous machine configuration (9 μs rf pulses). (b) Preliminary data set using the new pump and probe schemes (5 μs rf pulses). Blue: $F = 1$ population detected in region A. Red: $F = 0$ population detected in region B. All data sets analysed using a 20 μs gate for comparison.

The contrast of the interference fringe is defined as the amplitude over the average signal,

$$\mathcal{C} = \frac{S_0/2}{S_0/2 + S_b}, \tag{7.11}$$

where S_0 and S_b are defined by Equations (7.4) and (7.5). The example data set in Figure 7.6(a) has a contrast of $\mathcal{C} = 0.53$. However, before the upgrades, the contrast was reportedly as high as $\mathcal{C}^{(2013)} = 0.76$, when using 2 μs pulses of rf [89].

In comparison, the contrast of the $F = 1$ fringe recorded in detector A, shown in blue in Figure 7.6(b), is $\mathcal{C}^A = 0.43$, while the contrast of the $F = 0$ fringe recorded in detector B, shown in red in Figure 7.6(b) is $\mathcal{C}^B = 0.36$. This reduces measurement sensitivity of each detector by a factor of,

$$f_{\mathcal{C}}^A = \frac{\mathcal{C}^A}{\mathcal{C}^{(2013)}} = \frac{0.43}{0.76} = 0.56, \qquad f_{\mathcal{C}}^B = \frac{\mathcal{C}^B}{\mathcal{C}^{(2013)}} = \frac{0.36}{0.76} = 0.47. \tag{7.12}$$

In this preliminary data set, the rf π-pulses are 5 μs long. It is expected that, when we reduce the length of these pulses to 2 μs, the contrast will also improve. In addition, this example shows how the large background will reduce measurement sensitivity. If we can remove a significant proportion of this background, which we would like to do for systematic reasons, then measurement sensitivity will also improve.

7.2.3 Number of photons, $P^A,\ P^B$

The probability of detecting each molecule is the mean number of photons scattered per molecule (around 10) multiplied by the probability of detecting each photon (about 0.5%). Since the probability is small (about 5%), the ideal statistical sensitivity remains proportional to the square root of the number of detected photons.

Using the new pump scheme, we have increased the number of molecules that participate in the experiment by a factor of 5.8. This improves the statistical sensitivity of the machine by a factor of,

$$f_{\text{pump}} = \sqrt{5.7} = 2.4. \tag{7.13}$$

The new probe scheme has increased the number of photons a molecule scatters, directly increasing the probability of detection. In detector A, the molecules scatter 8.2 times more photons on average than previously, and in detector B, they scatter 11.5 times as many photons as previously. This leads to a sensitivity increase of,

$$f^A_{\text{probe}} = \sqrt{8.2} = 2.9 \qquad\qquad f^B_{\text{probe}} = \sqrt{11.5} = 3.4 \tag{7.14}$$

in each detector.

Preliminary results indicate that there is an additional gain from the new collection optics setup and increased detection volume. However, this is hard to quantify without a larger data set, and so for now it will be neglected from the predicted shot noise limit.

7.2.4 Conclusion

Finally, we can piece all these changes together to predict the final shot noise sensitivity for the next EDM measurement. Combining Equations (7.10), (7.12), (7.13) and (7.14), we find that the fractional improvement in sensitivity is,

$$\sigma^{(2016)}_{d_e} = \left(\frac{1}{f_\eta f_{\mathcal{C}}^{A/B} f_{\text{pump}} f^{A/B}_{\text{probe}}} \right) \sigma^{(2013)}_{d_e}. \tag{7.15}$$

Plugging the numbers into this expression, the detectors end up (coincidentally) with the same shot noise limit,

$$\sigma^A_{d_e} = \sigma^B_{d_e} = 0.3 \times \sigma^{(2013)}_{d_e} = (0.65 \times 10^{-26}/\sqrt{N_b})\ e.\text{cm}. \tag{7.16}$$

However, since twice as many measurements of d_e are recorded in a single shot, the total statistical uncertainty is reduced by an additional factor of $\sqrt{2}$ to give,

$$\sigma_{d_e} = (0.5 \times 10^{-26}/\sqrt{N_b})\ e.\text{cm} \tag{7.17}$$

which is a factor of 4.2 improvement in the shot noise limit from 2013, and a factor of 11.4 since 2011.

7.3 Outlook

Overall, the changes discussed in this thesis have improved the statistical sensitivity of the YbF EDM experiment by a factor of 11.4 relative to the previous YbF measurement. If we were to record a new data set (which typically consists of $\sim 10^5$ blocks) with this sensitivity, then the 90% confidence on the statistical uncertainty on the measurement would be,

$$\sigma_{d_e}(\text{stat}) = 2.4 \times 10^{-29}\ e.\text{cm} \tag{7.18}$$

This is a factor of 6 better than the current upper limit measured by the ACME collaboration [24], and a factor of 44 better than the previous YbF result [52]. In 2011 only 6194 blocks of data contributed to the final measurement, improved experimental stability will allow us to acquire more blocks of data, accounting for the extra improvement.

Over the next few months, as the measurement technique develops and the machine is collecting EDM data regularly, it is expected that there may be small additional gains to the sensitivity, including the polarisation factor as well as the number of detected photons. As discussed above, we also need to reduce the large background that is currently being detected by the P(1) probe lasers, which will help to improve the contrast in each detector.

However, the real test is to now ensure that every part of the experiment runs consistently and reliably over long period of time — 10^5 blocks of data takes around 3 months of running (day and night) to acquire. In addition, the improvements must be well characterised and thoroughly tested for systematic effects, before we can begin collecting data. Assuming no new systematics have been introduced by these changes, then we can consider Table 7.1 below, which excludes the high voltage supplies systematic. In this case, the projected systematic uncertainty is $3.7 \times 10^{-29}\ e.\text{cm}$, which would be slightly larger than the statistical error of our measurement. However, the error budget is now dominated by the dc shield magnetisation and leakage currents. There is considerable scope for a more careful offline measurement of the shield magnetisation and we are in the process of purchasing a SERF magnetometer. This will be able to sit inside the vacuum chamber and directly record the magnetic fields generated by the leakage currents, allowing us to make a better measurement of this systematic.

With these improvements in place, we can expect the YbF EDM experiment to make a new world leading measurement of the electron's electric dipole moment in the near future, with a total uncertainty of a few $10^{-29}\ e.\text{cm}$. This measurement continues the search for physics beyond the Standard Model using the molecular beam techniques described in this thesis.

Systematic error	Current upper limit (10^{-28} e.cm)	Projected upper limit (10^{-28} e.cm)
Uncorrected E-asymmetry*	0.5	0.1
Voltage offset	0.063	0.063
Residual rf1 detuning*	0.6	0.1
dc anf rf leakage currents	0.2	0.2
dc shield magnetisation**	0.5	0.25
ac shield magnetisation**	0.05	0.05
rf rotation	-	0.084
Geometric phase	0.01	0.01
Motional magnetic field	0.0005	0.0005
Sum in quadrature	0.95	0.37

Table 7.1: Table of of current and projected systematic errors and their contributions. *Indicates an upper limit determined by the statistical sensitivity of the machine. **Taken using auxillary offline measurements.

Bibliography

[1] E. M. Purcell & N. F. Ramsey. On the Possibility of Electric Dipole Moments for Elementary Particles and Nuclei. *Physical Review* **78**, 807 (1950).

[2] T. D. Lee & C. N. Yang. Question of Parity Conservation in Weak Interactions. *Physical Review* **104**, 254 (1956).

[3] C. S. Wu, E. Ambler, R. W. Hayward, D. D. Hoppes & R. P. Hudson. Experimental Test of Parity Conservation in Beta Decay. *Physical Review Letters* **105**, 1413 (1957).

[4] M. S. Sozzi. *Discrete Symmetries and CP Violation* (Oxford University Press, 2008).

[5] E. N. Fortson & L. L. Lewis. Atomic Parity Nonconservation Experiments. *Physics Reports* **113**, 289 (1984).

[6] L. Landau. On the conservation laws for weak interactions. *Nuclear Physics* **3**, 127 (1957).

[7] J. H. Christenson, J. W. Cronin, V. L. Fitch & R. Turlay. Evidence for the 2π Decay of the K_2^0 Meson. *Physical Review Letters* **13**, 138 (1964).

[8] BaBar Collaboration. Observation of CP Violation in the B^0 Meson System. *Physical Review Letters* **87**, 091801 (2001).

[9] Belle Collaboration. Observation of Large CP Violation in Neutral B Meson System. *Physical Review Letters* **87**, 091802 (2001).

[10] LHCb Collaboration. First Observation of CP Violation in the Decays of B_s^0 Mesons. *Physical Review Letters* **110**, 221601 (2013).

[11] LHCb Collaboration. Measurements of Indirect CP Asymmetries in $D^0 \to K^-K^+$ and $D^0 \to \pi^-\pi^+$ Decays. *Physical Review Letters* **112**, 041801 (2014).

[12] O. W. Greenberg. CPT Violation Implies Violation of Lorentz Invariance. *Physical Review Letters* **89**, 231602 (2002).

[13] R. N. Zare. *Angular Momentum* (John Wiley & Sons, Inc., 1988).

[14] I. B. Khriplovich & S. K. Lamoreaux. *CP Violation Without Strangeness* (Springer, 1997).

[15] C. G. Parthey, A. Matveev, J. Alnis, B. Bernhardt, A. Beyer, R. Holzwarth, A. Maistrou, R. Pohl, K. Predehl, T. Udem, T. Wilken, N. Kolachevsky, M. Abgrall, D. Rovera, C. Salomon, P. Laurent & T. W. Hänsch. Improved Measurement of the Hydrogen $1S - 2S$ Transition Frequency. *Physical Review Letters* **107** (2011).

[16] C. J. Foot. *Atomic Physics* (Oxford University Press, 2005).

[17] J. H. Smith, E. M. Purcell & N. F. Ramsey. Experimental Limit to the Electric Dipole Moment of the Neutron. *Physical Review* **108**, 120 (1957).

[18] BaBar Collaboration. Observation of Time-Reversal Violation in the B^0 Meson System. *Physical Review Letters* **109**, 211801 (2012).

[19] CPLEAR collaboration. First direct observation of time-reversal non-invariance in the neutral-kaon system. *Physics Letters B* **444**, 43 (1998).

[20] L. Wolfenstein. Violation of Time Reversal Invariance in K^0 Decays. *Physical Review Letters* **83**, 911 (1999).

[21] H.-J. Gerber. Evidence for time-reversal violation? *The European Physical Journal C: Particles and Fields* **35**, 195 (2004).

[22] M. Kobayashi & T. Maskawa. CP-Violation in the Renormalizable Theory of Weak Interaction. *Progress of Theoretical Physics* **49**, 652 (1973).

[23] B. L. Roberts & W. J. Marciano. *Lepton Dipole Moments* (World Scientific Publishing Co. Pte. Ltd., 2010).

[24] ACME Collaboration. Order of Magnitude Smaller Limit on the Electric Dipole Moment of the Electron. *Science* **343**, 269 (2014).

[25] A. D. Sakharov. Violation of CP invariance, C asymmetry, and baryon asymmetry of the universe. *JETP Letters* **5**, 24 (1967).

[26] A. Riotto & M. Trodden. Recent Progress in Baryogenesis. *Annual Review of Nuclear and Particle Science* **49**, 35 (1999).

[27] J. M. Pendlebury & E. A. Hinds. Particle electric dipole moments. *Nuclear Instruments and Methods in Physics Research A* **440**, 471 (2000).

[28] Y. Nir. CP Violation In and Beyond the Standard Model. *arXiv:hep-ph/9911321* (1999).

[29] E. E. Salpeter. Some Atomic Effects of an Electronic Electric Dipole Moment. *Physical Review* **112**, 1642 (1958).

[30] D. F. Nelson, A. A. Schupp, R. W. Pidd & H. R. Crane. Search for an Electric Dipole Moment of the Electron. *Physical Review Letters* **2**, 492 (1959).

[31] D. T. Wilkinson & H. R. Crane. Precision Measurement of the g Factor of the Free Electron. *Physical Review* **130**, 852 (1963).

[32] J. Goldemberg & Y. Torizuka. Upper Limit of the Electric Dipole Moment of the Electron. *Physical Review* **129**, 2580 (1963).

[33] E. S. Ensberg. *Bulletin of the American Physical Society* **7**, 534 (1962).

[34] E. S. Ensberg. Experimental Upper Limit for the Permanent Electric Dipole Moment of Rb^{85} by Optical-Pumping Techniques. *Physical Review* **157**, 270 (1967).

[35] P. G. H. Sandars & E. Lipworth. Electric Dipole Moment of the Cesium Atom. A New Upper Limit to the Electric Dipole Moment of the Free Electron. *Physical Review Letters* **13**, 718 (1964).

[36] T. S. Stein, J. P. Carrico, E. Lipworth & M. C. Weisskopf. Electric Dipole Moment of the Cesium Atom. A New Upper Limit to the Electric Dipole Moment of the Free Electron. *Physical Review Letters* **19**, 741 (1967).

[37] J. P. Carrico, E. Lipworth, P. G. H. Sandars, T. S. Stein & M. C. Weisskopf. Electric Dipole Moments of Alkali Atoms. A Limit to the Electric Dipole Moment of the Free Electron. *Physical Review* **174**, 125 (1968).

[38] M. C. Weisskopf, J. P Carrico, H. Gould, E. Lipworth & T. S. Stein. Electric Dipole Moment of the Cesium Atom. A New Upper Limit to the Electric Dipole Moment of the Electron. *Physical Review Letters* **21**, 1645 (1968).

[39] S. A. Murthy, D. Krause, Jr., Z. L. Li & L. R. Hunter. New limits on the electron electric dipole moment from cesium. *Physical Review Letters* **63**, 965 (1989).

[40] H. Gould. Search for an Electric Dipole Moment in Thallium. *Physical Review Letters* **24**, 1091 (1970).

[41] K. Abdullah, C. Carlberg, E. D. Commins, H. Gould & S. B. Ross. New experimental limit on the electron electric dipole moment. *Physical Review Letters* **65**, 2347 (1990).

[42] E. D. Commins, S. B. Ross, D. DeMille & B. C. Regan. Improved experimental limit on the electric dipole moment of the electron. *Physical Review A* **50**, 2960 (1994).

[43] B. C. Regan, E. D. Commins, C. J. Schmidt & D. DeMille. New Limit on the Electron Electric Dipole Moment. *Physical Review Letters* **88**, 071805 (2002).

[44] M. A. Player & P. G. H. Sandars. An experiment to search for an electric dipole moment in the $^3P_2$ metastable state of xenon. *Journal of Physics B: Atomic and Molecular Physics* **3**, 1620 (1970).

[45] S. K. Lamoreaux, J. P. Jacobs, B. R. Heckel, F. J. Raab & N. Fortson. New constraints on time-reversal asymmetry from a search for a permanent electric dipole moment of ^{199}Hg. *Physical Review Letters* **59**, 2275 (1987).

[46] J. P. Jacobs, W. M. Klipstein, S. K. Lamoreaux, B. R. Heckel & E. N. Fortson. Testing time-reversal symmetry using ^{199}Hg. *Physical Review Letters* **71**, 3782 (1993).

[47] J. P. Jacobs, W. M. Klipstein, S. K. Lamoreaux, B. R. Heckel & E. N. Fortson. Limit on the electric-dipole moment of ^{199}Hg using synchronous optical pumping. *Physical Review A* **52**, 3521 (1995).

[48] M. V. Romalis, W. C. Griffith, J. P. Jacobs & E. N. Fortson. New Limit on the Permanent Electric Dipole Moment of ^{199}Hg. *Physical Review Letters* **86**, 2505 (2001).

[49] W. C. Griffith, M. D. Swallows, T. H. Loftus, M. V. Romalis, B. R. Heckel & E. N. Fortson. Improved Limit on the Permanent Electric Dipole of ^{199}Hg. *Physical Review Letters* **102**, 101601 (2009).

[50] D. Cho, K. Sangster & E. A. Hinds. Tenfold improvement of limits on T violation in thallium fluoride. *Physical Review Letters* **63**, 2559 (1989).

[51] J. J. Hudson, B. E. Sauer, M. R. Tarbutt & E. A. Hinds. Measurement of the Electron Electric Dipole Moment Using YbF Molecules. *Physical Review Letters* **89**, 023003 (2002).

[52] J. J. Hudson, D. M. Kara, I. J. Smallman, B. E. Sauer, M. R. Tarbutt & E. A. Hinds. Improved measurement of the shape of the electron. *Nature* **473**, 493 (2011).

[53] S. Eckel, P. Hamilton, E. Kirilov, H. W. Smith & D. DeMille. Search for the electron electric dipole moment using Ω-doublet levels in PbO. *Physical Review A* **87**, 052130 (2013).

[54] H. Loh, K. C. Cossel, M. C. Grau, K. K. Ni, E. R. Meyer, J. L. Bohn, J. Ye & E. A. Cornell. Precision Spectroscopy of Polarized Molecules in an Ion Trap. *Science* **342**, 1220 (2013).

[55] B. V. Vasil'ev & E. V. Kolycheva. Measurement of the electric dipole moment of the electron with a quantum interferometer. *Journal of Experimental and Theoretical Physics* **74**, 243 (1977).

[56] B. J. Heidenreich, O. T. Elliott, N. D. Charney, K. A. Virgien, A. W. Bridges, M. A. McKeon, S. K. Peck, D. Krause Jr., J. E. Gordon, L. R. Hunter & S. K. Lamoreaux. Limit on the Electron Electric Dipole Moment in Gadolinium-Iron Garnet. *Physical Review Letters* **95**, 253004 (2005).

[57] Y. J. Kim, C-Y Liu, S. K. Lamoreaux & G. Reddy. Experimental search for the electron Electric Dipole Moment using solid state techniques. *Journal of Physics: Conference Series* **312**, 102009 (2011).

[58] S. Eckel, A. O. Sushkov & S. K. Lamoreaux. Limit on the Electron Electric Dipole Moment Using Paramagnetic Ferroelectric $Eu_{0.5}Ba_{0.5}TiO_3$. *Physical Review Letters* **109**, 193003 (2012).

[59] M. Pospelov & A. Ritz. Electric dipole moments as probes of new physics. *Annals of Physics* **318**, 119 (2005).

[60] J. Engel, M. J. Ramsey-Musolf & U. van Kolck. Electric dipole moments of nucleons, nuclei, and atoms: The Standard Model and beyond. *Progress in Particle and Nuclear Physics* **71**, 21 (2013).

[61] C. Patrignani *et al.* (Particle Data Group). Supersymmetry, Part II (Experiment). *Chinese Physics C* **40**, 100001 (2016).

[62] L. I. Schiff. Measurability of Nuclear Electric Dipole Moments. *Physical Review* **132**, 2194 (1963).

[63] E. A. Hinds. Testing Time Reversal Symmetry Using Molecules. *Physica Scripta* **T70**, 34 (1997).

[64] P. G. H. Sandars. The Electric Dipole Moment of an Atom. *Physics Letters* **14**, 194 (1965).

[65] V. A. Dzuba & V. V. Flambaum. Calculation of the (T, P)-odd electric dipole moment of thallium and cesium. *Physical Review A* **80**, 062509 (2009).

[66] P. G. H. Sandars. Measurability of the Proton Electric Dipole Moment. *Physical Review Letters* **19**, 1396 (1967).

[67] J. J. Hudson. *Measuring the electric dipole moment of the electron with YbF molecules.* Ph.D. thesis, University of Sussex (2001).

[68] L. V. Skripnikov, A. N. Petrov & A. V. Titov. Theoretical study of ThO for the electron electric dipole moment search. *Journal of Chemical Physics* **139**, 221103 (2013).

[69] M. K. Nayak & R. K. Chaudhuri. Calculation of the electron-nucleus scalar-pseudoscalar interaction constant W_s for YbF and BaF: A perturbative approach. *Physical Review A* **78**, 012506 (2008).

[70] S. Peterson, R. E. Adams & D. A. Douglas Jr. *Properties of Thorium, its Alloys, and its Compounds* (Oak Ridge National Laboratory, Tennesse, 1965). Available at: http://web.ornl.gov/info/reports/1965/3445601336962.pdf.

[71] M. G. Kozlov. Enhancement of the electric dipole moment of the electron in the YbF molecule. *Journal of Physics B: Atomic, Molecular and Optical Physics* **30**, L607 (1997).

[72] A. N. Petrov, A. V. Titov, T. A. Isaev, N. S. Mosyagin & D. DeMille. Configuration-interaction calculation of hyperfine and P, T-odd constants on ^{207}PbO excited states for electron electric-dipole-moment experiments. *Physical Review A* **72**, 022505 (2005).

[73] A. N. Petrov, N. S. Mosyagin, T. A. Isaev & A. V. Titov. Theoretical study of HfF^+ in search of the electron electric dipole moment. *Physical Review A* **76**, 030501 (2007).

[74] L. V. Skripnikov & A. V. Titov. Theoretical study of ThF^+ in the search for T, P-violation effects: Effective state of a Th atom in ThF^+ and ThO compounds. *Physical Review A* **91**, 042504 (2015).

[75] J. Lee, E. R. Meyer, R. Paudel, J. L. Bohn & A. E. Leanhardt. An electron electric dipole moment search in the $X^3\Delta_1$ ground state of tungsten carbide molecules. *Journal of Modern Optics* **56**, 2005 (2009).

[76] A. C. Vutha, W. C. Campbell, Y. V. Gurevich, N. R. Hutzler, M. Parsons, D. Patterson, E. Peitrik, B. Spaun, J. M. Doyle, G. Gabrielse & D. DeMille. Search for the electric dipole moment of the electron with thorium monoxide. *Journal of Physics B: Atomic, Molecular and Optical Physics* **43**, 074007 (2010).

[77] A. C. Vutha, B. Spaun, Y. V. Gurevich, N. R. Hutzler, E. Kirilov, J. M. Doyle, G. Gabrielse & D. DeMille. Magnetic and electric dipole moments of the $H\ ^3\Delta_1$ state in ThO. *Physical Review A* **84**, 034502 (2011).

[78] D. M. Kara, I. J. Smallman, J. J. Hudson, B. E. Sauer, M. R. Tarbutt & E. A. Hinds. Measurement of the electron's electric dipole moment using YbF molecules: methods and data analysis. *New Journal of Physics* **14**, 103051 (2012).

[79] N. R. Hutzler. *A New Limit on the Electron Electric Dipole Moment: Beam Production, Data Interpretation, and Systematics.* Ph.D. thesis, Harvard University (2014).

[80] C. D. Panda, B. R. O'Leary, A. D. West, J. Baron, P. W. Hess, C. Hoffman, E. Kirilov, C. B. Overstreet, E. P. West, D. DeMille, J. M. Doyle & G. Gabrielse. Stimulated Raman adiabatic passage preparation of a coherent superposition of ThO $H^3\Delta_1$ states for an improved electron electric-dipole-moment measurement. *Physical Review A* **93**, 052110 (2016).

[81] A. E. Leanhardt, J. L. Bohn, H. Loh, P. Maletinsky, E. R. Meyer, L. C. Sinclair, R. P. Stutz & E. A. Cornell. High-resolution spectroscopy on trapped molecular ions in rotating electric fields: A new approach for measuring the electron electric dipole moment. *Journal of Molecular Spectroscopy* **270**, 1 (2011).

[82] M. Grau. *Measuring the Electron Electric Dipole Moment with Trapped Molecular Ions.* Ph.D. thesis, University of Colorado (2016).

[83] D. N. Gresh, K. C. Cossel, Y. Zhou, J. Ye & E. A. Cornell. Broadband velocity modulation spectroscopy of ThF^+ for use in a measurement of the electron electric dipole moment. *Journal of Molecular Spectroscopy* **319**, 1 (2015).

[84] J. Lee, J. Chen, L. V. Skripnikov, A. N. Petrov, A. V. Titov, N. S. Mosyagin & A. E. Leanhardt. Optical spectroscpoy of tungsten carbide for uncertainty analysis in electron electric-dipole-moment search. *Physical Review A* **8**, 022516 (2013).

[85] M. R. Tarbutt, B. E. Sauer, J. J. Hudson & E. A. Hinds. Design for a fountain of YbF molecules to measure the electron's electric dipole moment. *New Journal of Physics* **15**, 053034 (2013).

[86] I. I. Rabi, J. R. Zacharias, S. Millman & P. Kusch. A New Method of Measuring Nuclear Magnetic Moment. *Physical Review* **53**, 318 (1939).

[87] N. F. Ramsey. A Molecular Beam Resonance Method with Separated Oscillating Fields. *Physical Review* **78**, 695 (1950).

[88] N. F. Ramsey. *Molecular Beams* (Oxford University Press, 1956).

[89] J. A. Devlin. *Progress towards a more sensitive measurement of the electron electric dipole moment with YbF*. Ph.D. thesis, Imperial College London (2015).

[90] I. J. Smallman. *A New Measurement of the Electron Electric Dipole Moment Using Ytterbium Fluoride*. Ph.D. thesis, Imperial College London (2013).

[91] J. Brown & A. Carrington. *Rotational Spectroscopy of Diatomic Molecules* (Cambridge University Press, 2003).

[92] J. Wang. *Laser and Radiofrequency Spectroscopy of Ytterbium Fluoride Ground State*. Ph.D. thesis, Yale University (1996).

[93] K. L. Dunfield, C. Linton, T. E. Clarke, J. McBride, A. G. Adam & J. R. D. Peers. Laser Spectroscopy of the Lanthanide Monofluorides: Analysis of $A^2\Pi - X^2\Sigma^+$ Transition in Ytterbium Monofluoride. *Journal of Molecular Spectroscopy* **174**, 433–445 (1995).

[94] B. E. Sauer, J. Wang & E. A. Hinds. Laser-rf double resonance spectroscopy of ^{174}YbF in the $X\ ^2\Sigma^+$ state: Spin-rotation, hyperfine interactions, and the electric dipole moment. *The Journal of Chemical Physics* **105**, 7412 (1996).

[95] B. E. Sauer, S. B. Cahn, M. G. Kozlov, G. D. Redgrave & E. A. Hinds. Perturbed hyperfine doubling in the $A\ ^2\Pi_{1/2}$ and [18.6]0.5 states of YbF. *The Journal of Chemical Physics* **110**, 8424 (1999).

[96] X. Zhuang, A. Le, T. C. Steimle, N. E. Bullied, I. J. Smallman, R. J. Hendricks, S. M. Skoff, J. J. Hudson, B. E. Sauer E. A. Hinds & M. R. Tarbutt. Franck-Condon factors and radiative lifetime of the $A^2\Pi_{1/2} - X^2\Sigma^+$ transition of ytterbium monofluoride, YbF. *Physical Chemistry Chemical Physics* **13**, 19013 (2011).

[97] D. J. Berkeland & M. G. Boshier. Destabilization of dark states and optical spectroscopy in Zeeman-degenerate atomic systems. *Physical Review A* **65**, 033413 (2002).

[98] M. O. Scully & M. Suhail Zubairy. *Quantum Optics* (Cambridge University Press, 1997).

[99] B. E. Sauer, J. A. Devlin, J. J. Hudson, D. M. Kara, I. J. Smallman, M. R. Tarbutt & E. A. Hinds. Time reversal symmetry violation in the YbF molecule. *Hyperfine Interactions* **214**, 119 (2013).

[100] S. Truppe. *New Physics with Cold Molecule: Precise Microwave Spectroscopy of CH and the Development of a Microwave Trap.* Ph.D. thesis, Imperial College London (2013).

[101] D. M. Kara. *Toward an electron electric dipole moment measurement using Ytterbium Fluoride.* Ph.D. thesis, Imperial College London (2010).

[102] B. E. Sauer, D. M. Kara, J. J. Hudson, M. R. Tarbutt, & E. A. Hinds. A robust floating nanoammeter. *Review of Scientific Instruments* **78**, 126102 (2008).

[103] G. E. Harrison, M. A. Player & P. G. H. Sandars. A multichannel phase-sensitive detection method using orthogonal square waveforms. *Journal of Physics E: Scientific Instruments* **4**, 750 (1971).

[104] J. J. Hudson, M. R. Tarbutt, B. E. Sauer & E. A. Hinds. Stochastic multi-channel lock-in detection. *New Journal of Physics* **16**, 013005 (2014).

[105] B. Efron & R. J. Tibshirani. *An Introduction to the Bootstrap* (Chapman & Hall/CRC, 1998).

[106] I. M. Rabey, J. A. Devlin, E. A. Hinds & B. E. Sauer. Low magnetic Johnson noise electric field plates for precision measurement. *Review of Scientific Instruments* **87**, 115110 (2016).

[107] S. M. Skoff. *Buffer gas cooling of YbF molecules.* Ph.D. thesis, Imperial College London (2011).

[108] S. M. Skoff, R. J. Hendricks, C. D. J. Sinclair, J. J. Hudson, D. M. Segal, B. E. Sauer, E. A. Hinds & M. R. Tarbutt. Diffusion, thermalization, and optical pumping of YbF molecules in a cold buffer-gas cell. *Physical Review A* **83**, 023418 (2011).

[109] H. Ashworth. *Towards an improved measurement of the electron electric dipole moment.* Ph.D. thesis, Imperial College London (2008).

[110] B. C. Regan. *A Search for Violation of Time-Reversal Symmetry in Atomic Thallium.* Ph.D. thesis, University of California at Berkeley (1992).

[111] M. R. Tarbutt, J. J. Hudson, B. E. Sauer & E. A. Hinds. Prospects for measuring the electric dipole moment of the electron using electrically trapped polar molecules. *Faraday Dicussions* **142**, 37–56 (2009).

[112] C. P. Pearman, C. S. Adams, S. G. Cox, P. F. Griffin, D. A. Smith & I. G. Hughes. Polarization spectroscopy of a closed atomic transition: applications to laser frequency locking. *Journal of Physics B: Atomic, Molecular and Atomic Physics* **35**, 5141 (2002).

[113] V. Zhelyazkova. *Laser Cooling of CaF Molecules*. Ph.D. thesis, Imperial College London (2014).

[114] V. Shah, S. Knappe, P. D. D. Schwindt & J. Kitching. Subpicotesla atomic magnetometry with a microfabricated vapour cell. *Nature* **1**, 649 (2007).

[115] C. T. Munger Jr. Magnetic Johnson noise constraints on electron electric dipole moment experiments. *Physical Review A* **72**, 012506 (2005).

[116] S. K. Lamoreaux. Feeble magnetic fields generated by thermal charge fluctuations in extended metallic conductors: Implications for electric-dipole moment experiments. *Physical Review A* **60**, 1717 (1999).

[117] T. Varpula & T. Poutanen. Magnetic field fluctuations arising from thermal motion of electric charge in conductors. *Journal of Applied Physics* **55**, 4015 (1984).

[118] A. C. Vutha. *A search for the electric dipole moment of the electron using thorium monoxide*. Ph.D. thesis, Yale University (2011).

[119] N. Solmeyer. *Progress towards an electron electric dipole moment measurement with laser-cooled atoms*. Ph.D. thesis, Pennsylvania State University (2013).

[120] J. J. Hudson, H. T. Ashworth, D. M. Kara, M. R. Tarbutt, B. E. Sauer & E. A. Hinds. Pulsed beams as field probes for precision measurement. *Physical Review A* **76**, 033410 (2007).

[121] R. A. Kishek, Y. Y. Lau, L. K. Ang, A. Valfells & R. M. Gilgenbach. Multipactor discharge on metals and dielectrics: Historical review and recent theories. *Physics of Plasmas* **5**, 2120 (1998).

[122] N. Balcon, D. Payan, M. Belhaj, T. Tondu & V. Inguimbert. Secondary Electron Emission on Space Materials: Evaluation of the Total Secondary Electron Yield From Surface Potential Measurements. *IEEE Transactions on Plasma Science* **40**, 282 (2012).

[123] M. I. Patino, Y. Raitses, B. E. Koel & R. E. Wirz. Analysis of secondary electron emission for conducting materials using 4-grid LEED/AES optics. *Journal of Applied Physics D: Applied Physics* **48**, 195204 (2015).

[124] B. K. Stuhl, B. C. Sawyer, D. Wang & J. Ye. Magneto-optical Trap for Polar Molecules. *Physical Review Letters* **101**, 243002 (2008).

[125] Y. Fan, H. Yang, M. Li & G. Zou. Evaluation of the microwave absoption property of flake graphite. *Materials Chemistry and Physics* **115**, 696 (2009).